Cryogenic Torsion Pendulum for Observing Low-frequency Gravity Gradient Fluctuation

低周波重力勾配変動観測のための低温ねじれ振り子の開発

Tomofumi Shimoda

Department of Physics, Graduate School of Science,

The University of Tokyo

December 2019

Abstract

Gravity gradient fluctuations are an essential observational target for precise measurements of the motion of mass. Currently, the low-frequency fluctuations around 0.1 Hz are targeted for earthquake early warning using terrestrial gravity gradient fluctuations, and for observing the gravitational waves from intermediate-mass black holes. Therefore, development of highly sensitive gravity gradiometers is essential for such scientific observations. A torsion-bar antenna (TOBA) is a ground-based detector proposed for measuring low-frequency gravity gradient fluctuations. The low mechanical resonant frequency of TOBA enables gravity gradient observations of frequencies around 0.1 Hz even on the ground where the detector is bound by the strong gravitational field. Several prototypes of TOBA and component technologies have been developed and investigated to understand the characteristics of detector noises. To realize the scientific observations using TOBA, the instrumental noise must be sufficiently reduced, based on the knowledge gained from the prototypes. The main technical issues are a cryogenic system for thermal noise reduction, a low-frequency vibration isolation system for seismic noise reduction, and an optical system for a precise measurement of the rotation of the torsion pendulum. In particular, the cryogenic cooling for the torsion pendulum is high priority as previous studies in this area have been few and far between. Moreover, earthquake detectability and localizability using TOBA have not been well clarified so far. Therefore, these topics must be investigated to establish a realistic gravity-based earthquake early warning system.

In this thesis, a 35 cm-scale TOBA (Phase-III TOBA) is proposed and developed for the purpose of technical demonstration as well as the earthquake early warning using TOBA. Both theoretical and experimental aspects have been investigated: On the theoretical side, the detectability of earthquakes using TOBA, which is sensitive only to the horizontal gravity gradient, was evaluated for the first time. A comparison with other types of gravity gradiometers showed that TOBA has a good detectability for both strike-slip and dip-slip earthquakes even without measuring the vertical gravity gradient. Additionally, the localizability of the epicenter using an array of TOBAs was also simulated to investigate a suitable detector arrangement, the required calibration accuracy of the detectors, and the necessary information of the source fault parameters.

On the experimental side, the system of Phase-III TOBA has been designed to achieve a sensitivity of $10^{-15}\ /\sqrt{\mathrm{Hz}}$, which is required for earthquake detection. In addition to the known noise-suppression methods, the design also includes the reduction of nonlinear vibration transfer noise, which has recently been discovered, and a newly proposed highly sensitive angular sensor. The cryogenic system, which is the most essential part of Phase-III TOBA, was then experimentally demonstrated by successfully cooling a prototype 35 cm-scale torsion pendulum to 6.1 K; this establishes the basis of the cryogenic system in Phase-III TOBA.

The abovementioned theoretical and experimental works have opened the path to development of gravity-based earthquake early warning system using Phase-III TOBA. This thesis reports the details of these results.

要旨 (in Japanese)

重力勾配の変動は質量の動きを精密に計測できる重要な観測量である。近年特に 0.1Hz 付近の低周波における地球重力勾配変動を地震速報に利用する研究や、同じく低周波の重力波観測による中間質量ブラックホール連星合体の研究などが注目されており、それらを観測しうる高感度な重力勾配計の開発が求められている。ねじれ振り子型重力勾配計 TOBA（TOrsion-Bar Antenna）はそれらの観測を目的として提案された地上低周波重力勾配計である。共振周波数が低いねじれ振り子を用いることで、重力による束縛の強い地上においても 0.1Hz 付近の重力勾配変動の観測が可能になるというメリットがある。これまでに複数のプロトタイプ開発や要素研究によって検出器雑音の特性などが明らかになってきた。地震速報や重力波観測を実現するためには、得られた知見をもとに検出器雑音を十分に低減する必要がある。主要な技術的課題としては、熱雑音低減のための低温化技術の開発、地面振動雑音低減のための低周波防振システムの開発、そして振り子回転の精密計測のための光学系開発などがある。特に低温化技術についてはねじれ振り子における先行研究が少ないため開発の必要性が高い。加えて理論面でも、地震観測については TOBA による検出能力や震源位置決定精度などは明らかになっていない点も多い。TOBA の高感度化および現実的な地震観測手法の確立のためにはこれらのトピックについて研究が必要である。

本研究では雑音低減の技術実証と地震観測の実現を目指した 35 cm スケールの TOBA (Phase-III TOBA) を提案し、理論と実験の両面で研究を行った。理論面では、水平重力勾配のみに感度を持つ TOBA について地震検出能力を初めて評価した。他タイプの検出器と比較した結果、鉛直重力勾配の観測ができなくとも strike-slip 型の地震については高い検出能力を持つことや dip-slip 型についても良い検出能力を持つことが明らかになった。さらに複数台の TOBA を用いた震源位置決定のシミュレーションも行い、十分な精度で位置決定するために必要な検出器配置やキャリブレーション精度、震源に関する事前情報の精度などについても初めて調査した。

実験面では地震観測に要求される感度 $10^{-15}\ /\sqrt{\mathrm{Hz}}$ を実現するための検出器設計を行った。設計にはこれまで知られていた問題に加え、最近明らかになった非線形振動伝達雑音の低減や新しく提案された高感度角度センサなども組み込まれている。検出器構成の中でも特に技術的な重要度が高い低温システムについては実験による実証も行い、35 cm スケールのねじれ振り子を 6.1 K まで冷却することに成功し Phase-III TOBA における冷却技術の基本的な部分を確立した。

これらの理論・実験の結果によって、TOBA による地震検出実現に向けた道を拓いた。本論文ではこれらの結果の詳細について報告する。

Contents

1 Introduction

Gravity gradient fluctuations are an important observational target for various purposes including earthquake detection using Newtonian gravity gradient and astronomical observations through the detection of gravitational waves (GWs). The measurement of gravity gradient fluctuations provides unique information regarding the source mass behavior; particularly, the low-frequency fluctuations around 0.1 Hz are an important observation target, which has not been achieved so far. As both the Newtonian gravity gradient and GWs act as a tidal force on masses, these can be measured by the same detector configuration.

Gravity-based earthquake early warning (EEW) was recently proposed as a new EEW method [1]. Observations of gravity fluctuation provide information on different aspects of earthquakes from the ones observed by the current EEW system using seismic waves. Moreover, the gravity-based EEW is also expected to have advantage in early detection and magnitude estimation [2]. Gravitational signals have been detected earlier for several earthquakes [3, 4, 5, 6, 7, 8], using broadband seismometers and gravimeters. However, for faster detection and/or detection of smaller earthquakes, the gradient of the gravitational field must be measured to filter out the effect of ground acceleration. Moreover, observations around 0.1 Hz are specifically essential, as this frequency corresponds to the timescale of early warning and fault ruptures ($\sim$10 s).

Similarly, GW is another observational target that has been attracting increasing interest in the field of astronomy. Recent detections of GWs from compact binaries [9, 10, 11] have enabled the exploration of black hole population [12], identification of the origin of short gamma-ray bursts [13], and the testing of general relativity under the strong gravity [14]. Therefore, improving the observational frequency band from the existing 10 Hz to a lower frequency is one of the important future steps, as it can allow the observation of additional phenomena such as coalescences of intermediate-mass black holes (IMBHs), which in turn can provide information regarding the formation of supermassive black holes at the center of galaxies [15].

To observe these targets, TOBA (Torsion-Bar Antenna) has been proposed as a ground-based low-frequency gravity gradiometer [16], which measures the horizontal rotations of a suspended bar, induced by horizontal gravity gradients. Owing to the low resonant frequency of its torsion pendulum, TOBA can be sensitive to low-frequency fluctuations. Therefore, the main objective of TOBA is to observe GWs and to detect earthquakes using 10 m-scale suspended bars; this phase is named Final TOBA. Some prototypes of this system have been developed, which were used for characterizing several noise sources [17, 18, 19, 20, 21, 22]. To achieve the abovementioned challenging objective of Final TOBA, issues in the theoretical and experimental aspects; such as a more detailed consideration of earthquake detectability and development of noise reduction technologies, need to be addressed.

Earthquake detectability using gravity gradiometers was discussed in [2], which was based on some analytical gravity fluctuation models derived in [23, 24]; according to the study, the required sensitivity is roughly $10^{-15}\ /\sqrt{\mathrm{Hz}}$ at 0.1 Hz. This study had also performed simulations of the localization and magnitude estimation in the 2011 Tohoku-oki earthquake. For the next step towards achieving a realistic EEW system, the characteristics of the detectors must be considered: Although the previous researches have considered vertical gravitational field measurement, some detectors including TOBA are sensitive only to the horizontal gravity gradient, which has different signal amplitudes. Hence, the earthquake detectability using TOBA needs to be clarified by comparing its performance with the other detector types, for which the required sensitivity for TOBA must be confirmed first. Additionally, studying the general parameter estimability (e.g., epicenter location, focal mechanism, or magnitude) would be useful for the design strategy of gravity-based EEW systems. Furthermore, information regarding the influence of detector configuration on the parameter estimability is essential for setting requirements on the detector.

The primary requirement for detector development is to establish noise reduction technology. TOBA fundamentally suffers from different types of noises such as thermal, quantum, seismic, and Newtonian noise. Among them, reduction of thermal noise using a cryogenic system is one of the largest technical difficulties. There have been few experimental setups using a cryogenic torsion pendulum for precise measurement. A previous study had designed and used a small-scale torsion pendulum ($40 \times 40 \times 3$ mm) to determine the gravitational constant G [25]. However, as the size of the pendulum and the required sensitivity are quite different from that of TOBA, this technology cannot be applied to TOBA as it is. Similarly, although a translational cryogenic pendulum has been used for the ground-based GW detector KAGRA [26], the requirement is qualitatively different because the measurement degree of freedom (DoF) is different. Additionally, the cryogenic system design affects almost all other systems such as the optical and the mechanical systems, and hence, components must be compatible with the cryogenic temperatures. Therefore, the development of the cryogenic system is high priority.

To demonstrate noise reduction and earthquake detection, a 35 cm-scale configuration named Phase-III TOBA has been proposed in this thesis. The target sensitivity was set to 10^{-15} $/\sqrt{\mathrm{Hz}}$ at 0.1 Hz, which is the required sensitivity for earthquake detection. Phase-III TOBA is considered to be a better choice than Final TOBA because of its lower cost and better feasibility. In terms of technical developments, Phase-III TOBA is an intermediate step before moving on to Final TOBA: some of the important technologies such as the cryogenic system are developed in Phase-III TOBA, and the experimental knowledge regarding its noise properties are to be accumulated.

Two aspects of Phase-III TOBA have been investigated in this thesis: computational work on earthquake detection and experimental work on developing Phase-III TOBA.

For the computational aspect, several simulations were performed to clarify the difference between the earthquake detectability using different detectors. The detectability using TOBA, which is sensitive only to the horizontal gravity gradient, was compared with other detectors to discuss the contribution of TOBA to EEW even without the vertical gravity gradient measurement. Then, the target sensitivity of Phase-III TOBA was validated based on this comparison. The localizability of earthquakes using an array of TOBAs has also been discussed to consider a detector configuration for the development of a realistic EEW system. Some of the results were then fed back to the requirements for the detectors.

For the experimental aspect, the system of Phase-III TOBA is designed, with particular emphasis on the high-priority cryogenic system design. Additionally, the reduction of the recently discovered vibration noise [22] and implementation of a highly sensitive angular sensor were also included in the design. The cryogenic technology was then investigated experimentally using a simplified configuration of Phase-III TOBA. The performance of the designed cryogenic system was demonstrated, and the noises of the torsion pendulum under cryogenic temperatures were studied.

This thesis consists of the following chapters, as shown in Fig. 1.1. First, the observational targets of this work are introduced in Chapter 2. Next an overview of TOBA is explained in Chapter 3. Then, the results of our works are shown in the subsequent chapters; the computational topics are described in Chapter 4, the design of Phase-III TOBA is explained in Chapter 5, and the experimental results on the cryogenic system are reported in Chapter 6. Some topics of the experimental results are discussed in Chapter 7, and the thesis is concluded in Chapter 8. Appendix A and B explain the details of the new topics in this thesis, namely the nonlinear vibration transfer in the torsion pendulums and the new sensitive angular sensor using an optical cavity, respectively.

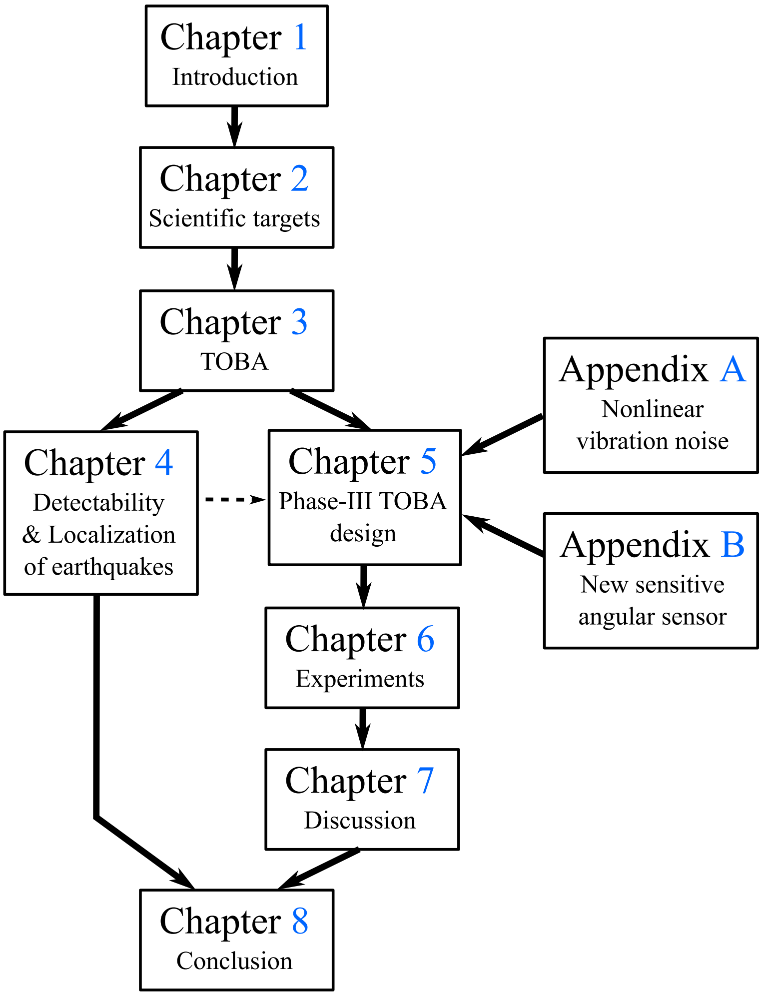

Figure 1.1: Configuration of this thesis.

2 Science of Gravity Gradient Observation

Scientific targets of gravity gradient observation around 0.1 Hz are introduced in this chapter. There are two main targets; one is a terrestrial source and another one is an astrophysical source. A representative terrestrial source is an earthquake, which redistributes the density of the ground and makes change in the Newtonian gravitational field. Such signal can be used for earthquake early warning (EEW) that is faster than seismic P-wave arrival. Another target, astrophysical sources such as binary black holes emit gravitational wave (GW). Since both the terrestrial gravity gradient and the gravitational waves act as tidal force on masses, they can theoretically be detected with a same configuration of gravity gradiometer.

In this chapter, calculation of gravity gradient signal from those sources are summarized. As preparation of mathematical framework, a gravity gradient tensor is defined in Sec. 2.1. Then the signal from earthquakes and gravitational waves are derived in Sec. 2.2 and Sec. 2.3, respectively. In Sec. 2.4, some proposed gravity gradiometers are briefly introduced.

2.1 Definition of gravity gradient tensor

A gravity gradient tensor $\boldsymbol{G}$ is defined as

$$\boldsymbol{G}(\boldsymbol{r}, t) = -\boldsymbol{\nabla} \otimes \boldsymbol{\nabla}\phi_g(\boldsymbol{r}, t). \tag{2.1}$$

Here $\phi_g(\boldsymbol{r}, t)$ is a gravitational potential. Relative gravitational acceleration between two close points $\boldsymbol{r}$ and $\boldsymbol{r} + \boldsymbol{\xi}$ is given by

$$\ddot{\boldsymbol{\xi}} = \boldsymbol{G}(\boldsymbol{r}, t) \cdot \boldsymbol{\xi} \tag{2.2}$$

Hence each component of the gravity gradient tensor represents tidal force on masses.

Dimensionless gravity strain is also used in the following sections. The

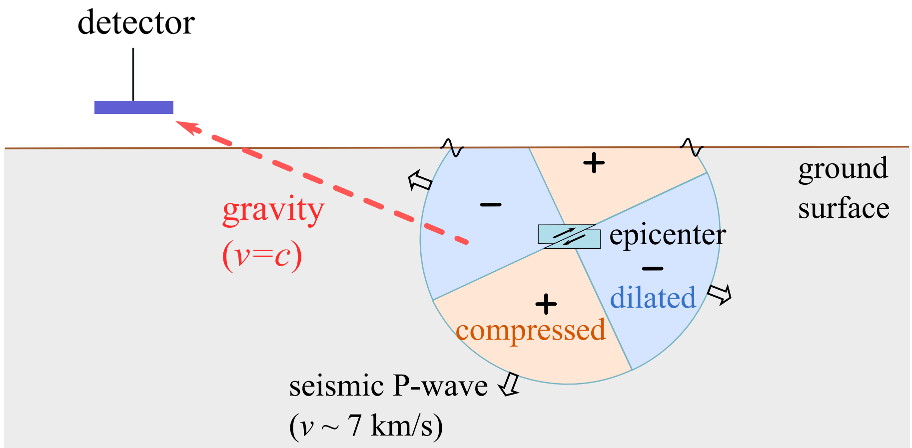

Figure 2.1: An overview of how an earthquake causes gravity perturbation preceding arrival of a seismic P-wave.

gravity strain tensor $\boldsymbol{h}(\boldsymbol{r},t)$ is related to the gravity gradient tensor by

$$\boldsymbol{h}(\boldsymbol{r},t) = \int_0^t dt' \int_0^{t'} dt'' \boldsymbol{G}(\boldsymbol{r},t'') = \begin{pmatrix} h_{xx} & h_{xy} & h_{xz} \\ h_{yx} & h_{yy} & h_{yz} \\ h_{zx} & h_{zy} & h_{zz} \end{pmatrix}. \tag{2.3}$$

Since G_{ij} is relative acceleration, its second integral h_{ij} represents the relative displacement between two free masses. Due to the apparent symmetry $G_{ij} = G_{ji}$ $(i,j = x,y,z)$ and Poisson equation $\Delta\phi_{\mathrm{g}}(\boldsymbol{r},t) = 0$, $\boldsymbol{h}$ and $\boldsymbol{G}$ has five independent components.

2.2 Earthquake early warning using gravitational signal

Earthquake is caused by dynamic rupture on a fault. The released energy propagates outward as seismic waves, and shakes the surface of the ground when the waves reach there. During this process, the density of crustal rocks is perturbed due to compression or dilation of the medium induced by the seismic waves. In an inhomogeneous medium, dislocation of the boundaries between layers of different density also contributes to the density change. These density redistributions cause detectable gravity fluctuation around the epicenter. The schematic figure is shown in Fig. 2.1.

Permanent change in gravity acceleration was first detected by a superconducting gravimeter during the 2003 Tokachi-oki earthquake (moment magnitude $M_w = 8.0$) [27]. After that, two-dimensional distributions of gravity changes were observed by GRACE (Gravity Recovery and Climate Experiment [28]) satellite for the 2004 Sumatra-Andaman earthquake ($M_w = 9.0-9.3$) [29], the 2010 Central Chile earthquake ($M_w = 8.8$) [30], and the 2011 Tohoku-oki earthquake ($M_w = 9.0$) [31]. These observations confirmed the static change of gravity by comparing the difference of gravitational field before and after the earthquakes.

Recently, it was proposed that transient changes in gravitational field associated with large earthquakes are detectable by sensitive gravimeters or gravity gradiometers [1]. It focuses on the gravity change in a short timescale ($\sim 10 - 100$ s) which is caused by propagating seismic waves. Since gravity change propagates at the speed of light, detection of such gravitational change can be a faster warning signal of earthquakes than the current warning using seismic P-waves. Additionally, the gravity signal amplitude is well correlated with the magnitude of earthquake, hence it can provide good early estimation of magnitude. The transient signal was observed during the 2011 Tohoku-oki earthquake by a superconducting gravimeter and broadband seismometers around Japan. The first detection was reported in [3], and detailed analysis in several stations are shown in [4, 5, 6, 7]. The signals agreed well with the simulation including gravity variation and induced acceleration of the ground due to the gravity change. Additional detections were recently reported for other five earthquakes [8].

Since a gravimeter or a seismometer measures relative acceleration between a free mass and a frame fixed on the ground, gravity acceleration on the free mass is not separable from the acceleration of the frame due to the equivalence principle. Hence the detections of small earthquakes ($M_w \lesssim 8$) are suffered from background seismic vibration noise. Additionally, large fraction of the gravity change in the initial few tens of seconds is cancelled with the acceleration of the ground induced by the gravity change as mentioned in [4]. This cancellation degrades the detectability of earthquakes in the early phases or from the close distances. These problems are solved by measuring the gravity gradient, or the difference of gravitational force between two close points. Since the local acceleration of the ground appears commonly in the two points, the gravity gradient signals are distinguishable from it. Therefore gravity gradiometers are suitable for actual earthquake early warning system.

The detectability of earthquakes with gravity gradiometers is discussed in [2]. It is shown that roughly $10^{-15}\ /\sqrt{\mathrm{Hz}}$ (in unit of dimensionless strain h) of sensitivity at 0.1 Hz is required to realize meaningful detections. The target frequency 0.1 Hz corresponds to the timescale of earthquakes and required warning time. With such a sensitivity, detectable range of $M_w = 7$ earthquakes within 10 seconds is about 100 km. At further distances up to 1000 km, the gravity signal can be detected preceding the arrival of seismic P-wave.

2.2.1 Transient gravitational signal in an infinite homogeneous medium

The simplest model of gravity change by earthquake is introduced in this subsection. A source of an earthquake is modeled as a point shear dislocation in an infinite homogeneous isotropic medium. The analytic formula of the transient gravity fluctuation in this case was first derived by Jan Harms [23]. The calculation is reviewed here to show how the gravity gradient is changed. The deformation is assumed to be small in the following calculations.

First, gravitational potential change $\delta\phi_g(\boldsymbol{r}, t)$ is calculated from the change of density distribution $\delta\rho(\boldsymbol{r}', t)$ as

$$\delta\phi_g(\boldsymbol{r}, t) = -G \int dV' \frac{\delta\rho(\boldsymbol{r}', t)}{|\boldsymbol{r} - \boldsymbol{r}'|}. \tag{2.4}$$

$G \simeq 6.674 \times 10^{-11}\ \mathrm{m}^3 \cdot \mathrm{kg}^{-1} \cdot \mathrm{s}^{-2}$ is Newton's gravitational constant. From the continuity equation

$$\frac{\partial\rho(\boldsymbol{r}, t)}{\partial t} = -\boldsymbol{\nabla} \cdot (\rho(\boldsymbol{r}, t)\boldsymbol{v}(\boldsymbol{r}, t)), \tag{2.5}$$

density change can be approximated to

$$\delta\rho(\boldsymbol{r}, t) \simeq -\rho_0 \boldsymbol{\nabla} \cdot \boldsymbol{u}(\boldsymbol{r}, t). \tag{2.6}$$

Here $\rho(\boldsymbol{r}, t) = \rho_0 + \delta\rho(\boldsymbol{r}, t)$ and ρ_0 is mean density of the medium. $\boldsymbol{v}$ and $\boldsymbol{u}$ are the local speed and displacement field of the medium, respectively. In the approximation, the density change and the displacement are assumed to be small. Gravitational potential can be calculated from the displacement field by using Eq. 2.4 and Eq. 2.6.

The displacement field $\boldsymbol{u}$ induced by a source in the medium is calculated from the equation of an elastic body. In a homogeneous and isotropic medium, the displacement equation for small deformation is

$$\rho_0 \frac{\partial^2 \boldsymbol{u}(\boldsymbol{r}, t)}{\partial t^2} = \boldsymbol{f}(\boldsymbol{r}, t) + (\lambda + \mu)\boldsymbol{\nabla}(\boldsymbol{\nabla} \cdot \boldsymbol{u}(\boldsymbol{r}, t)) + \mu \boldsymbol{\nabla}^2 \boldsymbol{u}(\boldsymbol{r}, t). \tag{2.7}$$

λ and μ are Lame's constants, and the first term $\boldsymbol{f}$ is body force on the medium.

Here the source of earthquake is modeled as a point shear dislocation as shown in Fig. 2.2. The slipping surface is called a fault, which lies in xy-plane, and the slip direction is set to x-axis. This dislocation source is equivalent to 'double couple' body force as

$$\boldsymbol{f}(\boldsymbol{r}, t) = -M(t) \begin{pmatrix} \frac{\partial}{\partial z}\delta(\boldsymbol{r}) \\ 0 \\ \frac{\partial}{\partial x}\delta(\boldsymbol{r}) \end{pmatrix}. \tag{2.8}$$

$M(t)$ is called seismic moment function which is defined as $M(t) = \mu A \bar{u}(t)$ from the area of the fault plane A and the averaged displacement of the fault

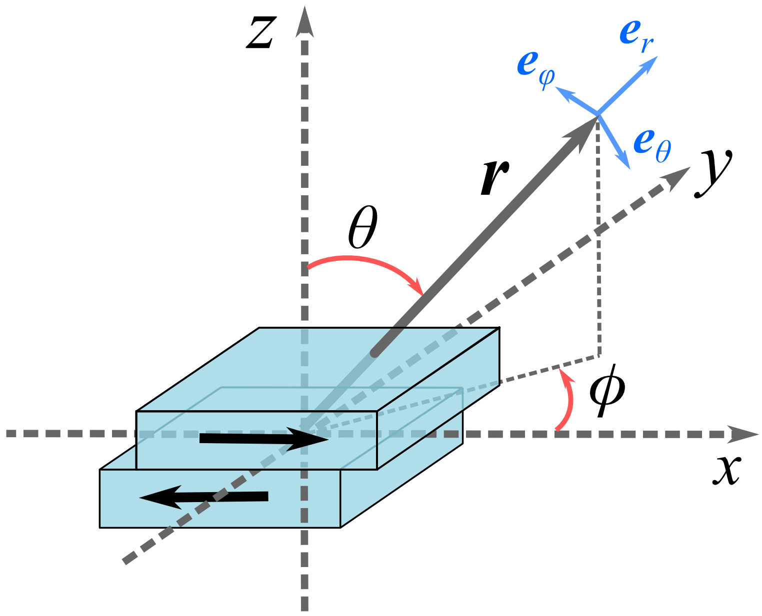

Figure 2.2: A point shear dislocation as a source of an earthquake. The origin is taken at the epicenter. The fault plane lies in xy-plane, and the slip direction is set to x-axis.

$\bar{u}(t)$. The final value of the seismic moment $M_0 \equiv M(t \to \infty)$ is associated with the moment magnitude M_w of the earthquake by

$$M_w = \frac{2}{3}(\log_{10} M_0 - 9.1). \tag{2.9}$$

The displacement field induced by the point shear dislocation can be calculated from Eq. (2.7) and (2.8). Detailed process of calculation is given by the textbook [32]. The resultant displacement field is

$$\begin{aligned} \boldsymbol{u}(\boldsymbol{r},t) &= \frac{1}{4\pi\rho_0 r^4}\boldsymbol{A}_N \int_{r/\alpha}^{r/\beta} d\tau \tau M(t-\tau) \\ &+\frac{1}{4\pi\rho_0\alpha^2 r^2}\boldsymbol{A}_{IP} M(t-r/\alpha) + \frac{1}{4\pi\rho_0\beta^2 r^2}\boldsymbol{A}_{IS} M(t-r/\beta) \\ &+\frac{1}{4\pi\rho_0\alpha^3 r}\boldsymbol{A}_{FP}\dot{M}(t-r/\alpha) + \frac{1}{4\pi\rho_0\beta^3 r}\boldsymbol{A}_{FS}\dot{M}(t-r/\beta), \end{aligned} \tag{2.10}$$

where

$$\begin{aligned} \boldsymbol{A}_N &= 9\sin 2\theta\cos\phi\,\boldsymbol{e}_r - 6(\cos 2\theta\cos\phi\,\boldsymbol{e}_\theta - \cos\theta\sin\phi\,\boldsymbol{e}_\phi) \\ \boldsymbol{A}_{IP} &= 4\sin 2\theta\cos\phi\,\boldsymbol{e}_r - 2(\cos 2\theta\cos\phi\,\boldsymbol{e}_\theta - \cos\theta\sin\phi\,\boldsymbol{e}_\phi) \\ \boldsymbol{A}_{IS} &= -3\sin 2\theta\cos\phi\,\boldsymbol{e}_r + 3(\cos 2\theta\cos\phi\,\boldsymbol{e}_\theta - \cos\theta\sin\phi\,\boldsymbol{e}_\phi) \\ \boldsymbol{A}_{FP} &= \sin 2\theta\cos\phi\,\boldsymbol{e}_r \\ \boldsymbol{A}_{FS} &= \cos 2\theta\cos\phi\,\boldsymbol{e}_\theta - \cos\theta\sin\phi\,\boldsymbol{e}_\phi. \end{aligned} \tag{2.11}$$

α and β are the speed of P-wave and S-wave given by

$$\alpha = \sqrt{\frac{\lambda + 2\mu}{\rho_0}}, \qquad \beta = \sqrt{\frac{\mu}{\rho_0}}. \tag{2.12}$$

Each column of Eq. (2.10) corresponds to near-field component, intermediate-field components and far-field components, respectively, which has different dependence of the distance r. $\boldsymbol{A}$ is the angular distribution of each term based on radial coordinates defined in Fig. 2.2. From divergence of Eq. (2.10), the density distribution Eq. (2.6) is

$$\delta\rho(\boldsymbol{r}, t) = \frac{3\sin 2\theta \cos\phi}{4\pi\alpha^2} \left(\frac{1}{r^3} M\left(t - \frac{r}{\alpha}\right) + \frac{1}{\alpha r^2}\dot{M}\left(t - \frac{r}{\alpha}\right) + \frac{1}{3\alpha^2 r}\ddot{M}\left(t - \frac{r}{\alpha}\right)\right) \tag{2.13}$$

The S-wave terms of Eq. (2.10) which contain β disappears in Eq. (2.13). This is because S-wave is a transverse shear wave that makes no density change in the infinite homogeneous medium. Hence the deformation expands at the speed of P-wave, α, which is typically around 7 km/s in the crust.

In order to calculate the gravitational potential, the following discussion is restricted to the time before P-wave arrives at the observation point $\boldsymbol{r}$. It mathematically means that $|\boldsymbol{r}| > |\boldsymbol{r}'|$ in the integral of Eq. (2.4). In this case, the inverse distance term $1/|\boldsymbol{r} - \boldsymbol{r}'|$ can be expanded using Legendre polynomials $P_l(x)$ as

$$\begin{aligned} \frac{1}{|\boldsymbol{r} - \boldsymbol{r}'|} &= \sum_{l=0}^{\infty} \frac{r'^l}{r^{l+1}} P_l(\cos\gamma) & (2.14) \\ &= \sum_{l=0}^{\infty} \sum_{m=-l}^{l} \frac{4\pi}{2l+1} \frac{r'^l}{r^{l+1}} \left(Y_l^m(\theta', \phi')\right)^* Y_l^m(\theta, \phi), & (2.15) \end{aligned}$$

where γ is the relative angle between $\boldsymbol{r}$ and $\boldsymbol{r}'$, and Y_l^m are spherical harmonics. In the second step, the spherical harmonic addition theorem is applied to $P_l(\cos\gamma)$. Since the angular dependence of Eq. (2.13) is

$$\sin 2\theta \cos\phi = \sqrt{\frac{8\pi}{15}} \left(Y_2^{-1}(\theta, \phi) - Y_2^1(\theta, \phi) \right), \tag{2.16}$$

the integral of Eq. (2.4) can be calculated to

$$\begin{aligned} \delta\phi_g(\boldsymbol{r}, t) &= -G \sum_{l=0}^{\infty} \sum_{m=-l}^{l} \int_0^r dr' r'^2 \int d\Omega' \delta\rho(\boldsymbol{r}', t) \frac{4\pi}{2l+1} \frac{r'^l}{r^{l+1}} \left(Y_l^m(\theta', \phi')\right)^* Y_l^m(\theta, \phi) \\ &= -\frac{3G \sin 2\theta \cos\phi}{5\alpha^2 r^3} \\ &\quad \times \int_0^r dr' \left(r' M\left(t - \frac{r'}{\alpha}\right) + \frac{r'^2}{\alpha}\dot{M}\left(t - \frac{r'}{\alpha}\right) + \frac{r'^3}{3\alpha^2}\ddot{M}\left(t - \frac{r'}{\alpha}\right)\right). \end{aligned} \tag{2.17}$$

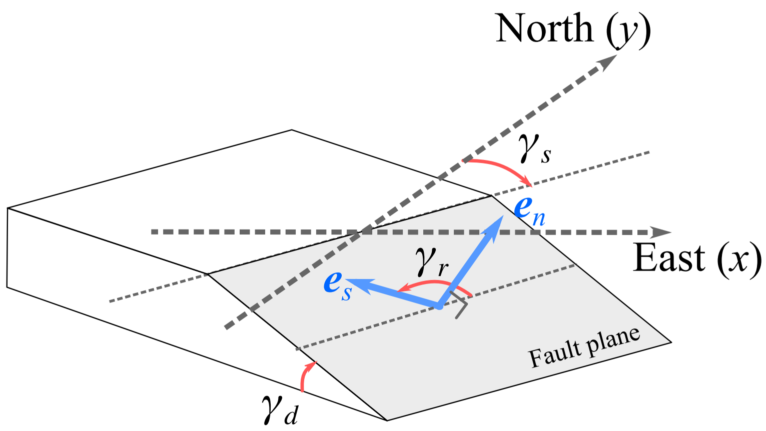

Figure 2.3: A focal mechanism and definitions of strike angle, dip angle and rake angle.

Here the orthonormality of Y_l^m is used in the angular integral $\int d\Omega'$. Using $\dot{M}(t-r'/\alpha) = -\alpha\frac{d}{dr'}M(t-r'/\alpha)$, the second and the third term in the integral of Eq. (2.17) are modified to

$$\int_0^r dr' \frac{r'^2}{\alpha}\dot{M}\left(t-\frac{r'}{\alpha}\right) = \int_0^r dr' \frac{r'^3}{3\alpha^2}\ddot{M}\left(t-\frac{r'}{\alpha}\right) = 2\int_0^r dr' r' M\left(t-\frac{r'}{\alpha}\right). \tag{2.18}$$

Moreover, the integral can be simplified to

$$\int_0^r dr' r' M\left(t-\frac{r'}{\alpha}\right) = \alpha^2 \iint dt^2 M(t) \equiv \alpha^2 \mathcal{I}_2[M(t)] \tag{2.19}$$

under the condition of $r > \alpha t$. The n-th integral is defined as $\mathcal{I}_n[\cdot]$ here. Then the gravitational potential change is

$$\delta\phi_g(\boldsymbol{r}, t) = -\frac{3G\sin 2\theta\cos\phi}{r^3}\mathcal{I}_2[M(t)]. \tag{2.20}$$

Derivatives of this equation give the gravity gradient tensor. Eq. (2.20) does not depend on α, hence the gravity change before the arrival of the P-wave behaves as caused by a point quadruple source at the epicenter.

Next Eq. (2.20) is rewritten for the general orientation of the source. The motion of the fault is called the focal mechanism, which is parametrized by three angles; the strike angle γ_s, the dip angle γ_d and the rake angle γ_r. These angles are defined as Fig. 2.3. The normal vector of the fault is $\boldsymbol{e}_n$, and the unit vector in the slip direction is $\boldsymbol{e}_s$. γ_s is the azimuth of the intersection line between the fault plane and the horizontal plane from the north direction. γ_d is the tilt of the fault plane, and γ_r is the direction of slip. In Fig. 2.2, $\boldsymbol{e}_n$ and $\boldsymbol{e}_s$ are aligned to z and x axis, respectively. Therefore Eq. (2.20) can be rewritten with $\boldsymbol{e}_n$, $\boldsymbol{e}_s$ and the radial vector $\boldsymbol{e}_r$ as

$$\delta\phi_g(\boldsymbol{r}, t) = -\frac{6G}{r^3}(\boldsymbol{e}_n\cdot\boldsymbol{e}_r)(\boldsymbol{e}_s\cdot\boldsymbol{e}_r)\mathcal{I}_2[M(t)], \tag{2.21}$$

where

$$\boldsymbol{e}_n = \begin{pmatrix} \cos\gamma_s \sin\gamma_d \\ -\sin\gamma_s \sin\gamma_d \\ \cos\gamma_d \end{pmatrix}, \quad \boldsymbol{e}_s = \begin{pmatrix} -\cos\gamma_s \cos\gamma_d \sin\gamma_r + \sin\gamma_s \cos\gamma_r \\ \sin\gamma_s \cos\gamma_d \sin\gamma_r + \cos\gamma_s \cos\gamma_r \\ \sin\gamma_d \sin\gamma_r \end{pmatrix}. \tag{2.22}$$

The gravity gradient tensor $\boldsymbol{G}$ is

$$\boldsymbol{G}(\boldsymbol{r},t) = -\boldsymbol{\nabla} \otimes \boldsymbol{\nabla}\delta\phi_g(\boldsymbol{r},t) = -\frac{6G}{r^5}\boldsymbol{S}(\theta,\phi)\mathcal{I}_2[M(t)], \tag{2.23}$$

where

$$\begin{aligned} \boldsymbol{S}(\theta,\phi) \;=\;& 5(\boldsymbol{e}_s \cdot \boldsymbol{e}_r)(\boldsymbol{e}_n \cdot \boldsymbol{e}_r)(3\boldsymbol{1} - 7\boldsymbol{e}_r \otimes \boldsymbol{e}_r) \\ & + 4(\boldsymbol{e}_n \otimes \boldsymbol{e}_s + \boldsymbol{e}_s \otimes \boldsymbol{e}_n) \\ & + 5\left((\boldsymbol{e}_n \times \boldsymbol{e}_r) \otimes (\boldsymbol{e}_s \times \boldsymbol{e}_r) + (\boldsymbol{e}_s \times \boldsymbol{e}_r) \otimes (\boldsymbol{e}_n \times \boldsymbol{e}_r)\right). \end{aligned} \tag{2.24}$$

The gravity strain (Eq. (2.3)) is

$$\boldsymbol{h}(\boldsymbol{r},t) = \int\!\!\int dt \boldsymbol{G}(\boldsymbol{r},t) = -\frac{6G}{r^5}\boldsymbol{S}(\theta,\phi)\mathcal{I}_4[M(t)]. \tag{2.25}$$

The gravity strain signal can be calculated by Eq. (2.25) with the information of focal mechanism $(\gamma_s, \gamma_d, \gamma_r)$ and seismic moment function $M(t)$. Note again that this solution is valid only before the seismic waves arrive at the observation point, i.e. $r > \alpha t$. This condition is reasonable because any detectors will not be able to get meaningful ovservational signal while they are shaken by the large seismic waves.

The time derivative of the seismic moment function, $\dot{M}(t)$, is called a moment rate function or a source time function. It means how much energy is released per unit time during the rupture of the fault. $\dot{M}(t)$ for actual earthquakes in the magnitude range of $7.3 < M_w < 7.7$ are shown in Fig. 2.4. Though the plotted earthquakes have similar final magnitudes, the shape of the functions are quite different for each event. Following [2], here the moment rate function is modeled as

$$\dot{M}(t) = \begin{cases} 1.48\frac{M_0}{T}(t/T)^2 & (0 < t < T) \\ 1.48\frac{M_0}{T}\left(1 - (t/T - 1)^2\right)^6 & (T < t < 2T) \end{cases}, \tag{2.26}$$

where T is the half duration of the fault rupture. Eq. (2.26) assumes self-similarity of the source, which means that the initial source evolution of a large earthquake is identical to a small earthquake. The duration of the rupture is empirically known to correlate with the magnitude [34] as

$$2T = (M_0/10^{16}\,\mathrm{N \cdot m})^{1/3}. \tag{2.27}$$

For example, $T = 14$ s for $M_w = 7.5$. This relation is used in the following calculations, Note that the deviation from Eq. (2.26) is large for the actual events, as indicated in Fig. 2.4.

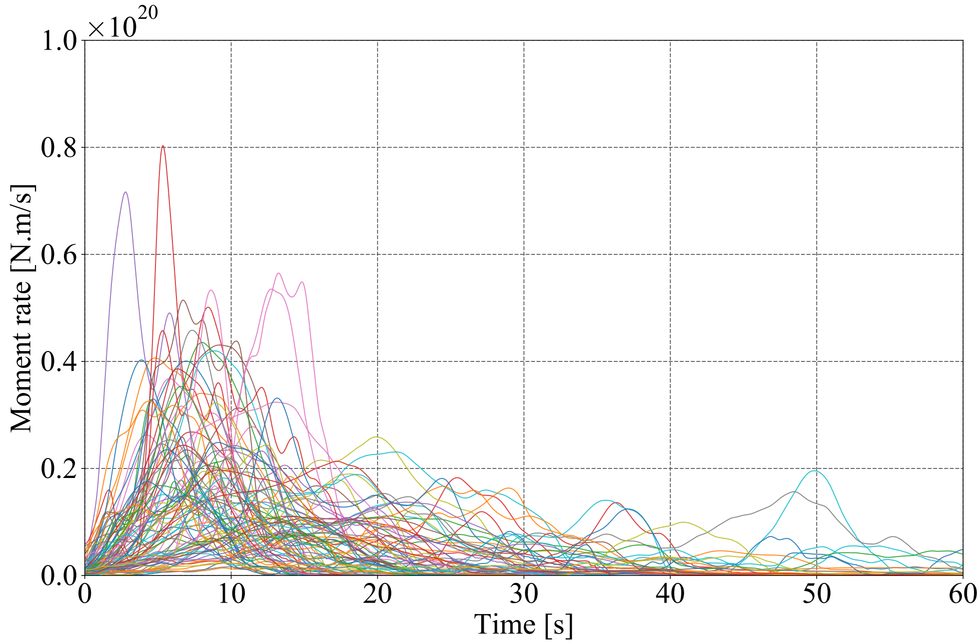

Figure 2.4: Moment rate functions $\dot{M}(t)$ of the actual earthquakes of $7.3 < M_w < 7.7$. The datas are taken from [33].

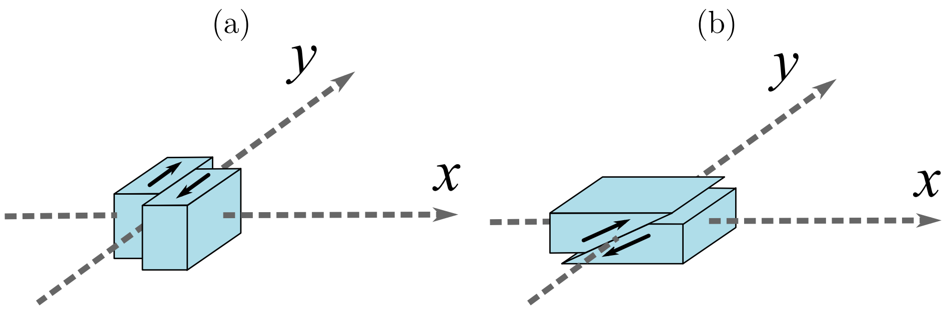

Figure 2.5: Focal mechanisms for (a)a strike-slip fault $(\gamma_s, \gamma_d, \gamma_r) = (180°, 90°, 180°)$ and (b)a dip-slip fault $(\gamma_s, \gamma_d, \gamma_r) = (180°, 20°, 90°)$.

Here the gravity strain tensors are calculated for two source parameters; $(\gamma_s, \gamma_d, \gamma_r) = (180°, 90°, 180°)$ and $(180°, 20°, 90°)$. These two focal mechanisms are called the strike-slip fault and the dip-slip fault, respectively, and depicted in Fig. 2.5. The calculated gravity strain tensor components are shown in Fig. 2.6 and 2.7. The signal amplitude is roughly in the order of 10^{-13} at 10 seconds after the onset of the fault rupture. Note that the signal amplitude varies in each component, and also depends on the azimuth and the focal mechanisms. For example, at least one component is large at any azimuths for

(a)

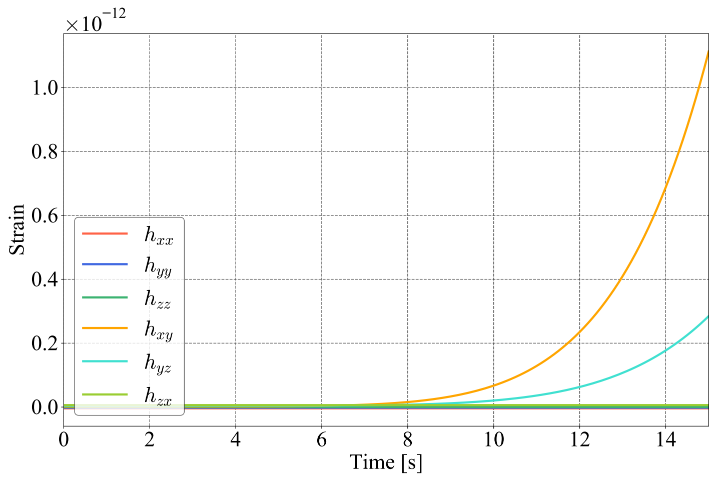

(b)

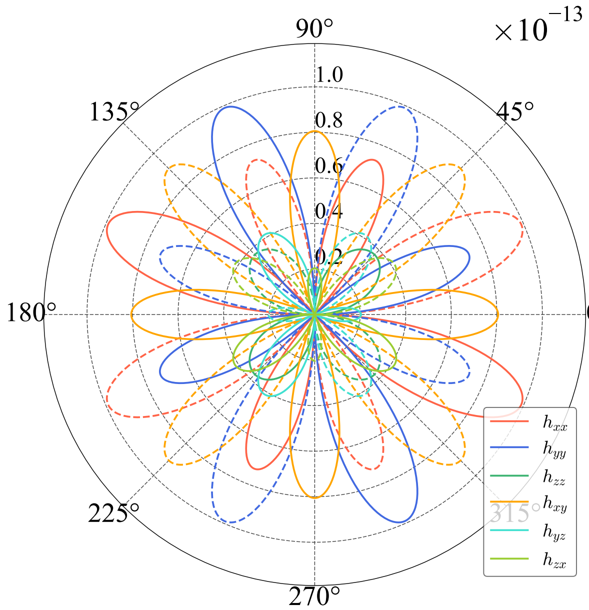

Figure 2.6: Gravity strain fluctuation of a strike-slip fault $(\gamma_s, \gamma_d, \gamma_r) = (180°, 90°, 180°)$ in a infinite homogeneous medium. The magnitude is set to $M_w = 7.5$. (a)The gravity strain tensor components observed at $(x, y, z) = (100\,\mathrm{km}, 0, 20\,\mathrm{km})$. (b)The azimuthal distribution of the gravity strain amplitude in xy-plane at z=20 km.The sign of the signal is expressed with solid lines (+) and dashed lines (-).

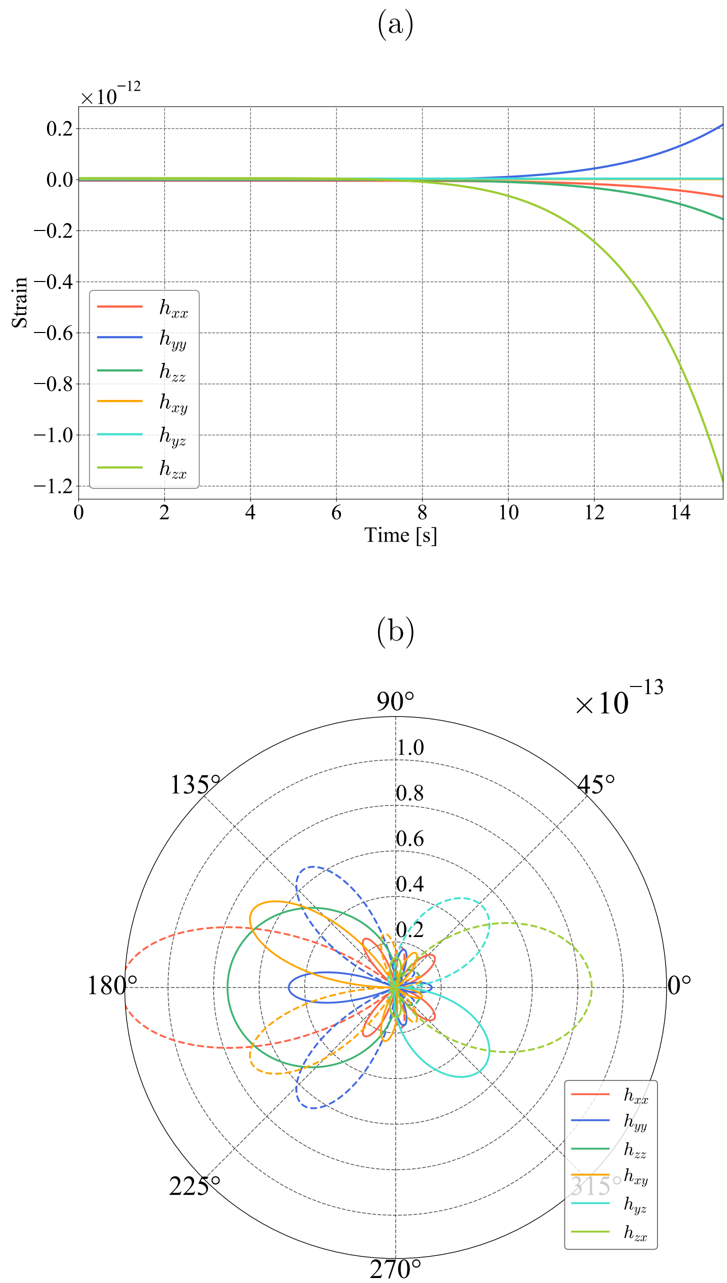

Figure 2.7: Gravity strain fluctuation of a dip-slip fault $(\gamma_s, \gamma_d, \gamma_r) = (180°, 20°, 90°)$ in a infinite homogeneous medium. The magnitude is set to $M_w = 7.5$. (a)The gravity strain tensor components observed at $(x, y, z) = (100\,\mathrm{km}, 0, 20\,\mathrm{km})$. (b)The azimuthal distribution of the gravity strain amplitude in xy-plane at z=20 km.The sign of the signal is expressed with solid lines (+) and dashed lines (-).

the strike-slip event, while every component is small at 90° and 270° for the dip-slip event. This suggests that the detectability of earthquakes depends on the configuration of the detectors and the focal mechanisms. This issue will be discussed further in Chapter 4.

2.2.2 Models for gravity calculation

A point shear dislocation source in an infinite homogeneous medium was assumed in the previous subsection. It gave us the simple analytical formula of the gravity fluctuation as Eq. (2.25), which was first derived by J. Harms in 2015 [23]. The resultant formula is useful to understand the general nature of the gravity change. Comparison to a numerical simulation indicates that the full-space model gives good approximation of actual gravity perturbation in the first few seconds after the onset of the rupture [1]. For the calculation up to a few hundreds of seconds, however, improvement of the calculation model is needed. J. Harms later improved his model by including the surface of the medium in 2016 (a homogeneous half-space model) [24]. The half-space model gives better approximation in the first few tens of seconds, after which the gravity perturbation can be influenced by the self-gravity of the medium.

Numerical models have also been developed. In the first detection of the transient gravity signal during the 2011 Tohoku-oki earthquake [4], the theoretical signals were calculated based on the AXITRA code [35] for a layered medium without self-gravitating effect. Recently K. Juhel et al. [36] performed the normal mode simulation which includes the self-gravitating effect for the layered Earth model. Though these numerical calculations require more computation cost than the analytical models, they provide more strict calculation of gravity perturbation.

2.2.3 Advantages of gravity-based earthquake early warning system

Since gravity-based earthquake detection is based on a completely new principle, it provides an independent observational information on the earthquakes. It will enable us to explore unprecedented aspect of earthquakes. In terms of warning, such an independent detection will improve the reliability of early warnings. There are also practical advantages compared to the current warning system using seismic P-waves. The first merit is shorter time of detection, and the second merit is better estimation accuracy of magnitude.

Detection time

In contrast to the seismic P-wave detection, the time of detection with gravitational signal strongly depends on the detector's sensitivity because gravitational signal gradually grows as shown in Fig. 2.6 (a) and 2.7 (a). Fig. 2.8

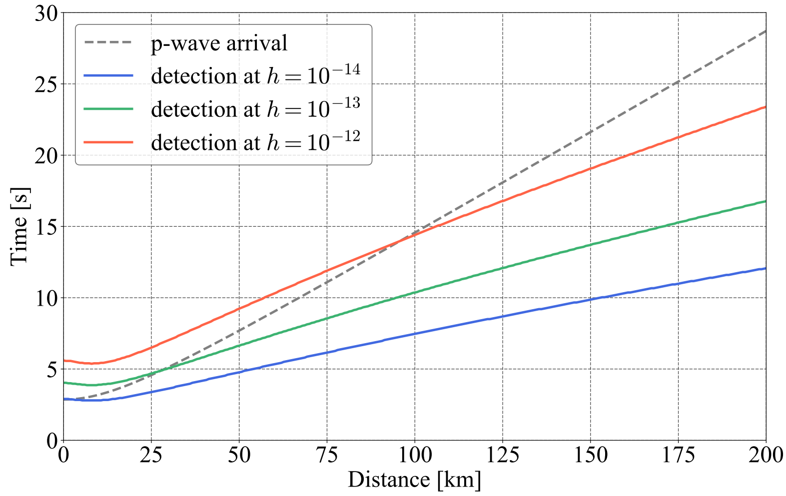

Figure 2.8: Distance dependence of achievable warning times for $M_w = 7.5$ of earthquake when the gravity perturbation is detected at $h = 10^{-12}$ (red), 10^{-13} (green) or 10^{-14} (blue). The depth of the epicenter is set to 20 km. The grey dashed line shows the P-wave arrival time.

shows the achievable warning times for $M_w = 7.5$ of strike-slip earthquake when the gravity gradient perturbation is detected at various signal amplitudes. Here the sum of the signals in the five independent components, which is then averaged over the azimuths are used for the calculation. With the proposed gravity gradiometer sensitivity of 10^{-15} $/\sqrt{\mathrm{Hz}}$ at 0.1 Hz, the gravity gradient perturbation of earthquakes can be detected around $h \sim 10^{-13}$ of the amplitude, which is the case shown in Fig. 2.8 with the green line. In this case, gravity gradient observation has the advantage of $\sim$4 seconds at 100 km epicentral distance than using P-wave. As shown in the figure, the advantage increases at further distances.

In terms of the warning time, the gravity-based warning system will have a primary merit for the events which happen in the place where seismometers are not placed yet or difficult to place. One of such examples is the off-shore events since a network of ocean-bottom seismometers needs much cost for installation or maintenance. This is because even if a gravity gradiometer can achieve earlier detection than a seismometer placed at the same location, another seismometer near the epicenter may detect it earlier than the gravity gradiometer in a area where a dense network of seismometers is already constructed. In any cases, detection of gravity gradient perturbation can provide an independent evidence of earthquake occurrence, which can improve the reliability and accuracy of the warning system.

Magnitude estimation

A fast magnitude estimation of an earthquake is also important. Magnitude estimations based on seismic waves are known to be uncertain for large earthquakes ($M_w \gtrsim 8.5$), because the seismic wave amplitude saturates for them. Actually, the magnitude of the 2011 Tohoku-oki earthquake was initially underestimated, which resulted in underestimation of tsunami amplitudes. In contrast, the signal amplitude of gravity perturbation is directly related to the energy of the earthquake as indicated in Eq. (2.25). Hence it is expected to give better early estimation of the magnitude, which also enables accurate tsunami warning. The estimation accuracy with a network of gravity gradiometers is simulated in [2]. The simulation shows that the gravity gradient measurement can successfully provide the real-time estimation of magnitude from only ∼15 second after the onset of the fault rupture.

2.3 Gravitational waves at low frequencies

Gravitational wave (GW) has recently been established as a new way to observe the universe. Since the first detection of gravitational wave from a binary black hole in 2015 [9], two Advanced LIGO detectors [37] have continued observation runs with gradually increasing sensitivities. Another laser interferometric detector Advanced Virgo [38] has joined the observation since 2017, and the detection rate and the localizability of gravitational wave source directions were improved. These three detectors have detected gravitational waves from more than ten compact binary coalescences so far [11]. Another detector KAGRA [26] is also about to start observation. The detections of binary black holes enabled the test of general relativity under the strong gravitational field [14]. With the increased number of detections in the near future, the mass distribution will help us to understand how massive (10–100 $M_\odot$) black holes are formed in the universe [12]. For the binary neutron star coalescence detected in 2017 [10], its electromagnetic counterpart was identified and follow-up observations were carried out by many telescopes, from radio wave to gamma ray [39, 13]. Those observations contributed to identify the physical scenario of short gamma-ray bursts that was unclear. Thus, gravitational waves have opened a new era of physics and astronomy.

The observational frequency band of the ground-based interferometric detectors are, however, limited above 10 Hz due to the large seismic noise.As the electromagnetic wave astronomy, expanding the observational band is essential since it enables us to see various sources of gravitational waves. Several attempts to observe low-frequency (below 1 Hz) gravitational waves have been made for that purpose. Since the most obstructive noise in the current GW detectors is the seismic noise, some of the proposals are space-based detectors LISA [40]. DECIGO [41], and so on. There are also proposals of terrestrial low-frequency detectors [42], some of which will be introduced in Sec. 2.4.

In this section, gravitational wave observation below 0.1 Hz is overviewed. First gravitational wave is derived by linearizing the Einstein equation and its effect on masses are described in Sec. 2.3.1. Then the main observational targets are introduced in Sec. 2.3.2.

2.3.1 Theory of gravitational wave

Gravitational wave is derived as a wave solution of the Einstein equation

$$R_{\mu\nu} - \frac{1}{2} g_{\mu\nu} R = \frac{8\pi G}{c^4} T_{\mu\nu}. \tag{2.28}$$

Here $g_{\mu\nu}$ is the metric tensor and $T_{\mu\nu}$ is the energy-momentum tensor. $R_{\mu\nu}$ and R are the Ricci tensor and the Ricci scalar defined as

$$\begin{aligned}
{\Gamma^\mu}_{\alpha\beta} &= \frac{1}{2} g^{\mu\lambda}(\partial_\beta g_{\lambda\alpha} + \partial_\alpha g_{\lambda\beta} - \partial_\lambda g_{\alpha\beta}) && (2.29)\\
{R^\mu}_{\alpha\beta\gamma} &= \partial_\beta {\Gamma^\mu}_{\alpha\gamma} - \partial_\gamma {\Gamma^\mu}_{\alpha\beta} + {\Gamma^\mu}_{\lambda\beta}{\Gamma^\lambda}_{\alpha\gamma} - {\Gamma^\mu}_{\lambda\gamma}{\Gamma^\lambda}_{\alpha\beta} && (2.30)\\
R_{\mu\nu} &= {R^\lambda}_{\mu\lambda\nu} && (2.31)\\
R &= {R_\mu}^\mu. && (2.32)
\end{aligned}$$

${\Gamma^\mu}_{\alpha\beta}$ is called the Christoffel symbol. Under the weak gravitational field, the metric $g_{\mu\nu}$ can be divided into the Minkowski metric $\eta_{\mu\nu}$ and small deviation from there $h_{\mu\nu}$, as

$$g_{\mu\nu} = \eta_{\mu\nu} + h_{\mu\nu} \qquad (|h| \ll 1). \tag{2.33}$$

By converting $h_{\mu\nu}$ to the trace-reversed metric $\bar{h}_{\mu\nu} \equiv h_{\mu\nu} - \frac{1}{2}\eta_{\mu\nu}{h^\lambda}_\lambda$, and applying the Lorenz gauge condition $\partial_\lambda \bar{h}^{\mu\lambda} = 0$, Eq. (2.28) can be linearized to the wave equation,

$$\Box \bar{h}_{\mu\nu} = -\frac{16\pi G}{c^4} T_{\mu\nu}, \tag{2.34}$$

where $\Box \equiv \frac{1}{c^2}\frac{d^2}{dt^2} + \Delta$ is the d'Alembertian.

Propagation of gravitational waves

In vacuum, $T_{\mu\nu} = 0$, the solution of Eq. (2.34) has a form of plane wave as

$$\bar{h}_{\mu\nu} = a_{\mu\nu} \exp(ik_\alpha x^\alpha). \tag{2.35}$$

Due to the symmetry of the metric and the wave equation (2.34), the coefficient $a_{\mu\nu}$ and the wave number vector k_α meet

$$a_{\mu\nu} = a_{\nu\mu}, \qquad k_\alpha k^\alpha = 0. \tag{2.36}$$

To remove the arbitrariness of coordinates, following transverse-traceless gauge (TT gauge) are adopted here :

$$\begin{aligned}
h_{\mu 0} &= 0 && (2.37)\\
\partial^i h_{\mu i} &= 0 \quad \text{(transverse)} && (2.38)\\
{h^\alpha}_\alpha &= 0 \quad \text{(traceless)}. && (2.39)
\end{aligned}$$

Here i denotes the spatial indices; $i = 1, 2, 3$. The second condition originates from the Lorenz gauge. Consider a wave propagating in the z-direction, hence $k^\alpha = (k, 0, 0, -k)$. Then the solution for the metric $h_{\mu\nu}$ shows

$$h_{\mu\nu} = h^{(\mathrm{TT})}_{\mu\nu} = \begin{pmatrix} 0 & 0 & 0 & 0 \\ 0 & h_+ & h_\times & 0 \\ 0 & h_\times & -h_+ & 0 \\ 0 & 0 & 0 & 0 \end{pmatrix} \exp(ik(ct - z)). \tag{2.40}$$

The resultant wave solution propagating at the speed of light is called gravitational wave. Here $h^{(\mathrm{TT})}_{\mu\nu}$ is used for the metric under the TT gauge. Gravitational wave in the general relativity has two polarization degrees of freedom, which is expressed as h_+ (plus-mode) and $h_\times$ (cross-mode) here.

Effects of gravitational waves

The geodesic equations for masses at x^μ and $x^\mu + \xi^\mu$ are

$$\frac{d^2 x^\mu}{d\tau^2} + \Gamma^\mu{}_{\alpha\beta}(x) \frac{dx^\alpha}{d\tau}\frac{dx^\beta}{d\tau} = 0, \tag{2.41}$$

$$\frac{d^2(x^\mu + \xi^\mu)}{d\tau^2} + \Gamma^\mu{}_{\alpha\beta}(x+\xi) \frac{d(x^\alpha + \xi^\alpha)}{d\tau}\frac{d(x^\beta + \xi^\beta)}{d\tau} = 0. \tag{2.42}$$

The difference of these equations gives the equation of geodesic deviation as

$$\frac{d^2 \xi^\mu}{d\tau^2} + 2\Gamma^\mu{}_{\alpha\beta} \frac{dx^\alpha}{d\tau}\frac{d\xi^\beta}{d\tau} + \xi^\lambda \partial_\lambda \Gamma^\mu{}_{\alpha\beta} \frac{dx^\alpha}{d\tau}\frac{dx^\beta}{d\tau} = 0. \tag{2.43}$$

Within a sufficiently small region around a point, the metric can be chosen to be flat. Such a frame is called the proper detector frame [43], in which the Christoffel symbol $\Gamma^\mu{}_{\alpha\beta}$ vanishes in the point. To linear order of h, $d\tau = dt$ then $\frac{dx^\alpha}{d\tau} \sim (c, 0, 0, 0)$ when the masses move non-relativistically. Under these conditions, the spatial components of Eq. (2.43) transform to

$$\ddot{\xi}^i = -\xi^\lambda \partial_\lambda \Gamma^i{}_{00} c^2 \tag{2.44}$$

$$= -c^2 \xi^j R^i{}_{0j0}. \tag{2.45}$$

Since the Riemann tensor is gauge invariant within the linearized metric, $R^i{}_{0j0}$ can be calculated in the TT gauge. This gives

$$\ddot{\xi}^i = \frac{1}{2}\ddot{h}^{(TT)}_{ij} \xi^j. \tag{2.46}$$

The right hand term shows the tidal force from gravitational wave in the proper detector frame. Compared to Eq. (2.2), the spatial components $\frac{1}{2}\ddot{h}^{(TT)}_{ij}$ corresponds to the gravity gradient tensor, hence $\frac{1}{2}h^{(TT)}_{ij}$ is identical to the gravity strain tensor defined in Eq. (2.3).

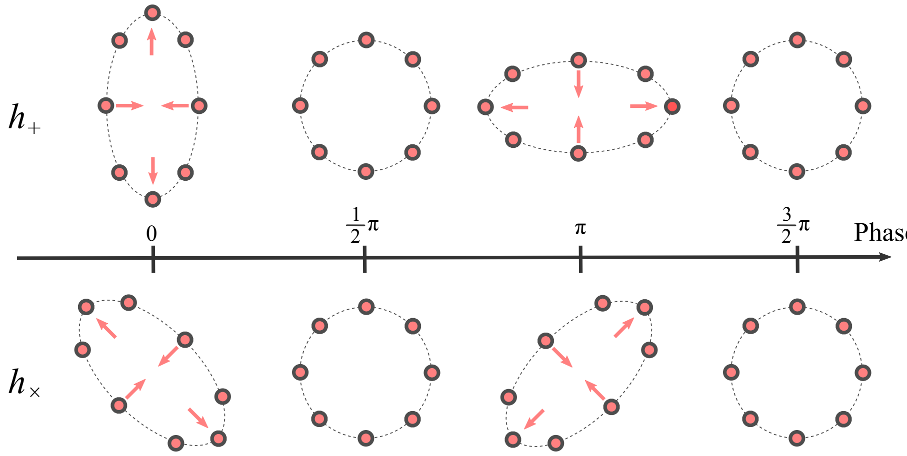

Figure 2.9: Effects of h_+ mode and $h_\times$ mode on masses.

The plus mode h_+ of Eq. (2.40) act as

$$\ddot{x} = \ddot{h}_+ x \cos(\omega t - kz), \qquad \ddot{y} = -\ddot{h}_+ y \cos(\omega t - kz). \tag{2.47}$$

$\omega = ck$ is the angular frequency of the wave. The real part of Eq. (2.40) is used above. h_+ expands the masses in x-direction and compresses them in y-direction, and vice versa. The effects of the cross mode $h_\times$ are

$$\ddot{x} + \ddot{y} = \ddot{h}_\times (x + y) \cos(\omega t - kz), \qquad \ddot{x} - \ddot{y} = -\ddot{h}_\times (x - y) \cos(\omega t - kz). \tag{2.48}$$

$h_\times$ expands the masses in $(x + y)$-direction and compresses them in $(x - y)$-direction, and vice versa. They are depicted in Fig. 2.9.

Emission of gravitational waves

The right hand term of Eq. (2.34) is the source of gravitational waves. Similar to electromagnetic waves, the solution is given by

$$h_{\mu\nu}(t, \boldsymbol{r}) = \frac{4G}{c^4} \int d^3\boldsymbol{r}' \frac{T_{\mu\nu}(t - |\boldsymbol{r} - \boldsymbol{r}'|/c, \boldsymbol{r}')}{|\boldsymbol{r} - \boldsymbol{r}'|}. \tag{2.49}$$

When the size of the source is much smaller than the wavelength of gravitational waves, $h_{\mu\nu}$ in the sufficiently far zone away from the source can be approximated to

$$h_{\mu\nu}(t, \boldsymbol{r}) = \frac{4G}{c^4 r} \ddot{I}_{ij}(t - r/c), \tag{2.50}$$

where $r = |\boldsymbol{r} - \boldsymbol{r}'|$ and

$$I_{ij}(t) = \int d^3\boldsymbol{r}' \rho(t, \boldsymbol{r}) \left(r'_i r'_j - \frac{1}{3} \delta_{ij} r'^2 \right) \tag{2.51}$$

is the quadruple moment of the source.

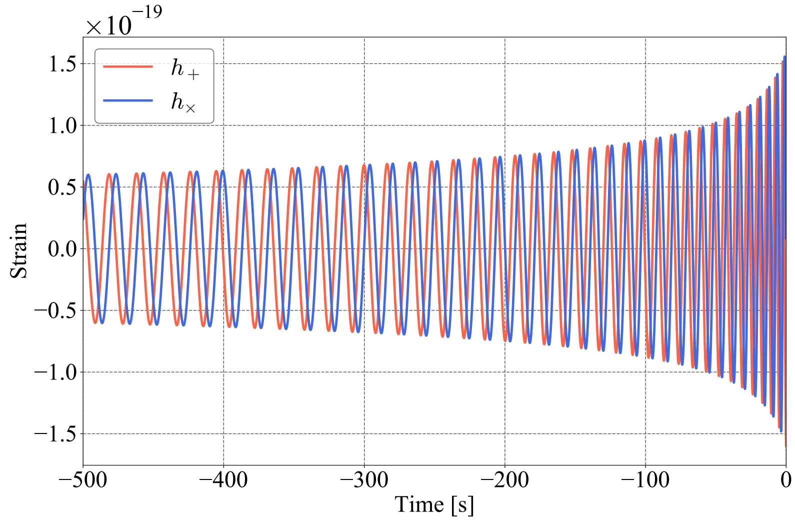

Figure 2.10: Chirp signal for $10^4 M_\odot - 10^4 M_\odot$ binary system observed from 1 Gpc away. The signal is cut at $2f_{\rm ISCO} \simeq 0.2$ Hz. The inclination angle is set to 0.

2.3.2 Source of gravitational wave around 0.1 Hz

Two representative sources of gravitational waves are introduced. Though there are many kind of sources, here we focus only on the valuable targets for observation around 0.1 Hz.

Intermediate mass black holes

As shown in Eq. (2.50), gravitational waves are radiated from time-varying quadruple moment of mass. One of promising sources in the universe is a binary system of compact stars, such as black holes, neutron stars and white dwarfs. The orbit of a binary system shrinks due to the energy loss via the gravitational wave radiation, and the angular frequency of the orbital motion gets higher [1]. As two objects get closer, the amplitude of the gravitational wave also increases since the gravitational interaction gets stronger. Such kind of waveform is called a chirp signal which has gradually increasing frequency and amplitude.

Consider a binary system of m_1 and m_2. The evolution of gravitational wave frequency $f_{\rm gw}(t)$ for it is given by

$$f_{\rm gw}(t) = \frac{1}{\pi}\left(\frac{5}{256}\right)^{\frac{3}{8}}\left(\frac{G\mathcal{M}_c}{c^3}\right)^{-\frac{5}{8}}(t_c - t)^{-\frac{3}{8}}, \tag{2.52}$$

[1]This was confirmed by Hulse & Taylor [44] as the first observational proof of gravitational waves.

where $\mathcal{M}_c \equiv (m_1 m_2)^{\frac{3}{5}}/(m_1+m_2)^{\frac{1}{5}}$ is the chirp mass of the binary, and t_c is the time of coalescence. Then the gravitational waveform in the lowest order approximation is

$$h_+(t) = \frac{1}{r}\left(\frac{G\mathcal{M}_c}{c^2}\right)^{\frac{5}{4}}\left(\frac{5}{c(t_c-t)}\right)^{\frac{1}{4}}\left(\frac{1+\cos^2\iota}{2}\right)\cos\Phi(t), \tag{2.53}$$

$$h_\times(t) = \frac{1}{r}\left(\frac{G\mathcal{M}_c}{c^2}\right)^{\frac{5}{4}}\left(\frac{5}{c(t_c-t)}\right)^{\frac{1}{4}}\cos^2\iota\sin\Phi(t), \tag{2.54}$$

where

$$\Phi(t) = \int_{t_0}^{t} dt' 2\pi f_{\rm gw}(t') = -2\left(\frac{5G\mathcal{M}_c}{c^3}\right)^{-\frac{5}{8}}(t_c-t)^{\frac{5}{8}} + \Phi_c \tag{2.55}$$

ι is the inclination angle between the line of sight and the normal vector of the orbit. Φ_c is the phase at the coalescence time. Fig. 2.10 shows the chirp signal for $m_1 = m_2 = 10^4 M_\odot$ observed from 1 Gpc away. The amplitude of gravity strain is in the order of 10^{-19} in this case. Therefore, much better sensitivity is required for detectors to observe gravitational waves than to detect earthquakes.

Though $f_{\rm gw}$ goes to ∞ at $t \to t_c$, the actual frequency evolution stops when two stars merge into a single star. The period before the coalescence is called an inspiral phase. The later phase during the coalescence is called a merger phase, in which the waveform is available only by numerical calculations. In the ringdown phase after the merger phase, the merged star lose angular momentum via gravitational waves. The overall waveform of a compact binary coalescence is given by these three phases. The frequency at the innermost stable circular orbit (ISCO), $f_{\rm ISCO}$, gives a characteristic frequency of the transition from the inspiral phase to the merger phase. The frequency is

$$f_{\rm ISCO} = \frac{c^3}{12\sqrt{6}\pi G M}. \tag{2.56}$$

Since $f_{\rm ISCO}$ is inversely proportional to the total mass $M \equiv m_1 + m_2$, binaries of heavy black holes are observed at low frequencies. The numerical value is

$$f_{\rm ISCO} \sim 0.1\,[{\rm Hz}] \times \left(\frac{2\times 10^4 M_\odot}{M}\right). \tag{2.57}$$

Hence observation of gravitational waves around 0.1 Hz is sensitive to $10^4 - 10^5$ $M_\odot$ black holes. Such black holes cannot be observed with the current ground-based detectors, which is sensitive only above 10 Hz.

Black holes of $10^2 - 10^5$ $M_\odot$ are called intermediate-mass black holes (IMBHs). It is meaningful to observe coalescences of IMBH binaries since they are one of the candidate formation scenario of supermassive black holes (SMBHs) at the center of galaxies [15]. There have been several reports of possible IMBHs; 400 $M_\odot$ in the galaxy M82 [45], 2.2×10^3 $M_\odot$ in the globular cluster 47 Tuc. [46], 3.2×10^4 $M_\odot$ in the central region of our galaxy [47], and so on. Though the existence of IMBHs have come to be confirmed, the statistical properties are not unclear and also binary systems of IMBHs have not been found yet. Hence gravitational wave observation will provide valuable information about the merger rate of binary IMBHs, which will be useful to identify the formation scenario of SMBHs.

Stochastic gravitational wave background from the early universe

Another important target is stochastic gravitational waves originate from space-time fluctuation in the early universe. Due to very weak interaction of gravitational waves with masses, gravitational waves can see the earlier universe before 0.38 Myr from the Big Bang, which cannot be observed with electromagnetic waves. It is one of the final goals of gravitational wave observation.

The power spectral density of the stochastic gravitational wave is given by

$$\sqrt{S_h(f)} = \sqrt{\frac{3{H_0}^2}{4\pi^2}\frac{\Omega_{\mathrm{gw}}(f)}{f^3}}, \tag{2.58}$$

where H_0 is the Hubble constant, and

$$\Omega_{\mathrm{gw}}(f) = \frac{1}{\rho_c}\frac{d\rho_{\mathrm{gw}}}{d(\log f)} \tag{2.59}$$

is a cosmological parameter defined from the energy density of gravitational waves ρ_{gw} and the critical density of the universe $\rho_c = 3c^2{H_0}^2/8\pi G$. Low-frequency observation has an advantage to detect this since the power spectral density Eq. (2.58) is proportional to $f^{-3/2}$. According to the calculation based on the inflation model, $\Omega_{\mathrm{gw}}(f)$ is estimated to $\sim 10^{-15}$ [48], hence $\sqrt{S_h(f)} \sim 10^{-24}\ /\sqrt{\mathrm{Hz}}$ at 0.1 Hz.

Note that since the waveform is stochastic, observation with a single detector cannot separate the waveform from the random detector noise. Taking correlation between several detectors is required to extract the waveform of such background gravitational waves.

2.4 Proposed detectors to observe gravity gradient below 1 Hz

Here we introduce proposed detectors to observe gravity gradient fluctuation below 1 Hz. As seen in the previous sections, both Newtonian gravity gradient and gravitational waves act as tidal force on masses. Therefore they can be measured with the same detector configuration in principle. Actually, some of gravity gradiometers introduced here are originally proposed as gravitational wave detectors.

The largest noise source of the current ground-based gravitational wave detectors below 1 Hz is the seismic noise. Moreover, the suspension systems of those detectors have the resonant frequency of ~ 1 Hz, which prevent the test masses from responding to the gravitational tidal forces below 1 Hz. Therefore it is necessary to lower the resonant frequency of the system to observe gravity gradient at low frequencies. The following detectors realize this by using sophisticated systems or going into space. Some of the prototype sensitivities of the following detectors are later shown in Fig. 3.9 in the next chapter.

2.4.1 Torsion bar antenna

A torsion bar antenna is a gravity gradiometer using a torsion pendulum. It was proposed as a low-frequency gravitational wave detector named TOBA (TOrsion-Bar Antenna) in 2011 [16]. TOBA measures tidal force from local gravity gradient fluctuation via the horizontal rotation of suspended bars. Since a torsion pendulum can have low resonant frequency, which is in the order of milihertz, the horizontal rotational mode of the suspended bar behaves as a free-falling mass down to milihertz band. This enables a good response to gravitational waves and good passive isolation of rotational seismic vibration. Rotation of the bar is measured with laser interferometric sensors. Hence the principle of TOBA is quite similar to the existing gravitational wave detectors, which also measures the motion of masses (mirrors) with the laser interferometer. Several prototypes have been developed so far [17, 18], and component researches are also ongoing [21]. The sensitivities of those prototypes are shown in Fig. 3.9 in the next chapter.

TOBA is sensitive to only horizontal components of gravity strain tensor, h_{xx}, h_{yy} or h_{xy}, because it uses horizontal rotations. The detailed mechanism of torsion bar antenna will be described in Chapter 3. In particular, detectability of earthquakes with horizontal components will be discussed in Chapter 4.

A similar torsion bar detector named TorPeDO (Torsion Pendulum Dual Oscillator) is also under development at Australian National University [49]. It focuses on the terrestrial targets such as earthquake early warning and Newtonian noise detection. Though the principle is same as TOBA, the configuration of rotation readout and vibration isolation is different from TOBA.

2.4.2 Superconducting gravity gradiometer

Superconducting gravimeters have been used for geophysical observations. They use superconductor masses levitated by the Meissner effect, which act as a free-falling mass in at least one degree of freedom. The free-falling degrees of freedom are sensitive to low frequency gravity fluctuation. By combining several levitated masses or by using the rotational mode of the mass, gravity gradient are also measurable. The motion of the superconductor mass induces current in the superconducting circuit loop due to the Meissner effect, and the induced current is measured with SQUID (Superconducting QUantum Interference Device). The principle is explained in [50].

Recently superconducting gravity gradiometers which are sensitive to the all components of gravity gradient tensor were proposed [51, 52], and the experimental result is also reported [52]. One of such configuration, SOGRO (Superconducting Omni-directional Gravitational Radiation Observatory), is targeting gravitational wave observation. As mentioned in [53], SOGRO is sensitive to gravitational waves coming from any directions. Additionally, observation of all the gravity gradient components provides advantages in detecting earthquakes, as discussed in Chapter 4.

2.4.3 Atom interferometer

Atom interferometers use interference of matter waves of free-falling atoms. After the first experimental demonstration reported in 1991 [54], an atom interferometer was used to measure the gravitational acceleration [55]. The atoms interact with a sequence of three laser pulses as follows, and work as a Mach-Zender interferometer. The first pulse (beam-splitter pulse) splits the atom into a superposition of two states in different momentum. Next the second pulse (mirror pulse) is applied to revere the two states. Then the third pulse (beam-splitter pulse) is applied again to interfere the states of the atom. The effects of gravitational field along the paths of the atoms are measured as the resulting interference pattern.

A combination of a laser interferometer and atom interferometers were recently proposed to achieve higher sensitivities [56]. MIGA (Matter-wave laser Interferometric Gravitation Antenna) [57] is a gravitational wave detector using such configuration. In these configurations, atom interferometers measure the phase of the laser imprinted on the atoms at each points. Hence they are sensitive to gravity gradient in the propagation direction of the laser. The first proposal [56] assumes the vertically propagating laser, while the laser propagates horizontally in the MIGA design.

2.4.4 Space-based gravitational wave detectors

There are several proposals of space-based detectors. Their primary merits are absence of seismic noise and low or zero resonant frequency of the system. For these reasons, the proposed sensitivities for gravitational waves are much better than those of the terrestrial detectors above. On the other hand, of course the space-based detectors are insensitive to earthquakes because the satellites are far away from the terrestrial sources. Here two projects, LISA and DECIGO, are briefly introduced below.

LISA

LISA (Laser Interferometer Space Antenna) [40] is a space-based laser interferometer which has 2.5 million km length of baseline. The sensitive frequency band is 0.1 mHz to 0.1 Hz, therefore one of the observational targets is coalescences of supermassive black holes. LISA consists of three spacecrafts each of which is drag-free controlled relative to the free-falling test masses inside the spacecraft. They orbit around the sun along the earth-like orbit. Relative displacement between the spacecrafts is measured by optical transponder to detect the spacetime distortion by gravitational waves. The performance of acceleration noise of the test mass is already demonstrated by LISA Pathfinder (LPF) launched in Dec. 2015 [58].

DECIGO

DECIGO (DECi-hertz Interferometer Gravitational Wave Observatory) has a baseline length of 1000 km. The main observational band is between 0.1 Hz and 10 Hz. It targets to observe the stochastic gravitational wave background from the early universe, coalescences of intermediate-mass black holes, and so on. DECIGO consists of three spacecrafts, and three Fabry-Perot cavities are placed along the baselines. The baseline length fluctuation are measured with the cavities to detect gravitational waves. The mirrors of the cavities are used as a reference mass for drag-free control of the spacecrafts. Currently the precursor detector B-DECIGO is planned to demonstrate the technologies for DECIGO and to achieve scientific observations.

3 Torsion Bar Antenna

A torsion bar antenna (TOBA) is a low-frequency gravity gradiometer using a torsion pendulum. Tidal force from gravity gradient act as torque on the suspended bars, which is then measured with a laser interferometric sensor. As briefly mentioned in Sec. 2.4, the low resonant frequency enables the bars to response the gravitational torque at low frequencies. TOBA has two observational targets which are described in the previous chapter:

- Terrestrial gravity gradient fluctuation induced by earthquakes
- Low-frequency gravitational wave from IMBH binaries

In this chapter, the principle of TOBA is mathematically described in Sec. 3.1. Then important noise sources for TOBA are explained in Sec. 3.2. The final development target and its scientific outcome are then described in Sec. 3.3. Previous experimental results, including the prototype developments and the component researches on noise reduction, are summarized in Sec. 3.4. At the end of this chapter, a 35 cm-scale configuration named Phase-III TOBA is proposed for technical demonstration and earthquake detection. The details are described in Sec. 3.5.

3.1 Principle

Fig. 3.1 shows the schematic figure of how TOBA works. In the following discussions, the vertical direction is set as z-axis.

Torque from gravity gradient

When a bar-shaped mass is suspended, it has the gravitational potential energy U_b of

$$U_b = \int_b dV \rho(\boldsymbol{r})\phi_g(\boldsymbol{r}). \tag{3.1}$$

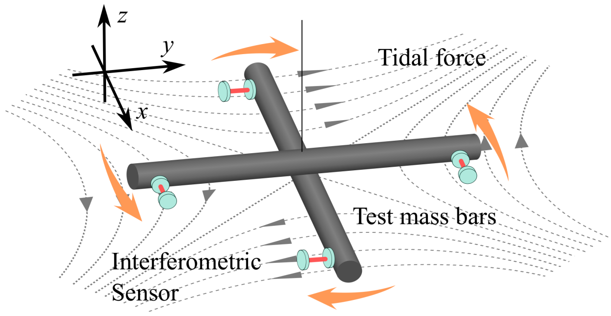

Figure 3.1: Principle of a torsion bar antenna.

The derivation of U_b with respect to rotational angle θ gives the gravitational torque on the bar, which is

$$N = -\frac{\partial U_b}{\partial \theta}. \tag{3.2}$$

Displacement of a point on the bar at $\boldsymbol{r}$ associated with the rotation is expressed as

$$d\boldsymbol{r} = \boldsymbol{w}(\boldsymbol{r})d\theta \tag{3.3}$$

where $\boldsymbol{w}(\boldsymbol{r})$ is called the mode function, which is $\boldsymbol{w}(\boldsymbol{r}) = (-y, x, 0)$ for the horizontal rotation. Then the derivation is

$$N = -\int_b dV \rho(\boldsymbol{r})\boldsymbol{w}(\boldsymbol{r}) \cdot \boldsymbol{\nabla}\phi_g(\boldsymbol{r}). \tag{3.4}$$

Assuming that the gravity gradient $-\boldsymbol{\nabla} \otimes \boldsymbol{\nabla}\phi_g(\boldsymbol{r}) = \boldsymbol{G}(\boldsymbol{r})$ is uniform within the size of the detector,

$$\partial_i \phi_g(\boldsymbol{r}) = -G_{ij}x^j, \tag{3.5}$$

then

$$\begin{aligned} N &= G_{ij}\int_b dV w^i(\boldsymbol{r})x^j && (3.6)\\ &= -\frac{G_{xx}-G_{yy}}{2}\int_b dV(2xy) + G_{xy}\int_b dV(x^2-y^2). && (3.7)\end{aligned}$$

The two integrals are the quadruple moments of the bar. Here we define

$$\begin{aligned} q_+ &\equiv -\int_b dV(2xy), && (3.8)\\ q_\times &\equiv \int_b dV(x^2-y^2), && (3.9)\\ & && (3.10)\end{aligned}$$

hence

$$N = \frac{G_{xx}-G_{yy}}{2}q_+ + G_{xy}q_\times, \tag{3.11}$$

or in terms of gravity strain tensor (Eq. (2.3)),

$$N = \frac{\ddot{h}_{xx} - \ddot{h}_{yy}}{2} q_+ + \ddot{h}_{xy} q_\times. \tag{3.12}$$

Eq. (3.11) or (3.12) tell that the horizontal rotation is sensitive to only three components of the gravity gradient tensor.

According to the correspondence between the metric tensor of gravitational waves and the gravity gradient tensor discussed in Sec. 2.3.1, the torque from gravitational waves is given by

$$N = \frac{\ddot{h}_+}{2} q_+ + \frac{\ddot{h}_\times}{2} q_\times. \tag{3.13}$$

Mechanical response of a torsion pendulum

The equation of motion about the horizontal rotational mode of a torsion pendulum is

$$I\ddot{\theta}(t) + \kappa_w \theta(t) = N(t). \tag{3.14}$$

Here I is the moment of inertia around the rotational axis (the vertical axis here), and κ is the torsional spring constant of the suspension wire. The Fourier transform of the equation of motion gives

$$\tilde{\theta}(f) = \frac{\tilde{N}(f)}{\kappa_w(1 + i\phi_w) - I(2\pi f)^2} = \frac{\tilde{N}(f)}{4\pi^2 I({f_0}^2(1 + i\phi_w) - f^2)}, \tag{3.15}$$

where

$$f_0 = \frac{\omega_0}{2\pi} \equiv \frac{1}{2\pi}\sqrt{\frac{\kappa_w}{I}} \tag{3.16}$$

is the resonant frequency of the torsion pendulum. Here the loss angle ϕ_w was introduced as the imaginary part of the spring constant based on the structure damping model. ϕ_w indicates the amount of energy loss of the pendulum, and the Q value of the pendulum is defined as $Q_w \equiv 1/\phi_w$. For a cylindrical wire which has diameter of d_w and length of l_w , κ_w is given by

$$\kappa_w = \frac{\pi E_w d_w^4}{64(1 + \nu_w) l_w}, \tag{3.17}$$

where E_w and ν_w are the Young's modulus and the Poisson's ratio of the wire, respectively. The following mechanical response function obtained from Eq. (3.15) is also often used in this thesis:

$$\tilde{\chi}(f) \equiv \frac{\tilde{\theta}(f)}{\tilde{N}(f)} = \frac{1}{4\pi^2 I} \frac{1}{{f_0}^2(1 + i\phi_w) - f^2}. \tag{3.18}$$

From Eq. (3.12) and Eq. (3.15), induced rotation of the bar is

$$\tilde{\theta}(f) = \left(\frac{q_+}{I} \frac{\tilde{h}_{xx}(f) - \tilde{h}_{yy}(f)}{2} + \frac{q_\times}{I} \tilde{h}_{xy}(f) \right) \frac{f^2}{{f_0}^2(1 + i\phi_w) - f^2}. \tag{3.19}$$

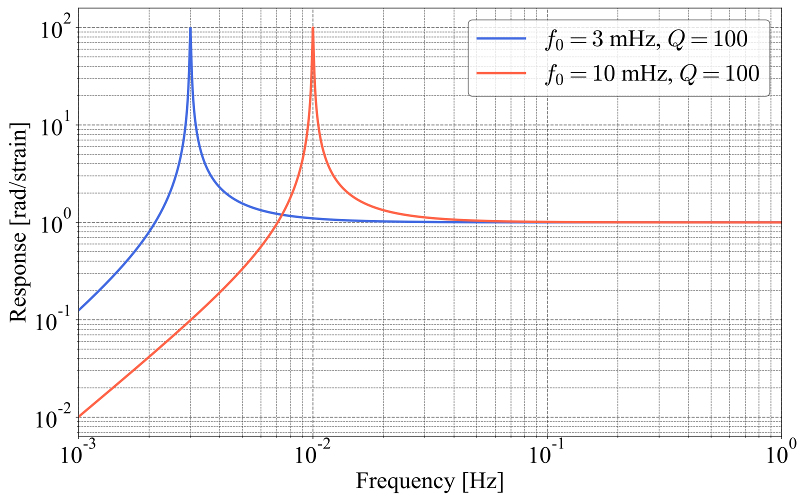

Figure 3.2: Frequency response of a torsion pendulum against gravity strain for $f_0 = 3$ mHz, $Q = 100$ (blue) and $f_0 = 10$ mHz, $Q = 100$ (red).

The moment of inertia I around z-axis is

$$I = \int_b dV \rho(x^2 + y^2). \tag{3.20}$$

When the bar is along x-axis and the aspect ratio is large enough, $q_\times/I \simeq 1$. In this case the frequency response $\tilde{\theta}/\tilde{h}$ corresponds to the last factor of Eq. (3.19). Fig. 3.2 shows the response $\tilde{\theta}/\tilde{h}$ for different resonant frequencies. $q_\times/I$ is fixed to 1. Above the resonant frequency, the pendulum has flat response to the gravity strain, while it decreases below the resonant frequency. Therefore the lower resonant frequency provides wider observational frequency band. That is one of the reasons why torsion pendulums are suitable for low-frequency observation. It seems that large signal is available at the resonant frequency since the frequency response has a peak there. However, signal-to-noise ratio does not increase there because the noise spectrum of the pendulum's rotation also has a peak at the resonant frequency in usual cases of TOBA.[1]

3.2 Noise sources

It is essential to reduce the noise of the detector or environmental fluctuations to achieve scientific observation. The main noise sources and how to reduce

[1] On the other hand, the initial gravitational wave detectors, the resonant mass detectors, used the signal amplification at their resonant frequencies. It is because their resonant frequencies were high (typically at a few kHz) hence the main noise sources were sensing noises which had flat spectrum.

them are explained in the following subsections. In this section, the amplitude spectral densities (ASDs) are given in the unit of rotational angle of the bar; rad/$\sqrt{\mathrm{Hz}}$.

3.2.1 Thermal noise

Thermal fluctuations of the detector components are one of the fundamental noise sources in TOBA. According to the fluctuation-dissipation theorem, the induced fluctuation in terms of the detector's DoFs is determined by the temperature and the energy dissipation of the system. As shown below, the amplitude spectral density of the thermal noise is given in the form of $\sqrt{S_{\mathrm{th}}(f)} \propto \sqrt{T\phi}$, where T is temperature and ϕ is loss angle of the relevant component. Therefore the common ways to reduce the following thermal noise are cooling the components and choosing the material which has small loss angle ϕ. Depending on the types of thermal noise, there are additional ways of noise reduction. Here three types of thermal noise are introduced and calculated. The first one is the suspension wire, which thermally shakes the suspended pendulum. The second one is the suspended bar, whose internal vibrations can couple to the angular measurement. The third one is the mirror attached on the bar as shown in Fig. 3.1. Since the laser interferometric sensor measures the displacement of the optical surface with the laser beam, thermal fluctuation of the surface becomes angular noise.

Suspension thermal noise

Energy loss via the suspension wire determines the torque noise of the wire. Thermal noise in mechanical suspension systems were investigated in [59]. In terms of the horizontal rotation of the bar, the amplitude spectral density (ASD) $\sqrt{S(f)}$ is given by

$$\sqrt{S_{\mathrm{th,sus}}(f)} = \sqrt{-\frac{4k_B T}{\omega}\mathrm{Im}\left[\frac{\tilde{\theta}(f)}{\tilde{N}(f)}\right]} = \sqrt{\frac{4k_B T\kappa_w\phi_w}{\omega}}|\tilde{\chi}(f)|, \tag{3.21}$$

where κ_w is the torsional spring constant of the suspension wire and ϕ_w is the loss angle of the wire that was introduced in Eq. (3.15). $\tilde{\chi}(f)$ is the mechanical response function of the pendulum defined as Eq. (3.18). Eq. (3.21) depends on the temperature T, loss angle $\phi = 1/Q$, the torsional spring constant κ and the moment of inertia I.

Above the resonant frequency, the thermal noise scales as $\propto \sqrt{\kappa_w/I^2}$. Therefore small κ_w and large I can reduce the thermal noise. Note that κ_w and I are not completely independent in an actual suspension system because the thickness of the wire is related to the mass to be suspended. When the size of the detector is fixed, mass should be concentrated at the outer ends (like a dumbbell) to increase I while keeping κ_w small.

Using low loss wire is essential to reduce the suspension thermal noise. In general, energy loss of the wire ϕ_w has several origins; loss of the bulk material, surface loss,

Bar thermal noise

Fluctuations of the internal modes of the bar are also important source of noise. It can be calculated by considering the eigenmodes of the bar. Since TOBA measures the rotation of the bar, odd functional modes are important here. In the following calculations, the bar is aligned to x-axis and consider the modes in xy-plane. The lowest order odd functional mode of a rectangular bar which has a dimension of $(x, y, z) = (L_b, l_y, l_z)$ $(L_b \gg l_y, l_z)$ is given by

$$y_2(x) = \sqrt{\frac{2}{\cosh^2 \alpha_2 + \cos^2 \alpha_2}} \left(\cos \alpha_2 \cdot \sinh \frac{2\alpha_2 x}{L_b} + \cosh \alpha_2 \cdot \sin \frac{2\alpha_2 x}{L_b} \right), \tag{3.22}$$

$$\alpha_2 \simeq 3.9266, \tag{3.23}$$

and the eigenfrequency ω_2 is

$$\omega_2 = \sqrt{\frac{4E_b l_z l_y^3}{3M_b L_b^3}} \alpha_2^2. \tag{3.24}$$

Here M_b and E_b are the mass and the Young's modulus of the bar, respectively. The eigenmode can be treated in the same way as the rotational mode of the suspension thermal noise. Note that the conversion to the angular fluctuation depends on how to measure the rotation. For simplicity, the angular fluctuation at the center of the bar is calculated below. The ASD of thermal fluctuation is

$$\sqrt{S_{\mathrm{th,bar}}(f)} \simeq \frac{5.3962}{L_b} \sqrt{\frac{4k_B T}{\omega} \frac{\omega_2^2 \phi_b}{M_b |\omega_2^2 (1 + i\phi_b) - \omega^2|^2}}. \tag{3.25}$$

Here ϕ_b is the loss angle of the bar.

The frequency band of interest (below 1 Hz) is usually below the eigenfrequency of the bar. In this case, larger ω_2 gives lower thermal noise. Hence the bar should be stiff against bending to suppress the noise.

Mirror thermal noise

Mirrors attached on the bar for the interferometric readout are also the sources of thermal noise. In principle this noise can be derived by considering the higher order modes of the bar in the same way as the bar thermal noise. However, it is convenient to treat them separately because the relevant scales are quite different for them; the bar length L_b is much larger than the laser beam width w.

Each mirror has a coating layer on the substrate surface to control the reflectivity. Both the substrate and the coating contribute to the thermal noise. Displacement thermal noise for an infinite substrate measured with Gaussian laser beam was calculated by Y. Levin [60] and later G. M. Harry included the contribution of the coating layer [61]. Based on their calculations, angular thermal noise when the rotation is measured by two Gaussian laser beam at two points separated by D is

$$\sqrt{S_{\rm th,mir}(f)} = \frac{\sqrt{2}}{D}\sqrt{\frac{4k_BT}{\omega}\frac{1-\nu_s^2}{\sqrt{\pi}E_s}\frac{\phi_{\rm mir}}{w}}, \tag{3.26}$$

$$\phi_{\rm mir} \equiv \phi_s + \frac{d_c}{\sqrt{\pi}w}\left(\frac{E_c}{E_s}\frac{(1+\nu_s)(1-2\nu_s)^2}{(1-\nu_s)(1-\nu_c^2)} + \frac{E_s}{E_c}\frac{(1+\nu_c)(1-2\nu_c)}{(1-\nu_s^2)(1-\nu_c)}\right)\phi_c. \tag{3.27}$$

w is the radius of the laser beam (where the intensity is $1/e^2$ of the maximum) and d_c is the thickness of the coating layer. E_s, ν_s and ϕ_s are the Young's modulus, the Poisson's ratio and the loss angle of the mirror substrate, respectively. E_c, ν_c and ϕ_c are those on the coating layer. Here ϕ_c is assumed to be isotropic.

Though the separation of measurement points D should be as large as possible, it cannot exceeds the bar length L_b. Using large beam is more effective to reduce the mirror thermal noise.

3.2.2 Quantum noise

Another fundamental noise is quantum noise, which originates from the quantum fluctuation of vacuum. The ASD of the quantum noise is

$$\sqrt{S_{\rm quantum}(f)} = \frac{\theta_{\rm SQL}(f)}{\sqrt{2}}\sqrt{\frac{1}{|\mathcal{K}(f)|} + |\mathcal{K}(f)|}, \tag{3.28}$$

$$\theta_{\rm SQL}(f) \equiv \sqrt{2\hbar|\tilde{\chi}(f)|}, \tag{3.29}$$

$$\chi(f) \equiv \tilde{\theta}/\tilde{N}. \tag{3.30}$$

Here $\tilde{\chi}(f)$ is given by Eq. (3.18). $\mathcal{K}(f)$ is a function depending on the sensing system, which is large as the system has high sensitivity, i.e. the motion of the bar generates large signal electric field. The first term of Eq. (3.28) is called shot noise, which originates from the fluctuation of the photon number to be sensed. The second term is called radiation pressure noise, induced from the fluctuation of radiation pressure due to the fluctuation of the photon number. If the shot noise is significant, a high sensitive rotational sensor is necessary to reduce the noise.

The shot noise and the radiation pressure noise are in the trade-off relation. This gives the standard quantum limit (SQL) $\theta_{\rm SQL}(f)$, which determines the standard lower limit of the noise spectrum. The SQL is not the absolute

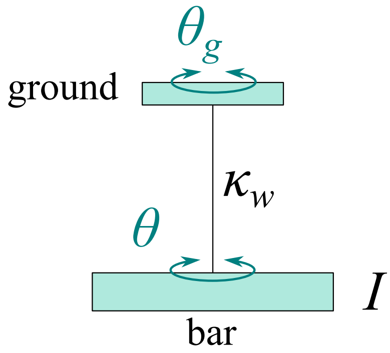

Figure 3.3: A single-stage torsion pendulum.

limit in all kind of detectors; it can be exceeded by quantum non-demolition measurement such as using squeezed vacuum, and so on [62].

3.2.3 Seismic noise

Vibration of the ground, or the suspension point of the pendulum, can be transferred to the rotation of the suspended bar via the suspension wires. There are two ways to reduce this noise; suppressing the vibration at the suspension point or reducing the vibration transfer of the pendulum. Here these reduction schemes are discussed for the following three different types of seismic noise.

Rotational seismic noise

Horizontal rotational vibration of the ground can be passively isolated by a multi-stage pendulum. The vibration isolation ratios of a single-stage torsion pendulum which is shown in Fig. 3.3 is

$$\frac{\tilde{\theta}(f)}{\tilde{\theta}_g(f)} = \frac{\kappa_w}{\kappa_w - I\omega^2} = \frac{f_0^2}{f_0^2 - f^2}. \tag{3.31}$$

Here the damping terms were ignored for simplicity. The vibration of the ground is isolated at the bar above the resonant frequency f_0. In general, a n-stage pendulum can suppress the vibration above the resonances in proportion to f^{-2n}. This is the same technique as the ground-based gravitational wave detectors.

When two bars are suspended in the same way, same vibration is transferred to each bar from the ground. Therefore the rotational vibration noise can be suppressed further by using the differential rotation of the bars for observations. This is called a common-mode rejection technique.

In total, the rotational seismic noise is given by

$$\sqrt{S_{\mathrm{seis,rot}}(f)} = C_{\mathrm{CMRR}} \tilde{H}_{\mathrm{rot}}(f) \sqrt{S_{g,\mathrm{rot}}(f)}, \tag{3.32}$$

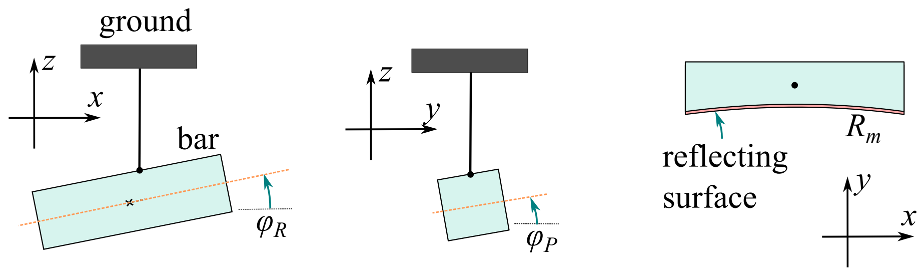

Figure 3.4: Routes of cross-coupling transfer.

where C_{CMRR} is the common-mode rejection ratio, $\tilde{H}_{\text{rot}}(f)$ is the vibration isolation ratio, and $\sqrt{S_{g,\text{rot}}(f)}$ is the ASD of the ground rotation.

Translational seismic noise (seismic cross-coupling noise)

Translational vibration of the ground are ideally not transferred to the horizontal rotation of the bar. However, asymmetries of the system can be a route of such cross-coupling transfers. This noise tends to be more significant than the rotational seismic noise. Many of the cross-coupling routes were identified in [21]. According to [21], most of the routes are the tilts of the system, such as the tilt of the bar, the mirror for the laser, the sensing axis of the optics, and so on. The important cross-coupling routes are shown in Fig. 3.4. The noise spectrums for them are expressed in the following form :

$$\sqrt{S_{\text{seis,trans}}(f)} = \left(\varphi_P|\tilde{H}_R(f)| + \varphi_R|\tilde{H}_P(f)| + \frac{1}{R_m}|\tilde{H}_x(f)|\right)\sqrt{S_{g,\text{trans}}(f)}, \tag{3.33}$$

where $\varphi_{P,R}$ is the tilt of the bar in pitch and roll directions, respectively. They are the relative tilt to the sensor-based axis in which the sensing system measures the rotation. The pitch and the roll are the rotations around x and y axis, respectively. $\tilde{H}_{P,R}(f)$ and $\tilde{H}_x(f)$ are the transfer functions to the bar's pitch, roll rotations and x-translation from the translation of the ground. R_m is the radius of curvature of the mirror, and $\sqrt{S_{g,\text{trans}}(f)}$ is the spectrum of translational ground vibration.

In addition to the suppression of translational ground vibrations, reducing the tilt of the system is effective way to reduce the noise. The tilt can be adjusted by balance weights, actuators, and so on. For the third route of Eq. (3.33), using a flat mirror surface or placing the mirrors in parallel at the points where the laser beam hits are necessary for noise reduction.

Nonlinear vibration noise

It was recently found by the author that nonlinear vibration noise induced by the synergy of translational seismic vibrations in two horizontal DoFs becomes significant noise source [22]. The detailed calculation is shown in the

Appendix A. The resultant Fourier spectrum of the horizontal rotation for a bar suspended in xy-plane is given as

$$\begin{aligned} \tilde{\theta}(f) &= \tilde{\chi}(f)\left[(I_y - I_z)\tilde{\theta}_P * \left(\omega^2\tilde{\theta}_R\right) + (I_z - I_x)\left(\omega^2\tilde{\theta}_P\right) * \tilde{\theta}_R \right. \\ &\quad \left. -(I_x - I_y)\left(\omega\tilde{\theta}_P\right) * \left(\omega\tilde{\theta}_R\right) + mh\left\{\left(\omega^2\tilde{x}\right) * \tilde{\theta}_P + \left(\omega^2\tilde{y}\right) * \tilde{\theta}_R\right\}\right]. \end{aligned} \tag{3.34}$$

Here "$*$" means frequency convolution.[2] $\tilde{x}$ and $\tilde{y}$ are the horizontal translation of the center of mass, and $\tilde{\theta}_P$ and $\tilde{\theta}_R$ are the pitch and the roll rotation around x and y axis, respectively. I_i are the moments of inertia around each axis.

The noise spectrum is determined by the DoFs other than the horizontal rotation, therefore translational vibration isolation is necessary to reduce this noise. Note that the vibration isolation by one order of magnitude results in noise reduction by two orders of magnitude, because every term of Eq. (3.34) is the product of two DoFs. Since the terms are frequency convolutions, the resonant peaks in each DoFs have dominant contributions in the total spectrum. Hence suppressing the resonant peaks by damping is effective to reduce the noise. The details are explained in Appendix A.

3.2.4 Newtonian noise

Since TOBA targets to measure the local gravity gradient, background fluctuations of the gravitational field also become noise sources. Such noise is called Newtonian noise (NN) or gravity gradient noise [64]. Newtonian noise is caused by any moving masses. Representative examples are seismic NN [65] and atmospheric NN [66, 63]. These Newtonian noises are estimated to be significant for the future gravitational wave detectors. Some noise reduction schemes have been proposed; feed-forward cancellation by estimating the gravity fluctuation based on environmental monitors [67, 68], or removing the mass around the detector [69]. However, the nature of the noise is not completely understood because Newtonian noise has not been directly measured yet.

Fig. 3.5 shows the estimated ASDs of NN. They are in the order of 10^{-15} $/\sqrt{\mathrm{Hz}}$ around 0.1 Hz, hence they can be problems for TOBA. Choosing the quiet place to build the detector, and developing the reduction scheme as mentioned above will be necessary to achieve the sensitivity of 10^{-15} $/\sqrt{\mathrm{Hz}}$. As shown in Fig. 3.5, the temperature NN is significantly suppressed in an underground site. In any cases, the first things to do are to measure NN directly and to investigate the nature of the noise. These are also important as research and development for another ground-based GW detectors.

[2] $(F * G)(f) = \int_{-\infty}^{\infty} F(x)G(f-x)dx \qquad (F(f), G(f) : \text{functions})$

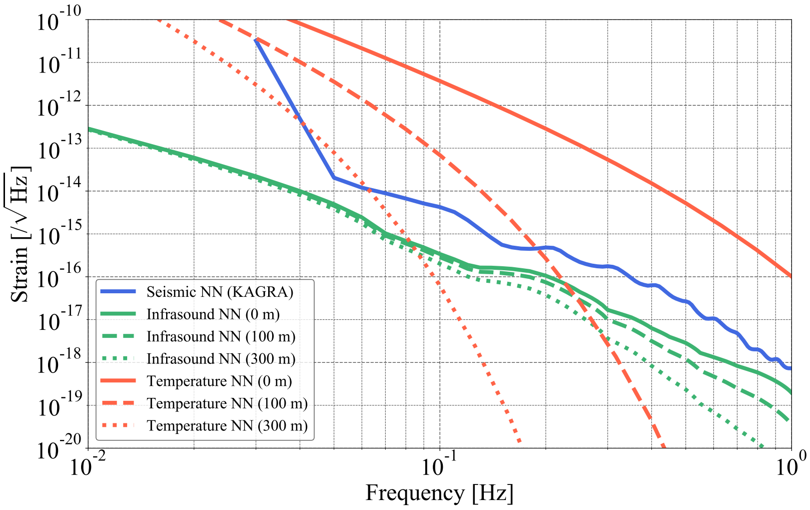

Figure 3.5: Estimated Newtonian noise spectrum for seismic NN (blue) , atmospheric infrasound NN [63] (green) and atmospheric temperature NN (red). The seismic NN was calculated based on the estimated spectrum for KAGRA [26]. The atmospheric NNs are plotted for different depths; 0 m (solid lines), 100 m (dashed lines) and 300 m (dotted lines).

3.2.5 Residual gas noise

The residual molecules in the vacuum chamber hit the suspended bar and excite the vibration. This noise can be calculated by considering the damping rate in the gas. For a rectangular bar which has a side area of A_b, the ASD of residual gas noise is given by

$$\sqrt{S_{\mathrm{gas}}(f)} = \sqrt{\frac{P_{\mathrm{vac}} A_b L_b^2 \sqrt{m_m k_B T}}{3\sqrt{2\pi}}} |\tilde{\chi}(f)|, \tag{3.35}$$

where m_m is the mass of the residual gas molecule, and P_{vac} is the pressure around the bar.

Improving the degree of vacuum is essential to suppress the residual gas noise. Though cooling is not directly very effective to reduce this noise because of the small dependency on the temperature ($\propto T^{1/4}$), the cryogenic part improves the degree of vacuum by adsorbing the molecules on the surface. This effect is known as a cryopump. Using a bar with small side area A_b is also important.

3.2.6 Magnetic noise

Fluctuation of environmental magnetic field can couple to the bar's rotation via the magnetic moment $\boldsymbol{\mu}$ or the magnetic susceptibility χ_m of the bar. Torque

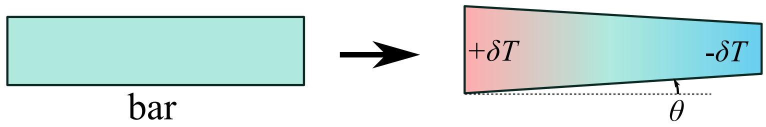

Figure 3.6: Asymmetric thermal expansion of the bar.

from from the coupling between $\boldsymbol{\mu}$ and $\boldsymbol{B}$ is

$$\boldsymbol{N} = \boldsymbol{\mu} \times \boldsymbol{B}. \tag{3.36}$$

This directly becomes a noise of the bar. Additionally, the gradient of the magnetic field can couple to the magnetic moment $\boldsymbol{\mu}$ and the magnetization. The force from the magnetic field gradient is

$$\boldsymbol{F} = \boldsymbol{\nabla}\left(\left(\boldsymbol{\mu} + \frac{\chi_m V_m \boldsymbol{B}}{\mu_0}\right) \cdot \boldsymbol{B}\right), \tag{3.37}$$

where V_m is the volume of the magnetized part and $\mu_0 = 1.257 \times 10^{-6}\,\mathrm{m} \cdot \mathrm{kg} \cdot \mathrm{s}^{-2} \cdot \mathrm{A}^{-2}$ is the magnetic permeability of vacuum. If the force is not uniform on the bar, it can be torque noise. Hence the nonuniformity of the magnetic parameters is the source of noise.

Reducing $\boldsymbol{\mu}$ or χ_m and suppressing $\boldsymbol{B}$ is necessary to reduce the magnetic noise. Magnetic materials should not be used for the bar or the attached components to make $\boldsymbol{\mu}$ small. For the magnetization, It is possible to adjust χ_m to be zero by using alloys of paramagnetic materials and diamagnetic materials. These parameters should be uniform in the bar. For $\boldsymbol{B}$, magnetic shielding is effective to suppress the fluctuation. Ferromagnetic materials or superconductor can be a good magnetic shield at low frequency. The reported magnetic shield using a high temperature superconductor Bi-Sr-Ca-Cu-O$_x$ can reduce the fluctuation by more than six orders of magnitude at 0.2 Hz [70]. Such a shield is compatible with a cryogenic system.

3.2.7 Temperature fluctuation noise

Temperature fluctuation of the bar or the surrounding materials can cause the fluctuation of thermal radiation and the distortion of the components.

Thermal radiation noise

Thermal radiation act as the torque noise when the temperature fluctuation is not uniform. The radiation pressure on the bar is given by

$$P_{\mathrm{rad}} = \epsilon_b \frac{\sigma_{\mathrm{sb}}}{6c} T_b^4 + (2 - \epsilon_{\mathrm{b}}) \frac{\sigma_{\mathrm{sb}}}{6c} T_{\mathrm{sur}}^4, \tag{3.38}$$

where ϵ_b is the emissivity of the bar, $\sigma_{\rm sb}$ is the Stefan-Boltzmann constant, and T_b and $T_{\rm sur}$ are the temperature of the bar and the surrounding materials, respectively. The first term is the reaction of radiation from the bar, and the second term is the absorption and reflection of the radiation from the surrounding materials. When the temperature fluctuation is completely differential at the both ends of bar, the total torque becomes the maximum. In this pessimistic case, the ASD of noise is given by

$$\sqrt{S_{\rm temp,rad}(f)} \simeq \left(\frac{\epsilon_b \sigma_{\rm sb} T_b^3 A_b L_b}{12c} \sqrt{S_{T_b}(f)} + \frac{(2-\epsilon_{\rm b})\sigma_{\rm sb} T_{\rm sur}^3 A_b L_b}{12c} \sqrt{S_{T_{\rm sur}}(f)} \right) |\tilde{\chi}(f)|. \tag{3.39}$$

A_b and L_b are the side area and the length of the bar respectively. $S_{T_b}(f)$ and $S_{T_{\rm sur}}(f)$ are the spectrum of temperature fluctuations.

Cooling has a significant advantage about this noise due to the strong dependence on the temperature; $\propto T^3$. Suppressing the temperature fluctuation by surrounding the bar with a material which has high thermal conductivity is also effective way of noise reduction.

Thermal distortion noise

Asymmetric thermal expansion as depicted in Fig. 3.6 introduces the fluctuation of angular signal. The ASD of this noise is

$$\sqrt{S_{\rm temp,dist}(f)} = \frac{l_y}{L_b} \alpha_b(T_b) \sqrt{S_{\Delta T_b}(f)} + \frac{l_y}{L_b} \Delta\alpha_b(T_b) \sqrt{S_{T_b}(f)}, \tag{3.40}$$

where $\alpha_b(T_b)$ is the thermal expansion coefficient of the bar, and $\Delta\alpha_b(T_b)$ is the difference of the coefficient at the both ends of the bar. $\sqrt{S_{\Delta T_b}(f)}$ is the spectrum of temperature difference at the both ends of the bar.

Cooling is effective here to reduce the noise because most of materials have small thermal expansion coefficient at cryogenic temperatures. The bar should have high thermal conductivity to reduce the differential temperature fluctuation.

3.3 Target of TOBA

TOBA targets to observe earthquakes and gravitational waves as explained in Chapter 2. The gravity-based observation of earthquakes will provide new information of earthquakes, which is directly associated with induced density perturbation, and also enable earlier detection than using seismic waves. Observation of gravitational waves from intermediate mass black holes will let us study the origin of SMBHs at the center of galaxies. The required sensitivity is predicted to be 10^{-15} $/\sqrt{\rm Hz}$ at 0.1 Hz for the detection of earthquake [2], and 10^{-19} $/\sqrt{\rm Hz}$ for the observation of gravitational waves.

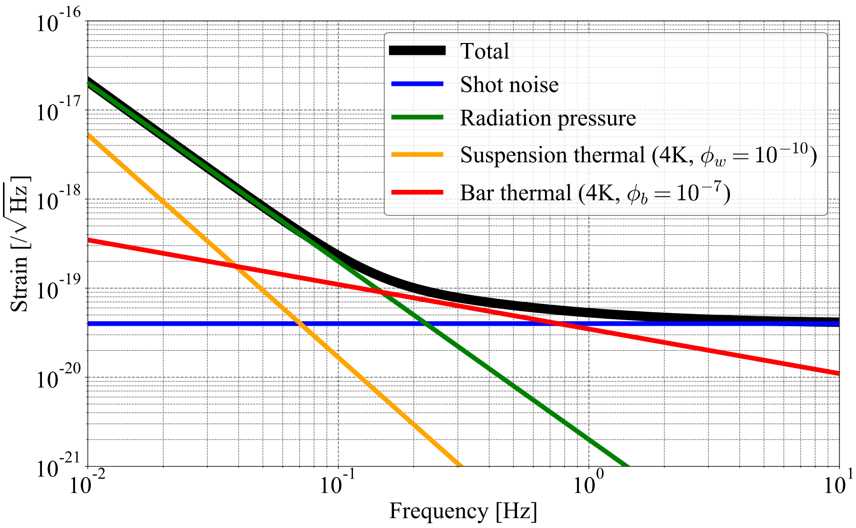

Figure 3.7: Design sensitivity of Final TOBA [16].

Final TOBA

The final target sensitivity of TOBA is 10^{-19} /$\sqrt{\text{Hz}}$ at 0.1 Hz to observe gravitational waves from IMBH binaries and to realize a gravity-based earthquake early warning. For that purpose, a 10 m-scale detector, Final TOBA, is planned to be developed in the future. Detailed noise budget about the design sensitivity is shown in Fig. 3.7 [16]. In this design, the bars are made of aluminum with 10 m length and 0.6 m diameter. The bar has a mass $M_b = 7600$ kg, a moment of inertia $I_b = 6.4 \times 10^4$ kg $\cdot$ m^2, and internal loss angle $\phi_b = 10^{-7}$. The resonant frequency is $f_0 = 1$ mHz, and the loss angle of the wire is $\phi_w = 10^{-10}$. The bar and the wire are kept at cryogenic temperature $T = 4$ K to reduce the thermal noise. Rotation of the bar is measured with a pair of Fabry-Perot cavities at both ends of the bar. The input laser power is set to 10 W, and the cavity has a finesse of 100.

The observable range for IMBH binaries with the target sensitivity is shown in Fig. 3.8 [16]. It reaches 10 Gpc for $10^4 - 10^5 M_\odot$ IMBHs. Though the expected event rate is uncertain due to the lack of information on IMBHs, a cosmological N-body simulation suggests that a few events will be observed per a year [71].

For earthquake, Final TOBA has much better sensitivity than 10^{-15} /$\sqrt{\text{Hz}}$, which is required to detect $M_w = 7$ earthquakes within 10 seconds from 100 km distance [2]. Since the gravity strain signal is proportional to r^{-5} (r:distance) as indicated in Eq. (2.25), the observable range with Final TOBA is about 600 km. Note that this estimation is based on the result for vertical gravity gradient measurement [2]. Taking the cost of the detector into account, a smaller scale configuration will be enough for the purpose of earthquake early

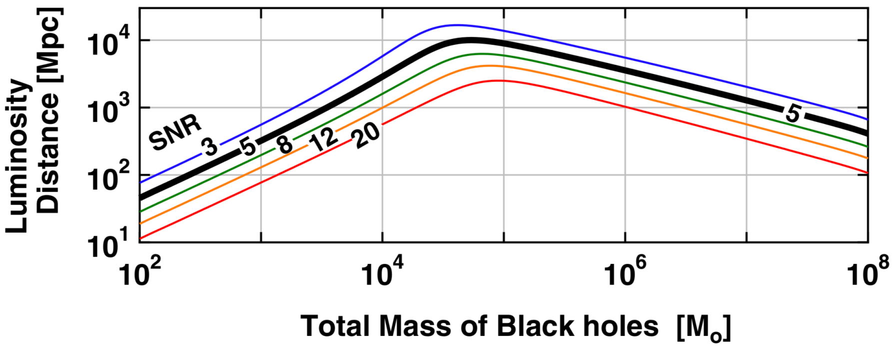

Figure 3.8: Detectable range for equal-mass IMBH mergers with the design sensitivity of TOBA [16].

warning.

3.4 Previous results

Towards the challenging target of Final TOBA, component researches have been performed with smaller scale prototypes. The prototypes developed some of the essential technologies for TOBA, investigated advanced configurations, and also did gravitational wave observations. The overview of these results are reviewed here. The achieved sensitivities of the prototypes are shown in Fig. 3.9 with the sensitivities of other detectors including the superconducting gravity gradiometer (SGG [52]) and LISA pathfinder [72]. The design sensitivity of the TorPeDO prototype is also plotted in the figure. Though currently the superconducting gravity gradiometer has better sensitivity than the prototypes of TOBA, no detector has achieved a sufficient sensitivity required for the observation of earthquakes or gravitational waves. Therefore intense upgrades of the detector are required.

First prototype (Phase-I TOBA)

The first prototype was developed in 2011 for the proof of principle [17]. The bar was suspended by superconducting magnetic levitation, and the horizontal rotation of it was measured with a Michelson interferometer on the ground. The noise spectrum of the first prototype was dominated by magnetic noise below 0.1 Hz and seismic noise above 0.1 Hz. Below 0.1 Hz, a large magnet for levitation introduced magnetic torque noise on the bar. Above 0.1 Hz, translational seismic vibration was transferred to the rotational signal of the bar via the tilt of the interferometer mirrors. The achieved noise level was about $10^{-8}\ /\sqrt{\mathrm{Hz}}$ at 0.1 Hz.

Using a pair of this prototype, the upper limit on the stochastic background gravitational wave was also set to $\Omega_{\mathrm{gw}} h_0^2 < 1.9 \times 10^{17}$ at 0.035–0.830 Hz [73]

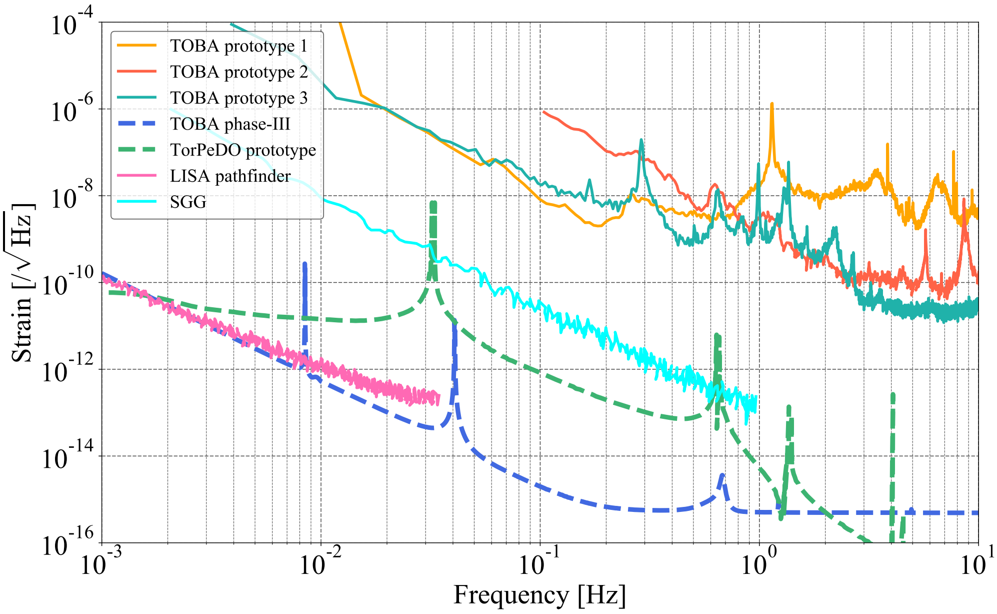

Figure 3.9: Sensitivities of low-frequency gravity strainmeters developed so far. The orange, red and green solid lines are the prototype sensitivity of TOBA, and the dashed blue line shows the design sensitivity of Phase-III TOBA, which will explained in Chapter 5. The dashed green line shows the design sensitivity of TorPeDO prototype [49]. The solid pink and the solid cyan lines are the achieved noise level of LISA pathfinder [72] and the superconducting gravity gradiometer [52], respecrively. For these two detectors, acceleration noise spectrum given in the paper was converted to strain noise using the detector scale D by $\tilde{h} = \tilde{a}/(D\omega^2)$. Note that LISA pathfinder is not sensitive to terrestrial gravity fluctuations since it is in the space.

Second prototype (Phase-II TOBA)

The second prototype developed in 2014 used a wire suspension system [18, 74]. Two bars were suspended orthogonally with double wires each from an intermediate mass. The fiber interferometer was constructed on a optical bench, which was also suspended with wires. At the suspension point, an active vibration isolation table was implemented to suppress seismic noise. It is a feedback stabilization system using seismometers and hexapod actuators. This prototype has multiple observation signals which consists of the rotations around three axes. Such a configuration is called as multi-output configuration. The multi-output configuration can compensate the blind direction of the detector and improve the detection volume and the parameter estimation accuracy [75]. The noise spectrum of this prototype was limited by the seismic noise and the vibration noise of the fiber optics. The achieved noise level was about 10^{-10}

$/\sqrt{\mathrm{Hz}}$ around 5 Hz.

Using this sensitivity, the presence of $200M_{\odot}$ IMBH binariy within $r < 2.1 \times 10^{-4}$ pc was excluded [74]. The upper limit on the stochastic background gravitational wave was also set to $\Omega_{\mathrm{gw}} h_0^2 < 1.2 \times 10^{20}$ at 2.6 Hz [76].

Satellite experiment using rotating TOBA

Spaceborne experiment of TOBA was performed from 2009 to 2010. The satellite was named SWIM$_{\mu\nu}$, which contained a small bar (50 g) whose motion was measured with photo-reflective displacement sensors [19]. This was the first spaceborne gravitational wave experiment. The bar and the housing satellite rotated at $f_{\mathrm{rot}} = 46.5$ mHz. Rotation of the satellite up-converts the low-frequency gravitational wave signal to around the rotational frequency. This improves the signal-to-noise ratio when the noise spectrum has steeper frequency dependence than $\sqrt{S(f)} \propto f^{-2}$ between the target frequency and f_{rot}. Additionally, the rotating configuration is directly sensitive to circular polarizations of gravitational waves which are defined as $h = (h_+ \pm i h_\times)/\sqrt{2}$. Two polarizations of the gravitational wave at f_{gw} appears separately at $f_{\mathrm{rot}} + f_{\mathrm{gw}}$ and $f_{\mathrm{rot}} - f_{\mathrm{gw}}$.

Observation data was taken for six hours. Using the data, SWIM$_{\mu\nu}$ set upper limits of $\Omega_{\mathrm{gw}}^{\mathrm{FW}} < 1.7 \times 10^{31}$ and $\Omega_{\mathrm{gw}}^{\mathrm{RE}} < 3.1 \times 10^{30}$ for two circular polarizations of the gravitational wave background.

Research on seismic noise

In order to investigate the way to reduce the seismic cross-coupling noise in TOBA, an experimental demonstration using a simple double-stage pendulum was performed in 2016 [21]. This experiment successfully reduced the cross-coupling transfer functions down to 5×10^{-6} rad/m at 0.1 Hz. Though the achieved values are insufficient for the future sensitivity of TOBA, this work have establish the basic way to reduce the translational seismic noise.

3.5 Next step : Phase-III TOBA

From the prototype developments explained in Sec. 3.4 and the theoretical calculations listed in Sec. 3.2, many issues have been clarified. Among them, the main difficulties to achieve the required sensitivity for scientific observations are as follows :

- Thermal noise reduction with a cryogenic system
- Seismic noise reduction with a low frequency vibration isolation
- Precise measurement of the pendulum rotation with a laser interferometric sensor

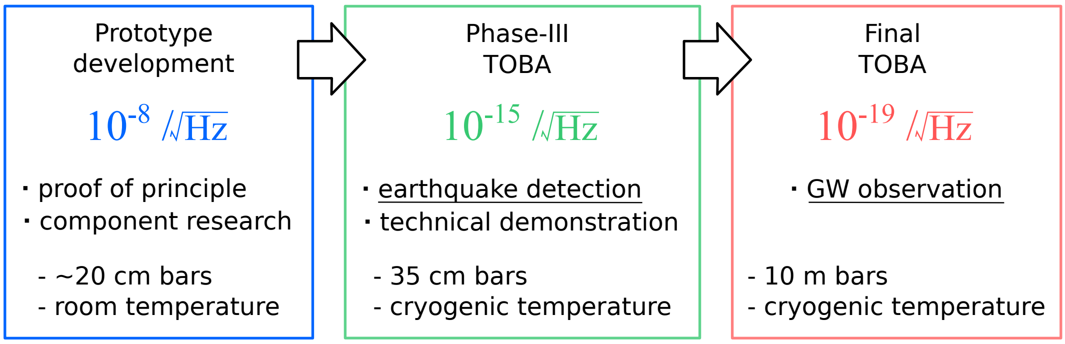

Figure 3.10: Development plan of TOBA. Three steps are shown with each target sensitivity at 0.1 Hz.

- Newtonian noise reduction

The first three points are about the instrumental noise, hence technical developments are necessary for the noise reduction. The last topic is about the environmental noise. Since Newtonian noise has never been measured directly, the noise properties should be investigated to establish reduction method. As a first step, it is better to investigate these issues with a small scale configuration before developing the 10 m-scale Final TOBA.

Phase-III TOBA

In this thesis, we propose a 35 cm-scale detector named Phase-III TOBA. Phase-III TOBA targets to demonstrate noise reduction and to realize earthquake detection at the same time. The target sensitivity is set to $10^{-15}\ /\sqrt{\mathrm{Hz}}$ at 0.1 Hz, which is required to detect earthquakes [2]. Some of the important technical issues mentioned above are to be solved with Phase-III TOBA at first, then the technologies are scaled up for Final TOBA in a future step. One of the key features is the cryogenic system, which is introduced to TOBA for the first time. The vibration isolation system and the optical system are also implemented for Phase-III TOBA to achieve the target sensitivity. About the Newtonian noise, direct measurement is expected to be achievable with the target sensitivity as indicated in Fig. 3.5. The noise properties are investigated with Phase-III TOBA to establish the noise reduction method, which will use auxiliary environmental sensors. Fig. 3.10 summarizes the development plan of TOBA. Phase-III TOBA is the intermediate step before developing Final TOBA. Table 3.1 compares the configurations of Phase-III TOBA and Final TOBA.

Theoretical and experimental topics about Phase-III TOBA are investigated in this thesis. On the theoretical side, the observation ability of earthquake with TOBA is studied in Chapter 4 to confirm the expected scientific

Table 3.1: Parameters of Phase-III TOBA and Final TOBA.

Parameter	Unit	Phase-III	Final
Target sensitivity at 0.1 Hz	[$/\sqrt{\mathrm{Hz}}$]	10^{-15}	10^{-19}
Bar length	[m]	0.35	10
Moment of inertia	[kg·m^2]	0.056	6.4×10^4
Resonant frequency	[mHz]	9	1
Temperature	[K]	4	4
Laser power	[W]	0.05	10

outcome with Phase-III TOBA. As mentioned in Chapter 1, TOBA is sensitive to horizontal gravity gradient, while the previous study [2] assumed vertical gravity gradient measurement. The detectability of earthquake with TOBA is calculated, and the difference from other types of detectors is clarified in this thesis for the first time. In addition, localization of epicenter is simulated using an array of TOBA to consider a realistic system of gravity-based EEW. The experimental topics are described in Chapter 5–7. In Chapter 5, the system of Phase-III TOBA is designed with a focus on the cryogenic system to achieve the target sensitivity of 10^{-15} $/\sqrt{\mathrm{Hz}}$. The fundamental part of the cryogenic system is experimentally demonstrated in this thesis, which is reported in Chapter 6. Both of these theoretical study and the technical developments are essential for TOBA project.

4 Detectability of Earthquake

Detectability of earthquakes with TOBAs is investigated in this chapter. The purpose of this chapter is to clarify the requirement on TOBA to realize meaningful gravity-based EEW.

First, achievable signal-to-noise ratio of TOBA is calculated and compared with other types of gravity gradiometers. This comparison is an extension of the previous work [2] that evaluated the detectability with vertical gravity gradients. As mentioned in Chapter 3, TOBA is sensitive to only horizontal gravity gradient (or equivalently, horizontal gravity strain) while some of other types of detectors are sensitive to vertical gravity gradient (strain). From the comparison between them, the earthquake detectability of TOBA with a sensitivity of 10^{-15} / $\sqrt{\text{Hz}}$ is evaluated to clarify how TOBA can contribute to EEW. More general information that what kind of detector is preferred for effective earthquake detection is also available from this result.

Second, the localizability of earthquake is simulated for several cases and compared to each other to investigate what kind of detection system should be constructed after the target sensitivity is achieved for a single detector. Though the localizability for the 2011 Tohoku-oki earthquake with vertical gravity strain was already examined in the previous work [2], here more general cases are investigated with horizontal gravity gradient observation. Some of the simulation results are then fed back to the requirement on the detectors, such as the arrangement of detectors or the calibration accuracy of them.

Throughout this chapter, the following spectrum of the detector noise in terms of gravity strain is used for calculation:

$$\sqrt{S_h(f)} = 10^{-15}\frac{(0.1\ \text{Hz})^2 + f^2}{f^2} \quad /\sqrt{\text{Hz}}, \tag{4.1}$$

by assuming that it is limited by sensing noise (flat spectrum) above 0.1 Hz and force noise ($\propto f^{-2}$) below 0.1 Hz. The value 10^{-15} is close to the sensitivity of proposed gravity gradiometers including Phase-III TOBA.

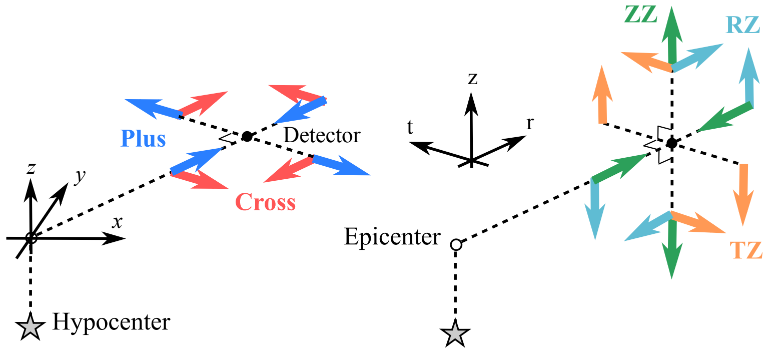

Figure 4.1: The definition of coordinate and five gravity strain components.

The SNR and the localizability are basically investigated around 10 seconds after the onset of the fault rupture. This target time is set to discuss about the ability of early warning with gravity-based observations. It is also a suitable period for gravity strain measurement around 0.1 Hz. Since seismic P wave travels about 70 km in 10 seconds, the gravity-based detection has chance to precede the current detection method using seismic waves for distant ($>$ 70 km) earthquakes.

The definition of coordinate is shown in Fig. 4.1. Instead of the earth-based coordinates (x, y, z), the gravity strain tensor is defined based on the detector-centered coordinates (r, t, z). The five independent components in the gravity strain tensor are set as follows :

$$\text{(horizontal)} \qquad h_+ \equiv \frac{h_{rr} - h_{tt}}{2}, \quad h_\times \equiv h_{rt}, \tag{4.2}$$

$$\text{(vertical)} \qquad h_{zz}, \quad h_{rz}, \quad h_{tz}. \tag{4.3}$$

Two horizontal strain components (plus h_+ and cross $h_\times$) are defined in analogy to gravitational waves. The remaining three components are chosen as the vertical strain components. TOBA and some kind of atomic interferometer such as MIGA are sensitive only to the horizontal components. A superconducting gravity gradiometer SOGRO is sensitive to both the horizontal and the vertical components.

4.1 Signal-to-noise ratio with different types of gravity gradiometers

In this section, detectability of earthquakes with different types of proposed gravity gradiometers are calculated and compared to each other. Then the detectability of TOBA, which is sensitive to only horizontal gravity strain, is discussed by comparing it to the detectability with vertical gravity strain. The detectability is quantified by available signal-to-noise ratio with the detector sensitivity of 10^{-15} $/\sqrt{\text{Hz}}$ (Eq. (4.1)). The gravity strain signals are calculated with the analytical half-space model [24] in this section. To investigate the early detectability, SNRs are calculated at 10 seconds after the onset of the fault rupture.

4.1.1 Calculation of signal-to-noise ratio

Optimal signal-to-noise ratio (SNR) for a strain signal $h(t)$ under an instrumental noise $n(t)$ with a spectrum of $S_n(f)$ is given by a matched filtering as

$$\mathrm{SNR} = \int df \frac{\tilde{h}(f)\tilde{s}^*(f)}{S_n(f)} = \int df \frac{\tilde{h}(f)}{\sqrt{S_n(f)}} \frac{\tilde{s}^*(f)}{\sqrt{S_n(f)}}, \tag{4.4}$$

where $s(t) = h(t) + n(t)$ is the recorded signal. In time-domain, the SNR is given by a convolution of two filtered signals $h_w(t)$ and $s_w(t)$ as follows

$$\mathrm{SNR}(t) = \int_0^t d\tau h_w(t-\tau) s_w(\tau), \tag{4.5}$$

$$h_w(t) = \int df \frac{\tilde{h}(f)}{\sqrt{S_n(f)}} e^{2\pi i f}, \quad s_w(t) = \int df \frac{\tilde{s}(f)}{\sqrt{S_n(f)}} e^{2\pi i f}. \tag{4.6}$$

The applied filter $1/\sqrt{S_n(f)}$ works as a whitening filter for the instrumental noise $n(t)$. For the noise spectrum given in Eq. (4.1), the whitening filter is a second-order high-pass filter with a cutoff frequency of 0.1 Hz.

In the calculation flow, the signal template $h(t)$ is numerically calculated base on the half-space model. Then ten timeseries of the instrumental noise $n(t)$ are randomly generated. Each time series is whitened and convolved to calculate the SNR. The averaged value of the SNRs for ten random noise timeseries is used as a final SNR.

4.1.2 Source parameters

Three focal mechanisms are investigated in this section; one strike-slip fault and two dip-slip faults. The pictures of the strike-slip and the dip-slip faults are shown in Fig. 2.5. The parameters used here are $(\gamma_s, \gamma_d, \gamma_r) = (180°, 90°, 180°)$ for the strike-slip fault, and $(180°, 10°, 90°)$ and $(180°, 20°, 90°)$ for the dip-slip faults. The dip angles are selected as the typical ones for oceanic plates [77]. The depth of the hypocenter is set at 20 km as a typical value of earthquakes, because most of earthquakes happen in the region shallower than 50 km depth as shown in Fig. 4.2.

The used source time function is plotted in Fig. 4.3. The functions are based on Eq. (2.4), which assumes the self-similarity of source fault evolution. As mentioned above, signal-to-noise ratio is calculated at 10 seconds after the onset of the fault rupture. The half duration of the source fault rupture is assumed to be longer than 10 seconds, which is correct for $M_w > 7.3$ in

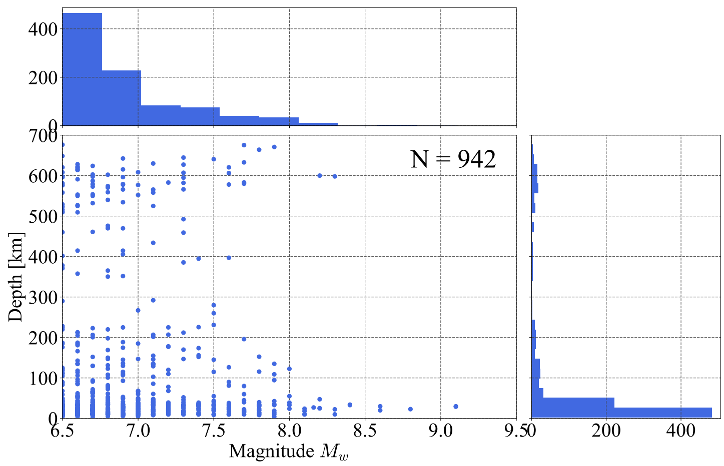

Figure 4.2: Depth distribution of hypocenter for $M_w > 6.5$ earthquakes that happened after 2000. The datas ares taken from USGS (https://earthquake.usgs.gov/).

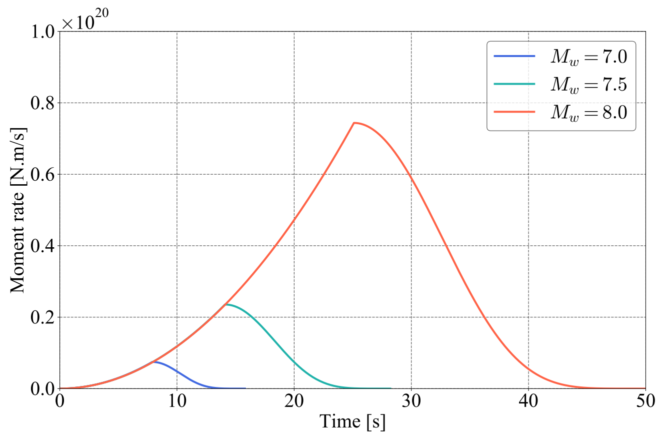

Figure 4.3: Model source time functions for $M_w = 7.0$ (blue), $M_w = 7.5$ (green) and $M_w = 8.0$ (red). The initial 10 seconds of the function for $M_w > 7.3$ is used for signal-to-noise ratio calculations.

the model (Eq. (2.27)). Since the initial fault evolution is assumed to be independent to the magnitude, the following calculations are valid for any magnitudes larger than 7.3 under the assumption of the self-similarity.

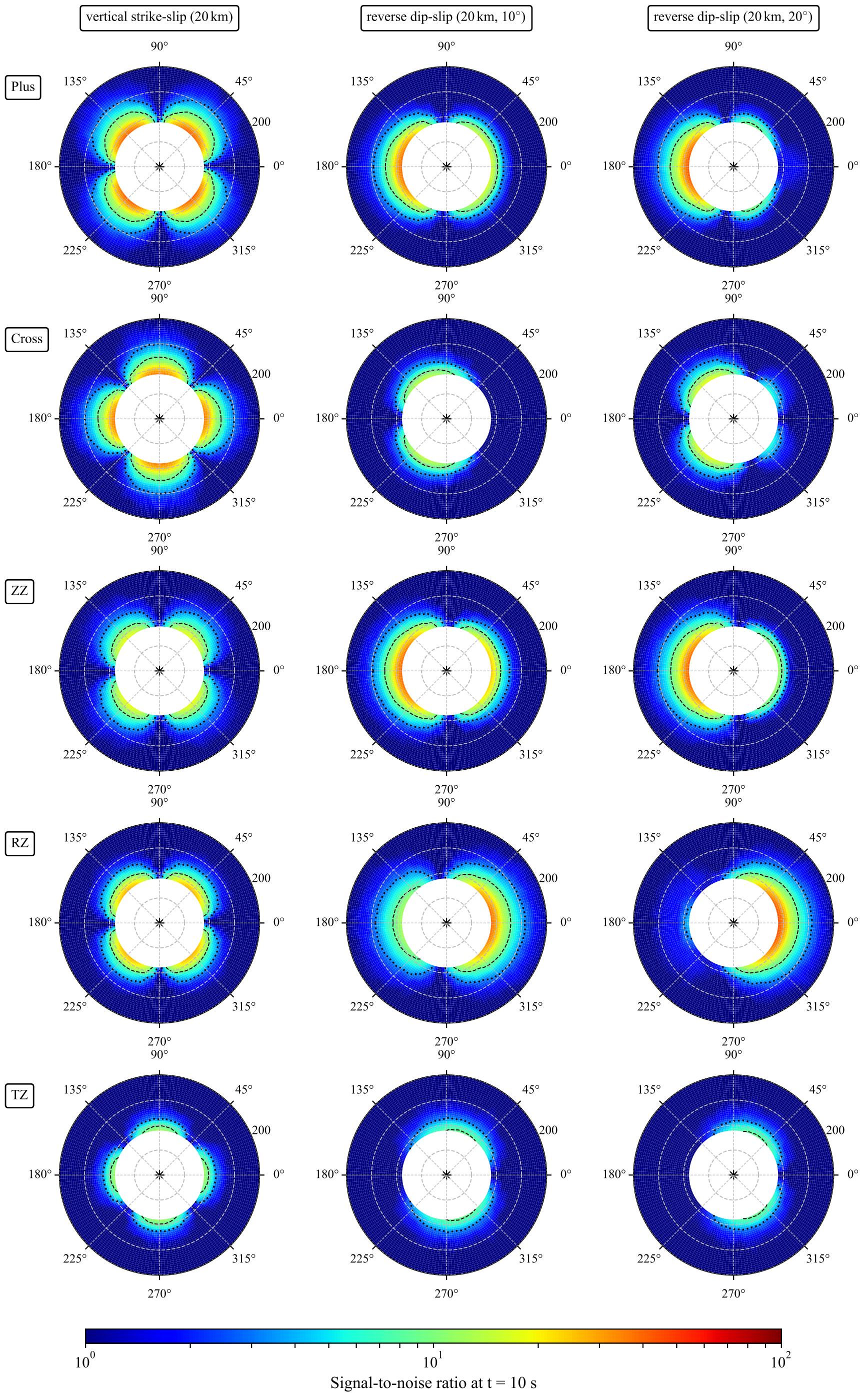

Figure 4.4: Azimuth-distance distributions of SNR available with gravity strain measurement with 10^{-15} $/\sqrt{\mathrm{Hz}}$ sensitivity of the detector. 0° is the East and 90° is the North. The color indicates the SNR as shown in the color bar at the bottom. Each column and row corresponds to the focal mechanism and the component of gravity gradient tensor, respectively. The dashed grey circles are the grid lines of 50, 100 and 150 km distance. The dashed and the dotted black contours show the area of SNR=8 and 3, respectively. The white blank area at the center of each figure ($\lesssim$ 85 km) is the region where seismic P-wave arrives within 12 seconds.

4.1.3 Signal-to-noise ratio distribution for each gravity strain component

First, the SNR distributions are calculated for each component of the gravity strain tensor. To investigate the early detectability, the SNRs are calculated at 10 seconds after the onset of the fault rupture. Fig. 4.4 shows the azimuth-distance distribution of SNR for each component and each focal mechanism up to 200 km distance. The color indicates the SNR as shown in the color bar at the bottom. SNR is below 1 outside the plotted region (> 200 km). Each column corresponds to the focal mechanism, and each row corresponds to the gravity strain component. The white blank area at the center of each figure ($\lesssim$ 85 km) is the region where seismic P-wave arrives within 12 seconds. The East and the North direction is set to 0° and 90° respectively, hence the strikes are along to 90°–270° line.

About the strike-slip event, the quadruple pattern of the SNR distribution reflects the induced density change. More SNRs are available for the horizontal plus and cross components than the vertical components. This is because the density change evolves in horizontal directions, then the shallower parts of the ground is mainly deformed. The SNR with h_+ is roughly twice higher than with h_{zz} or h_{rz} components. Only $h_\times$ can give large SNR at 0°, 90°, 180° and 270° directions.

About the dip-slip events, the vertical gravity strain components give larger SNRs than the horizontal components. In these earthquakes, the density change evolves vertically therefore the deeper part of the ground is deformed, which results in larger signal amplitudes in the vertical components. h_+ and h_{zz} give similar SNRs, which are important at 180° direction. At 0° direction, only h_{rz} can have high SNR. It is difficult to detect the dip-slip earthquakes from the direction along the strike line (90° or 270°), because no components have sufficient SNR in those directions. The dependence on the dip angle is insignificant at early phases, though asymmetry of the distribution between the left half and the right half slightly increases as the dip angle.

4.1.4 Signal-to-noise ratio distribution for each type of detector

Next, Fig. 4.5 shows the sum of the SNR in three sets of the strain components. The "all" in the first row is the sum of the five strain components, hence this gives the maximum available SNR. The "horizontal" in the second row is the sum of two horizontal components, h_+ and $h_\times$, which are detectable with TOBA. The "vertical" in the third row is the sum of the three vertical components, h_{zz}, h_{rz} and h_{tz}. To make the distribution quantitatively clear, the azimuth distribution of the SNR at 100 km distance is plotted in Fig. 4.6.

It is clear that the horizontal components have dominant contribution in the strike-slip event. 80 % of the maximum SNR is available at any azimuths with

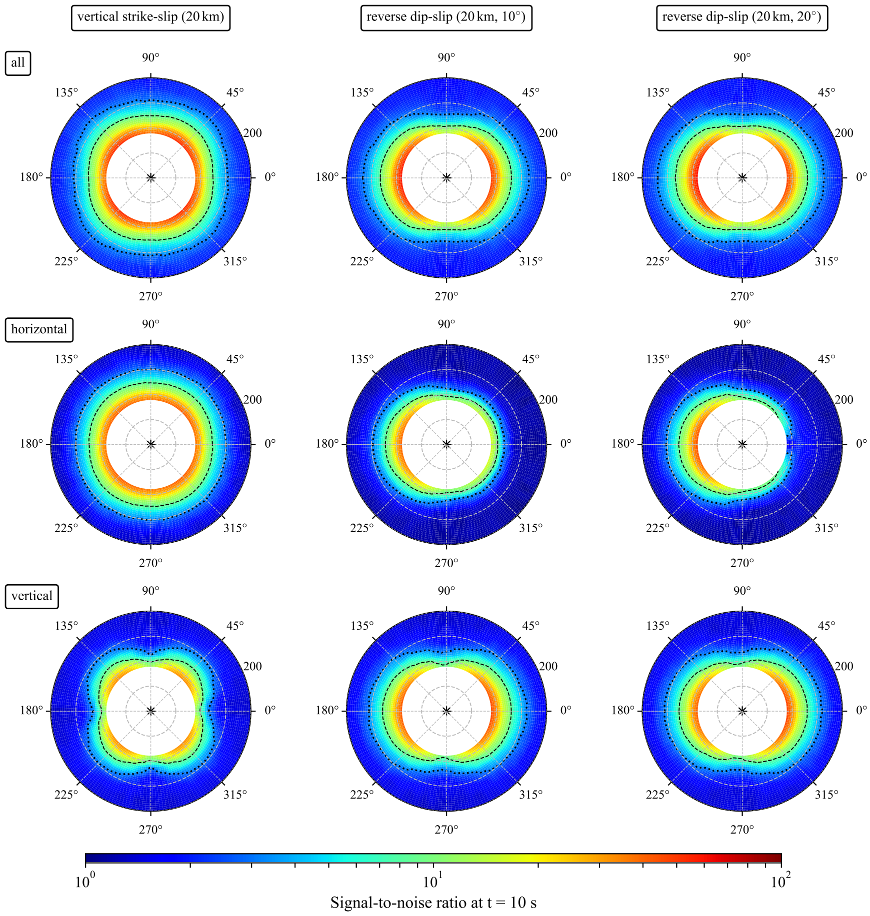

Figure 4.5: Sum of the SNR distribution for the set of gravity strain components. Each row corresponds to the sum of the all components, the horizontal components and the vertical components, respectively. The dashed and the dotted contour show the area of SNR=8 and 3, respectively.

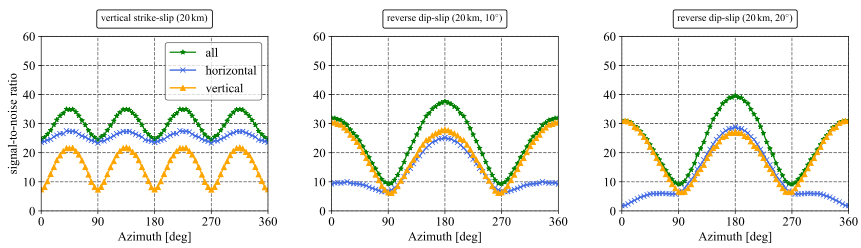

Figure 4.6: Azimuth dependence of the SNR distribution at 100 km distance from the epicenter.

the horizontal components. Though the vertical components give good SNR at several azimuths, their detectability is lower than the horizontal components and also depends on the azimuths. From these results, TOBA has a dominant contribution in detecting strike-slip earthquakes.

On the other hand, the vertical components have advantages in detecting dip-slip earthquakes. The horizontal and the vertical components have almost same SNR in 180° direction, which is about 70 % of the maximum SNR. The difference is significant in 0° direction, where the vertical components is dominant and the contribution from the horizontal components is only 30 % of the maximum. However, in usual case the coast is in the direction of 180° and there is no land in the direction of 0°, to which the hanging wall moves. Since detectors cannot be placed without land, the horizontal strain components and the vertical strain components will provide similar contribution in detecting actual dip-slip earthquakes.

In summary, good SNRs of gravitational signals are available with the horizontal gravity strain components. They give better SNRs than the vertical components in strike-slip earthquakes, and similar SNRs as the vertical components in dip-slip earthquakes at $90° - 270°$ azimuths. Though observing both of horizontal and vertical components is always the best way, at least 70 % of SNR will be available only with the horizontal components. The detectable range of the horizontal components with SNR=8 is isotropically 130 km at 10 seconds for strike-slip earthquakes. Though the range for a dip-slip earthquake depends on the azimuths, it is 130 km at 180° direction, where there is a land in usual cases. Thus TOBA can contribute well to detect earthquakes. As demonstrated by the calculations, the assumed sensitivity 10^{-15} $/\sqrt{\mathrm{Hz}}$ is enough for the detections.

4.2 Localization

In this section, the localizability of earthquakes using torsion-bar type detectors is investigated to consider a configuration of earthquake detection system. Here we basically follow the method proposed in [78]. The proposed method is to use the amplitude ratio of the gravity signal between two detectors placed at the same point in different orientations offset by 45°. Such a set of detectors can constrain the direction of the epicenter to four directions from the signal amplitude ratio between the two detectors. Then, by using the three sets of detectors, the location of the epicenter can be identified in a single point. This idea is to use $\boldsymbol{S}(\theta, \phi)$ in Eq. (2.25) which depends only on the direction of the epicenter and the orientation of the fault. The primary merit will be that the dependence on the source time function $\mathcal{I}[M(t)]$ can be omitted. Otherwise the information of $M(t)$ is required to localize the epicenter, which is quite hard due to the variance of $M(t)$ as shown in Fig. 2.4.

In this thesis, their method is a bit generalized; N_d detectors are placed at different points (not necessarily paired), and a N_d-component vector of signal amplitude ratio between the detectors is used for localization. By choosing this way, the signals at different distances are directly compared. Therefore the r^{-5} dependence in Eq. (2.25) is also taken into account, which will help the localization more.

The calculated localized area is then compared to 100 km^2, which is the minimum unit of the current early warning system in Japan based on seismic waves.

4.2.1 Calculation flow

Here Monte-Carlo simulations were performed to calculate the localizability. The calculation flow is as follows

1. The xy-plane is divided into a grid, and detectors are placed at several points. Then the gravity strain signals recorded by each detector are calculated for the epicenters at the grid points (x, y).

2. The signal amplitude ratio between the detectors is saved as a template of N_d-component vector. The vector is normalized to an unit length vector.

3. An event is injected at arbitrary point, and gravity strain signals are calculated at the position of the detectors.

4. Instrumental noise is added to the signal, and the signal amplitude ratio is estimated from the signal timeseries of each detector.

5. Step3 and Step4 are repeated 10000 times for randomly generated instrumental noise, and the probability distribution is derived.

The simulated area is 200×200 km area, and the detectors are placed around the left end of the area. Such arrangement assumes the case of detecting offshore earthquakes from the detectors placed along the coast line. As mentioned in Sec. 2.2.3, gravity-based earthquake detection will play an important role in such a case. Though there can be other cases in general, the most practical case is investigated here for the first step.

The primary target is to determine the location of the epicenter (x, y) which are most important for early warnings. Hence the other parameters, the focal mechanisms and the depths are fixed in the first step (Sec. 4.2.2). This is based on the assumption that large earthquakes will happen along the known faults. The effect of the fixed parameters is then discussed in Sec. 4.2.3 and Sec. 4.2.4. The simulation area is divided into 1×1 km grids, which is sufficiently small as the localization accuracy to use early warnings of earthquakes. The gravity strain signals are calculated with the analytical full-space model (see Sec. 2.2.1 or [23]) in this section.

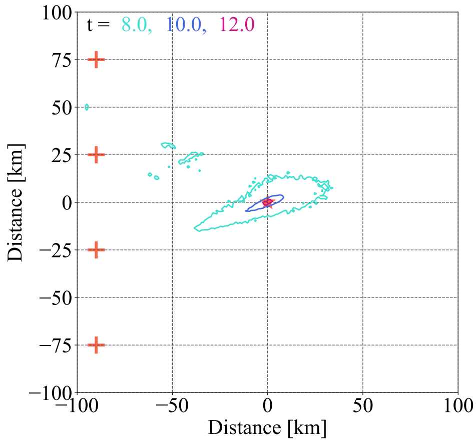

Figure 4.7: An example of a localization map. 95 % confident localized area at t =8 s, 10 s and 12 s are shown with the cyan, blue and violet contours, respectively. The orange + (or ×) at the left indicates the arrangement of the detectors, and the orange star at the center of the contour is the epicenter.

As is the case of the SNR calculation, the localizability is investigated around 10 seconds after the onset of the fault rupture. The source fault evolution shown in Fig. 4.3 is used here again, hence the following results at 10 seconds are valid for $M_w > 7.3$ as explained in Sec. 4.1.2.

4.2.2 Localizability with different detector arrangements

First, the localizabilities of earthquakes with different arrangement of detectors are compared to derive how dense arrays of detectors are required for sufficient localization. In this subsection, four, five or six detectors are placed along $x = -90$ km, -75 km$< y < 75$ km area with different arrangement. The localization map is calculated for each arrangement. To show how the results are expressed in this subsection, an example is shown in Fig. 4.7. The different colors show the localized area at different times from the onset of the fault rupture ($t = 0$); $t = 8$ s (cyan), $t = 10$ s (blue) and $t = 12$ s (violet). If the localized area is larger than 1000 km^2, the contour is not shown for the ease of viewing.

In the following simulations, the events are injected in -25 km$< x < 75$ km and -75 km$< x < 75$ km area as shown in Fig. 4.8, and localization for each event is simulated. As previous section, two focal mechanisms are investigated here; a strike-slip earthquake $(\gamma_s,\ \gamma_d,\ \gamma_r) = (150°,\ 90°,\ 180°)$ and a dip-slip earthquake $(\gamma_s,\ \gamma_d,\ \gamma_r) = (150°,\ 20°,\ 90°)$, where γ_s, γ_d and γ_r are strike, dip, and rake angle defined in Fig. 2.3. The depth of the hypocenter is set at 20 km for the same reason as the previous section.

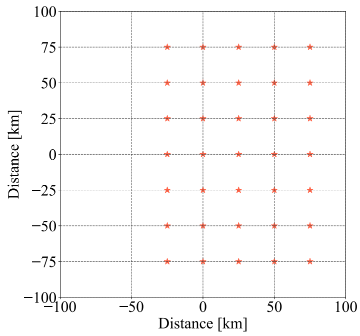

Figure 4.8: Epicenters of injected events (red stars) in the simulation.

Localization of strike-slip earthquakes

Fig. 4.9 show the localization maps of the strike-slip earthquake with four, five or six torsion bars that are placed in + arrays and × arrays. Fig. 4.10 shows the case that three pairs of + and × torsion bars are used (hereafter this arrangement is called as "three-pair" configuration). The arrangement of the detectors are shown with red + or × in the figure. The localized area at 8, 10 and 12 seconds are plotted with cyan, blue and violet contour, respectively. Each contour shows the 95 % confidence area in each Monte-Carlo simulation. The contours are not shown when the localized area is larger than 1000 km^2. 35 events were injected (Fig. 4.8), whose epicenters are also shown with red stars in each figure. The localized area of each event is overlapped in the single figure.

With four detectors (the top row in Fig. 4.9), the localized area is largely distorted and the accuracy is not good at early times. Though five detectors (the medium row in Fig. 4.9) give better localizations, the localized area at early time (t=8 s) is still not good at some points (e.g. $(x, y) = (-25, \pm 50)$ km in the left middle panel of Fig. 4.9). By using six detectors, the detection area is almost uniformly good. The error in $y = \pm 75$ km is not a problem when detectors are sequentially placed outside the simulation area ($|y| > 100$ km). Difference between the + arrangement and the × arrangement is not qualitatively significant. The three-pair arrangement shown in Fig. 4.10 also gives the similar localization maps as the six + or × arrangement of detectors. In terms of a cost to build detector stations, the three-pair arrangement will be a better choice since the number of stations is less. The localized area depends almost only on the distance from the detectors, and there is no blind area in this configuration.

Fig. 4.11 shows the distance dependence of the localized area at 10 seconds. The horizontal axis is the distance to the closest detector from each injection point. The symbols and colors of the markers indicate the arrangements of the detectors; the number of detectors and their orientations are specified in the

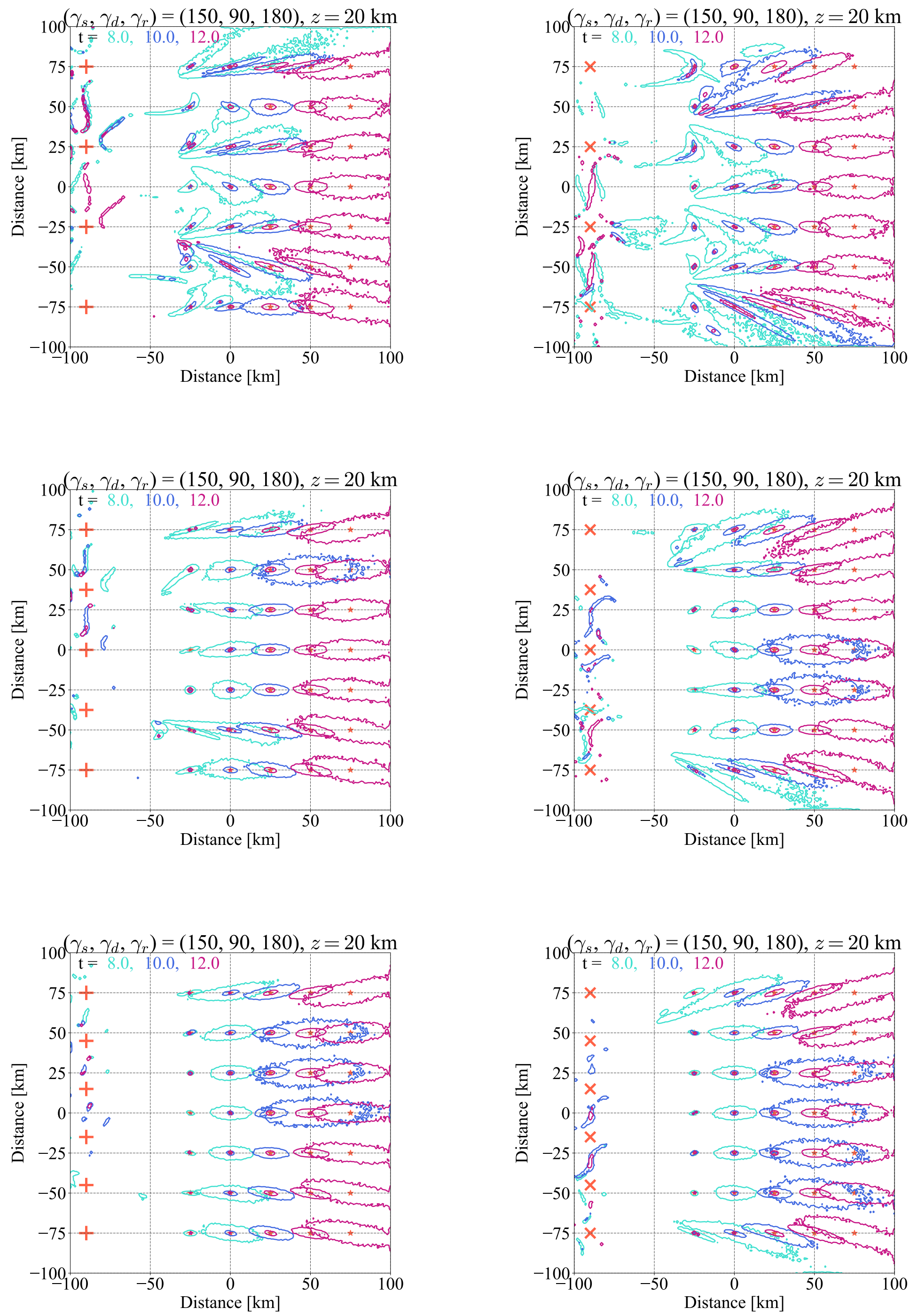

Figure 4.9: Localization map for $(\gamma_s,\ \gamma_d,\ \gamma_r) = (150°,\ 90°,\ 180°)$ strike-slip earthquake with various arrangement of detectors. Localized area at 8 seconds (cyan), 10 seconds (blue) and 12 seconds (violet) after the onset of the fault rupture are shown. The contours are not plotted when the localized area is worse than 1000 km^2. The localized contours for the events in Fig. 4.8 are overlapped in the single figure. The arrayed orange stars are the epicenters of the injected events. The detector arrangements are shown with red + or $\times$, which represents the orientation of suspended bars.

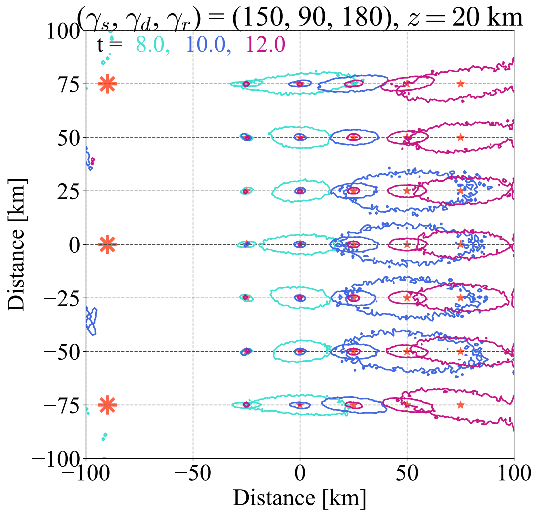

Figure 4.10: Localization map for $(\gamma_s,\ \gamma_d,\ \gamma_r) = (150°,\ 90°,\ 180°)$ strike-slip earthquake with three pairs of torsion-bar detectors.

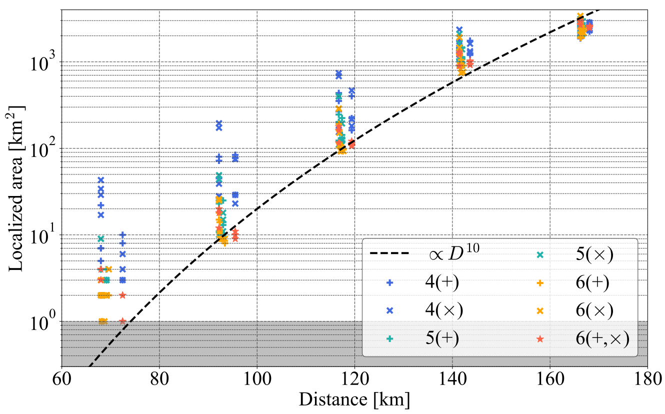

Figure 4.11: Localized area vs distance from the epicenter for different arrangement of detectors at 10 sec after the onset of the fault rupture, for the strike-slip earthquake. The horizontal axis is the distance to the closest detector from each epicenter. The number and orientation of the detectors are specified in the legend for each symbol. The black dashed line shows $\propto D^{10}$ dependence which is simply expected from the distance dependence of gravitational signal amplitude. The shaded area is below the resolution of simulation grid, which is 1 km^2.

legend. Since the signal amplitude is inversely proportional to D^5 as shown in Eq. (2.25), where D is the distance from the hypocenter, the localized area is expected to be proportional to D^{10}, which is the inverse-square of the signal-to-noise ratio. The simulated localized area has similar dependence as this expectation which is shown with black dashed line, hence the localizability is almost determined by the signal-to-noise ratio. The localized area up to about 120 km distance is below 100 km^2, which is the minimum unit of the current warning system based on seismic waves. Therefore the gravity strain observation can localize the epicenter within 120 km with better accuracy in 10 seconds. Additionally, the localization time can be improved because it takes about 17 seconds for seismic P wave to propagate 120 km distance.

The deviation between the detector arrangements is large at close distances ($<$ 120 km), while it is insignificant at distant points ($\sim$ 160 km). This will be because not enough number of detectors can detect the signal with high SNR when the epicenter is too close to the detector arrays. As the number of detectors increases, the chance to detect signals is also enhanced hence higher SNRs are available. Such difference is not significant for distant events which are detected by almost all detectors, since three detector signals are sufficient to identify the two free parameters in principle.

Localization of dip-slip earthquakes

Fig. 4.12, and 4.13 show the localization maps for the dip-slip earthquake. Though the localizability is worse than for the strike-slip earthquake, the trend about the detector arrangement is similar. For the dip-slip earthquake, roughly six arrayed detectors or three-pair arrangement are required for uniform localization. The lower localizability than the strike-slip earthquake is mainly due to the small amplitude of the gravity gradient signal as shown in Sec. 4.1. The relatively weaker dependence on the azimuth for the dip-slip earthquake than the strike-slip earthquake, which can be seen in Fig. 4.4 for the h_+ component, will also contribute it. As shown in Fig. 4.14, the localized area is about 100 km^2 up to 110 km distance. This is not quite different from the strike-slip earthquake, because of the strong distance dependence of the gravity strain signal. As is the case of the strike-slip earthquake, the localization time is shortened compared to the current warning system.

4.2.3 Requirement on presumption accuracy

In the previous subsection, the focal mechanism and the depth was fixed by assuming that large earthquakes will happen along known faults. Here the effect of presumption error about the focal mechanism or the depth is investigated. The calculation flow is basically same as the previous subsection. Here the template signal ratio is calculated for slightly offset parameters from the injected event, to take into account the effect of mis-presumption. Then the localized position is systematically offset from the position of the epicenter. The amount of offset is evaluated to derive the requirement on the presumption ac-

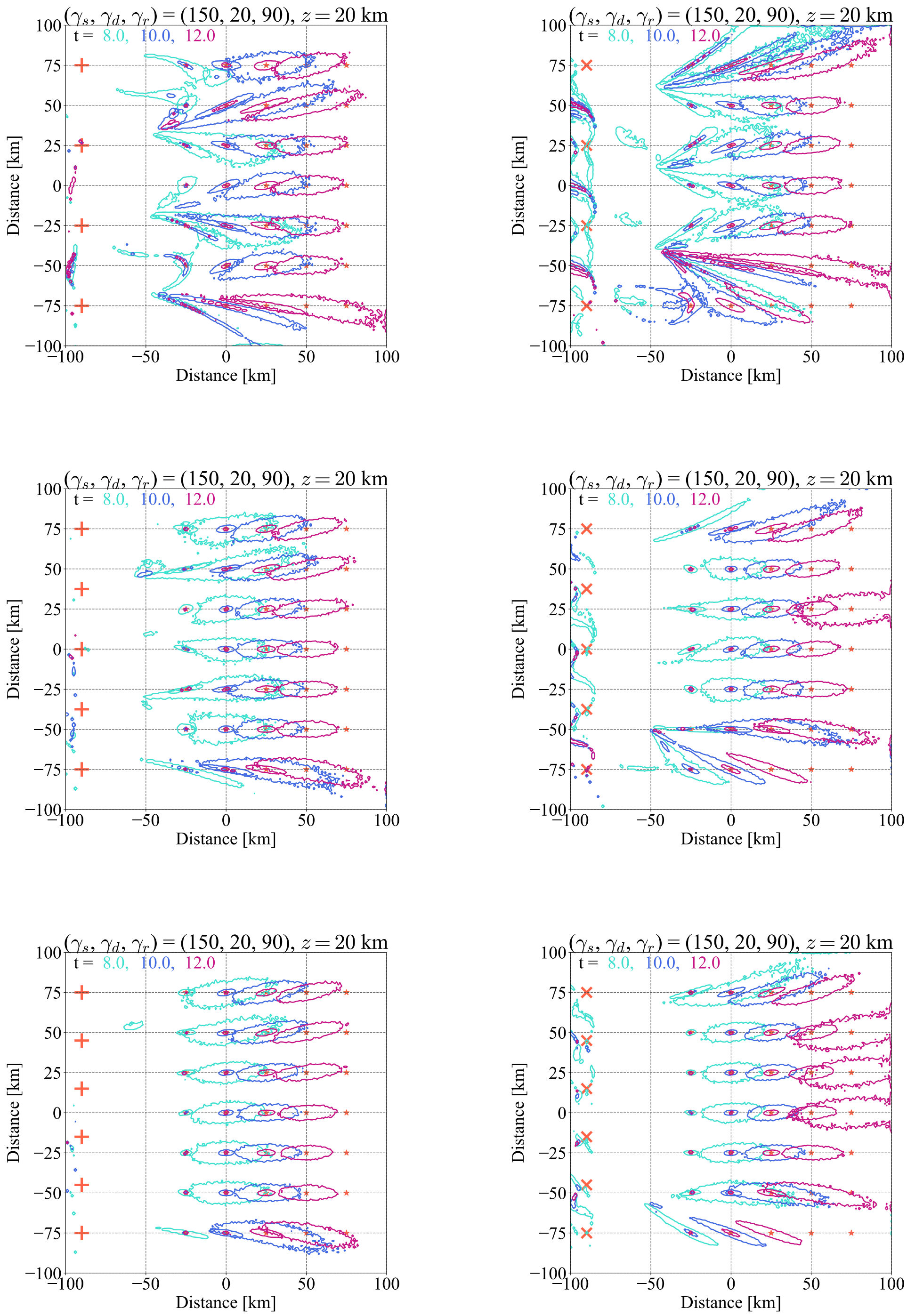

Figure 4.12: Localization map for $(\gamma_s,\ \gamma_d,\ \gamma_r) = (150°,\ 20°,\ 90°)$ dip-slip earthquake with various arrangement of detectors. Plot conditions are same as Fig. 4.9.

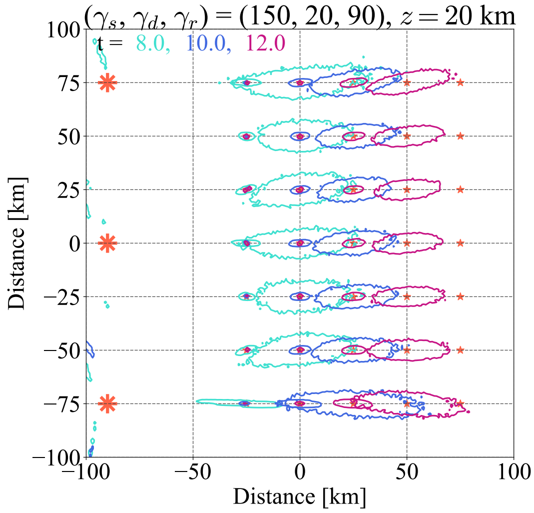

Figure 4.13: Localization map for $(\gamma_s,\ \gamma_d,\ \gamma_r) = (150°,\ 20°,\ 90°)$ dip-slip earthquake with three pairs of torsion-bar detectors.

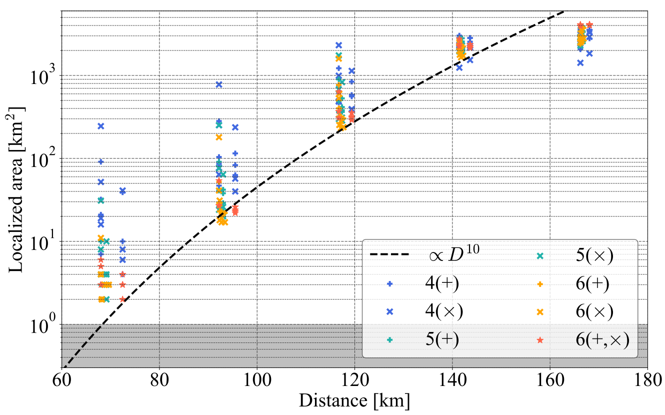

Figure 4.14: Localized area vs distance from the epicenter for different arrangement of detectors at 10 seconds, for the dip-slip earthquake.

curacy of focal mechanisms when preparing the template of signals amplitude ratio.

Fig. 4.15 shows the systematic errors due to the presumption error about the strike angle by 10 deg (red), about the dip angle by 10 deg (blue), about the rake angle by 10 deg (orange), and about the depth by 20 km (green). These presumption errors result in roughly 10 km error of localization within the simulated area. In other word, the error of presumption needs to be suppressed below 10 deg and 20 km for the focal mechanisms and the depth of the

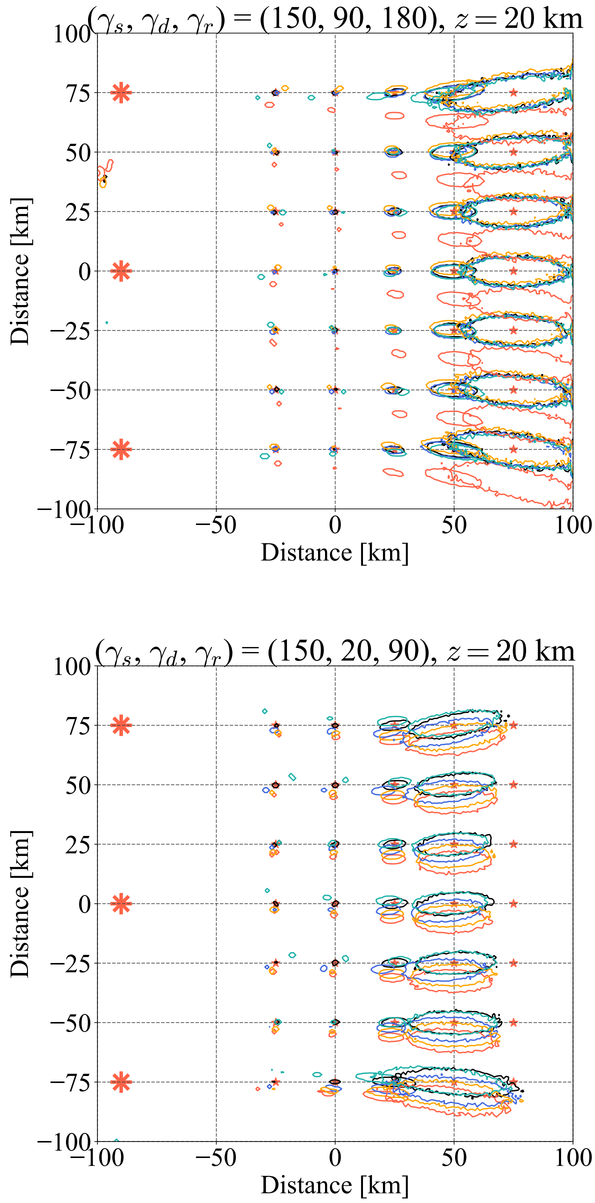

Figure 4.15: Localization error due to mis-presumptions of templates for a strike-slip event (upper; $(\gamma_s, \gamma_d, \gamma_r) = (150°, 90°, 180°)$) and a dip-slip event (lower; $(\gamma_s, \gamma_d, \gamma_r) = (150°, 20°, 90°)$). The localized areas at 12 seconds are plotted when the prepared templates are correct (black), or the parameters are offset by $+10°$ for γ_s (red), $-10°$ for γ_d (blue), $-10°$ for γ_r (orange) and -20 km for the depth (green).

hypocenter to determine the location of the epicenter in accuracy of 10 km. It seems that the 10 deg accuracy is not quite hard since the geometries of fault plane is given in the precision of a few degrees [77]. However, statistical research on actual faults and earthquakes is necessary to confirm this, which is left as a future work.

4.2.4 Localization without presumption of focal mechanisms

Though the simulations above assumed the focal mechanisms and the depth to be fixed and known in advance, it is possible to treat them as free parameters in estimating the location of earthquakes. Here three focal mechanism parameters are also included in the free parameter to investigate more general detectability of earthquake. To save the computation cost, the depth of the hypocenter was left to be fixed to 20 km. The calculation flow is the same as the previous subsections.

Fig. 4.16 and 4.17 shows the localized area in this case for the strike-slip event and the dip-slip event, respectively. The localized area is roughly three times wider than the case when the focal mechanisms are treated as fixed parameters (Fig. 4.10 and 4.13). The focal mechanisms can also be estimated, though those parameters are not very important in terms of earthquake early warnings. Therefore even if sufficient information on the focal mechanisms is not available, the epicenter can be localized to some extent. Note that this is just a case study, hence more general conditions should be investigated as a future work.

4.2.5 Requirement on detector calibration

Since the signal amplitude ratio is used for the parameter estimation, calibration error of the detectors directly affects the estimated parameters. Here the effect of calibration error on the localizability is investigated to set a srequirement on the detector side. The condition of calculation is the same as Sec. 4.2.2; the focal mechanisms are treated as fixed parameters again. When the detectors have calibration accuracy of 10 %, for example, the measured signal amplitude ratio also deviates systematically by about 10 %. Hence the epicenter can be localized to different points from the true epicenter.

Fig. 4.18 shows the contour of the template vector difference from the injection point of earthquakes. Each contour corresponds to the area of systematic error due to the calibration error of 10 % (cyan), 3 % (blue) and 1 % (violet). 10 % error of calibration results in more than 15 km error of localization. To localize the epicenter within 10 km accuracy, 3 % of calibration accuracy is required for the detectors. This value is not difficult in usual experiments, hence the effect of the calibration error will not be a serious problem in the detection scheme used here.

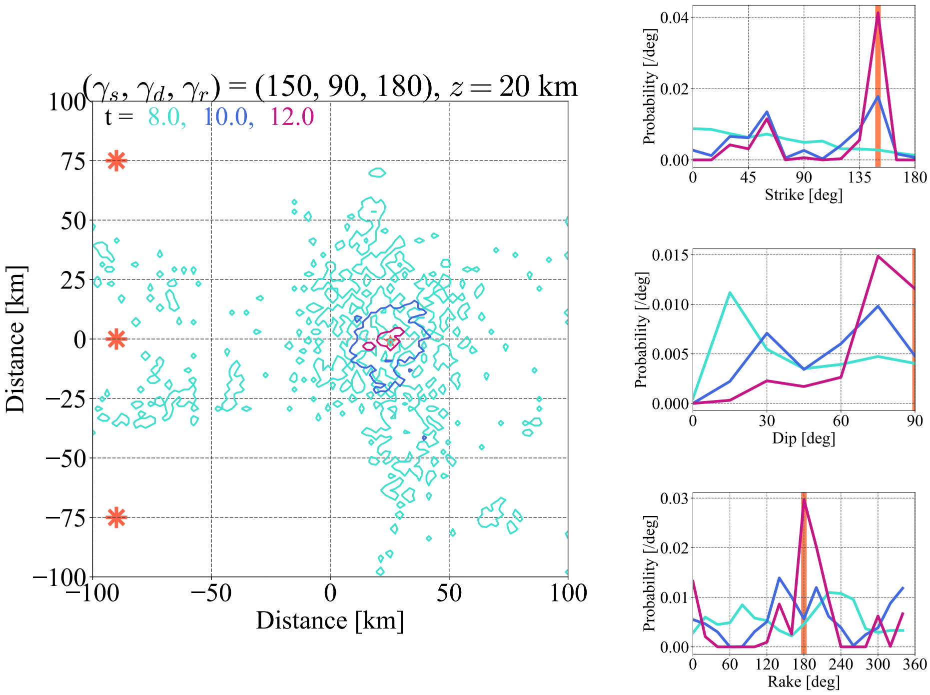

Figure 4.16: Parameter estimation for strike-slip earthquake without presumptions about focal mechanisms. Only the depth was treated as a fixed parameter. The left figure is the localization map, and the right figures are estimations of focal mechanisms. The orange star in the left figure and the orange band in each figure on the right show the injected location and the fault parameters, respectively.

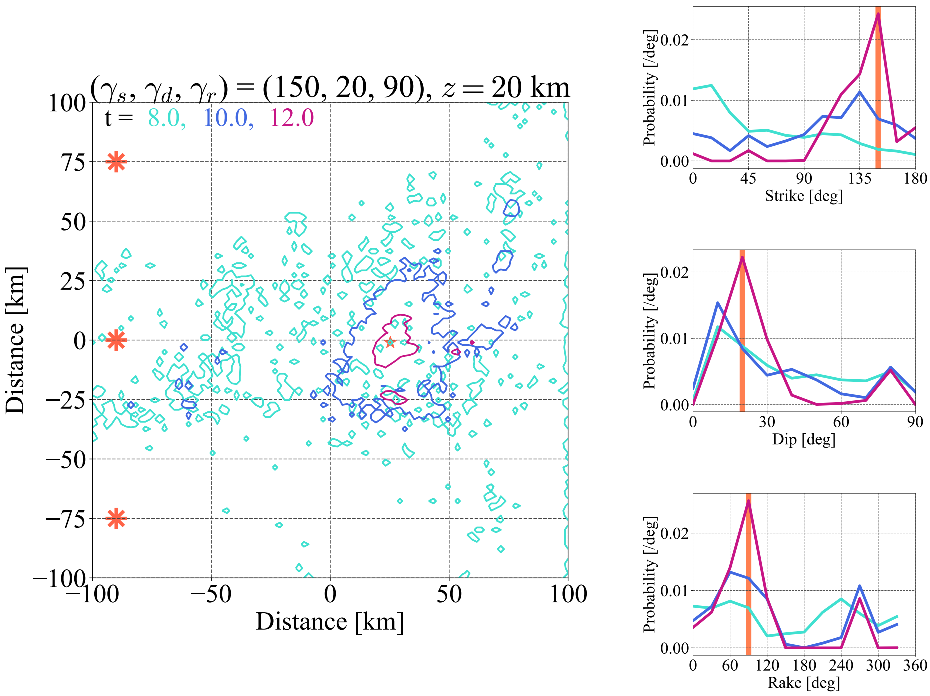

Figure 4.17: Parameter estimation for dip-slip earthquake without presumptions about focal mechanisms. The plot conditions are same as Fig. 4.16.

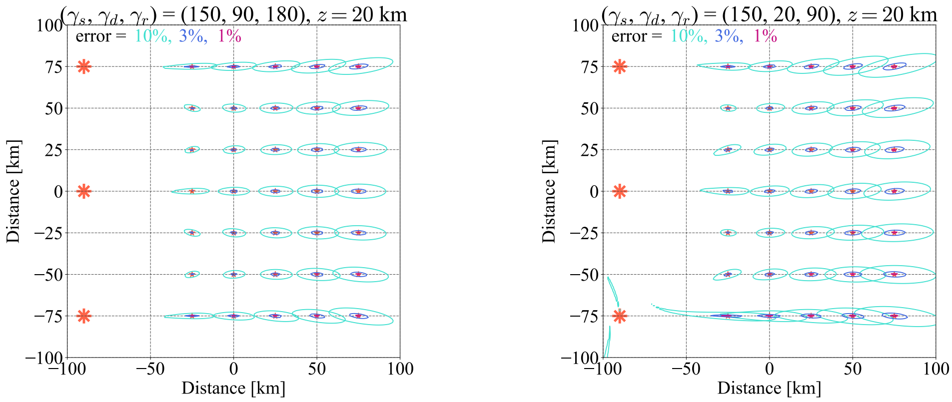

Figure 4.18: Systematic localization error due to the calibration error of the detectors for a strike-slip event (upper; $(\gamma_s, \gamma_d, \gamma_r) = (150°, 90°, 180°)$) and a dip-slip event (lower; $(\gamma_s, \gamma_d, \gamma_r) = (150°, 20°, 90°)$). Each contour shows the case when the detectors has calibration uncertainty of 10 % (cyan), 3 % (blue), and 1 % (violet).

4.3 Summary and discussion

Two topics have been investigated to realize a gravity-based EEW with TOBA. The first topic is the difference between the types of detectors. The detectability of earthquakes with TOBA that is sensitive to horizontal gravity strain was first investigated in this work while the detectability with vertical gravity gradient was calculated in the previous work [2]. The second topic is the localizability of epicenters, which is important to consider an actual system of gravity-based EEW. These topics were investigated at 10 seconds after the onset of the fault rupture, which is suitable for the gravity strain observation around 0.1 Hz.

Detectability of earthquakes with TOBA

For the first topic, three types of focal mechanisms were investigated, including one vertical strike-slip earthquake and two reverse dip-slip earthquakes with different dip angles, 10° and 20°. The detector sensitivity of 10^{-15} $/\sqrt{\text{Hz}}$ at 0.1 Hz was assumed in the calculation. The calculated signal-to-noise ratio (SNR) distributions suggested that horizontal gravity gradient component is essential for the strike-slip earthquakes, while vertical components are important for the dip-slip earthquakes. For the strike-slip earthquakes, the total SNR of the horizontal components is almost isotropic hence there is no preferred direction for detection. Available SNR with the vertical components is about half of the horizontal components in average. The dip-slip earthquakes show strong azimuth dependence, and only vertical components have good SNR in the direction to which the hanging wall moves (0° direction). However, the coast is in the opposite direction (180° direction) in usual cases, where the horizontal and vertical components have similar SNRs. Therefore horizontal components will have a good contribution in an actual warning system. These results indicate that TOBA, which is sensitive to horizontal gravity strain components, can play an important role in gravity-based earthquake detection. It is also shown that the target sensitivity 10^{-15} $/\sqrt{\mathrm{Hz}}$ of Phase-III TOBA is sufficient for meaningful detection.

Localizability of earthquakes with arrayed TOBAs

Localization simulations with arrayed TOBA were also performed. The simulations assumed the case that off-shore earthquakes are detected by an array of detectors placed along the coastline. Again, the detector sensitivity of 10^{-15} $/\sqrt{\mathrm{Hz}}$ at 0.1 Hz was assumed here. A generalized method of the proposed localization way [78], which uses the signal amplitude ratio between several detectors, was adopted in this thesis. First we investigated the required number of detectors to localize the epicenter of the earthquake. Pairs of two TOBA placed at 75 km space in the line will be a good arrangement, which can localize the epicenter uniformly up to $\sim$ 120 km distance. When the focal mechanisms and depth of the hypocenter is known in advance, epicenter location of a strike-slip earthquake can be well constrained in 10 seconds within 100 km^2 up to 120 km distance from the detector array. The localized area is about 2 $\sim$ 3 times wider for a dip-slip earthquake, and the localized area is below 100 km^2 up to about 110 km distance. These results show that gravity strain observation has better localizability than the current warning system using seismic waves, which takes 16–17 seconds to propagate 110–120 km. The localizability with less number of detectors is not uniformly good because the signal cannot be detected by the sufficient number of detectors at some locations.

The localized point can be systematically offset if the presumed focal mechanism is different from the actual mechanism. To keep the systematic localization error below 10 km, which is close to the statistical uncertainty of the localization ($\sim$100 km^2 as mentioned above), the fault parameters have to be known in the accuracy of 10 degrees. Though this requirement seems not very hard, statistical investigation should be performed for actual faults, which is left as a future work. Even if the information about focal mechanism is not available in advance, those parameters can be estimated with the location at the same time, though the localized area without those information is worsen by $\sim$ 3 times. Similarly, the calibration accuracy of the detectors should also be below 3 % to suppress the systematic error below 10 km.

Though there may be better ways of localization, these results have demonstrated the validity of at least one method. As mentioned at the beginning of Sec. 4.2, the method used here does not require the information of the source time function, which will be a primary advantage in the realistic detection. These results will help us to design a concrete system of the gravity-based

EEW. Note that the mechanisms of earthquakes were simplified to the point source in a homogeneous medium. Though it has already been checked that the analytical signal based on those simplified model provides good approximation of the actual signal in the first few seconds, the effect of those simplification on the localizability should be evaluated. Such an effect can be roughly tested by localizing the signal of actual earthquakes with analytically prepared signal templates. These things are left as future works.

5 Design of Phase-III TOBA

As described in Sec. 3.5, following two things are the targets of Phase-III TOBA :

- Detection of earthquakes using gravity gradient fluctuation
- Technical demonstration of noise reduction before large-scale TOBA

As confirmed in Sec. 4.3, the required sensitivity to detect earthquakes is 10^{-15} $/\sqrt{\mathrm{Hz}}$ at 0.1 Hz. In this chapter, the design of Phase-III TOBA to achieve this target sensitivity is explained. First, an overview of the design is shown in Sec. 5.1 with the requirements on the system. Then the noise budget and the cooling performance are evaluated in the following sections Sec. 5.2 and Sec. 5.3, respectively. The required sensitivity 10^{-15} $/\sqrt{\mathrm{Hz}}$ and the target temperature 4 K are shown to be achievable with the proposed design.

5.1 Design overview

A designed configuration of Phase-III TOBA is shown in Fig. 5.1. It mainly consists of the following three systems :

- A cryogenic suspension system
- A highly sensitive angular sensor using an optical cavity
- An active vibration isolation system

Details of each system are explained in this subsection.

5.1.1 Cryogenic suspension system

A cryogenic technique is essential for TOBA to suppress thermal fluctuations. It is required for the cryogenic system to cool the suspended masses to 4 K within acceptable time. The main difficulty in cooling the pendulum originates

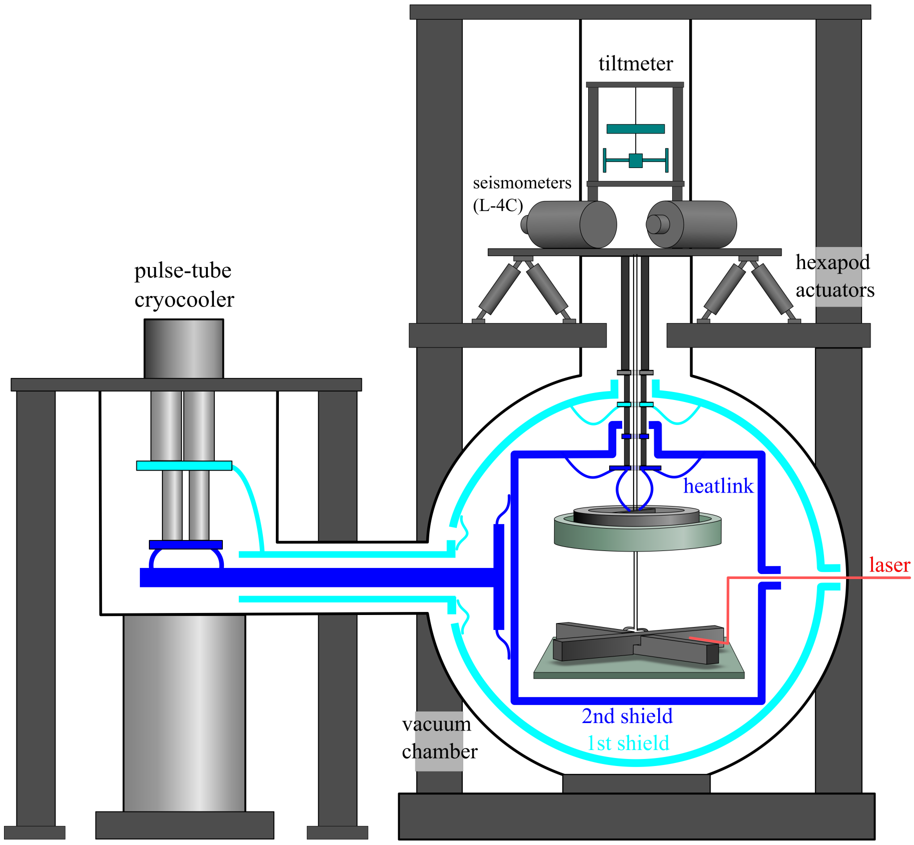

Figure 5.1: Configuration of Phase-III TOBA.

from the vibration introduction via the cooling components. That problem is serious especially in a torsion pendulum which is sensitive to tiny forces. Effective heat extraction is therefore essential for the cooling system to minimize the vibration transfer.

In this subsection, the configuration of the mechanical suspension system and the actuator to control it is described first. Then the cryogenic equipments and components are explained.

Suspension system

The suspension configuration and the parameters of the masses are shown in Fig. 5.2 and Table 5.1, respectively. The suspension system consists of five masses, which are separated into two suspension sequences. Two test masses, TM1 and TM2, are suspended orthogonally (Fig. 5.3) from the intermediate mass (IM1), and the optical bench (OB) is suspended from another intermediate mass (IM2). Both of the intermediate masses are suspended from the active vibration isolation stage. The horizontal rotations of the TMs are excited in the opposite direction to each other in response to gravity gradient fluctuation. Such differential rotation is measured with the optics on the opti-

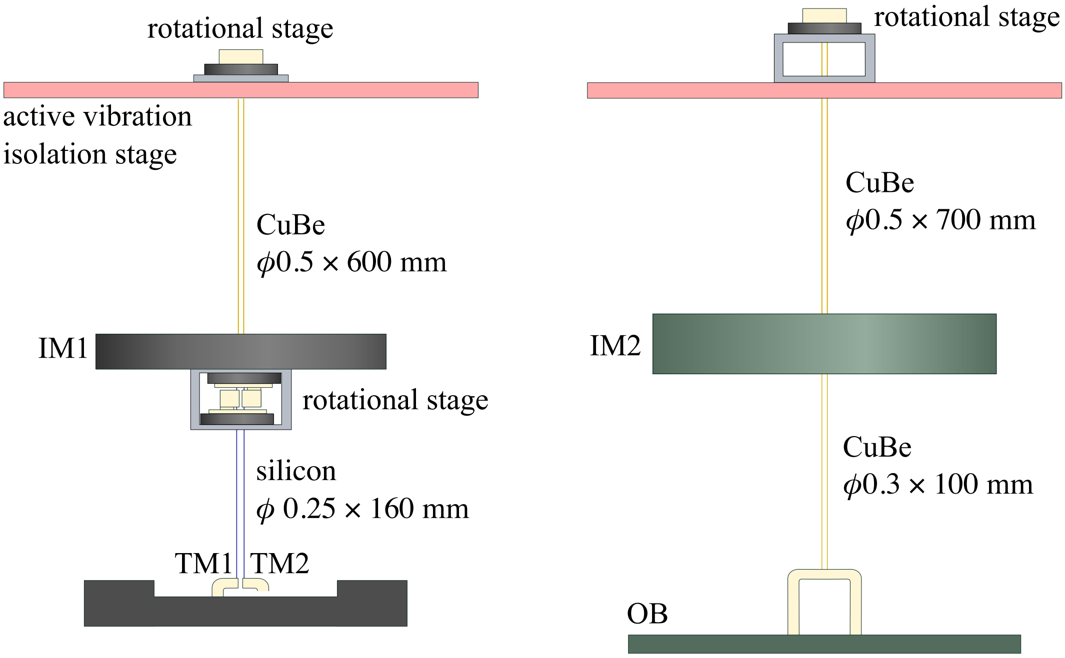

Figure 5.2: Suspension configurations of Phase-III TOBA. TM suspension series (left) and OB suspension series (right).

cal bench. Since OB is designed to have no quadruple moment, Yaw rotation of OB is not excited by gravity gradient. The relative rotation between TM1 - OB and TM2 - OB are measured independently, then differential rotational signal is calculated from them. Hence the rotation of OB can be largely canceled. At the top stage, the suspension wires for IM1 and IM2 are clamped on the rotational stages, which are for the adjustment of the suspension torsional angles. The angle of two TMs are adjusted by another rotational stages placed on the IM1.

The test mass bars are made of oxygen free copper (OFC). High thermal conductivity of OFC at cryogenic temperatures can suppress the temperature inhomogeneity so that the distortion noise due to the differential temperature fluctuation of the bar (see Sec. 3.2.7) is reduced. Additionally, copper has small magnetic susceptibility, which gives an advantage in the magnetic noise. Relatively high density is also good for external torque noise.

The suspension wires of TMs are made of silicon, which is known to have very small loss angle ϕ_w [79, 80] and high thermal conductivity [81] at cryogenic temperatures. The thickness of the silicon wire is 0.25 mm in diameter, and the required loss angle is $\phi_w = 10^{-8}$. Reported loss angles of silicon are 10^{-9} for a bulk [79], and 3×10^{-8} for a thin flexure [80] at cryogenic temperatures. In general, thin wires are suffered from surface loss compared to bulk materials. Therefore surface treatment is essential to achieve small loss in a thin wire. Such research and development are currently ongoing for TOBA to improve

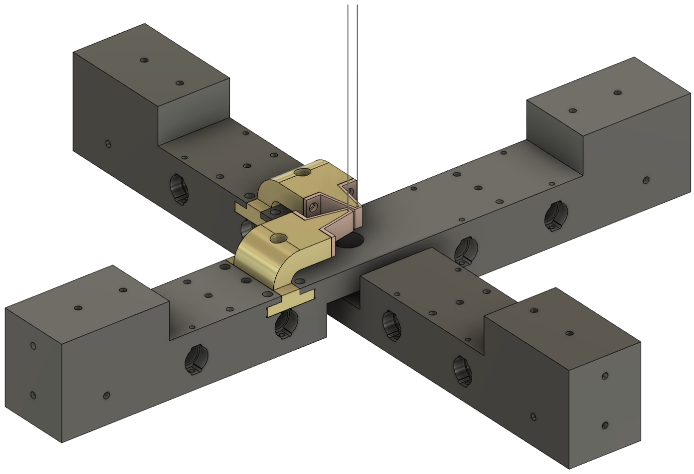

Figure 5.3: Two test mass bars are suspended orthogonally.

the recorded loss angle 3×10^{-8} by three times.

The other masses are suspended by CuBe (Beryllium copper) wires, which have relatively small loss angle ($\sim 3 \times 10^{-7}$ for a bulk at 4 K [82]) and can be treated easier. Since the fluctuations of IMs or OB are largely cancelled in differential rotation signal of TMs, the loss angle of CuBe is sufficient in TOBA. Additionally CuBe has much lower thermal conductivity [83], so that the conductive heat inflow from the suspension stage into the IMs are reduced.

Coil-coil actuator

To apply a force on TMs for position controls, coil-coil actuators are attached on TMs. The coil-coil actuator consists of a pair of coils, one of which is attached on the control target (TM) and a drive current is applied to the counterpart coil. Here we call these coils the mass coil and the drive coil, respectively. When sinusoidal current is applied to the drive coil, generated magnetic field induce the current in the mass coil at the drive frequency. The induced magnetic moment interacts with the driven magnetic field, then force is applied between the coils.

Consider the case as Fig. 5.4, when two coils are attached on the mass, which are sandwiched with a pair of drive coils. Two mass coils are connected each other. Each mass coil has a inductance of L_0 and a resistance of R_0, and the mutual inductance between the mass coil and the drive coil is M. Then the applied force F_{cc} is given by

$$F_{cc} = M\frac{dM}{dx}\frac{\omega_d}{R_0^2 + \omega_d^2 L_0^2}\left(\omega_d L_0 (i_1^2 - i_2^2) + 2R_0 i_1 i_2 \sin\phi\right). \tag{5.1}$$

Here i_1 and i_2 are the current amplitude of two drive coils, ϕ is the phase offset between the drive currents, and ω_d is the angular drive frequency.

Table 5.1: Parameters of suspension masses

parameter	symbol	value
Test mass bar (TM)		
material	-	Copper (surface oxidized)
length	L_b	0.35 m
mass	M_b	4.2 kg
moment of inertia	I_b	0.056 kg·m^2
surface area	S_b	0.058 m^2
Intermedaite mass 1 (IM1)		
material	-	Copper (surface oxidized)
mass	M_{i1}	5.0 kg
moment of inertia	I_{i1}	0.046 kg·m^2
surface area	S_{i1}	0.069 m^2
Optical bench (OB)		
material	-	Copper (surface oxidized)
mass	M_{ob}	10.0 kg
moment of inertia	I_{ob}	0.24 kg·m^2
surface area	S_{ob}	0.2 m^2
Intermedaite mass 2 (IM2)		
material	-	Copper (surface oxidized)
mass	M_{i2}	4.5 kg
moment of inertia	I_{i2}	0.0634 kg·m^2
surface area	S_{i2}	0.085 m^2

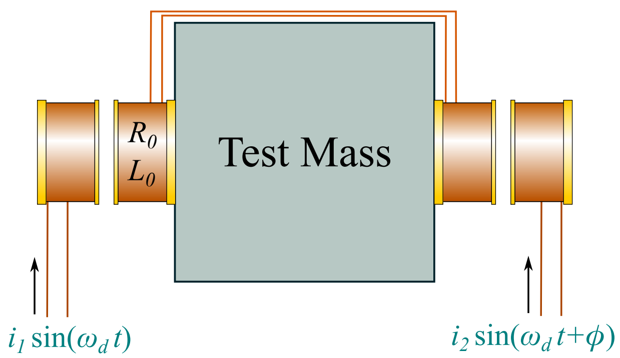

Figure 5.4: A coil-coil actuator.

The specified parameters of the coils for TOBA are $R_0 = 14.0\ \Omega$ and $L_0 = 3.28$ mH. The mutual inductance and its gradient when two coils are separated by 2 mm were measured to be $M = 0.64$ mH and $\frac{dM}{dx} = 0.11$ H/m, respectively, for the $\omega_d/2\pi = 1$ kHz. These are the values at room temperature. Then the maximum drive force is about 0.2 mN at room temperature when 0.1

A of drive currents are applied. The electrical wire for the coils are made of pure copper to reduce the resistivity at cryogenic temperatures for the reduction of heat generation. Though the change of the resistivity affects the drive force at cryogenic temperatures, the same order of the force is expected to be available as the room temperature, because the first term of Eq. (5.1) is not changed so much when $R_0 < \omega_d L_0$.

The coil-coil actuator has two primary merits in using for TOBA. One is a low magnetic noise, because the induced magnetic moment oscillates at the drive frequency and the averaged moment is zero. This enables to reduce the coupling with environmental magnetic field fluctuation which grows at low frequency. Another merit is adjustability of the actuator efficiency for the reduction of actuator noise. The electrical noise contained in the control signal of the actuator becomes the force noise through the actuator. By changing the applied current amplitude i_1 or i_2, the coupling from electrical noise can be optimized remotely.

Cryocooler

A pulse-tube cryocooler SRP-082B2S (Sumitomo Heavy Industries, Ltd.) is used for cooling since this type of a cryocooler is known for low vibration. The cryocooler is set behind the vacuum chamber, and the housing is built independently to the chamber. The cooling head is connected to the radiation shields in the vacuum chamber with a pure (5N) aluminum rod. At the connection points, flexible thermal links are used to isolate the vibration. The cryocooler consists of two cooling stages, each of which is cooled to 50 K (1st stage) and 3 K (2nd stage), respectively. The specified cooling ability is 35 W at the 1st stage, and 0.9 W at the 2nd stage.

Radiation shields

The suspension system is surrounded by two radiation shields to block the thermal radiation from the room temperature parts. The outer shield (1st shield) and the inner shield (2nd shield) are connected to the 1st stage and the 2nd stage of the cryocooler, respectively. Each shield is cooled to 50 K (1st shield) and 3.5 K (2nd shield). Without the suspension system, the shields reach these temperatures in two days. The 1st shield is made of aluminum, and the 2nd shield is made of oxygen free copper. The material of the 2nd shield was chosen to have high thermal conductivity so that temperature deviation among the shield is minimized. Black alumite plates are attached on the inner wall of the 2nd shield to improve the emissivity, which is required to accelerate the cooling speed. The outer surface of each shield is covered with super insulator made of multi-layer aluminum deposited films to reduce the radiative heat inflow to the shield. The temperature rise against applied heat (heat load capacity) was measured to be 3.5 K/W.

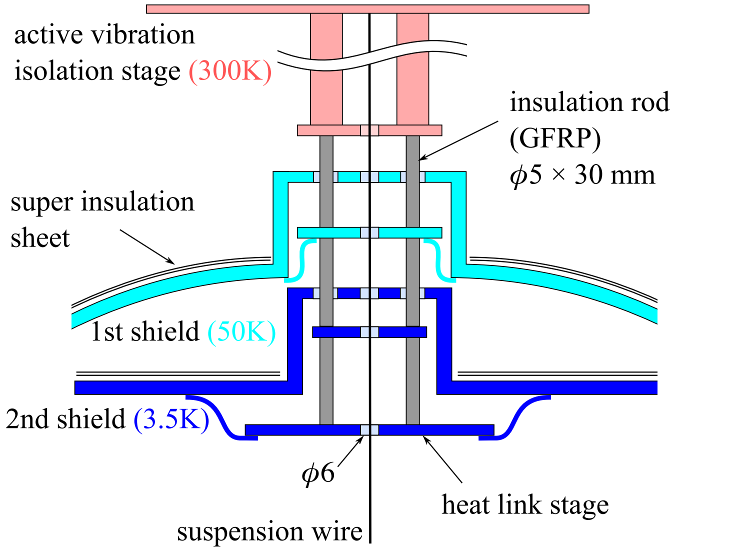

Figure 5.5: A configuration of the radiation shields around the suspension wire.

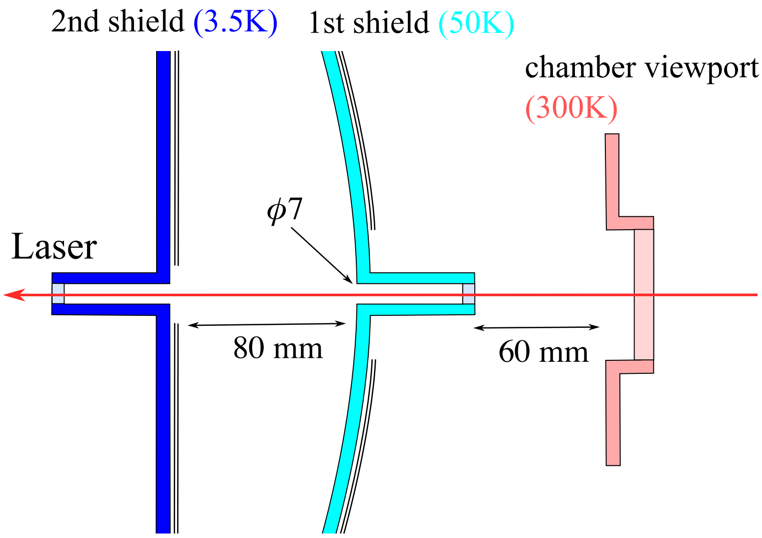

Figure 5.6: A configuration of laser injection port.

The shields have two holes for the suspension wires and the laser beam. The configuration of the shields around each hole is shown in Fig. 5.5 and 5.6. The solid angle of the 300 K part viewed from the 2nd shield is designed to be sufficiently small to reduce the thermal radiation from there.

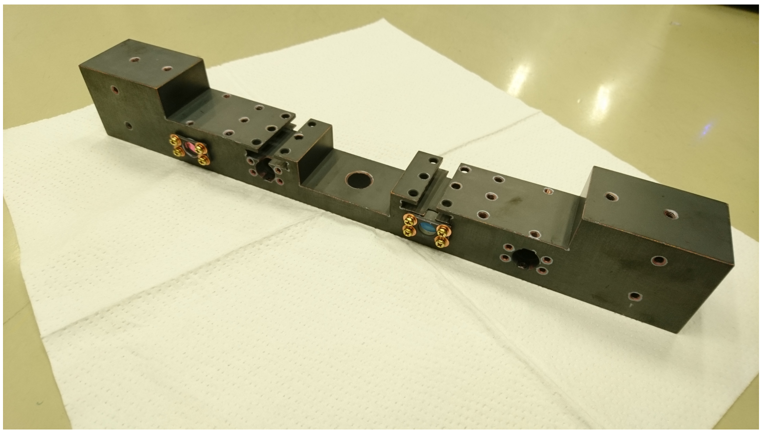

Figure 5.7: Oxidized test mass bar

Surface oxidization of suspension masses

The surface of the suspension masses made of copper are oxidized to accelerate the radiative cooling. Radiated energy from a body with surface area of S at temperature T is determined by Stefan-Boltzmann law as follows:

$$Q_{\mathrm{rad}} = \epsilon(T)\sigma T^4 S. \tag{5.2}$$

Here $\sigma = 5.67 \times 10^{-8}\ \mathrm{W\,m^{-2}\,K^{-4}}$ is Stefan-Boltzmann constant, and $\epsilon(T)$ is a total emissivity of the surface of the body. Total emissivity is defined as the radiative energy ratio of the body to an ideal blackbody, hence it takes a value between 0 and 1. In a high vacuum, thermal radiation is a dominant path of heat extraction at high temperatures ($\gtrsim 100$ K) because of the strong temperature dependence: $\propto T^4$. Therefore the high emissivity is essential for effective cooling at the initial cooling phase.

Heavily oxidized copper is known to have a high emissivity, which is ~ 0.6 [84]. Though there are other high-emissive materials such as black alumite ($\epsilon \sim 0.8$) or sapphire ($\epsilon \sim 0.5$ [85]), copper is chosen here because of the advantages in density, thermal conductivity and magnetic property, as mentioned above. Sapphire was excluded because non-metallic materials can be suffered from electrostatic force due to charge on the surface. The suspension masses are heated in a muffle furnace (in air) at 800 °C for three hours for oxidization. About 170 μm of oxidized layer is formed on the surface. Fig. 5.7 shows the appearance of the oxidized test mass bar. For a safety margin, emissivity of 0.5 is set as the design value of Phase-III TOBA.

Heat link (pure aluminum wire)

Below 100 K, conductive cooling becomes a dominant path since radiative heat transfer decreases as $\propto T^4$. In order to improve the conductive cooling, the

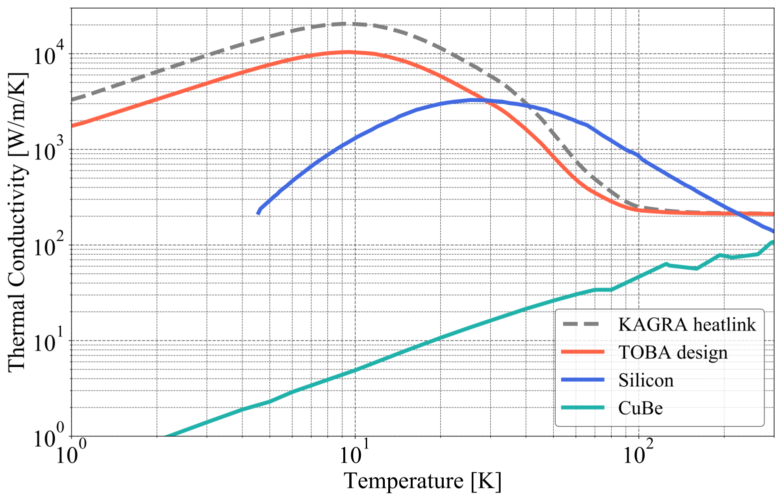

Figure 5.8: Thermal conductivity of a pure aluminum heat link and suspension wires. The measured value for KAGRA (dashed grey) and design value for TOBA (red) which is the half of KAGRA's one below 100 K. Pure silicon [81] (blue) and beryllium copper [83] (green) are also plotted.

suspended intermediate masses (IM1 and IM2) and the 2nd shield are connected by heat links. Heat links are also set between IM2 and OB because some components on OB generates heat. As depicted in Fig. 5.1 or 5.5, heat links from IMs are once attached to the heat link stage, then connected to the 2nd shield. The heat link stage is rigidly fixed to the active vibration isolation stage by insulation rods made of GFRP (Glass fiber reinforced plastics), which has a thermal conductivity of 0.091 W/m/K at 4 K. Thus the vibration introduction via the heat links are suppressed at this stage. The system of the active vibration isolation stage which will be explained later.

The heat links are made of stranded ϕ0.15 mm pure aluminum (6N, 99.9999%) wires, which are the same one as used for KAGRA. Pure aluminum has high thermal conductivity at cryogenic temperatures, therefore it can extract heat effectively without introducing significant vibrations. Thermal conductivity at cryogenic temperatures is determined by the purity of metal. The experimental relation below 30 K is known as [86]

$$k_{Al}(T) = \frac{1}{1.8 \times 10^{-7} T^2 + \frac{1.1}{RRR} T^{-1}}, \tag{5.3}$$

where the residual resistivity ratio $RRR \equiv R_{300\mathrm{K}}/R_{4\mathrm{K}}$ represents the purity. High RRR gives high thermal conductivity at cryogenic temperatures. The heat links for KAGRA has $RRR = 3570$, and its thermal conductivity is shown in Fig. 5.8. As a pessimistic assumption, half of the conductivity of

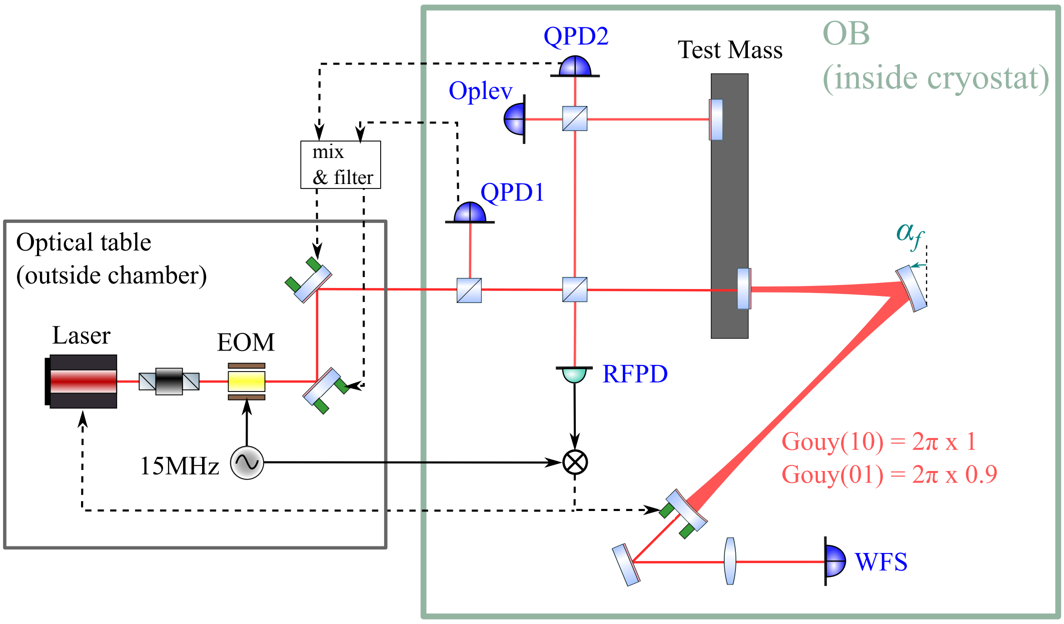

Figure 5.9: A schematic design of the optical system

the KAGRA heat link is assumed below 100 K for the design of TOBA. The design conductivity is also shown in Fig. 5.8.

The bending spring constant of N heat link wires is given by $3\pi N E_{\mathrm{Al}} d^4/(64 l^3)$, which is derived from elastic deformation of a cantilever. Here E_{Al}, d and l are the Young's modulus, diameter and length of the wire. In our case, an expected spring constant of the stranded heat link ($\phi 0.15 \times 100\mathrm{mm} \times 14$) is 0.073 N/m. This small spring constant can reduce the vibration introduction to the suspension masses.

5.1.2 Optical system

A schematic design of optical system is shown in Fig. 5.9. Laser beams are introduced from the optical table outside the vacuum chamber into the optical bench inside the cryostat. There are three parts of the system for each TM; a highly sensitive wave front sensor for the main sensor of rotation, an optical lever as an auxiliary monitor, and a beam jitter control system.

Highly sensitive wave front sensor

In order to reduce the quantum shot noise, an angular sensor using an optical cavity is used to measure the rotation of TM. The detailed principle of this new sensor is explained in Appendix B. Here the overview of the sensor is briefly summarized.

Fig. 5.10 shows the overview of the principle. The target is to measure the tilt of the mirror which is fixed on TM. The basic principle is the amplifica-

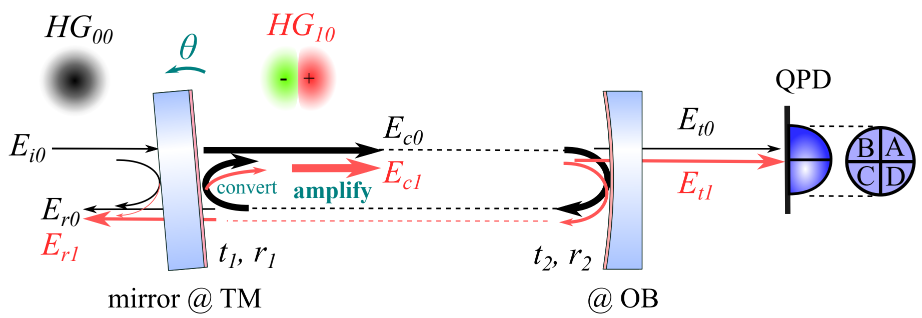

Figure 5.10: A principle of a wave front sensor using coherent amplification of angular signal HG_{10} mode.

tion of the cavity. An optical cavity can amplify the input field by coherently stacking the sequence of reflected beams between the cavity mirrors. In an usual usage of a cavity, only the fundamental mode of the laser beam (HG_{00} mode; see Appendix B for the Hermite-Gaussian modes) is amplified. Therefore the other modes including the angular signal components remains to be small. However, by choosing a proper configuration of the cavity, the angular signal component can be amplified. This kind of angular sensor was recently proposed by the author.

Consider an input HG_{00} mode with an amplitude of E_{i0}, which is then amplified to E_{c0} inside the cavity. As shown in Fig. 5.10, when one of the mirror is tilted, a fraction of the intra-cavity HG_{00} mode is converted into HG_{10} mode which has asymmetric profile. The generated HG_{10} mode is again amplified by the cavity, and transmit from the cavity. It is then detected as the displacement of the beam by the quadrant photo diode (QPD) outside the cavity. From the calculations in Appendix B, the transmission field amplitude for HG_{00} and HG_{10} modes are given by

$$E_{t0} = \frac{t_1 t_2 e^{i\phi_c/2}}{1 - r_1 r_2 e^{i\phi_c}} E_{i_0}, \tag{5.4}$$

$$E_{t1} \simeq \frac{-i t_1 t_2 r_1 r_2 \frac{2\pi}{\lambda} e^{i(3\phi_c+\zeta_c)/2}}{(1 - r_1 r_2 e^{i\phi_c})(1 - r_1 r_2 e^{i(\phi_c+\zeta_c)})} w_0 \theta E_{i_0}, \tag{5.5}$$

where λ, w_0 are the wavelength and the beam radius of the beam at the tilted mirror. t_i and r_i are the amplitude transmittance and reflectivity of each mirror. ϕ_c and ζ_c are the round-trip phase of the laser and the Gouy phase of the cavity, respectively. When both of the resonance conditions $\phi_c = 2\pi n$ and $\zeta_c = 2\pi m$ $(n, m:$ integer) are satisfied, the transmission field is written as

$$E_{t0} = \frac{t_1 t_2 \mathcal{F}}{\pi} E_{i0}, \tag{5.6}$$

$$E_{t1} = -i \frac{2 t_1 t_2 \mathcal{F}^2}{\pi \lambda} w_0 \theta E_{i_0}, \tag{5.7}$$

where the finesse $\mathcal{F}$ is defined as $\mathcal{F} \equiv \pi\sqrt{r_1 r_2}/(1 - r_1 r_2) \simeq \pi/(1 - r_1 r_2)$. The phase difference of these components gradually evolves with Gouy phase of the beam during the propagation to the QPD. The maximum angular signal is available when the phase difference goes to be $\pi/2$ and the phases of HG_{00} and HG_{10} modes are aligned. Then the difference of the power between the left (A+B) and the right (C+D) segments of the QPD in Fig. 5.10 is

$$\begin{aligned}
\Delta P(\theta) &= E_{t0}E_{t1}\left(\int_0^{\infty} dx \int_{-\infty}^{\infty} u_{00}u_{10} - \int_{-\infty}^{0} dx \int_{-\infty}^{\infty} u_{00}u_{10}\right) \\
&= \frac{\sqrt{2}\pi}{\lambda} P_i \left(\frac{t_1 t_2 \mathcal{F}}{\pi}\right)^2 \mathcal{F} w_0 \theta \qquad (5.8) \\
&\sim \frac{\sqrt{2}\pi}{\lambda} P_i \mathcal{F} w_0 \theta. \qquad (5.9)
\end{aligned}$$

$t_1 t_2 \mathcal{F}/\pi \sim 1$ is used in the last step, though it depends on the choice of transmittances in general. P_i is the input laser power of the cavity. As apparent from Eq. (5.9), high input power, high finesse and large beam radius gives larger angular signal. For Phase-III TOBA, the designed values for those parameters are $P_i = 50$ mW, $\mathcal{F} = 300$ and $w_0 = 3.5$ mm. These values are chosen to suppress the quantum noise and the mirror thermal noise sufficiently, while keeping the heat inflow on TM sufficiently small.

The Gouy phase of the cavity is determined by the geometry, such as the radius of curvature (RoC) of the mirrors and the length of the cavity. Here the Gouy phase ζ_c is set to 2π to resonate HG_{10} mode by folding the beam with a curved mirror as shown in Fig. 5.9, which is referred as a "folded cavity configuration" in Appendix B. As an optional choice, the Gouy phase is set independently for HG_{10} and HG_{01} modes to avoid the resonance of HG_{01} mode. This is because small horizontal rotation of the bar is measured via HG_{10} mode under much larger vertical rotation which appears as HG_{01} mode. The difference between the Gouy phases of two modes are adjusted by the folding angle α_f. The RoC of the folding mirror R_f is then seen as $R_f \cos\alpha_f$ from HG_{10} mode and $R_f/\cos\alpha_f$ from HG_{01} mode, which result in Gouy phase difference. In the design, Gouy phase for the two modes are set to 2π and 1.8π, respectively.

The length of the cavity is sensed by PDH method [87]. The phase of the input laser is modulated at 15 MHz, then the reflection signal measured by the RFPD (Radio-frequency photo detector) is demodulated to gain a linear signal of the cavity length. The length signal is fed back to the actuators on the cavity mirror and the input laser frequency to stabilize the length fluctuations to keep the cavity on resonance.

Optical lever

Optical levers (Oplev) are used as auxiliary sensors. An optical lever is a simple sensor which measures the displacement of laser beam reflected by a

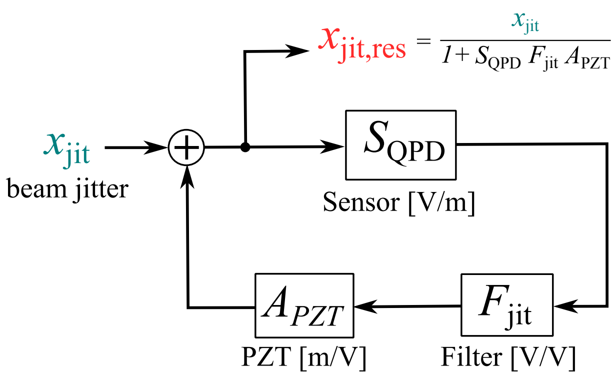

Figure 5.11: A block diagram of the beam jitter control.

tilted mirror. As shown in Fig. 5.9, the splitted beam is sent to the mirror on TM, then reflected to the QPD. The amplitude of signal is given by

$$\Delta P_{\text{oplev}}(\theta) = P_{\text{QPD}} \frac{8}{\sqrt{2\pi}} \frac{d}{w_{\text{QPD}}} \theta, \tag{5.10}$$

where P_{QPD} and w_{QPD} are the laser power and beam radius at the QPD, respectively, and d is the distance between the mirror and the QPD. Though the signal is smaller than the high sensitive wave front sensor, the optical lever has wider range, therefore it is suitable for auxiliary rotational monitor.

Beam jitter control

Since the laser beam is sent to the suspended OB inside the cryostat, the relative position of the beam and OB is not stable due to the vibration of OB or the fluctuation of air around the optical table. To keep the relative position to be stable, the beam jitter is monitored by two QPDs on OB (QPD1 and QPD2 in Fig. 5.9). The signals from the QPDs are then fed back to the piezoelectric (PZT) actuators attached on the mirrors on the optical table. By fixing the beam position at two QPDs, the laser beam is fixed to the optical bench.

A block diagram of the beam jitter control is shown in Fig. 5.11. Under this control loop, the beam jitter x_{jit} is suppressed to

$$x_{\text{jit,res}} = \frac{x_{\text{jit}}}{1 + S_{\text{QPD}} F_{\text{jit}} A_{\text{PZT}}} \tag{5.11}$$

where S_{QPD}, F_{jit} and A_{PZT} are the efficiency of the QPD, the control filter and the PZT actuator, respectively. The product of them $G_{\text{jit}} \equiv S_{\text{QPD}} F_{\text{jit}} A_{\text{PZT}}$ is called the open-loop transfer function. At the frequencies where $G_{\text{jit}} \gg 1$, the fluctuation is suppressed by G_{jit}.

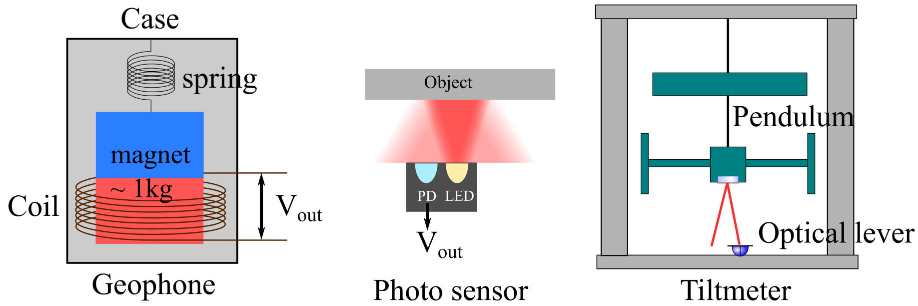

Figure 5.12: Sensors for active vibration isolation system; the geophone L-4C, the photo sensor and the tiltmeter.

5.1.3 Active vibration isolation system

In order to suppress the vibration of the ground, active vibration isolation system (AVIS) is implemented at the suspension stage. AVIS is a feedback stabilization system using inertia sensors and hexapod actuators. Some auxiliary sensors are also used to compensate the frequency response of the sensor. This system for TOBA were first designed by A. Shoda [74], then upgraded by S. Takano. The overview of the system is briefly explained here.

Sensors

Geophones (L-4C; Sercel) are use to measure the motion of the suspension stage relative to the inertial frame. The geophone used here consists of a magnet mass and a spring as shown in Fig. 5.12. The relative velocity between the suspended magnet and the coil fixed on the stage induces voltage on the coil, which is measured as a vibration signal. The transfer function from the displacement of the stage to the output voltage is given by

$$\frac{\tilde{V}}{\tilde{x}_g} = S_0 \frac{2\pi i f^3}{f_0^2 + i f_0 f/Q - f^2}, \tag{5.12}$$

where $S_0 \simeq 250$ V/(m/s) is the velocity sensitivity of the geophone, $f_0 \simeq 1$ Hz is the resonant frequency of the magnet, and $Q \simeq 1.8$ is the Q-value of the spring.

Since Eq. (5.12) decreaces with f^3 below f_0, the geophones cannot measure the motion at low frequency. This can result in low-frequency noise introduction such as long-time drift of the table beyond the range of the actuators. To avoid it, photo sensors are used for low-frequency control. The photo-sensor measures the relative distance between the table and the ground through the change of reflected LED light power (Fig. 5.12). Therefor it does not work to suppress the vibration relative to the inertial frame, but just suppress the drift at low frequency.

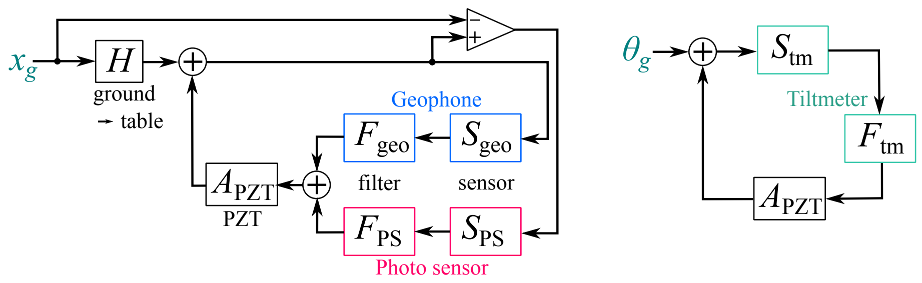

Figure 5.13: Control loops of the active vibration isolation system (AVIS). The left loop is the control of translation, the right loop is the control of tilt.

Another problem of the geophone is coupling from the tilt of the table. When a geophone for the horizontal measurement is tilted, gravitational force displaces the suspended mass along the axis of the geophone and induces a signal voltage. The axial acceleration is given by $g\tilde{\theta}/\omega^2$ where g and θ is the gravitational acceleration and the tilt angle of the stage, respectively, hence this coupling becomes serious at low-frequencies. This coupling is suppressed by using a tiltmeter shown in Fig. 5.12. The suspended pendulum works as a inertial reference, then the tilt of the ground (table) is measured by the optical lever. Using the signal of the tiltmeter, the tilt fluctuations of the suspension stage is suppressed by control to reduce the coupling to the geophones.

The geophones and the tiltmeter are implemented as Fig. 5.1. The photo sensors are placed at the base stage of the hexapod actuators, and the relative displacement to the suspension stage is measured with them.

Actuators

Piezoelectric (PZT) actuators P-844.60 (Physik Instrumente (PI) GmbH & Co. KG) is used for moving the position of the suspension stage. It has an actuation range of 90 μm with 100 V of input voltage range. Six actuators are placed in a hexapod configuration so that they can actuate the table in any degrees of freedom. Due to the large electrostatic capacity of the PZT, the frequency range is limited below few tens of Hz, which is enough for the target frequency of AVIS.

Control loop

The control loops of AVIS is shown in Fig. 5.13. The loops are separated into the translational control loop and the tilt control loop. The main target is the translational control, while the tilt control is essential to realize the translational control. In a similar way as the beam jitter control, the fluctuation of the ground is suppressed by the open-loop transfer functions. The target vibration levels are shown in the next section.

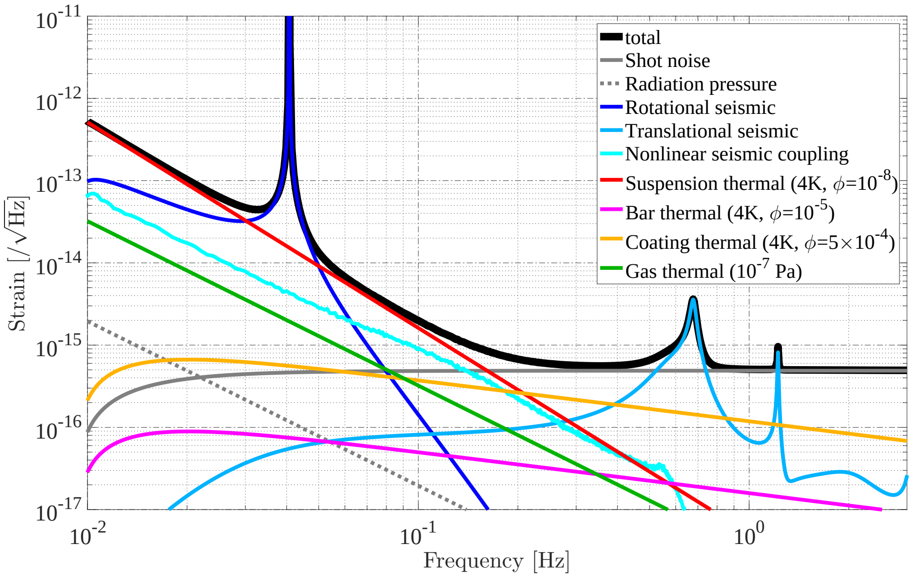

Figure 5.14: Design sensitivity of Phase-III TOBA

5.2 Noise budget

Fig. 5.14 shows the designed noise budget of Phase-III TOBA. The graph shows the spectrum around 0.1 Hz, which is important for the detection of earthquake [2]. The total noise level is $10^{-15}\ /\sqrt{\mathrm{Hz}}$ at 0.15 Hz, or equivalently 5×10^{-16} rad/$\sqrt{\mathrm{Hz}}$ in unit of rotational angle of the bar. This is designed to meet the requirement to detect earthquakes as confirmed in Sec. 4.3. Here requirements on these systems are summarized in Table. 5.2. The details of the calculation are described in the following subsections.

5.2.1 Suspension thermal noise

As mentioned in the previous section, silicon wire is planned to be used for Phase-III TOBA. Using the Young's modulus and the Poisson's ratio of silicon, which are $E_{\mathrm{Si}} = 193$ GPa and $\nu_{\mathrm{Si}} = 0.28$ respectively, the torsional spring constant of the wire and the resonant frequency are

$$\kappa_w = 1.8 \times 10^{-4}\ \mathrm{N \cdot m/rad}, \qquad f_0 = \frac{1}{2\pi}\sqrt{\frac{\kappa_w}{I_b}} = 9.1\ \mathrm{mHz}. \tag{5.13}$$

Then Eq. (3.21) is calculated to be

$$\sqrt{S_{\mathrm{th,sus}}(f)} \simeq 8.1 \times 10^{-16} \times \left(\frac{T}{4\ \mathrm{K}}\right)^{\frac{1}{2}} \left(\frac{\phi_w}{10^{-8}}\right)^{\frac{1}{2}} \left(\frac{f}{0.1\ \mathrm{Hz}}\right)^{-\frac{5}{2}}\ \mathrm{rad}/\sqrt{\mathrm{Hz}}, \tag{5.14}$$

or twice of this value in unit of gravitational wave strain amplitude h, according to Eq. (3.13) and (3.15).

Table 5.2: Requirements on the system of Phase-III TOBA

Parameter	Requirement
Test mass bar(s)	
Mass M_b	4.0 kg
Moment of inertia I_b	0.056 kg·m^2
Loss angle ϕ_b	10^{-5}
Cryogenic suspension system	
Temperature T	4.2 K
Loss angle of the wire ϕ_w	10^{-8}
Temperature fluctuation of the bar $\sqrt{S_T}$	$\lesssim 10^{-4}$ K/$\sqrt{\mathrm{Hz}}$
Vibration isolation system	
Translational vibration $\sqrt{S_{g,\mathrm{trans}}}$	10^{-7} m/$\sqrt{\mathrm{Hz}}$ at 0.1 Hz, 10^{-10} m/$\sqrt{\mathrm{Hz}}$ at 1 Hz
Cross-coupling transfer function $\tilde{H}_c$	10^{-9} rad/m at 0.1 Hz
Rotational vibration $\sqrt{S_{g,\mathrm{rot}}}$	10^{-10} rad/$\sqrt{\mathrm{Hz}}$
Passive vibration isolation (rotational) $\tilde{H}_{\mathrm{rot}}$	10^{-6} rad/rad at 0.1 Hz
Rotational common-mode rejection C_{CMRR}	10^{-3}
Optical system	
Input power P_{in}	50 mW
Finesse $\mathcal{F}$	300
Loss angle of mirror substrate ϕ_s	1×10^{-8}
Loss angle of coating ϕ_c	5×10^{-4}
Residual gas pressure P_{vac}	10^{-7} Pa

In the calculation above, Eq. (3.21) was divided by $\sqrt{2}$ because gravity gradient torque is applied to two TMs in the opposite direction while the noise is independently random for them. The same factor is also used in the following calculations.

5.2.2 Mirror thermal noise

Assuming the substrate of the mirror on TM is made of sapphire, the material parameters in Eq. (B.56) are $E_s = 335$ GPa, $\nu_s = 0.28$ and $\phi_s = 10^{-8}$ for the substrate. Silica-tantala coating is assumed for the coating layer, whose parameters are set to $E_c = 100$ GPa, $\nu_s = 0.17$ and $\phi_s = 5 \times 10^{-4}$. The averaged values of the silica and the tantala are used for the Young's modulus and the Poisson's ratio. The loss angles are based on the literature [88] which summarizes the previously measured parameters. It reports 2×10^{-9} of the loss angle for sapphire, and 2×10^{-4} for tantala coating. Slightly worse values are required here for TOBA. The thickness of the coating layer is set to 8 μm, which corresponds 30 layers of $\lambda/4$ coatings.

Then Eq. (B.56) is calculated to be

$$\sqrt{S_{\mathrm{th,mir}}(f)} \simeq 8.0 \times 10^{-18} \times \left(\frac{T}{4\ \mathrm{K}}\right)^{\frac{1}{2}} \left(\frac{\phi_s}{10^{-8}}\right)^{\frac{1}{2}} \left(\frac{w_0}{3.5\ \mathrm{mm}}\right)^{-\frac{3}{2}} \left(\frac{f}{0.1\ \mathrm{Hz}}\right)^{-\frac{1}{2}} + 1.9 \times 10^{-16} \times \left(\frac{T}{4\ \mathrm{K}}\right)^{\frac{1}{2}} \left(\frac{\phi_c}{5 \times 10^{-4}}\right)^{\frac{1}{2}} \left(\frac{w_0}{3.5\ \mathrm{mm}}\right)^{-2} \left(\frac{f}{0.1\ \mathrm{Hz}}\right)^{-\frac{1}{2}} \mathrm{rad}/\sqrt{\mathrm{Hz}}. \tag{5.15}$$

Hence the mirror thermal noise is dominated by the contribution from the coating layer.

5.2.3 Bar thermal noise

TM is a dumbbell-shaped bar whose geometry is $350 \times 40 \times 30$ mm bar with additional $60 \times 40 \times 20$ weights at both ends. Here it is approximated to $350 \times 40 \times 40$ rectangular shape to calculate the bar thermal noise. TM is made of copper hence the Young's modulus is $E_b = 128$ GPa. The second eigenfrequency (Eq. (3.24)) is 4 kHz. Assuming the loss angle of $\phi_b = 10^{-5}$, the bar thermal noise is

$$\sqrt{S_{\mathrm{th,bar}}(f)} \simeq 2.5 \times 10^{-17} \times \left(\frac{T}{4\ \mathrm{K}}\right)^{\frac{1}{2}} \left(\frac{\phi_b}{10^{-5}}\right)^{\frac{1}{2}} \left(\frac{f}{0.1\ \mathrm{Hz}}\right)^{-\frac{1}{2}} \mathrm{rad}/\sqrt{\mathrm{Hz}}, \tag{5.16}$$

which is not significant in Phase-III TOBA.

5.2.4 Quantum noise

Around 0.1 Hz, the mechanical response Eq. (3.18) can be approximated to $\chi(f) \simeq 1/I(2\pi f)^2$. Then the quantum noise Eq. (B.42) is given by

$$\sqrt{S_{\mathrm{quantum}}(f)} \simeq 2.4 \times 10^{-16} \times \left(\frac{P_i}{50\ \mathrm{mW}}\right)^{-\frac{1}{2}} \left(\frac{\mathcal{F}}{300}\right)^{-1} \left(\frac{w_0}{3.5\ \mathrm{mm}}\right)^{-1} + 9.8 \times 10^{-18} \times \left(\frac{P_i}{50\ \mathrm{mW}}\right)^{\frac{1}{2}} \left(\frac{\mathcal{F}}{300}\right) \left(\frac{w_0}{3.5\ \mathrm{mm}}\right) \left(\frac{f}{0.1\ \mathrm{Hz}}\right)^{-2} \mathrm{rad}/\sqrt{\mathrm{Hz}}. \tag{5.17}$$

The radiation pressure noise is not large, while the shot noise dominates the overall noise above 0.2 Hz as shown in Fig. 5.14. The requirement on the optical parameters P_i, $\mathcal{F}$ and w_0 are therefore determined by the shot noise level.

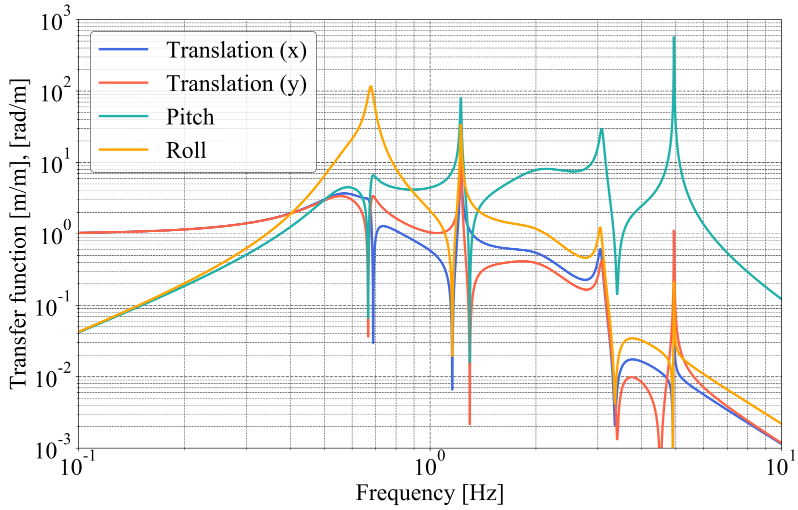

Figure 5.15: Transfer functions from the translation of the suspension point and the translations and rotations of the pendulum.

5.2.5 Translational seismic noise

Seismic cross-coupling noise

As explained in Sec. 3.2.3, translational seismic vibration is transferred to the rotation through the tilt of the system. Below the resonant frequency of the pendulum ($\sim$ 1 Hz), the transfer function to Pitch/Roll rotation is given by $\tilde{H}_{P(R)} \simeq \omega^2/g$, because the horizontal acceleration of the ground $\ddot{x}_g$ act like changing the direction of gravity by $\theta = \ddot{x}_g/g$. In Phase-III TOBA, the tilt angle $\varphi_{P(R)}$ is required to be suppressed below 10^{-8} rad. For the translational vibration of the ground, the requirement on the active vibration isolation system is set to 10^{-7} m/$\sqrt{\text{Hz}}$ at 0.1 Hz. The resulting noise level is

$$\sqrt{S_{\text{seis,trans}}} \simeq 4.1 \times 10^{-17} \times \left(\frac{\varphi_{P(R)}}{10^{-8}\ \text{rad}}\right)\left(\frac{\sqrt{S_g}}{10^{-7}\ \text{m}/\sqrt{\text{Hz}}}\right) \text{rad}/\sqrt{\text{Hz}}. \quad (5.18)$$

The seismic cross-coupling noise in the actual system is plotted in Fig. 5.14 with $\tilde{H}_{P(R)}$ calculated from the designed pendulum parameters. The small tilt angle of TM is planned to be achieved by control with tilt sensors and actuators. An optional choice is to sense the tilt using the cross-coupling signal itself at a certain frequency.

Nonlinear vibration transfer

As explained in Appendix A, the seismic vibration around the resonant frequencies of the translation or Pitch/Roll rotations of the pendulum (typically

~ 1 Hz) is nonlinearly down-converted to the noise in the horizontal rotation. To suppress the nonlinear vibration transfer, vibration isolation down to 10^{-10} m/Hz is required at 1 Hz to the active vibration isolation system in Phase-III TOBA. With this vibration level and the transfer functions of the pendulum which are shown in Fig. 5.15, the nonlinear vibration noise Eq. (3.34) is calculated to be

$$\sqrt{S_{\mathrm{seis,NL}}} \simeq 4.1 \times 10^{-17} \times \left(\frac{f}{0.1\ \mathrm{Hz}}\right)^{-2} \mathrm{rad}/\sqrt{\mathrm{Hz}}, \tag{5.19}$$

which is plotted in Fig. 5.14. The contribution is not ignorable around 0.1 Hz, therefore the active vibration isolation at 1 Hz is essential for Phase-III TOBA though it is out of the main observational frequency.

5.2.6 Rotational seismic noise

From the moments of inertia of TMs and IM1 listed in Table 5.1, and the parameters of the suspension wires shown in Fig. 5.2, transfer function about the horizontal rotation from the ground to TM is calculated to be $\tilde{H}_Y = 1.4 \times 10^{-3}(f/0.1\ \mathrm{Hz})^{-4}$ around 0.1 Hz. The rotational seismic vibration have not been directly measured, then here it is assumed to be $\sqrt{S_{g,\mathrm{rot}}(f)} \sim 10^{-10}$ rad/$\sqrt{\mathrm{Hz}}$ below 0.1 Hz. Then the rotational seismic noise is

$$\sqrt{S_{\mathrm{seis,rot}}(f)} \simeq 7.2 \times 10^{-17} \times \left(\frac{C_{\mathrm{CMRR}}}{10^{-3}}\right)\left(\frac{f}{0.1\ \mathrm{Hz}}\right)^{-4} \mathrm{rad}/\sqrt{\mathrm{Hz}}. \tag{5.20}$$

Here the common-mode rejection ratio is assumed to be $C_{\mathrm{CMRR}} = 10^{-3}$, which corresponds to 0.05 % difference of the resonant frequency. Hence careful adjustment of the moment of inertia is required in Phase-III. Optionally, common rotation of two TMs can be used for the feedback control of the vibration at the suspension point.

5.2.7 Residual gas noise

The cryostat is required to be evacuated to 10^{-7} Pa to suppress the residual gas noise. Here we assume that the residual gas is composed of water molecules whose mass is $m_m = 3 \times 10^{-26}$ kg. The side area and the length of the bar is $A_b = 0.012\ \mathrm{m}^2$ and $L_b = 0.35$ m, then the residual gas noise Eq. (3.35) is

$$\sqrt{S_{\mathrm{gas}}(f)} \simeq 1.6 \times 10^{-16} \times \left(\frac{P_{\mathrm{vac}}}{10^{-7}\ \mathrm{Pa}}\right)\left(\frac{T}{4\ \mathrm{K}}\right)^{\frac{1}{4}} \mathrm{rad}/\sqrt{\mathrm{Hz}}. \tag{5.21}$$

The cryopump effect helps to achieve the degree of vacuum.

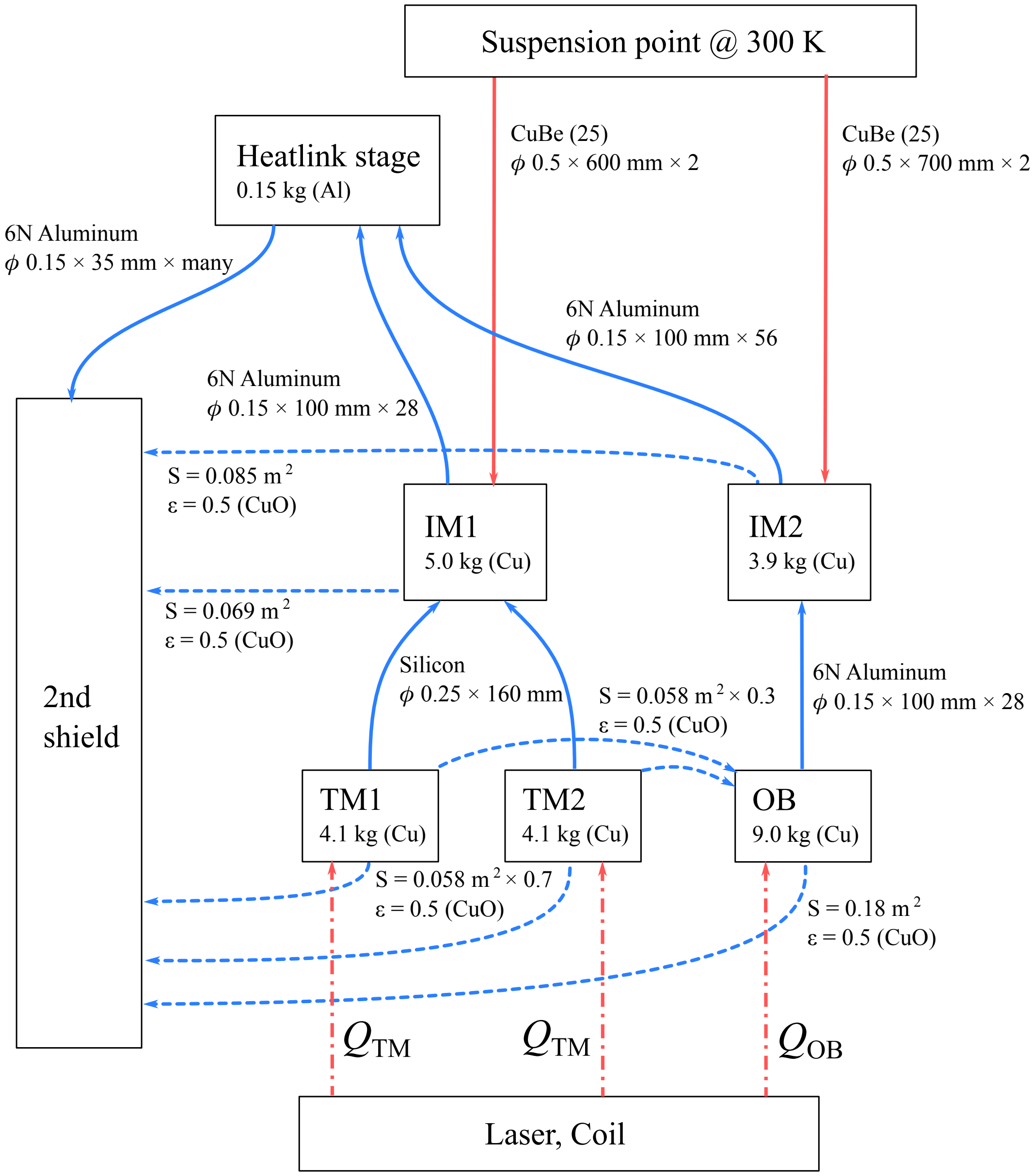

Figure 5.16: A schematic diagram of cooling method.

5.3 Cooling performance

The suspended masses are designed to be cooled down to 4 K by thermal radiation from the surface and thermal conducting via the wire or the heat links. The cooling flow is summarized in the schematic diagram Fig. 5.16. Conductive heat transfer and radiative heat transfer is expressed as the solid arrows and the dashed arrows, respectively. Heat conduction happens between the connected masses. Though thermal radiation can transfer the heat to any masses in principle, here the masses are basically assumed to exchange heat by radiation only with the 2nd shield, for simplicity. As an exception, thermal interact between 30% of the TM surface and OB is taken into account, since the bottom surface of TM is close to OB.

The conductive heat transfer from T_1 part to T_2 part via a thin wire is

$$Q_{\mathrm{cond}}(T_1, T_2) = \frac{T_1 - T_2}{R_w}, \tag{5.22}$$

where R_w is a thermal resistance of wire. Between T_1 part and T_2 part, R_w is given by

$$R_w(T_1, T_2) = \frac{l_w}{A_w}\left(\int_{T_1}^{T_2} k_w(T)dT\right)^{-1}, \tag{5.23}$$

where $k_w(T)$, A_w and l_w are the thermal conductivity at T, the cross section and the length of the wire, respectively.

The radiated energy from a surface of a mass is given by Eq. (5.2). In an actual system, however, the total energy transfer is affected by the surrounding materials due to the radiation from it and the reflection of the thermal radiation from the mass. The total heat transfer between a mass (at temperature of T_m) and the surrounding shield (at temperature of T_s) can be expressed as

$$Q_{\mathrm{rad}}(T_m, T_s) = \sigma\epsilon_{\mathrm{eff}}S_m\left(T_m^4 - T_s^4\right), \tag{5.24}$$

where S_m and S_s are the surface area of the mass and the shield, respectively. The effect of the shield is included in the effective emissivity ϵ_{eff}. It is affected by the geometry of the system, hence the exact value is given by a ray-tracing simulation. For a simple case when the mass and the shield has spherical shapes and the thermal radiation is reflected to a random direction at the surface (diffusive reflection), ϵ_{eff} can be approximated to

$$\epsilon_{\mathrm{eff}} = \left(\frac{1}{\epsilon_m} + \frac{S_m}{S_s}\left(\frac{1}{\epsilon_s} - 1\right)\right)^{-1}, \tag{5.25}$$

where ϵ_m and ϵ_s are the emissivity of the mass and the shield, respectively. Under the condition of diffusive reflection, only small fraction of the radiated rays from the mass are reflected back to the mass. This holds for our case because the suspension masses have rough surfaces. Hence Eq. (5.25) is adopted to approximate the radiative heat transfer here.

Using Eq. (5.22)–(5.25), the total cooling time of Phase-III TOBA is calculated as Fig. 5.17. The amount of heat transfer in TM and IM1 are also shown in Fig. 5.18. TMs are designed to reach to 4.2 K in 14 days. The heat load capacity of TM is about 7.5×10^3 K/W. Here the incident heat Q_{TM} is assumed to be 0.03 mW, which corresponds to 550 ppm absorption of 50 mW input laser. For a sapphire mirror used in KAGRA, absorption in the substrate is measured to be 43.4 ppm/cm [89]. This satisfies the absorption requirement since the thickness of the mirror for TOBA is around 1 cm. Inside the optical cavity for angular sensing of TOBA, the input power is amplified by

$\mathcal{F}/\pi \sim 100$. Therefore the intra-cavity absorption has to be less than 5.5 ppm. This is a feasible value compared to the measured absorption for silica-tantala coating, which is less than 1 ppm [37].

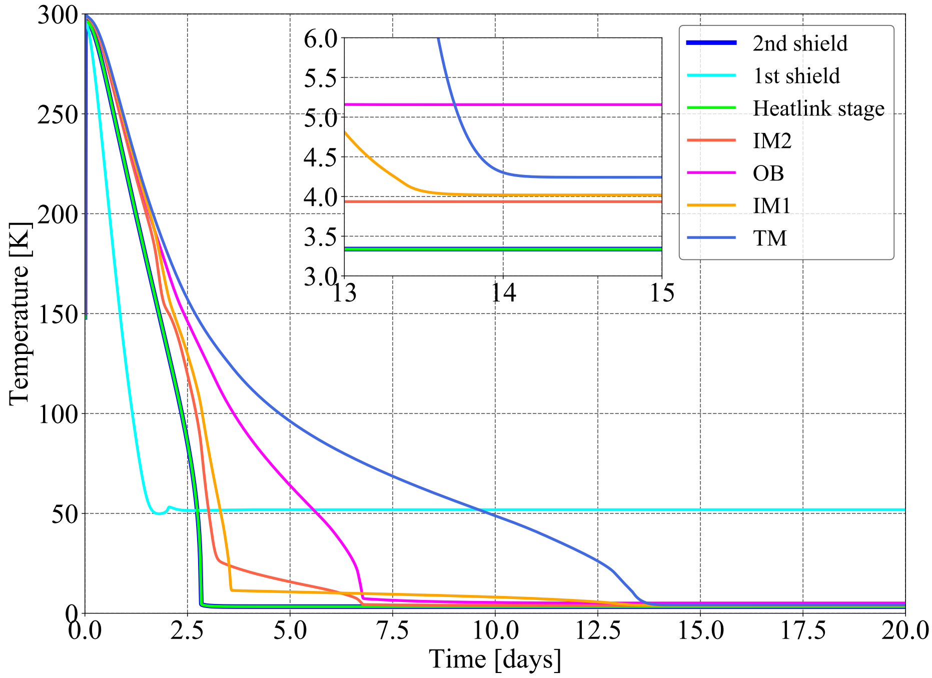

Figure 5.17: Designed cooling curve of Phase-III TOBA.

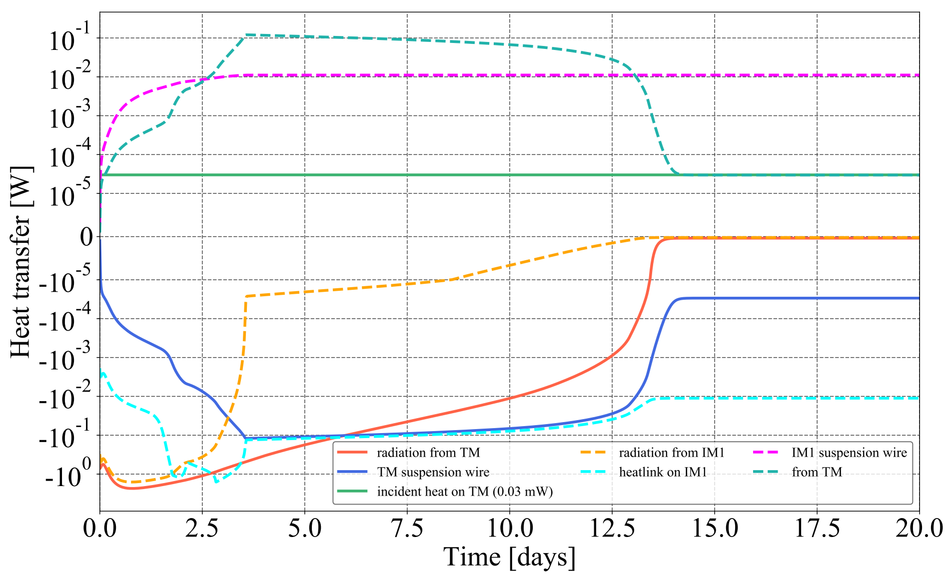

Figure 5.18: Heat flow during the cooling process of Phase-III TOBA. The solid and the dashed lines are relevant to TM and IM1, respectively.

6 Experimental Results of Cryogenic Prototype

Experimental results on the cryogenic system of TOBA is reported here. The purposes of the experiment are

- Demonstration of the cryogenic technique in a large-scale torsion pendulum
- Investigation of noise performance of a cryogenic torsion pendulum

Since there have been no research on a large-scale cryogenic torsion pendulum, this work is an essential step for the development of Phase-III TOBA. The experimental demonstration is important to confirm that the components in the designed system work correctly, and to check the effect of changes in the material properties on the performance of the detector.

For those purposes, a simplified setup of Phase-III TOBA is constructed and tested. The configuration of the setup is explained in Sec. 6.1. Characterization of component properties and evaluation of cooling performance are described in Sec. 6.2 and 6.3, respectively. Then the suspension control under the cryogenic temperature is explained in Sec. 6.4. The noise performance is investigated in Sec. 6.5.

6.1 Setup

The setup for the experiment here is shown in Fig. 6.1. It is close to the designed system of Phase-III TOBA. The main differences from the design of Phase-III are as follows:

- The silicon suspension wire is replaced to a CuBe wire and heat links ($\phi 0.15 \times 100\mathrm{mm} \times 3$).
- Optical levers are used to measure the rotation of the bars.

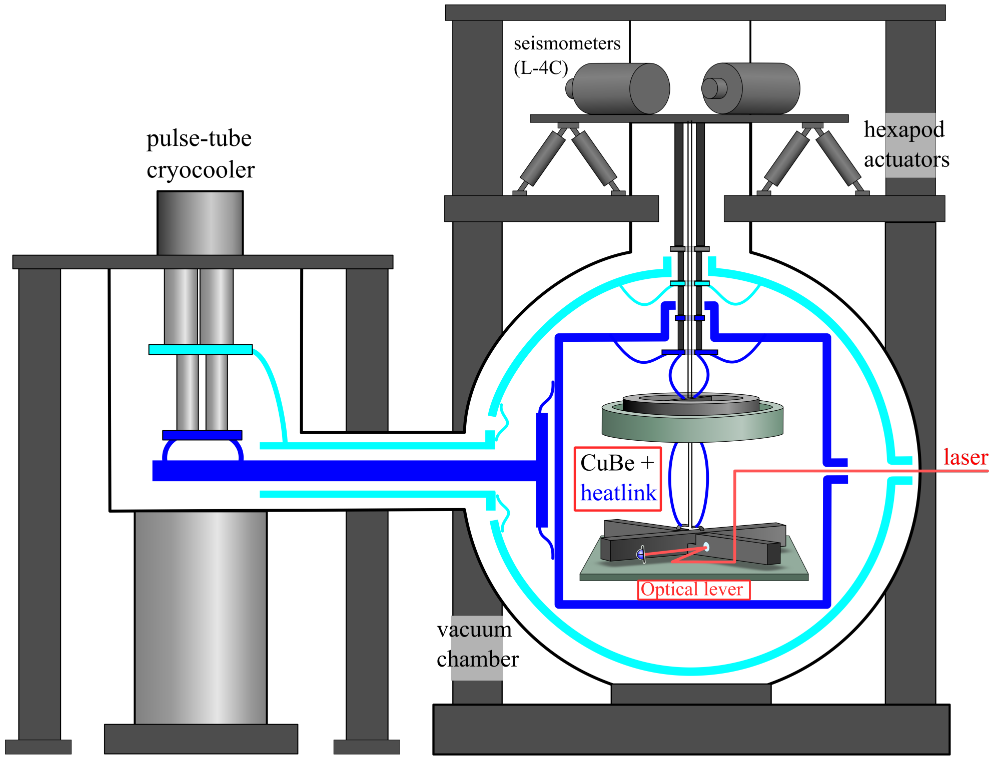

Figure 6.1: An experimental setup for the demonstration of cryogenic system performance for TOBA. This is a simplified configuration of Phase-III TOBA. The main differences from Phase-III TOBA are emphasized with red boxes.

Other parts such as the suspended mass configuration are almost identical to the design in Phase-III TOBA. Two test mass bars (TM1 and TM2) are orthogonally suspended from an intermediate mass (IM1). Optics for the optical levers are constructed on the optical bench (OB) which is suspended from another intermediate mass (IM2). Both of IM1 and IM2 are suspended from the active vibration isolation stage. The amount of the heat links is also same as the configuration of Phase-III TOBA, which is shown in Fig. 5.16. IMs were damped with Sm-Co magnets placed on the heat link stage.

The analog electrical signals were converted to digital signals, and stored in the digital system. The input voltage range, the resolution and the sampling frequency were ± 20 V, 16bit and 4096 Hz, respectively. Some of them were then digitally filtered and converted to analog signals again for feedback controls.

Using this setup, the following things were experimentally investigated;

- A performance of the designed cooling system
- A behavior of the torsion pendulum under cryogenic temperatures

The results are shown in the following sections.

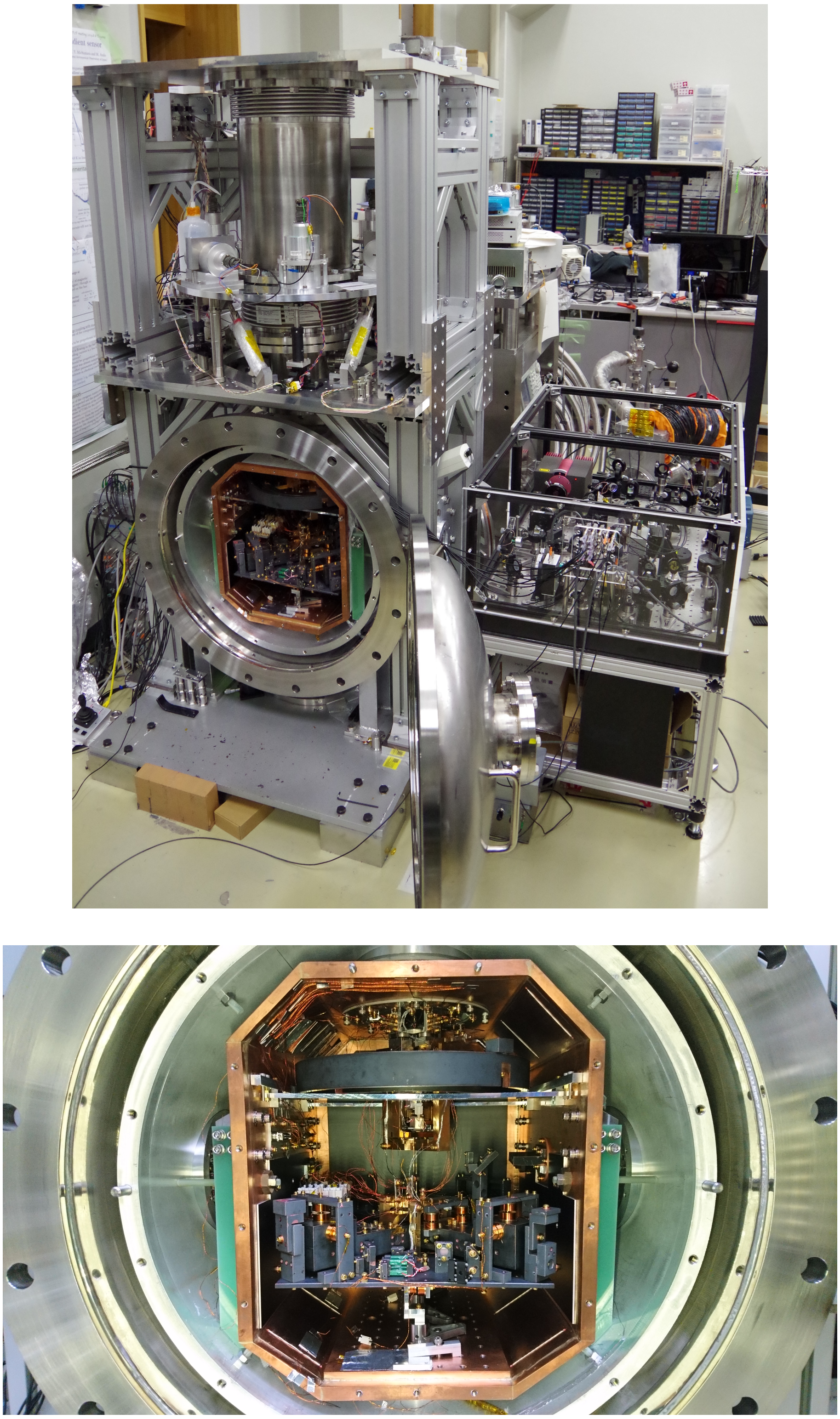

Figure 6.2: Pictures of the experimental setup; an overview picture (upper) and the details inside the cryostat (lower).

Table 6.1: Measured parameters and requirements of the components.

parameter	unit	measured	designed
emissivity of CuO	-	0.54 @ 300 K 0.41 @ 150 K	0.5 0.5
thermal conductivity of heat link	[W/m/K]	1.3×10^4 @ 11 K 5.9×10^3 @ 4.8 K	1.0×10^4 7.4×10^3
spring constant of heat link	[N/m]	0.080 (ϕ0.15 × 100mm×14)	0.073
remnant magnetic moment of TM bar	[A·m^2]	5×10^{-6} @ 4 K	-

6.2 Component characterization

First, in order to confirm the properties of the cryogenic components used in Phase-III TOBA, the important parameters of the coomponents were measured. The same components were also used in the experiments in this thesis. The evaluated parameters and the requirement in Phase-III TOBA is summarized in Table. 6.1. The details of the measurement process are described in the following subsections.

6.2.1 Emissivity of oxidized copper

Total emissivity of the oxidized copper, which determines the initial cooling speed, was measured using $150 \times 30 \times 30$ mm sample bar surrounded by $250 \times 250 \times 150$ mm box. The sample bar is suspended with a thin wire as Fig. 6.3, and the temperatures of the bar and the box were measured with silicon-diode thermometers. From the temperature change of the bar when the box is cooled, heat transfer by radiation can be measured, which is then converted to the emissivity of the bar. The sample bar was oxidized by heating in a muffle furnace at 800 °C for three hours in air, which is the same way as the test mass of phase-III TOBA. The surface of the box was chemically oxidized using oxidant. The chemical treatment was done by Yahata-seito Industrial Company, and the detailed process was not opened.

As indicated in Eq. (5.25), the directly measured emissivity is the effective value which is affected by the surrounding box. Hence the emissivity of the heat-treated oxidized surface was evaluated in the following two steps. First, the emissivity of the chemically oxidized surface $\epsilon_{\mathrm{CuO,chem}}(T)$ was characterized as a reference by using the box and another sample bar, both of which was chemically oxidized. In this case, the measured emissivity is given by

$$\epsilon_{\mathrm{meas}}(T) = \left(\frac{1}{\epsilon_{\mathrm{CuO,chem}}(T)} + \frac{S_{\mathrm{bar}}}{S_{\mathrm{box}}}\left(\frac{1}{\epsilon_{\mathrm{CuO,chem}}(T)} - 1\right)\right)^{-1}, \tag{6.1}$$

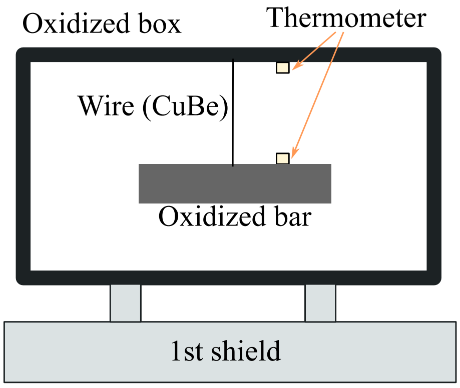

Figure 6.3: A schematic diagram of the measurement setup of emissivity. The emissivity was calculated from temperature change of the bar and the box when the box is cooled down to 100 K.

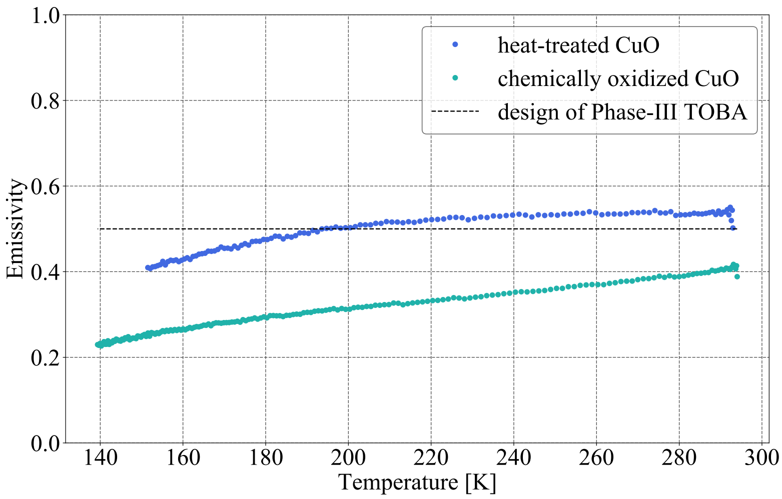

Figure 6.4: Measured emissivity of the heat-treated CuO (blue) and chemically oxidized CuO (green). The heat-treated CuO satisfies the required emissivity (dashed black) above 200 K, while the emissivity slightly degrades for lower temperatures.

because the bar and the box has a common emissivity. Emissivity of the chemically oxidized surface $\epsilon_{\mathrm{CuO,chem}}(T)$ is then calculated from $\epsilon_{\mathrm{meas}}(T)$ with the surface area ratio $S_{\mathrm{bar}}/S_{\mathrm{box}}$. Second, the same measurement is repeated by replacing the chemically oxidized bar to the heat-treated oxidized sample bar. The measured emissivity is converted to the emissivity of the heat-treated oxidization surface $\epsilon_{\mathrm{CuO,heat}}(T)$ using Eq. (5.25) wtih $\epsilon_{\mathrm{CuO,chem}}(T)$ and $S_{\mathrm{bar}}/S_{\mathrm{box}}$, by the following equation:

$$\epsilon_{\mathrm{meas}}(T) = \left(\frac{1}{\epsilon_{\mathrm{CuO,heat}}(T)} + \frac{S_{\mathrm{bar}}}{S_{\mathrm{box}}}\left(\frac{1}{\epsilon_{\mathrm{CuO,chem}}(T)} - 1\right)\right)^{-1}, \tag{6.2}$$

Fig. 6.4 shows the measured temperature change and the calculated emissivity. The temperature dependence was measured down to 150 K, where the radiation has dominant contribution to the cooling. The heat-treated surface has a emissivity of 0.54 at 300K, which decreased below 200 K. Though this value is slightly smaller than the literature value 0.6 (see Sec. 5.1.1), it almost meets the required value for the design of Phase-III TOBA.

6.2.2 Thermal conductivity of aluminum heat link

The thermal conductivity of the heat link, which is essential for cooling below 100 K, was measured. Thermal conductivity of a wire can be measured from the temperature difference at the both end when heat is flowing along the wire. The heat flow Q_{heat} and the temperature difference ΔT obeys the following relation :

$$\Delta T = \frac{l}{Ak} Q_{\mathrm{heat}}, \tag{6.3}$$

where l, A and k are length, cross section, and thermal conductivity of the wire, respectively.

Fig. 6.5 shows the setup for measuring thermal conductivity of the heat link. Fourteen $\phi 0.15 \times 100$ mm heat link wires are stranded, and suspended from an aluminum block on the 2nd shield. 220 Ω resistance is attached as a heater at the bottom of the heat link. Temperatures at the both end of the heat link were measured with Si diode thermometers. Thermal conductivity of the lead wires for the thermometer and the heater is estimated to be sufficiently small, therefore most of the applied heat is transferred via the heat link. The measurement temperature was adjusted by heating the 2nd shield with an attached film heater. The heat links are pressed to the aluminum blocks with M4 screws. Here thermal conductivity was measured for two tightening torque of the screws, 0.5 N·m and 1.0 N·m.

Measured thermal conductivities are shown in Fig. 6.6. The horizontal axis is the averaged temperature between the top and bottom point. The dependence on the tightening torque was clearly seen below 20 K. With 1.0 N·m of tightening torque, the heat link satisfies the designed thermal conductivity of TOBA above 10 K. Therefore the heat links in the following setup were tightened with 1.0 N·m of torque, though there may be more optimal torque.

6.2.3 Stiffness of heat links

For the evaluation of vibration noise introduced via the attached heat links, the translational spring constant of the heat links were measured. The measurement setup is simple as Fig. 6.7. A weight (1.09 g) is suspended via the heat link ($\phi 0.15 \times 100\mathrm{mm} \times 14$), and its resonant frequency was measured by the position sensor (photo-sensor). The total spring constant can be calculated from the weight and the resonant frequency. Then the contribution from

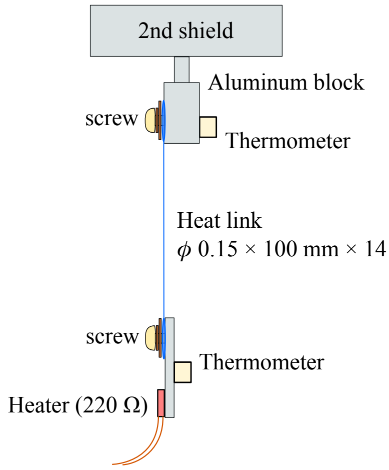

Figure 6.5: Measurement setup for thermal conductivity of the aluminum heat link. Thermal conductivity was calculated from the temperature difference between two end points of the heat link when the bottom point is heated.

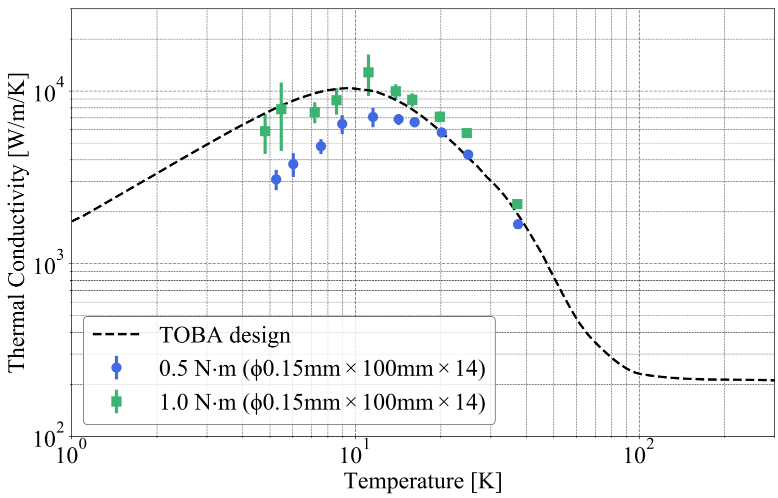

Figure 6.6: Measured thermal conductivity of 6N aluminum heat link with the tightening torque of 0.5 N·m (blue) and 1.0 N·m (green). The dashed black line shows the design of Phase-III TOBA. The heat links has better conductivity than the design with the tightening torque of 1.0 N·m above 10 K, while it slightly degrades below 10 K.

gravitational restoring force is calculated and subtracted to derive the elastic spring constant.

The measurement was performed in two configurations; with the straight heat link and with the bent heat link as depicted in Fig. 6.7. The actual heat links in TOBA are implemented in the latter way. The measured resonant frequencies and the calculated spring constants are shown in Table 6.2. The elastic spring constant was of the straight heat link was 0.050 N/m, which

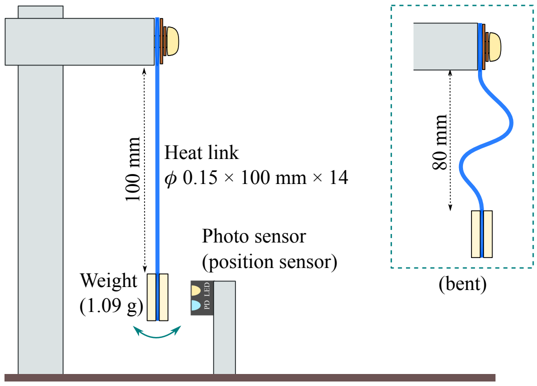

Figure 6.7: Measurement setup for the spring constant of the heat link.

Table 6.2: Measured spring constants of the heat liinks

	resonant frequency [Hz]	gravitational spring [N/m]	elastic spring [N/m]
straight	1.85	0.147	0.050
bent	2.21	0.210	0.080

increased to 0.080 N/m when the heat link is bent. It is assumed that torsional deformation in the bent heat link brought additional spring constant. The measured values are close to the expected value of 0.073 N/m. In Phase-III TOBA and the current setup, $\phi 0.15 \times 100\text{mm} \times 28$ of heat links are used, which will then have 0.16 N/m of the spring constant.

6.2.4 Magnetic properties of copper

To evaluate the magnetic noise, remnant magnetic moment of copper and oxidized copper were measured using two $4 \times 4 \times 4$ mm samples. The samples were made of oxygen free copper. One of sample was oxidized by heating in the same way as TMs of TOBA. A superconducting susceptometer MPMS-5S was used for the measurements. These measurements were performed by the Cryogenic Research Center, the University of Tokyo.

The measurement steps are as follows. At the room temperature, the samples were first demagnetized, and 0.1 T of external magnetic field was applied to the sample, then the external field was turned off. Then the samples were cooled down to 4 K, and the remnant magnetic moments were measured at several temperatures. Fig. 6.8 shows the measured remnant moments. It was clearly seen that the oxidized layer increased the remnant moment. From the measurements, the total remnant magnetic moment of the test mass bar of Phase-III TOBA is estimated to be 5×10^{-6} A·m^2 at 4 K.

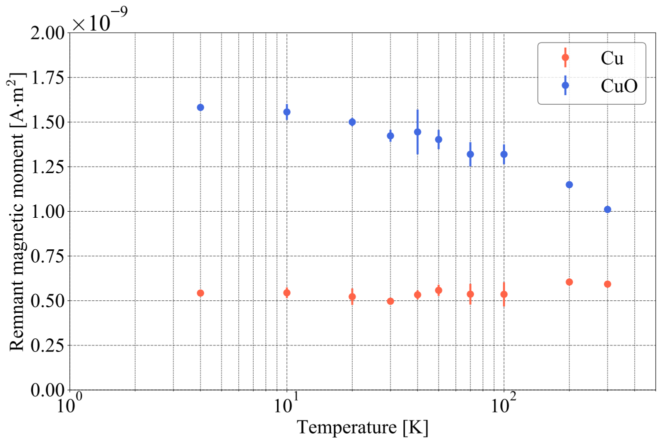

Figure 6.8: Measured remnant magnetic moments for the non-oxidized sample (red) and the oxidized sample (blue). 0.1 T of magnetic field was applied to the samples before cooling them.

Table 6.3: Temperature of the suspension masses just after the cooling. The uncertainty of the temperature is ±0.01 K.

mass	achieved	expected	expected (for low-k)
1st shield [K]	55.71	51.8	51.8
2nd shield [K]	4.82	3.34	3.34
Heat link stage [K]	5.23	3.34	3.34
IM2 [K]	6.68	3.83	4.28
OB [K]	7.91	4.25	4.81
IM1 [K]	6.04	3.87	4.18
TM1 [K]	6.14	3.87	4.18
TM2 [K]	6.10	3.87	4.18

6.3 Cooling performance

6.3.1 Cooling curve

Using the assembled cryogenic suspension, a cooling test was performed to demonstrate the performance of the cryogenic system. The result of cooling is shown in Fig. 6.9 with the expected curves from calculation. The suspension system was successfully cooled in 10 days down to 6.1 K at TMs. The achieved temperatures just after the end of cooling are summarized in Table 6.3. The uncertainty of the temperature is 0.01 K due to the uncertainty of the thermometer.

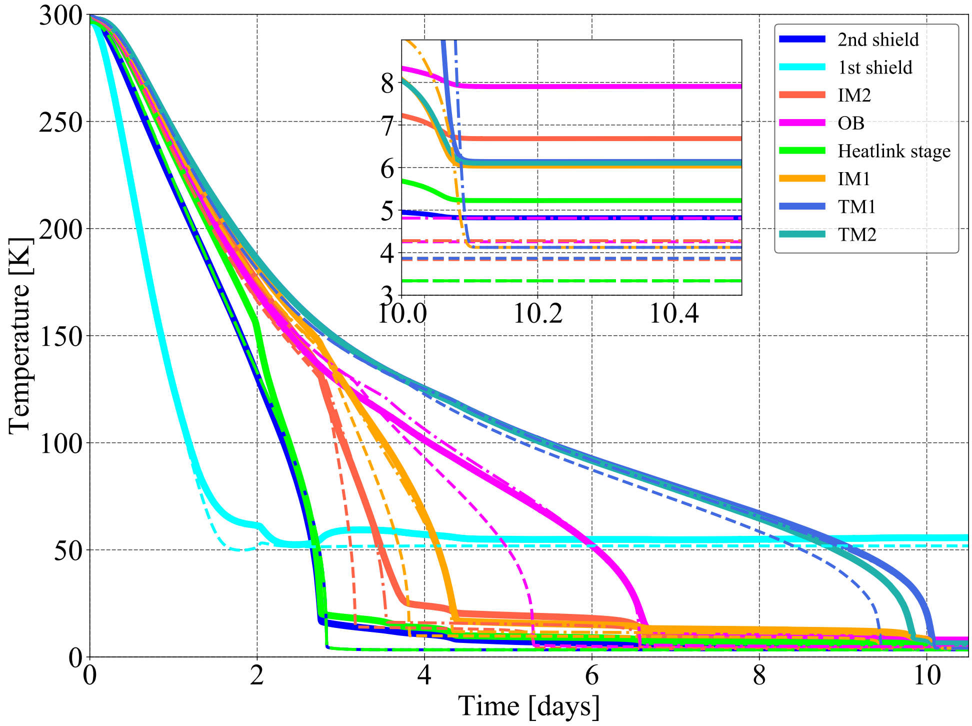

Figure 6.9: Cooling curve of the suspension masses. The solid lines shows the measured curve, and the dashed lines are the expected curve from calculation. The dot-dashed lines show the case when thermal conductivity is lower than the design by 35% for IM1, 50% for IM2 and 30 % for OB.

The difference of the achieved temperature 6.1 K and the target temperature 4 K is a factor of 1.2 in terms of the fundamental thermal noise level that is proportional to $\sqrt{T}$ (Sec. 3.2.1). Hence the fundamental requirement on the cooling performance has almost been achieved, though there are some possibilities of upgrade. Two issues, the slightly slow cooling speed and the heat inflow that was limiting the achieved temperature, are examined below.

Cooling speed

The cooling curve is slower than expected (the dashed lines in Fig. 6.9) below 120 K, where the conductive cooling dominates the heat extraction. Therefore the thermal conductivity is suggested to be lower than the expected values. The dot-dashed lines in Fig. 6.9 show the case when the thermal conductivity of the heat link is lower than the design 35% for IM1, 50% for IM2 and 30 % for OB. They explain the measured cooling speed well. Thermal conductivity can be degraded by contact thermal resistances between the components of the suspension. The assumed degradation of the conductivity becomes larger as the number of heat links increases (28 for IM1, 56 for IM2, and 28 for OB), which suggests the effect of contact thermal resistance.

Heat inflow to the suspension system

The expected final temperatures with the degraded thermal conductivities are also shown in the last column of Table 6.3. The achieved temperatures are higher than expected by 2.0 K for TM, 1.9 K for IM1, 1.9 K for the heat link stage, and 1.5 K for the 2nd shield.

The 1.5 K of temperature increase in the TM suspension series is due to the rise in temperature of the 2nd shield. The expected 2nd shield temperature is based on the measurement without suspension systems. As mentioned in Sec. 5.1.1, the heat load capacity of the shield is 3.53 K/W. Therefore the 1.5 K of temperature rise corresponds to 420 mW incident heat at the 2nd shield. The radiative heat introduction is expected to be small; 0.26 mW from the hole for suspension wires, and 0.01 mW from the holes for lasers. The most suspicious heat introduction path is the copper lead wires ($\phi 0.125 \times 200$ mm$\times 36$) connected between the 2nd shield and the 1st shield to transfer the electrical signals to outside the chamber. Though the properties of the wires are not characterized, the thermal conductivity can be on the order of 10^3 W/m/K if the purity of the wire corresponds to $RRR \simeq 30$. The expected heat is about 110 mW, which can be larger if the purity of the wire is higher. Thermal conductivity of the lead wires have to be confirmed, or the wires should be replaced to lower conductivity ones such as phosphor bronze. Additionally, the performance of the cryocooler needs to be examined again because the cooling ability might be degraded due to the trouble of the vacuum system during this experiment. The gas molecules flowed from the troubled vacuum pump, and they could transfer the heat from high temperature parts to the 2nd shield.

Additional 0.4 K increase happens at the heat link stage. This suggests that heat is incoming on the stage and the thermal resistance between the stage and the 2nd shield is not sufficient. Currently $\phi 0.15$ mm $\times$ 50 mm $\times$ 112 of heat link wires are attached between them. Considering the degradation of the thermal conductivity in the same degree as IM2 (~ 50 %), the corresponding heat inflow is about 60 mW. When this assumption is true, the temperature rise can be explained by the heat generation on OB. The temperature difference between OB, IM2 and the heat link stage corresponds to heat flows of 39 mW from OB to IM2, and 57 mW from IM2 to the heat link stage. The discrepancy between the two heat flows can be because of the error in the thermal conductivity at around 6 K. The error of the measured thermal conductivity is large below 10 K as shown in Fig. 6.6, and it is also difficult to estimate from the cooling curve because the curve is mostly determined by the conductivity above 10 K.

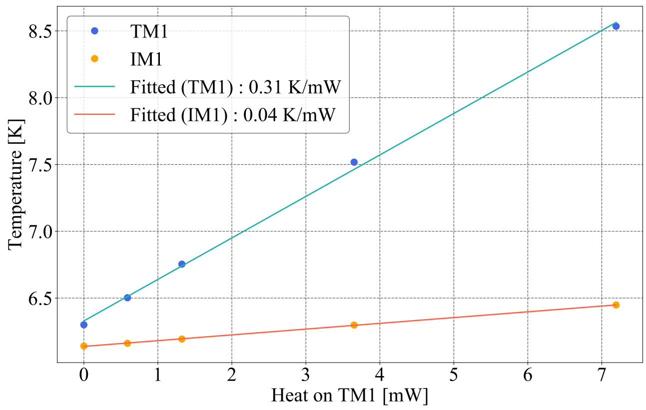

Figure 6.10: Temperature change of TM1 and IM1 vs applied heat on TM1.

The main source of the heat on OB will be the coils for actuator.

For the TM suspension series, IM1 has the same temperature as the heat link stage, which suggests that there is no significant heat inflow directly on IM1. 0.1 K difference between TM and IM1 is due to the applied heat load on TM. Based on the measurement of heat load capacity, 0.1 K difference corresponds to 0.37 mW heat, which comes from the laser and the actuator coils. The test of heat load capacity is described later. When the laser and the coils were turned off, the temperature decreased by 0.03 K and 0.2 K, respectively. Therefore the heat from the coils for actuation seems to be the origin of the temperature rise between TM and IM1.

Temperature change by heat load

For the evaluation of incident heat on TM, temperature rise against applied heat was measured. Heat load was applied on TM1 using a heater attached on the surface. The heater is made of phosphor bronze wire whose resistance is 15.7 Ω at 300 K. Based on the specification value of the wire, the resistance at the cryogenic temperatures is predicted to be 13.0 Ω. The applied heat was calculated from the resistance and the applied current. Fig. 6.10 shows the measured temperature change vs the applied heat. The fitted heat load capacity is 0.31 K/mW for TM1, and 0.04 K/mW for IM1.

6.3.2 Change of suspension parameters

To check if any serious problems happen in the suspension system or not, change of the suspension parameters during the cooling was measured. The characterized parameters also provide useful information for future upgrades.

Table 6.4: Resonant frequency and Q value at 300 K and at 6 K, for common and differential rotational modes.

Temperature	Resonant frequency		Q value	
	Common	Differential	Common	Differential
300 K	12.30 mHz	13.16 mHz	340	420
6 K	11.40 mHz	13.64 mHz	230	710

Resonant frequency and Q value

The resonant frequency and the Q values of the torsional modes (Yaw modes) were measured by ringdown method at 300 K and 6 K. Rotation of TM was excited by applying a pulse force on TM, then f_0 and Q were calculated from the oscillational frequency and the decay time of amplitude. During the measurement, the current on the actuators were turned off so that the measured parameters were determined only by the suspension wires and the heat links. The measured resonant frequencies and Q values are listed in Table 6.4. The common and differential modes are the modes in which two TMs and IM1 rotates in the same direction, or two TMs rotates in opposite direction while IM1 is stable, respectively.

The parameter change was not significantly large, which suggests that there is no serious problem in the suspension such as the break of the components. The resonant frequency change of the differential mode can be explained by the change in the Young's modulus of beryllium copper, which increases by 10 % at cryogenic temperatures [90]. On the other hand, the common mode frequency decreased by 10 % at 6 K, which cannot be explained by the Young's modulus change. Thermal shrinks of the attached heat links or the suspension wire clamp might contribute to the resonant frequency change.

Rotational drift during the cooling

During the cooling, the angular position of TMs moved by roughly 14 mrad for TM1 and 7 mrad for TM2. The amounts of drift were estimated from the actuator force which is applied to adjust the positions of TMs. It is inferred that the cause of the drift is the thermal deformation around the suspension point. When there is 1 % of asymmetry in the amount of the thermal shrinks, 1 %$= 10^{-2}$ rad of rotational angle change can happen. Considering that several components are assembled at the suspension point, the 1 % asymmetry will be feasible.

Though these drifts were able to be compensated with coil-coil actuators, they should be adjusted with rotational stages in Phase-III TOBA, because large DC actuator force introduces large actuator noise. From this experiment, the required range was found to be few tens of mili-radians.

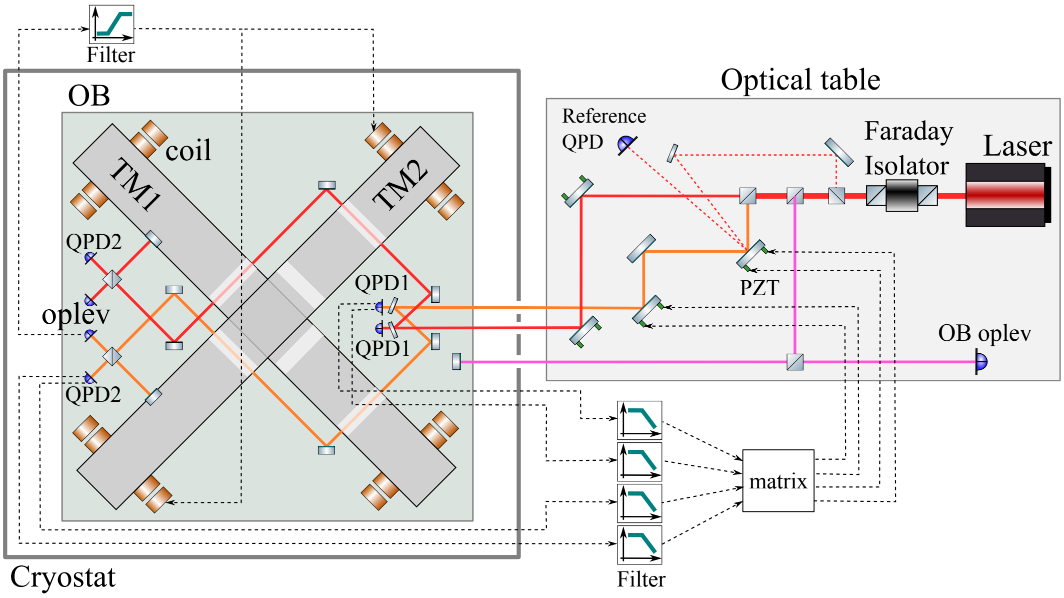

Figure 6.11: A configuration of optics and control system for the cryogenic prototype experiment. Jitter of the laser beam is monitored by two QPDs (QPD1 and QPD2), and the rotation of the bars are measured by the optical lever QPDs (“oplev” in the figure). Feedback paths are shown with the dotted lines.

6.4 Sensing and control

A schematic diagram of the optics and the control system of the cryogenic prototype are shown in Fig. 6.11. Optics are constructed on OB in the cryostat or on the optical table outside the vacuum chamber. Two laser beams are injected from outside the chamber into the cryostat. On OB, two jitter monitor QPDs (QPD1 and QPD2) are placed for each TM to monitor the displacement of the beam. Each QPD measures vertical and horizontal displacement of the center of the beam. The signals of QPD1 and QPD2 are fed back to the PZT actuators outside the vacuum chamber to stabilize the beam jitter. By fixing the beam center at the two QPDs, the beam is fixed relative to the OB so that the optical lever can measure the relative rotation between TM and OB. An optical lever QPD (Oplev) measures the position of the reflected beam from the mirror on the bar. Its signal is then fed back to the coil-coil actuators for the TM bar to damp the resonance of the bar.

Each QPD has three signals; beam displacement signal in the horizontal direction (Yaw) and the vertical direction (Pitch), and total power signal (Sum). Yaw and Pitch signals were calculated from the power difference between left and right segments, and upper and lower segments, respectively. Sum signal is the sum of the four segments of the QPD.

6.4.1 Calibration of QPD

The position sensitivity of QPDs on the OB was measured to calibrate the voltage signals to the rotations or displacements of the system. The beam was shaken by the PZT actuators attached on the mirror in the beam path. During the calibration, the tilt angle of the injecting mirror was monitored with a reference QPD, as shown in Fig. 6.11. First, the position sensitivity of the reference QPD on the optical table was calibrated by scanning the QPD position with a micrometer. Then the mirror was shaken at 10 Hz and the signals from four QPDs (the reference QPD, QPD1, QPD2 and the oplev QPD) were measured. Using the reference QPD signal and the beam path lengths from the injecting mirror to each QPD, the displacement amplitude of the beam at each QPD was calculated. The position sensitivity of each QPD was then calibrated by comparing the electrical signal amplitude and the calculated displacement amplitude. As a result, the sensitivity of the oplev QPDs were measured to be 3.34 V/mm for TM1 and 9.11 V/mm for TM2. The sensitivities of the other QPDs were also in the same order around 3–16 V/mm. The variation of the sensitivities originates from the difference in the beam size, the beam position offset from the center of the QPD or the trans-impedance of the QPD circuit.

6.4.2 Beam jitter suppression

As explained with Fig. 5.11, beam jitter was controlled using QPD1 and QPD2. The actual control scheme is shown in Fig. 6.11. Four signals from the QPD1 and QPD2 are filtered and mixed, then applied to each PZT actuator. The mixture matrix is set to decouple the signals because each PZT actuator shakes the beam position at both QPDs. A low pass filter and gain booster filters were used for the control, which is designed to get high suppression gain below 0.1 Hz. The open-loop transfer function is given by $G_{\mathrm{jit}} = S_{\mathrm{QPD}} F_{\mathrm{jit}} A_{\mathrm{PZT}}$, where S_{QPD}, F_{jit}, and A_{PZT} are the sensitivity of the QPD [V/m], the transfer function of control filter, and the efficiency of the PZT actuator, respectively.

G_{jit} was measured by injecting a signal into the control loop. Fig. 6.12 shows the measured G_{jit} for one of the jitter degrees of freedom. The beam jitter control loop was confirmed to be working almost as expected. The gain exceeds 10^4 below 0.05 Hz, which gives the achievable suppression factor of beam jitter. The resulting beam jitter is evaluated in the next section.

6.4.3 Active damping of TM

TMs were actively damped by using the coil-coil actuators. The damping scheme is shown in Fig. 6.11. The measured rotational signal is filtered and then applied to the actuator. This is a kind of feedback control, while the open-loop gain exceeds 1 only around the resonance of the pendulum. Here

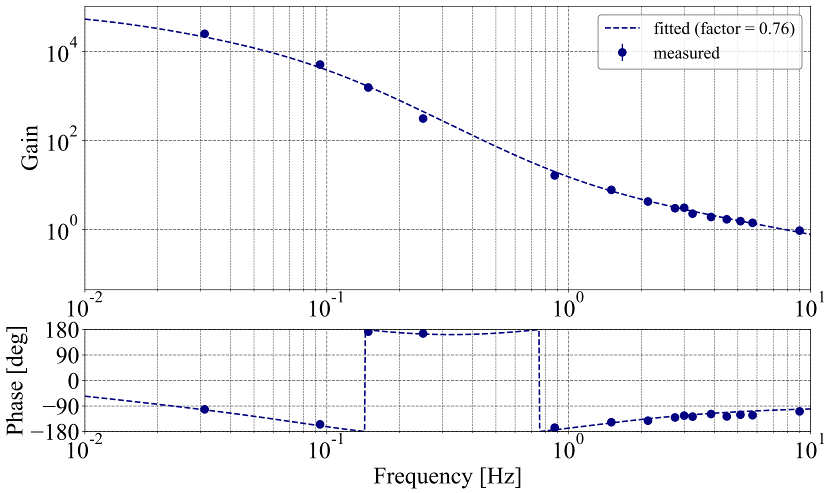

Figure 6.12: Measured open-loop transfer functions for the beam jitter suppression. The dots are the measured points, and the solid line is the expected function multiplied by a factor of 0.76.

the open-loop transfer function is given by

$$G_{\mathrm{TM}} = S_{\mathrm{oplev}} F_{\mathrm{TM}} A_{\mathrm{coil}} H_{\mathrm{TM}}. \tag{6.4}$$

From the calibrated position sensitivity of the QPD and the distance between TM and the QPD, 75mm, the sensitivity of the optical lever in unit of TM's angle is $S_{\mathrm{oplev}} = 501$ V/rad for TM1 and 1370 V/rad for TM2. The control filter F_{TM} and the mechanical response from applied force on the end to rotational angle, H_{TM}, are

$$F_{\mathrm{TM}}(f) = \frac{1 + i(f/0.003\ [\mathrm{Hz}])}{1 + i(f/1\ [\mathrm{Hz}])} \times 0.01, \tag{6.5}$$

$$H_{\mathrm{TM}}(f) = \frac{0.3\ [\mathrm{m}]}{4\pi^2 I_b} \frac{1}{f_0^2 + i f_0 f/Q - f^2}. \tag{6.6}$$

where $I_b = 0.056$ kg·m^2 as given in Table 5.1, and the resonant frequency and the Q values were evaluated by ringdown measurement. The actuator efficiency A_{coil} was estimated from the applied current amplitude and the gain of coil drivers. In this experiment we set $i_1 \neq 0$ and $i_2 = 0$. From Eq. (5.1) and the parameters of the coils at room temperature, A_{coil} is calculated to be 130 μN/V for TM1 and 27 μN/V for TM2.

Fig. 6.13 shows the measured open-loop transfer functions for two TMs. The dashed lines were fitted with the actuator efficiency A_{coil} as a fitting parameter. The shapes of the measured datas well fitted to the theoretical expectation. As designed, G_{TM} exceeded 1 only around the resonance frequency,

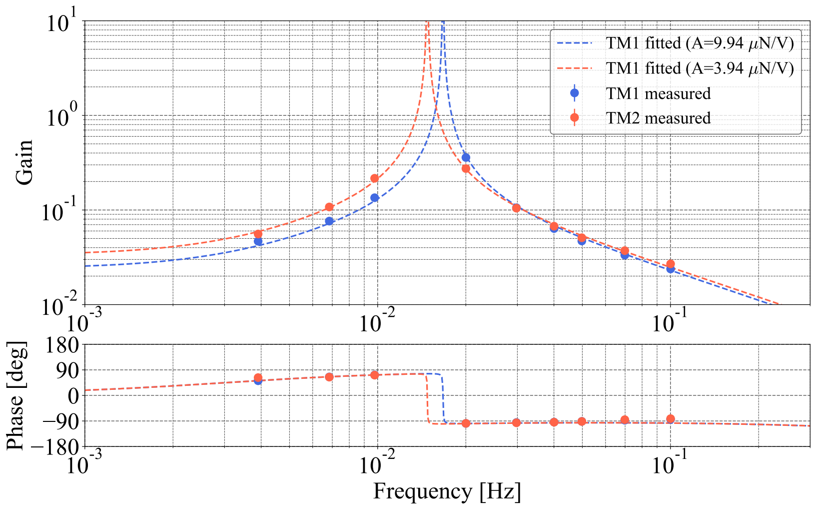

Figure 6.13: Measured open-loop transfer functions for TM1 (blue) and TM2 (red). The dots are the measured points, and the lines are the fitted functions.

hence it acted as an active damping control. On the other hand, the fitted actuator efficiencies were 9.94 μN/V for TM1 and 3.94 μN/V for TM2, which were smaller than the calculated values by about 10 times. This may be because the electrical conductivity of the bar on which the coils are attached was significantly increases at cryogenic temperature, hence the inductances of the coils were modified.

6.5 Noise investigation

Using the operated prototype, the coupling mechanisms for some important noise sources were investigated to gather the knowledge of the performance of the cryogenic torsion pendulum.

First, Fig. 6.14 shows the sensitivity and the noise budget of the current cryogenic prototype. The vertical axis is plotted in unit of strain amplitude of gravitational waves. According to Eq. (3.13) and (3.15), the conversion between the rotational angle θ of the single bar and equivalent GW strain amplitude h is given by

$$\frac{\tilde{\theta}}{\tilde{h}_{\mathrm{GW}}} = \frac{q_b}{2I_b}\frac{f^2}{f_0^2 + if_0 f_Q - f^2} \tag{6.7}$$

in the frequency domain. The ratio between the quadruple moment and moment of inertia of TM, q_b/I_b, is approximated to 1. The solid black line in Fig. 6.14 is the overall sensitivity, which was calculated from the difference between the rotational signals of TM1 (solid blue line) and TM2 (solid red line).

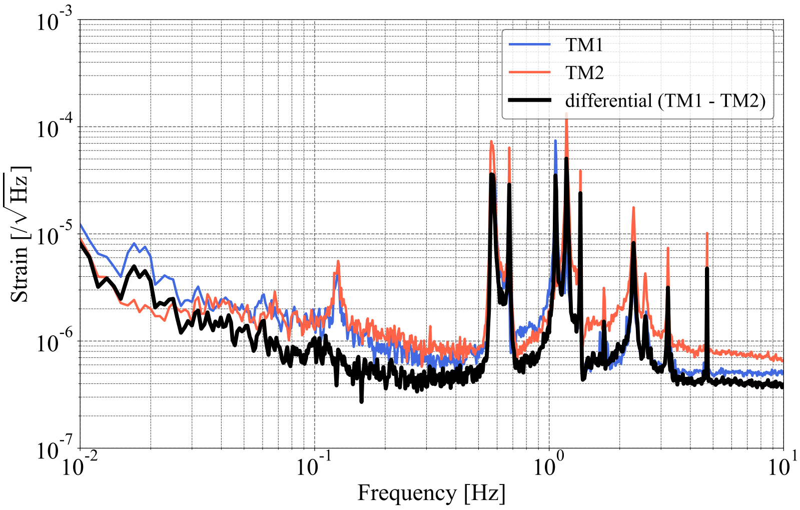

Figure 6.14: Noise levels in unit of gravity strain for TM1 (blue), TM2 (red), and the differential rotation between them (black).

Some evaluated or estimated noise sources for each TM are plotted in Fig. 6.15. Their details are explained in the following subsections. First, the dominant noise sources in the current system were evaluated to characterize the performance of this prototype. Then the following three technical noises were investigated; temperature fluctuation noise, vibration noise via the heat links and magnetic noise. These are important technical noise sources that are relevant to the cryogenic environment.

6.5.1 Dominant noise sources in the current system

First, performance of the current prototype system was characterized. In the current system, stray light noise and beam jitter noise were dominant noise sources as described below.

Stray light noise

Interference fringes were observed in the angular signals of the optical levers as shown in Fig. 6.16. The same kind of fringes were also observed in the QPD2 for beam jitter control. They indicate a coupling from a stray light to the main laser beam. The origin of the stray light was identified to the optics around the TMs, because the interference pattern changes at the pendulum frequency (around 1 Hz), as clearly seen in the TM1 signal in Fig. 6.16. Additionally, the interference fringe in the QPD2 disappeared when the beam going to TM was blocked.

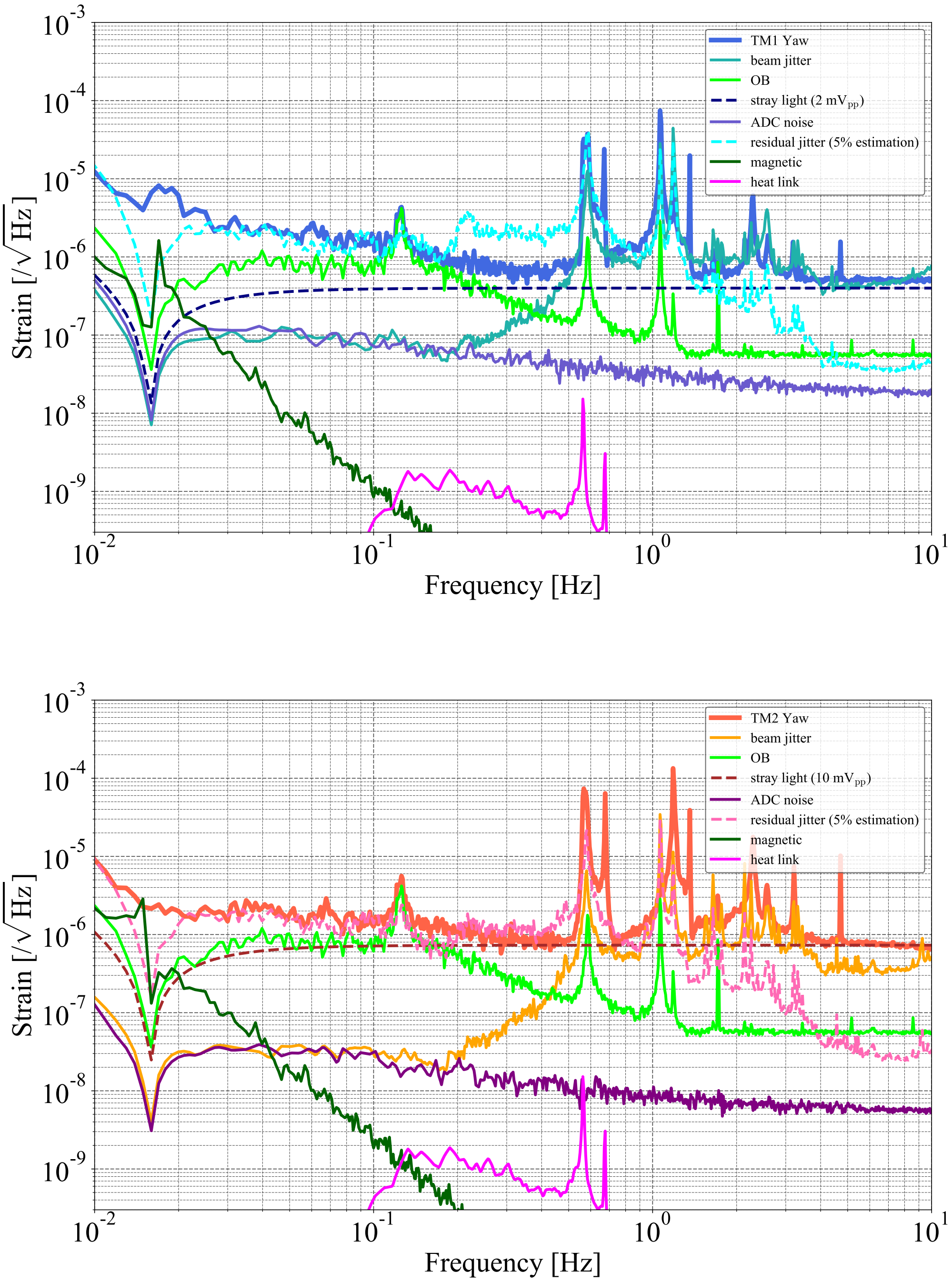

Figure 6.15: Noise budgets for TM1 (upper) and TM2 (lower). The stray light noise limits the sensitivity around 0.3 Hz and above 3 Hz. The peaks around 1 Hz are the contribution of beam jitter noise. Below 0.1 Hz, the residual beam jitter originates from the signal coupling at the QPDs is inferred to be dominant.

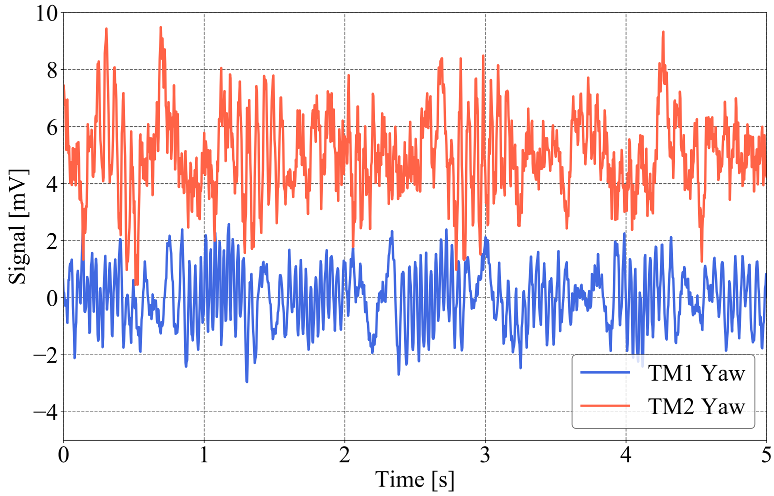

Figure 6.16: Interference fringe observed in the signal.

The width of interference fringe was about 1–10 mV, which corresponds to about 0.01 % of the stray light intensity compared to the main laser beam. Such a stray light can originate from the reflection at the surface of the beam splitters or the QPDs. For example, the reflectivity of the AR coated surface of the beam splitter is specified to be 0.1 %, which can explain the observed interference fringe.

Since the the stray light behaves like a random noise within the width of the interference fringe, it turns to be a flat noise spectrum. The bandwidth of the signal is determined by the speed of passing the interference fringe. In our case, the band width was confirmed to be 100 Hz from the cutoff frequency of the signal spectrum. And the width of the fringes were roughly 2 mV for TM1 and 10 mV for TM2. Based on these parameters, the amplitude spectral density due to the stray light interferences are plotted in Fig. 6.15. It explains the floor noise level of $4 \times 10^{-7}\ /\sqrt{\mathrm{Hz}}$.

To remove the stray light noise, the beamsplitter should be replaced from the cube-shaped one to a plate-shaped one, which can separate the surface reflection from the main beam path. Proper beam damping of the stray beams is also important to reduce the noise. Note that the stray light noise will be largely eliminated with the wave front sensor in Phase-III TOBA, because such a beam splitter is not placed near the photo detector.

Beam jitter noise

Bean jitter control can suppress the jitter and introduce the noise from the control system at the same time. The block diagram of the control, Fig. 6.17, explains how noises are introduced in the control loop. Here three noise sources

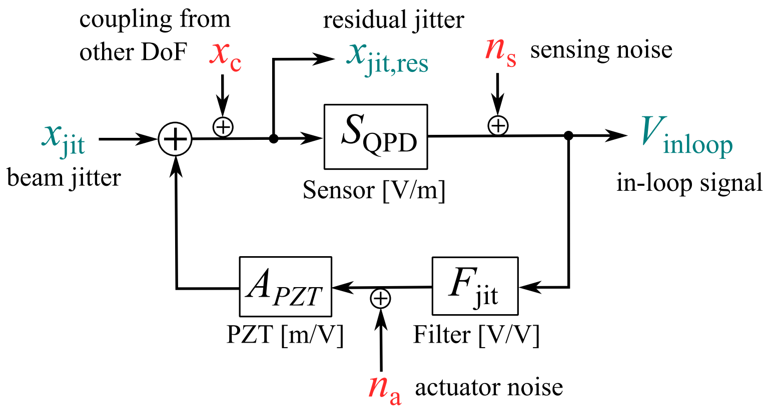

Figure 6.17: Block diagram of beam jitter control with noise.

are taken into account; signal coupling from other degrees of freedom (DoFs), noise of the sensing electrics and noise of the circuits for the actuator. From the block diagram, their contributions in the residual beam jitter are calculated to be

$$x_{\text{jit,res}} = \frac{1}{1+G_{\text{jit}}}\left(x_{\text{jit}} - G_{\text{jit}}x_c - A_{\text{PZT}}n_a - F_{\text{jit}}A_{\text{PZT}}n_s\right) \tag{6.8}$$

$$\simeq \frac{1}{G_{\text{jit}}}x_{\text{jit}} - x_c - \frac{A_{\text{PZT}}}{G_{\text{jit}}}n_a - \frac{1}{S_{\text{QPD}}}n_s. \tag{6.9}$$

The original jitter level x_{jit} was estimated using in-loop signal as follows

$$x_{\text{jit,estimation}} = \frac{1+G_{\text{jit}}}{S_{\text{QPD}}}V_{\text{inloop}} \tag{6.10}$$

which gives a good estimation when the sensing noise n_s or the coupling from other DoFs x_c are sufficiently smaller than the original jitter x_{jit}.

Fig. 6.18 summarizes the estimated noise contributions. These spectrums are calculated from the measured noise levels and the open-loop transfer functions evaluated in Fig. 6.12. The vertical axis is converted to equivalent angle of TM. For the sensing noise, analog to digital conversion (ADC) noise (light-purple and red-purple lines) had a dominant contribution, which was more than ten times larger than the dark noise of the QPD circuits (grey line). The thick green and orange lines show the sum of the in-loop fluctuations and the sensing noise (ADC noise here). These lines give the residual beam jitter noises in the absence of the coupling from other DoFs x_c. The PZT driver noise (black line) had only ignorable contribution because it is suppressed by G_{jit}.

Eq. 6.9 indicates that the contribution of x_c cannot be suppressed, hence it can be a serious noise source. The contribution of x_c is suggested by the coherence between the Yaw signal of the Oplev QPD and the Sum signals of jitter monitor QPDs. Fig. 6.19 shows the coherence between them for TM1

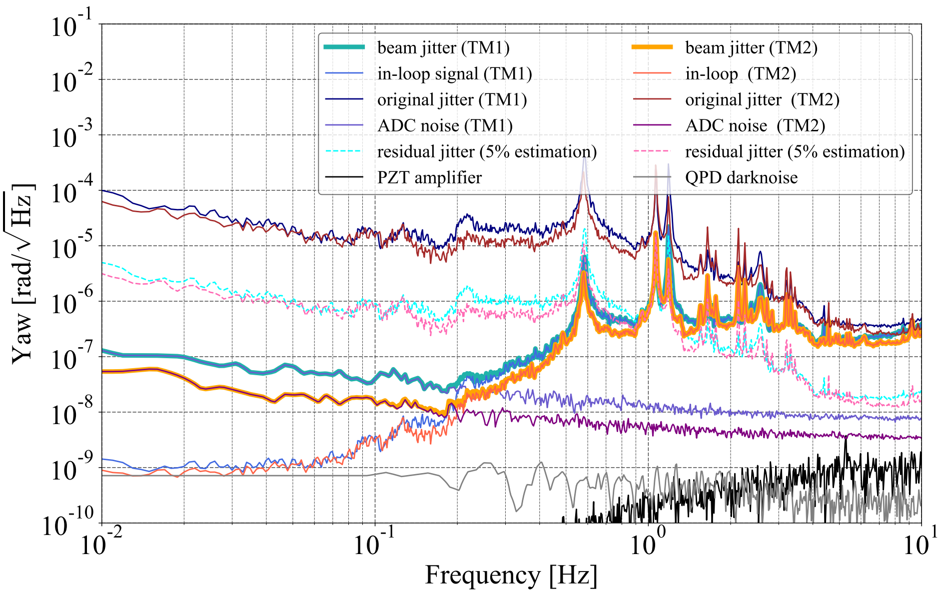

Figure 6.18: Estimated beam jitter noise budget under the feedback control.

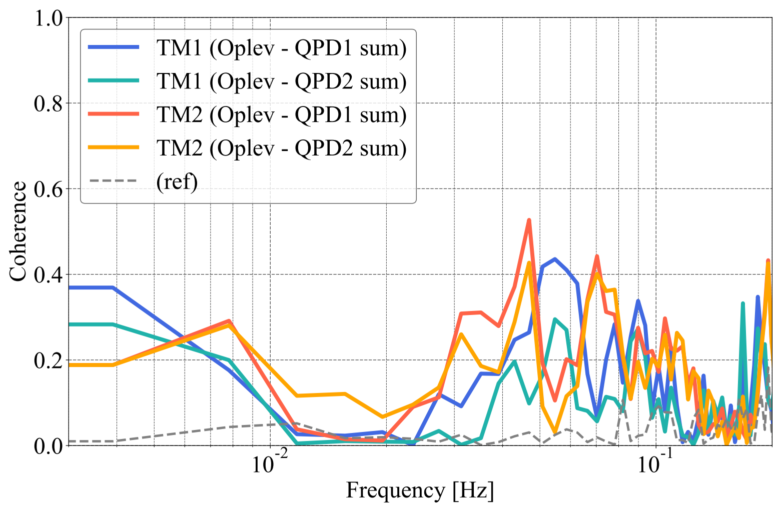

Figure 6.19: Coherence between the Yaw signals of the oplev QPD and the Sum signals of jitter monitor QPDs. The black dashed line is the coherence between uncorrelated signals shown as a reference.

and TM2. They were partly correlated to each other, which indicates that the power fluctuation or the beam expansion was coupling as x_c, then appeared in the residual beam jitter fluctuation. The direct coupling from the power

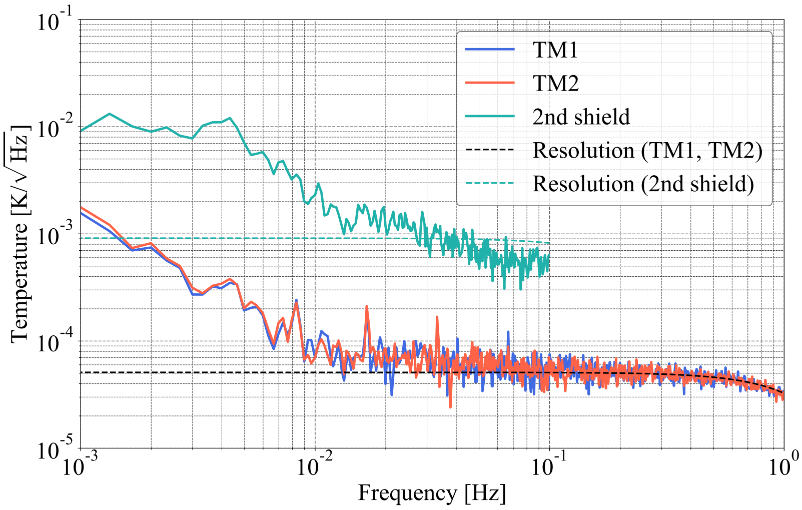

Figure 6.20: Amplitude spectral density of temperature fluctuation for TM1 (blue), TM2 (red), and the 2nd shield (solid green). The noise floor due to the resolution of the thermometers are plotted with dashed lines.

fluctuation to the Yaw signal of the Oplev is thought to be small because there was no coherence between the Yaw and the Sum signals of the QPD for the Oplev.

The amount of x_c is hard to confirm since it requires measurements of all possible fluctuation of the beam. Here 5 % of the original beam jitter fluctuation is assumed as x_c, whose contributions are plotted with the dashed cyan line for TM1 and the dashed pink line for TM2. Although this is just an assumption, this contribution can explain the noise floor of TMs between 0.01–1 Hz (Fig. 6.15). Qualitatively speaking, incoherence between the signals of TM1 and TM2, and consistency of the spectrum shape between the beam jitter and the TM signals supports this hypothesis.

6.5.2 Temperature fluctuation noise

Using the thermometer signals on TMs, temperature stability was evaluated because the fluctuation can be a noise as explained in Sec. 3.2. Fig. 6.20 shows the temperature fluctuation of two TMs and the 2nd radiation shield. The temperature fluctuation of the 2nd shield was about 6×10^{-4} K/$\sqrt{\text{Hz}}$ at 0.1 Hz. Based on Eq. (3.39), the thermal radiation pressure noise is calculated to be 3×10^{-19} rad/$\sqrt{\text{Hz}}$ in this system. Hence the temperature stability of the shield is small enough in terms of this noise.

The measured spectrum of TM temperature fluctuations were limited by the resolution of the thermometer, hence they are below 5×10^{-5} K/$\sqrt{\text{Hz}}$ at 0.1 Hz. To evaluate the contribution to the noise in TOBA, response to the

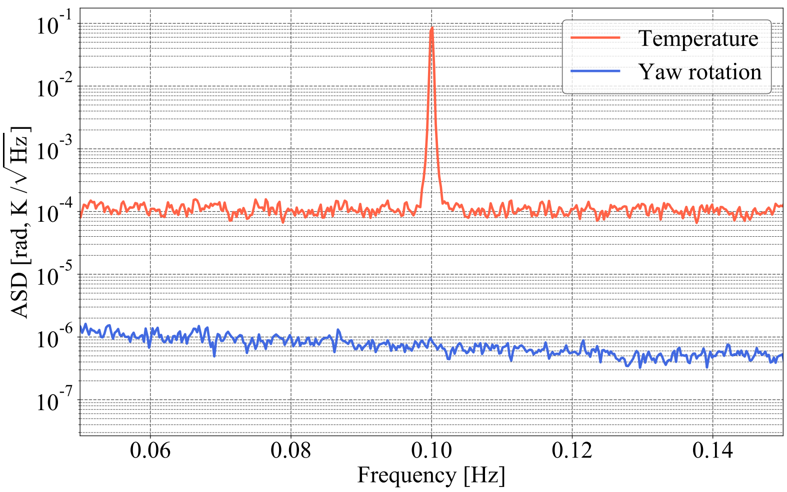

Figure 6.21: The ASD of the temperature and the rotational angle of TM1 during the injection of heat fluctuation in 0.1 Hz on TM1. No coupling was observed.

temperature fluctuation was measured for TM1. A time-varying current at 0.1 Hz was applied to the heater on TM1, then the temperature fluctuation and the rotational angle were measured. Fig. 6.21 shows the measured spectrum of them during the heat injection. Though the temperature of TM1 fluctuates at 0.1 Hz, no fluctuation of the rotational angle of TM1 was observed. From the transfer function between them, an upper limit of 7×10^{-6} rad/K was set to the response to temperature fluctuation. With the upper limit of the temperature fluctuation, the temperature fluctuation noise in the current system is below 3.5×10^{-10} rad/$\sqrt{\mathrm{Hz}}$ at 0.1 Hz.

Expected temperature distortion noise is smaller than this. The coefficient of thermal expansion of copper is about 9×10^{-9} /K at 6 K [83]. The aspect ratio in Eq. (3.40) is $l_y/L_b \sim 0.1$ in our case. Assuming 1 % of the asymmetry in the thermal expansion, $\Delta\alpha_b = 9 \times 10^{-11}$ /K at 6 K. Hence the total thermal distortion noise is calculated to be 4.5×10^{-16} rad/$\sqrt{\mathrm{Hz}}$ from the measured upper limit of temperature fluctuation. Since the actual temperature fluctuation is smaller than the upper limit, the noise will be sufficiently smaller than the target sensitivity of Phase-III TOBA.

6.5.3 Vibration noise via heat links

The amount of vibration noise induced via the heat links is estimated from the measured spring constant. The heat links are bent by relative translation between the suspension masses, then the elastic force acts on the attached point. Some fraction of the force act as torque in proportional to the asymme-

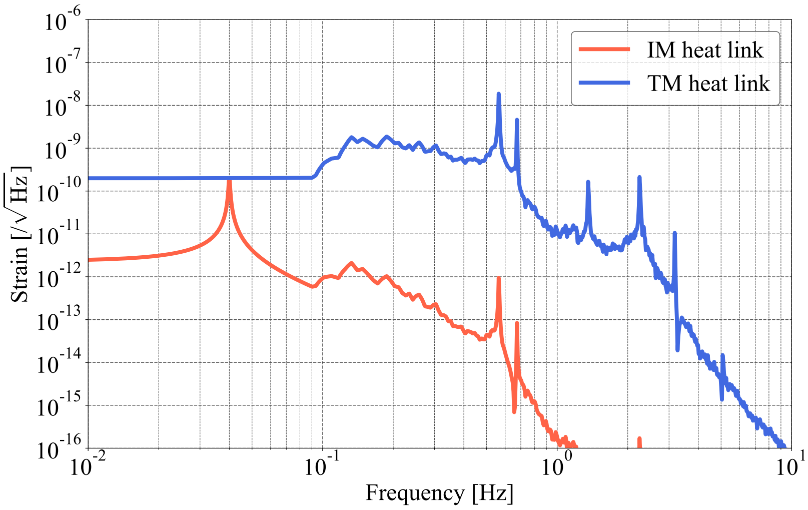

Figure 6.22: The vibration noise induced from the heat links. The contribution from the IM heat link and the TM heat links are shown with a red and a blue lines, respectively.

try of the force on the mass. The introduced noise in terms of the differential rotational angle between TM1 and TM2, θ_{diff}, is given by

$$\begin{aligned}\tilde{\theta}_{\mathrm{diff}}(f) &= C_{\mathrm{CMRR}} C_{\mathrm{asym}} D_{\mathrm{hl}} k_{\mathrm{hl,IM}} \tilde{\chi}_{\mathrm{IM}}(f) \tilde{H}_{\mathrm{IM}\to\mathrm{TM}}(f) \left(1 - \tilde{H}_{\mathrm{IM,trans}}(f)\right) \tilde{x}_{\mathrm{seis}} \\ &\quad + D_{\mathrm{hl}} k_{\mathrm{hl,TM}} \tilde{\chi}_{\mathrm{TM}}(f) \left(\tilde{H}_{\mathrm{IM,trans}}(f) - \tilde{H}_{\mathrm{TM,trans}}(f)\right) \tilde{x}_{\mathrm{seis}}, \end{aligned} \tag{6.11}$$

where C_{CMRR} is the common-mode rejection ratio in the rotational vibration transfer from IM1 to TM, $\tilde{H}_{\mathrm{IM}\to\mathrm{TM}}(f)$ is the transfer function of horizontal rotation from IM1 to TM, $\tilde{H}_{\mathrm{IM(TM),trans}}(f)$ is the translational transfer function from seismic vibration to IM1 or TM, and $\tilde{x}_{\mathrm{seis}}$ is the translational seismic vibration. $\tilde{\chi}_{\mathrm{IM(TM)}}(f)$ is the mechanical response of IM1 or TM against applied torque. About the heat links, D_{hl} is distance from the suspension point to the attached point of the heat links. $k_{\mathrm{hl,IM(TM)}}$ is the translational spring constant of the heat links for IM1 and TM, which are 0.16 N/m for IM ($\phi 0.15 \times 100\mathrm{mm} \times 28$) and 0.017 N/m for TM ($\phi 0.15 \times 100\mathrm{mm} \times 3$) based on the measurement in Sec. 6.2.3. For IM1, two set of the heat links were attached across the suspension wire, and C_{asym} is the asymmetry factor between them.

The calculated result for each term in Eq. (6.11) is shown in Fig. 6.22. Here $C_{\mathrm{CMRR}} = 0.1$, $C_{\mathrm{asym}} = 0.05$ and $D_{\mathrm{hl}} = 20$ mm were used for the calculation. The contribution of TM heat links is dominant because it is attached at one side of the bar ($C_{\mathrm{asym}} = 1$), and independent to TM1 and TM2 ($C_{\mathrm{CMRR}} = 1$). The total contribution is below 2×10^{-9} $/\sqrt{\mathrm{Hz}}$, hence not dominant in the current noise budget.

The measured vibration at the suspension stage was used for the noise estimation. It is worth mentioning that there was no significant excess of vibration around 0.1 Hz due to the cryocooler. The vibration of the cryocooler was low enough, or it was sufficiently isolated at the suspension stage without active vibration isolation system.

The prospect about the heat link vibration in Phase-III TOBA is discussed in the next chapter. Note that the heat links on TM will not be used and the seismic vibration will be actively suppressed in Phase-III TOBA, hence the noise will be much lower than the current noise level.

6.5.4 Magnetic noise

Magnetic noise was evaluated since it is an important noise that directly depends on material properties at cryogenic temperature. Response to the fluctuation of the environmental magnetic field were measured by injecting magnetic fluctuation with a pair of injection coils sandwiching the chamber. The coils have 40 cm of diameter, 1 cm of thickness and 200 turns. Then the environmental magnetic field fluctuation was measured with a magnetometer to evaluate the noise. This noise was unexpectedly large as shown below, therefore an additional experiment with a simpler torsion pendulum was performed, which is explained later.

Magnetic shielding of the radiation shield

First, the magnetic shielding ratio of the radiation shield (5 mm thick oxygen free copper) was measured at the room temperature. The applied field was calculated from the applied current on the injection coils, and the actual field inside the shield was measured with a magnetometer Mag649 (Bartington Instruments Ltd.). The measured shielding ratio is shown in Fig. 6.23, which had a cutoff frequency of 3 Hz. Since the shielding effect at higher frequencies is caused by the induction current, the cutoff frequency is expected to be lower at cryogenic temperature. Based on the specified RRR (residual resistivity ratio) of 100, the cutoff frequency at 4 K is estimated to be 0.03 Hz.

Response of the pendulum to magnetic field fluctuation

Next the response of TMs were measured by injection in the same way. The measured magnetic coupling functions are plotted in Fig. 6.24. They were fitted with the following function

$$\tilde{H}_{mag}(f) \equiv \frac{\tilde{\theta}_{\mathrm{TM}}}{\tilde{B}_{\mathrm{ext}}} = (\mu_1 + 2\pi i f \mu_2)\tilde{\chi}(f)\tilde{H}_{sh}(f), \tag{6.12}$$

where $\tilde{\chi}(f)$ is the mechanical response of TM, and μ_i are the coefficients which are used as fitting parameters. $\tilde{H}_{sh}(f)$ is the magnetic shielding of the cryostat which evaluated above. The first term of Eq. (6.12) represents the direct coupling between the magnetic moment or susceptibility of the bar, and the

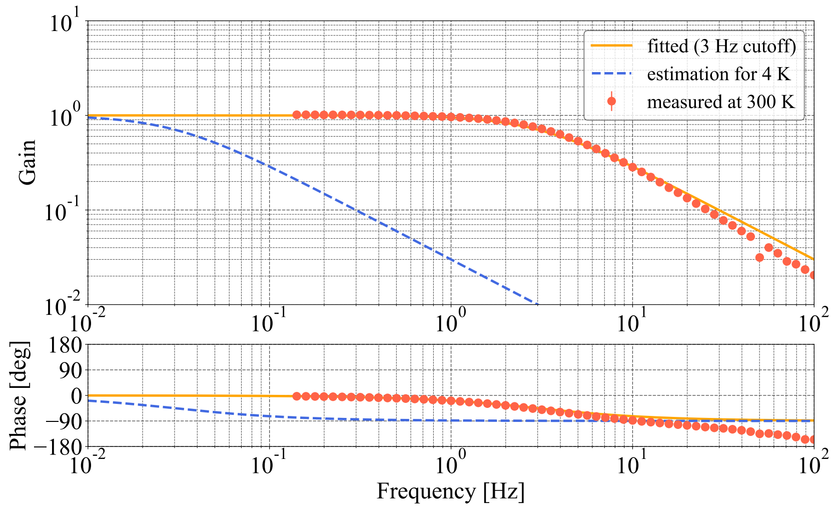

Figure 6.23: Transfer functions from magnetic field fluctuation applied from outside the chamber to the fluctuation inside the cryostat. The red points shows the measured value at the room temperature, and the orange line is the fitted low-pass filter. The dashed blue line is the estimated shielding ratio at 4 K.

Table 6.5: Fitted coefficients of magnetic coupling functions for TM1 and TM2 in the direction along to the bar ($\parallel$) and perpendicular to the bar ($\perp$).

		μ_1 [A·m^2]	μ_2 [A·m^2·s]
TM1	$\parallel$	-3.39×10^{-3}	-1.32×10^{-2}
	$\perp$	-1.58×10^{-3}	1.58×10^{-2}
TM2	$\parallel$	-2.66×10^{-3}	4.60×10^{-2}
	$\perp$	-4.17×10^{-3}	-9.49×10^{-3}

magnetic field or its gradient. The second term is a coupling with the time varying magnetic field $\dot{B}$. The fitted parameters for TM1 and TM2 are shown in Table 6.5. μ_1 corresponds to the magnetic dipole moment of the bar if we assume that the coupling is caused by a torque of $\boldsymbol{N} = \boldsymbol{\mu} \times \boldsymbol{B}$. The fitted values were in the order of $\mu_1 \sim 3 \times 10^{-3}$ A·m^2, which is a similar value as a $\phi 1 \times 5$ mm Nd magnet.

Magnetic noise evaluation

Fig. 6.25 shows the spectrum of environmental magnetic field fluctuation measured around the vacuum chamber. The measured fluctuation was in the order

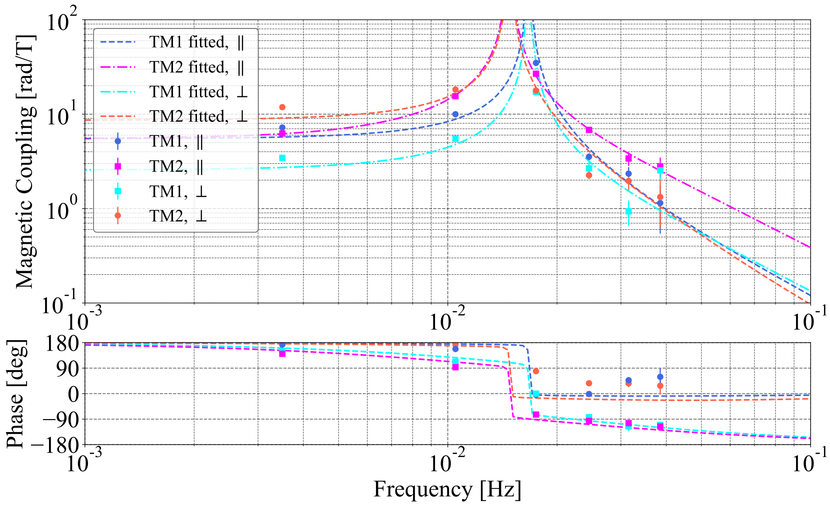

Figure 6.24: Transfer functions from applied magnetic field fluctuation to rotation of the bar. Magnetic fluctuation was injected in two directions; along to (||) and perpendicular to (⊥) each bar. The blue and cyan dots are the measured values for TM1, and the red and pink dots are for TM2. Fitted functions are plotted with dashed or dot-dashed lines.

of 10^{-8} T/$\sqrt{\text{Hz}}$ for the horizontal (x and y), which are relevant here. Note that there was no significant excess of fluctuation due to the cryocooler below 1 Hz. From the measurements above, the total contribution of the magnetic field fluctuation to the sensitivity was calculated. The result is plotted in Fig. 6.15 with a green line. The magnetic noise in the current system is more than 10^{-9} /$\sqrt{\text{Hz}}$ at 0.1 Hz, which is serious in the future sensitivity. These values were much larger than expected from the characterized magnetic properties shown in Sec. 6.2.4. Note that the magnetic field around TM bars can be largely deformed by the components on OB, which are made of copper. The induction current in such high conductive components can generates local magnetic field then enhance the magnetic noise.

Magnetic coupling in a simple torsion pendulum

To investigate the origin of the unexpectedly large magnetic coupling, additional experiment was performed using a simples torsion pendulum which consisted of a single bar without intermediate mass as shown in Fig. 6.26. The bar is the same one as TM of TOBA, while some components such as brass counter weights were not put in this measurement. Instead of suspended OB, the rotation of the bar was measured from the optical lever constructed at the bottom of the 2nd shield. The magnetic field was applied from outside the chamber in a horizontal direction perpendicular to the bar. As seen in

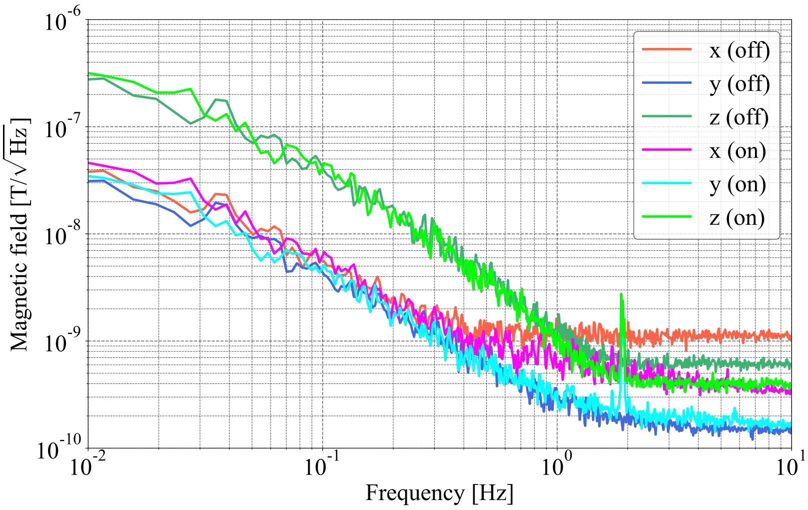

Figure 6.25: Measured spectrums of environmental magnetic field fluctuation in x (red), y (blue) and z (green) directions. Lighter colors show when the cryocooler is ON, and darker lines show when it is OFF. The noise floor was high in the red line, due to the trouble of the digital system.

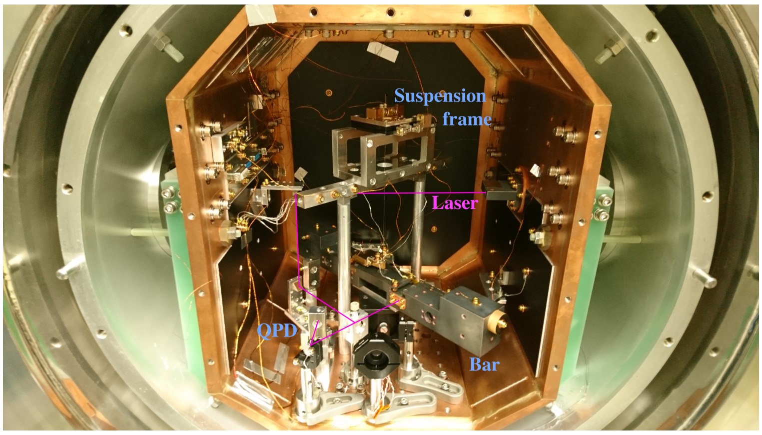

Figure 6.26: A measurement setup of magnetic noise with a simple torsion pendulum. It consists of a single suspended bar and the optical lever on the ground.

the picture, the bar is surrounded by less component than the current setup, hence the distortion of the magnetic field is expected to be smaller.

The response of the bar to the magnetic field fluctuation was measured in the same way as Sec. 6.5.4. By changing the temperature of the bar using a heater on it, temperature dependence of the magnetic response was investigated. During the measurement, the temperature of the 2nd shield was

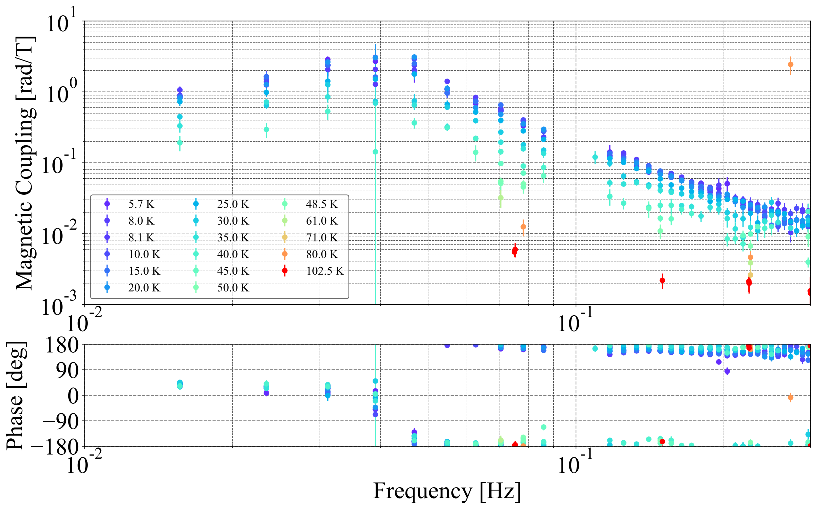

Figure 6.27: Measured transfer functions from magnetic field to the bar rotation. The gains and the phases of the transfer functions are shown in the upper box and the lower box, respectively. The different colors show different measurement temperatures from 5.7 K to 102.5 K.

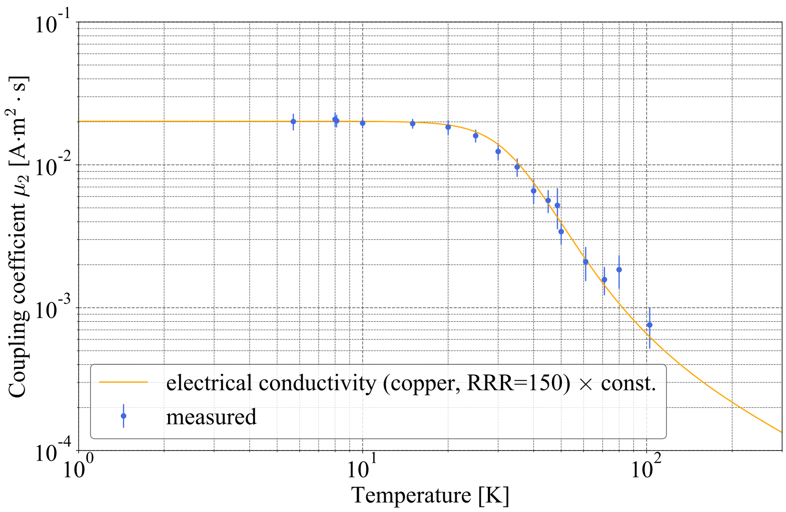

Figure 6.28: Fitted magnetic coupling coefficients vs temperature of the bar. The blue dots are the measured values, and the yellow line shows the temperature dependence of electrical conductivity of pure copper.

kept around 4 K.

The measured transfer functions from magnetic field to the bar rotation at various temperatures from 5.7 K to 102.5 K are shown in Fig. 6.27. The resonant frequency was about 40 mHz In this experiment. Above the resonant frequency, the transfer functions were inversely proportional to square of frequency. Taking into account the magnetic shielding effect of the 2nd shield, the torque from the magnetic field fluctuation is proportional to the frequency, which is expressed with the second term in Eq. (6.12).

Fig. 6.28 shows the fitted coupling coefficient μ_2 which is used in Eq. (6.12). As shown in the figure, the measured temperature dependence of the magnetic coupling was clearly proportional to the electrical conductivity of pure copper, which is the substrate of the bar. Here the residual resistivity ratio of copper was assumed to be 150, which is a typical value for oxygen free copper. This temperature dependence and the frequency dependence of torque ($\propto f$) suggest that the origin of magnetic coupling is induced current in the bar. When time-varying magnetic field is applied, current is induced in the bar, then induced magnetic moment couples to the magnetic field. Since pure copper has very high electrical conductivity, the contribution is not ignorable in the cryogenic torsion pendulum. The quantitative discussions are described in the next chapter.

On the other hand, the measured coupling functions contained less μ_1 terms than the value in Table 6.5. There can be two reasons. One is because some brass screws was removed in this experiment. Those components was likely to have a magnetic moment. Another reason is the distortion of the magnetic field is expected to be smaller because the bar is surrounded by less components.

6.6 Summary of experiment

Here the experimental results are briefly summarized. The achievements of this work are following things:

- The suspension system was successfully cooled down to the cryogenic temperature, 6.1 K.
- The torsion pendulum was operated at the cryogenic temperature.
- The performance of the cryogenic TOBA was investigated, and some problems have been identified.

The designed cooling technique has been basically demonstrated, and the pendulum was successfully operated at the cryogenic temperature. As mentioned at the beginning of this chapter, these are the essential steps for Phase-III TOBA since there have been no work on a large-scale cryogenic torsion pendulum. The achieved temperature in this work 6.1 K, which is close to the target temperature 4 K. Their difference in terms of fundamental thermal noise level is only a factor of 1.2.

From the noise investigation using the current prototype, a few issues in Phase-III TOBA have been identified. The beam jitter noise was inferred to be large due to the signal coupling at the QPDs. The vibration noise via the heat links and the magnetic noise are the issues that are relevant to the cryogenic system. The prospects of solving these issues for Phase-III TOBA are discussed in the next chapter. On the other hand, the temperature fluctuation level is already meets the requirement of Phase-III TOBA.

7 Discussion about Experimental Results

In this chapter, we discuss about the problems that were found in the previous chapter. The main target of the discussion is how to achieve the requirement of Phase-III TOBA based on our experimental results. The problems discussed here are follows:

- Improvement of cooling performance
- Magnetic noise reduction
- Vibration reduction via heat links
- Beam jitter reduction

Each topic is discussed in the following sections.

7.1 Improvement of cooling performance

Our cooling system worked almost as designed. Therefore it will also work for Phase-III TOBA in principle by replacing the suspension wire to a silicon wire. Ongoing R&D of silicon wire development is hence the primary topic among the issues about the cryogenic system. In terms of cooling, it is important to achieve the designed thermal conductivity of the silicon wire which is shown in Fig. 5.8.

The remnant problems in the current system are that the thermal conductivity of the heat links was lower than expected and the achieved temperature of the suspension system was higher than the target. Though properties of the heat link will not directly affect the cooling of TMs because no heat link is connected to TMs in Phase-III TOBA, the temperature of IM1 is determined by the thermal conductivity of the heat links.

The current cooling curve shows that the thermal conductivity of the heat links is lower than expected by 30$\sim$50 %. It is suspected that contact thermal resistance at the attachment point of the heat links degrades the conductivity,

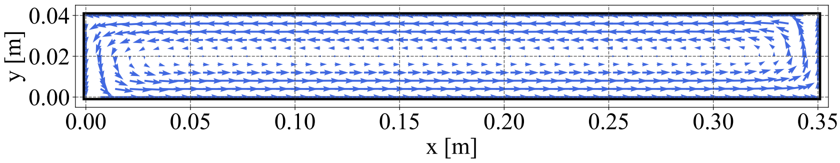

Figure 7.1: Distribution of induced eddy current in the bar.

because the amount of degradation is correlated to the number of heat links. As the thermal resistance of heat link is low, it is affected by the small contact resistance more. Currently the heat links are pressed to the components with M4 washers (ϕ10 mm). The contact area can be increased more to reduce the thermal resistance at the contact point.

The achieved temperature, 6.1 K, was slightly higher than 4 K, mainly because the temperature of the shield was higher than previously measured value by 1.5 K. The most possible heat source is the electrical lead wires connected between the vacuum chamber flange and the 2nd shield. By replacing the material of the wire from copper to phosphor bronze, the expected heat introduction can be suppressed by two orders of magnitude, so that the temperature rise will be below 20 mK. The heat generation of the coils for actuators on OB also contributed to the temperature of TM by 0.4 K, via the temperature rise at the heat link stage. This can be reduced by lowering the actuation force, which is required to compensate the angular drift of the pendulum. A cryogenic rotational stage should be implemented at the suspension point of TM to reduce the actuation force. Required rotational range is roughly 15 mrad, which corresponds to the observed drift during this experiment. Such rotational stages will also reduce the heat on TMs, which is generated by the induction current of the coils for the actuators.

7.2 Magnetic noise reduction

7.2.1 Origin of magnetic coupling

Coupling with magnetic field fluctuation was unexpectedly large in the current system. The origin of the dominant coupling path was identified to be the induced current in the bar because the temperature dependence of the coupling was quite well agreed with the electrical conductivity of the bar. Here, the coupling via the induced current is quantitatively evaluated. An analytical formula of induced current in a thin rectangular metal plate is given in the previous work [91]. Though our bars are not thin plates, here we adopt the formula to our case for an order estimation. The shape of the bar is simplified to be 350 × 40 × 10 mm plate, and external magnetic field $B(t) = B\cos(2\pi ft)$ is applied perpendicular to the plate. The distribution of the induced current derived from the analytical formula is shown in Fig. 7.1. The Joule heat from the induction current is 10^{-14} W for 10 nT amplitude of the magnetic field oscillating at 0.1 Hz, hence the heat is negligible in the cryogenic system. From the current distribution, the induced magnetic moment μ_i is calculated to be

$$\mu_{ind}(f) \sim 1 \times 10^{-6}\ \mathrm{A} \cdot \mathrm{m}^2 \times \left(\frac{f}{0.1\ Hz}\right)\left(\frac{B}{10^{-8}\ T}\right)\sin(2\pi f t). \tag{7.1}$$

This induced moment is then couples to the DC geomagnetic field, which is typically $B_{\mathrm{geo}} \sim 5 \times 10^{-5}$ T, then act as a torque $N = \mu_{ind} B_{\mathrm{geo}}$ on the bar. The fluctuation of environmental magnetic field induces the fluctuating magnetic moment, which turns to be fluctuating torque. Therefore the transfer from the magnetic field fluctuation to the rotational angle of the bar is given by

$$\begin{aligned} \frac{\tilde{\theta}}{\tilde{B}} &= \mu_{ind} B_{\mathrm{geo}} \tilde{\chi} \tilde{H}_{\mathrm{sh}} \\ &\sim 1 \times 10^{-2}\ \mathrm{A} \cdot \mathrm{m}^2 \cdot \mathrm{s} \times 2\pi f \tilde{\chi} \tilde{H}_{\mathrm{sh}}. \end{aligned} \tag{7.2}$$

Here $\tilde{\chi}$ and $\tilde{H}_{\mathrm{sh}}$ are the mechanical response of the pendulum and the magnetic shielding effect of the cryostat, respectively. By comparing this to Eq. (6.12), the estimated coupling coefficient μ_2 is 1×10^{-2} A $\cdot$ m^2 $\cdot$ s. The order of the estimated value corresponds to the measured coupling constant listed in Table. 6.5. Therefore the order of the measured magnetic coupling can be explained with the induced current in the bar.

The simplest way to reduce the magnetic noise is shielding the magnetic field fluctuation. This will be discussed in the next subsection. Another choice is to change the material of the pendulum to a non-conducting one. However, such a non-conducting pendulum will be suffered from electrostatic force from the surrounding staffs. Hence a careful design about electrostatic force noise should be considered in that case.

7.2.2 Magnetic shield

The magnetic noise level in the current system is about $2 \times 10^{-9}\ /\sqrt{\mathrm{Hz}}$ (see Fig. 6.15). To achieve the target sensitivity of Phase-III TOBA, magnetic shielding by at least six orders of magnitude is required. Such a shielding ratio is within a reach with recent technologies. For example, superconducting magnetic shield for neuromagnetic measurements recorded the shielding factor of 10^6 at 0.2 Hz [70]. It used a helmet-shaped high-T_c superconductor kept in liquid nitrogen. Since superconducting magnetic shielding is frequency-independent, it is suitable for our low-frequency purpose. Additionally, superconductor is compatible to our cryogenic systems; the magnetic shield can be installed on the wall of the cryostat. By improving the current shielding factor by 2 times or using additional shielding materials, the target of Phase-III TOBA is achievable. Of course careful design of the magnetic shield is required to achieve the target, it will be possible in principle.

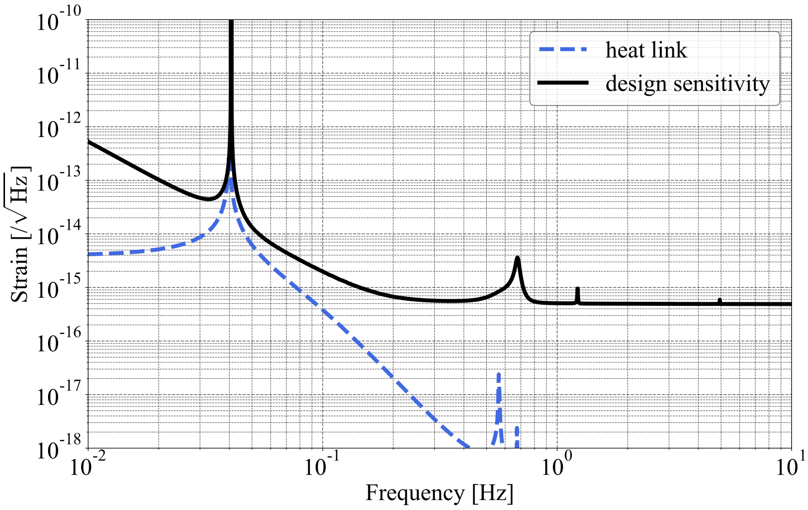

Figure 7.2: Estimated vibration introduced via heatlinks in phase-III TOBA.

7.3 Vibration noise via heat links

As shown in Fig. 6.22, large vibration noise is introduced via the heat links in the current system. Note that the contribution from the TM heat links in the current system does not matter in Phase-III TOBA since TMs are suspended by silicon wires without heat links. Therefore the main target to reduce is the contribution from the IM heat links.

There are several factors to reduce the vibration noise. The first one is the active vibration isolation system, which is designed to suppress the vibration of the ground by two orders of magnitude around 0.1 Hz. Since the heat links are attached to the heat link stage fixed to the vibration isolation stage, the induced vibration noise is reduced by two orders of magnitude. The second factor is the common mode rejection ratio (CMRR) between two TMs, which suppresses the induced IM vibration in the differential rotation of TMs. Though CMRR=0.1 is assumed in the current vibration noise estimation, the designed CMRR in Phase-III TOBA is 10^{-3}, which corresponds to 5 μHz difference of resonant frequencies. The adjustment of resonant frequency in this accuracy is already achieved by another torsion-bar detector, TorPeDO [49]. By combining these factors, the vibration noise is reduced sufficiently as shown in Fig. 7.2. The vibration noise via the heat links can be suppressed below the design sensitivity of Phase-III TOBA.

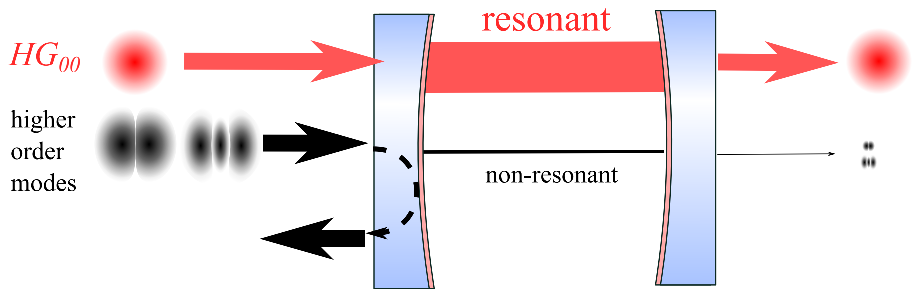

Figure 7.3: Principle of a mode cleaner cavity.

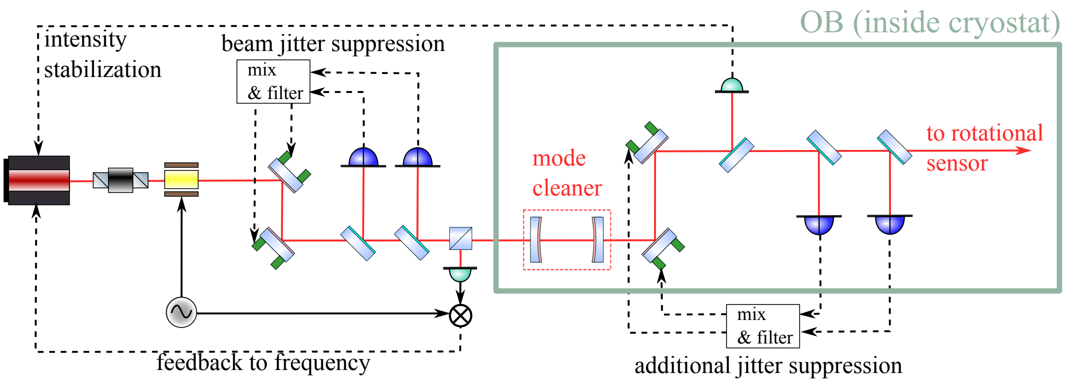

Figure 7.4: Improved beam jitter suppression scheme with a mode cleaner cavity.

7.4 Beam jitter reduction

Though the beam jitter was planned to be suppressed by control, contributions from the signal couplings at the QPDs were found to be remaining as the residual jitter noise after control. Such noise was quite large compared to the target sensitivity. It is required to reduce the signal coupling at the QPD or to suppress the original fluctuation of the incident beam. One of the possible origins of signal coupling is the mis-centering of the beam at the QPDs. In this case, the power fluctuation or beam expansion changes the power at each segment of QPD, then a fraction of the fluctuation couples to the beam displacement signal. Hence the fine tuning of the alignment can possibly reduce the signal coupling, so that reduce the noise level.

A possible way to suppress the original beam jitter is using a mode cleaner cavity on the optical bench. A mode cleaner is a transmissive optical cavity to filter out the higher order mode of the laser beam using the different transmissivity between the laser modes (see Appendix B). Its principle is shown in Fig. 7.3. By placing the mode cleaner at the entrance of the optical bench, beam jitter is largely suppressed.

The possible actual configuration is shown in Fig. 7.4. The incident beam jitter relative to the mode cleaner cavity is measured using RF signals of QPDs, which are acquired by modulating the input laser phase at an RF frequency ($\sim$10 MHz) and then demodulating the QPD signals at the modulation frequency. This is the same method as the PDH signal [87]. Such RF angular signals can sense the phase difference of the wave fronts between the reflected HG_{00} mode and the reflected HG_{10} mode. Since the relative phase between the reflected modes is measured, the beam jitter in the reflection beam of the mode cleaner can be cancelled. Using these signals, the input beam jitter is pre-stabilized before the mode cleaner cavity. Then the mode cleaner passively filters out the fluctuation of beam. The maximum contrast of the transmittance between a resonant mode and a non-resonant mode is given by $\mathcal{F}/2\pi$ for a critical-coupled cavity. Assuming the finesse of the mode cleaner to be 10000, incident jitter is suppressed by three orders of magnitude. Additionally, the wave front sensors for TMs can suppress the incident jitter modes relative to the angular signal as described in Appendix B.3.1. In our design of Phase-III TOBA, the contrast is 10^2. If the input beam jitter is stabilized by a factor of 10^4, the total jitter noise is suppressed by nine orders of magnitude, so that suppressed below 10^{-15} $/\sqrt{\mathrm{Hz}}$ at 0.1 Hz.

8 Conclusion

8.1 Conclusion

In this thesis, we have performed simulations on the earthquake detectability, and experimental work on the cryogenic system of Phase-III TOBA. The conclusions of these topics and the overall conclusion are described in this chapter.

Detectability of earthquakes using TOBA

First, we performed a computational investigation on the earthquake detectability using different types of gravity gradiometers and compared the results. The earthquake detectability using TOBA, which is sensitive only to the horizontal gravity strain, has been evaluated in this work for the first time. A comparison of the signal-to-noise ratio (SNR) distribution for each component of the gravity strain tensor showed that the horizontal strain components are essential for the detection of strike-slip earthquakes, while the vertical strain components are important for the detection of dip-slip earthquakes. Considering the realistic case that the coast is in the opposite direction to which a hanging wall moves, the SNRs for the horizontal and vertical components are similar for the dip-slip earthquakes at the region where the detectors can be placed. The detectable distance where SNR $= 8$ with the horizontal components is about 130 km at all azimuths for the strike-slip earthquakes, and 130 km at maximum, which is shorter at the other azimuths, for the dip-slip earthquakes. Thus, the horizontal components are sufficient for earthquake detection. Therefore, TOBA is considered to be a good choice as a detector for gravity-based EEW. Moreover, the required sensitivity of TOBA for EEW has also been confirmed to be $10^{-15}\ /\sqrt{\mathrm{Hz}}$ at 0.1 Hz, which is similar to the value reported in a previous study for vertical gravity strain measurement [2]. Although a detector that is sensitive to all gravity strain components such as SOGRO is always the best choice, the vertical strain measurement is not always indispensable.

Localizing simulations were also performed using an array of TOBAs to determine the type of detector system that should be constructed for a gravity-based EEW. The detector sensitivity was assumed to be $10^{-15}\ /\sqrt{\mathrm{Hz}} \times \frac{f^2+(0.1\ \mathrm{Hz})^2}{f^2}$, which is close to the design of Phase-III TOBA. A comparison of the localizability using different detector array arrangements suggests that three pairs of two TOBAs placed 75 km apart along a coast line would be suitable to localize off-shore earthquakes; localizability using fewer detectors was not uniformly good. In the localization process, information on the focal mechanism is important because it can be used to constrain the locations of the epicenters within 100 km^2 up to 120 km distances in 10 s; in the absence of this information, this area can increase by more than three times. As large earthquakes generally occur along the existing fault plane, the information on the focal mechanisms will usually be available in advance in actual cases. The required presumption accuracy to suppress the systematic localization error below 10 km is roughly 10°. However, the available accuracy for actual faults needs to be statistically investigated in a future work. For this level of of systematic localization error (<10 km), the calibration error of the detectors should also be below 3 %, which is not very difficult.

Thus these works have settled some of the requirements for Phase-III TOBA and EEW systems using TOBA. The detectability study has confirmed the required sensitivity, and the localizability study has clarified the suitable detector arrangement, the required calibration accuracy of each detector, and the necessary information regarding the focal mechanisms, which are important in constructing an actual gravity-based EEW system. Although there may be better localization schemes, the validity of at least one possible method has been confirmed by our work. Further investigations on topics such as the accuracy of presumed fault parameters, and the differences between the analytical model and the actual gravity gradient fluctuations, will further improve the concreteness of the detection scheme.

Development of the cryogenic system for Phase-III TOBA

We have created a design for Phase-III TOBA, including the cryogenic suspension system, optical system, and vibration isolation system, to achieve the required sensitivity of $10^{-15}\ /\sqrt{\mathrm{Hz}}$ at 0.1 Hz for meaningful earthquake detection. This is also an important technical demonstration before moving on to the larger scale (∼10 m), i.e., Final TOBA. In addition to the suppression of known noise sources, the designed system also suppresses the recently discovered nonlinear vibration transfer noise.

The main topic in this thesis is a cryogenic technique in a torsion pendulum, which is essential for TOBA to reduce the thermal noise. Experimental demonstrations were performed using a simplified configuration of Phase-III TOBA. The suspended pendulum was successfully cooled to 6.1 K, and the operation of the sensing system at the cryogenic temperatures was achieved. This is the first example of a large-scale cryogenic torsion pendulum, and hence, it is technically essential for Phase-III TOBA. The current system can be basically applied to Phase-III TOBA by replacing the suspension wire with a silicon wire. The achieved temperature could be further lowered by replacing the electrical lead wire on the shield, and by implementing a cryogenic rotational stage at the suspension point of the TM wire to reduce the actuator force on the TM. Additionally, the cooling speed could be improved by increasing the contact area of the heat links on the suspension masses.

The noise performance of the cryogenic torsion pendulum was also investigated using the developed prototype. Although the current sensitivity is not sufficient for the scientific observations, the noise injection measurement and component characterizations revealed some important information regarding the noise of the cryogenic torsion pendulum. The current setup already meets the temperature stability requirement ($< 5 \times 10^{-5}$ K/$\sqrt{\mathrm{Hz}}$; Fig. 6.20), and the vibration noise via the heat links can be sufficiently suppressed below 4×10^{-16} /$\sqrt{\mathrm{Hz}}$ at 0.1 Hz (Fig. 7.2) using the designed vibration isolation system and suspension parameter tuning in Phase-III TOBA. The most serious noise source relevant to the cryogenic technique is the coupling with the magnetic field fluctuation via the induction current in the bar, which significantly increases at cryogenic temperatures as the electrical conductivity increases; therefore, a magnetic shield must be installed in the cryostat to reduce this magnetic coupling. Additionally, the beam jitter noise, which is not specific to the cryogenic environment, must also be suppressed by using a mode cleaner cavity.

Thus, these experimental works have established the fundamental part of the cryogenic system in Phase-III TOBA and identified some problems in achieving the target sensitivity of Phase-III TOBA. However, to realize the design sensitivity of Phase-III TOBA, developments of components such as a high-quality silicon wire, active vibration isolation system, a highly sensitive angular sensor, and a magnetic shield are required, which can be integrated into the cryogenic system. The information gained from the prototype experiment in this work will help such future works.

Conclusion of the thesis

In summary, the theoretical works in this thesis have clarified that the measurement of horizontal gravity strain using TOBA could significantly contribute to earthquake detection. Then, Phase-III TOBA was designed to achieve the required sensitivity of 10^{-15} /$\sqrt{\mathrm{Hz}}$ for the gravity-based EEW. The cryogenic system, which is technically important, was experimentally demonstrated, and the basis of the cryogenic system for Phase-III TOBA was established. These works have opened a path towards the development of gravity-based EEW system using Phase-III TOBA.

8.2 Future prospects

Towards making future scientific observations using Phase-III TOBA or Final TOBA, the following developments are necessary in the experimental aspect.

For Phase-III TOBA, some of the problems were discussed in Chapter 7. Technical upgrades for the magnetic shield, the vibration isolation system, and optics are necessary to improve the current sensitivity. Another important component is the suspension wire for the test masses. To suppress the thermal noise below $10^{-15}\ /\sqrt{\mathrm{Hz}}$, a low-dissipation ($\phi_w < 10^{-8}$) silicon wire needs to be developed. As pointed out by the previous work [80], energy dissipation on the surface of the material will dominate the total loss angle. Therefore, surface treatment will be a key to achieving the required dissipation. Component research and development regarding the dissipation of silicon wires is required. By integrating these systems, the target sensitivity is expected to be achieved in principle. However, there may be unknown noise that is relevant to cryogenic temperatures, because no previous work has investigated the noise of a cryogenic torsion pendulum in detail. Therefore, the noise performance of the cryogenic TOBA needs to be characterized step-wise with gradually increasing sensitivities, in the future.

Research on the Newtonian noise is an essential step towards improving the sensitivity to $10^{-15}\ /\sqrt{\mathrm{Hz}}$ or below. When the instrumental noise is suppressed to $10^{-15}\ /\sqrt{\mathrm{Hz}}$, the Newtonian noise induced from the fluctuations of the ground or the atmosphere will be measurable, as estimated in Sec. 3.2.4. Using the measured Newtonian noise, the models of Newtonian noise will be examined at first, followed by a discussion and testing of the reduction method. To examine the noise models, it is necessary to place environmental monitors around the detector to measure the ground vibrations and the atmospheric temperature or pressure fluctuations. To verify the models, the gravity fluctuations are estimated from the environmental measurements and the noise models, and then compared with the TOBA signal. If the measured TOBA signal is successfully reproduced from the environmental monitors, noise subtraction will also be possible using the environmental measurements. Therefore, development of the environmental monitor system and establishing the noise models are important to achieve these goals; for the environmental monitor system development, the required number and arrangement of the sensors need to be discussed.

Further technical investigations are required towards achieving the design of Final TOBA. Although the principle noise sources such as quantum noise and thermal noise will be suppressed in the design of Final TOBA, as explained in Sec. 3.3, a concrete design of the system must be considered. For example, the cryogenic system in Phase-III TOBA will be insufficient for Final TOBA just by scaling up from 35 cm to 10 m. This is because the total heat of the 10 m-pendulum is much larger than the 35 cm-pendulum—by roughly 4×10^3

times, while the thermal conduction path of the suspension wire ($\propto$ (wire length)$^{-1}$) and the thermal radiation path from the surface ($\propto$ (surface area)) are not scaled up at the same ratio. Therefore, additional heat extraction path may be necessary for Final TOBA.

The selection of the observation site is also important for good sensitivity and stable operation. In terms of Newtonian noise, an underground site would be suitable to suppress some kind of the Newtonian noise, as indicated in Fig. 3.5. Other sources of gravity fluctuations such as the oceanic and the human activities, which are not included in Fig. 3.5, should also be estimated or characterized. The investigations on the Newtonian noise with Phase-III TOBA would provide valuable information for the actual site selection.

A Nonlinear Vibration Transfer in Torsion Pendulums

Nonlinear vibration transfer was recently found as a noise source in torsion pendulums. Though it is not so serious in usual experiments, it can be significant noise in precise measurement of environmental gravity gradient such as the targets of TOBA. That nonlinear noise can be simply derived from classical mechanics. Here the principle of the noise is introduced, and the amount of noise is calculated. The following calculations are reported in [22].

A.1 Derivation

A simple torsion pendulum as depicted in Fig. A.1 is assumed in the following calculation. The length of the suspension wire is l, and the vertical offset of the suspension point (SP) and the center of mass (CM) is h. The definition of coordinates is also shown in the figure. The translation of the CM and the rotation around the CM are (x, y, z) and $(\theta_P, \theta_R, \theta_Y)$, respectively, where P (Pitch), R (Roll) and Y (Yaw) denote the rotations around x, y and z axes as defined in Fig. A.1.

The Lagrangian and the dissipation function of the system are given by

$$\mathcal{L} = \frac{1}{2}m\left(\dot{x}^2 + \dot{y}^2\right) + \frac{1}{2}\vec{\omega}\cdot\boldsymbol{I}\vec{\omega} - mgz - \frac{1}{2}\kappa_w\theta_Y^2, \tag{A.1}$$

$$\mathcal{D} = \frac{1}{2}\Gamma_x\dot{x}^2 + \frac{1}{2}\Gamma_y\dot{y}^2 + \frac{1}{2}\Gamma_P\dot{\theta}_P{}^2 + \frac{1}{2}\Gamma_R\dot{\theta}_R{}^2 + \frac{1}{2}\Gamma_Y\dot{\theta}_Y{}^2, \tag{A.2}$$

where m and $\boldsymbol{I}$ are the mass and the inertia tensor of the bar, respectively. g is the gravitational acceleration, and κ_w is the torsional spring constant of the wire. $\vec{\omega} = (\dot{\theta_P}, \dot{\theta_R}, \dot{\theta_Y})$ is the angular velocity vector. Γ_α ($\alpha = x, y$,P, R, Y) are the damping coefficient for each DoF.

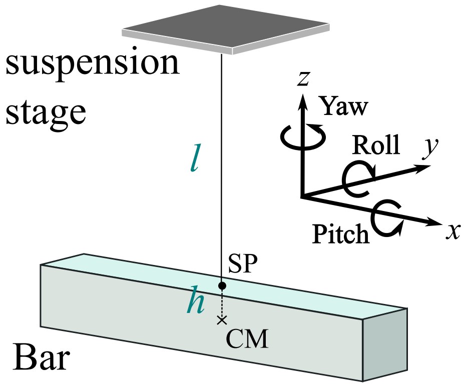

Figure A.1: A model of a simple torsion pendulum and definition of coordinates.

Under the seismic vibration x_g and y_g at the suspension stage, the bar's DoFs fluctuate in time. The inertia tensor is then time-dependent as

$$\boldsymbol{I}(t) = \begin{pmatrix} I_P & 0 & \theta_R(I_Y - I_P) \\ 0 & I_R & \theta_P(I_R - I_Y) \\ \theta_R(I_Y - I_P) & \theta_P(I_R - I_Y) & I_Y \end{pmatrix}, \tag{A.3}$$

where I_α (α =P, R, Y) are the moment of inertia around the principal axes. The vertical position of the CM is geometrically calculated to be

$$z = \frac{1}{2l}\left\{(x + h\theta_R + h\theta_P\theta_Y - x_g)^2 + (y - h\theta_P + h\theta_R\theta_Y - y_g)^2\right\} + \frac{1}{2}h\left({\theta_P}^2 + {\theta_R}^2\right). \tag{A.4}$$

The non-diagonal parts in Eq. (A.3) and the terms of θ_Y in Eq. (A.4) are the source of nonlinear transfer.

The Euler-Lagrange equation for the horizontal rotation θ_Y is

$$\kappa_Y\theta_Y + I_Y\ddot{\theta}_Y = -(I_R - I_Y)\theta_P\ddot{\theta}_R - (I_Y - I_P)\ddot{\theta}_P\theta_R + (I_P - I_R)\dot{\theta}_P\dot{\theta}_R - mh(\ddot{x}\theta_P + \ddot{y}\theta_R). \tag{A.5}$$

The Fourier spectrum $\tilde{\theta}_Y$ is then given by

$$\begin{aligned} \tilde{\theta}_Y \quad = \quad & \frac{1}{\kappa_Y - I_Y\omega^2}\Big[(I_R - I_Y)\tilde{\theta}_P * \left(\omega^2\tilde{\theta}_R\right) + (I_Y - I_P)\left(\omega^2\tilde{\theta}_P\right) * \tilde{\theta}_R \\ & -(I_P - I_R)\left(\omega\tilde{\theta}_P\right) * \left(\omega\tilde{\theta}_R\right) + mh\left\{\left(\omega^2\tilde{x}\right) * \tilde{\theta}_P + \left(\omega^2\tilde{y}\right) * \tilde{\theta}_R\right\}\Big]. \end{aligned} \tag{A.6}$$

Here "$*$" denotes a frequency convolution between two Fourier spectrums.[1] The nonlinearly introduced horizontal rotation is determined by the vibration of two DoFs out of x, y, θ_P and θ_R. By the definition of frequency convolution,

[1] $(F * G)(f) = \int_{-\infty}^{\infty} F(x)G(f - x)dx \qquad (F(f), G(f)$: functions)

large vibration at the resonance of each DoF is down-converted to be low-frequency noise; e.g. $\tilde{x}$(1 Hz) and $\tilde{\theta_P}$(1.1 Hz) are convolved to be $\tilde{\theta_Y}$(0.1 Hz).

x, y, θ_P and θ_R are also derived from Eq. (A.1). The Euler-Lagrange equations for them are

$$\begin{aligned}
m\ddot{x} &= -\frac{mg}{l}\left(x + h\theta_R - x_g\right) - \Gamma_x \dot{x}, && \text{(A.7)}\\
m\ddot{y} &= -\frac{mg}{l}\left(y - h\theta_P - y_g\right) - \Gamma_y \dot{y}, && \text{(A.8)}\\
I_P\ddot{\theta}_P &= \frac{mgh}{l}\left(y - h\theta_P - y_g\right) - mgh\theta_P - \Gamma_P \dot{\theta}_P, && \text{(A.9)}\\
I_R\ddot{\theta}_R &= -\frac{mgh}{l}\left(x + h\theta_R - x_g\right) - mgh\theta_R - \Gamma_R \dot{\theta}_R, && \text{(A.10)}
\end{aligned}$$

where x_g and y_g are the translational seismic vibrations. Then the Fourier spectrums for them are given by

$$\begin{aligned}
\tilde{x} &\simeq \frac{{f_x}^2}{{f_x}^2 + i\frac{f_x}{Q_x} f - f^2}\tilde{x}_g, && \text{(A.11)}\\
\tilde{y} &\simeq \frac{{f_y}^2}{{f_y}^2 + i\frac{f_y}{Q_y} f - f^2}\tilde{y}_g, && \text{(A.12)}\\
\tilde{\theta}_P &\simeq \frac{4\pi^2 {f_y}^2 {f_P}^2 f^2}{g\left({f_y}^2 + i\frac{f_y}{Q_y} f - f^2\right)\left({f_P}^2 + i\frac{f_P}{Q_P} f - f^2\right)}\tilde{y}_g, && \text{(A.13)}\\
\tilde{\theta}_R &\simeq -\frac{4\pi^2 {f_x}^2 {f_R}^2 f^2}{g\left({f_x}^2 + i\frac{f_x}{Q_x} f - f^2\right)\left({f_R}^2 + i\frac{f_R}{Q_R} f - f^2\right)}\tilde{x}_g, && \text{(A.14)}
\end{aligned}$$

where f_α and Q_α are the resonant frequencies and Q values for each DoF, respectively. The resonant frequencies are given by

$$f_x \simeq f_y \simeq \frac{1}{2\pi}\sqrt{\frac{g}{l+h}}, \qquad f_P \simeq \frac{1}{2\pi}\sqrt{\frac{mgh}{I_P}}, \quad \text{and} \quad f_R \simeq \frac{1}{2\pi}\sqrt{\frac{mgh}{I_R}}. \qquad \text{(A.15)}$$

The Q values are determined by the damping coefficients.

A.2 Calculation

The nonlinear noise can be calculated by using Eq. (A.6) and (A.11)–(A.14). Here some calculation results are shown as examples. The parameters for the calculation are listed in Table A.1, which are the similar order as Phase-III TOBA. For the seismic vibration, assumed spectrums are show in Fig. A.2. The red line is the measured vibration in Tokyo and the green line shows the model spectrum. The introduced x, y, θ_P and θ_R motions in case of the model seismic vibration is shown in Fig. A.3. To demonstrate the effect from the resonant peaks ($\sim$1 Hz), vibration isolation around 1 Hz as the blue line is tested.

Table A.1: The parameters used for the calculation.

Parameter		Symbol	Value	Unit
mass		m	1.0	kg
moment of inertia	(Pitch)	I_P	0.23×10^{-3}	kg·m^2
	(Roll)	I_R	7.64×10^{-3}	kg·m^2
	(Yaw)	I_Y	7.58×10^{-3}	kg·m^2
length of wire		l	0.3	m
suspension point height		h	0.005	m
Q values		Q_x, Q_y, Q_P, Q_R	10^3	-
resonant frequency	x	f_x	0.912	Hz
	y	f_y	0.901	Hz
	Pitch	f_P	2.469	Hz
	Roll	f_R	0.405	Hz

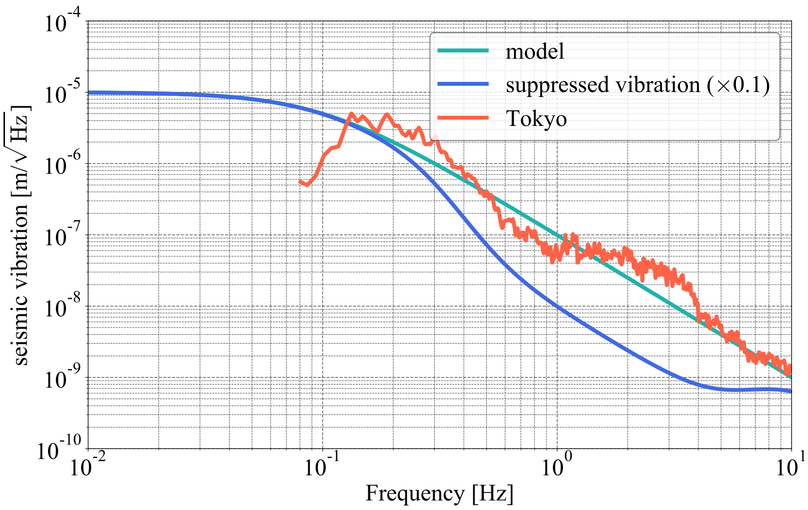

Figure A.2: Amplitude spectral densities of seismic vibration. A model (green) and the measured one in Tokyo (red). The blue line shows the case when the seismic vibration is suppressed by 10 times around 1 Hz.

The calculated nonlinear vibration noise spectrums are shown in Fig. A.4. For the model seismic vibration, the nonlinear noise is about 10^{-9} rad/$\sqrt{\text{Hz}}$ at 0.1 Hz, which is higher than the target sensitivity of Phase-III TOBA by more than 6 orders of magnitude. Though the parameters are different from Phase-III TOBA, the similar amount of noise can appear in Phase-III TOBA. Therefore reducing this noise is essential for realization of scientific observations with Phase-III TOBA.

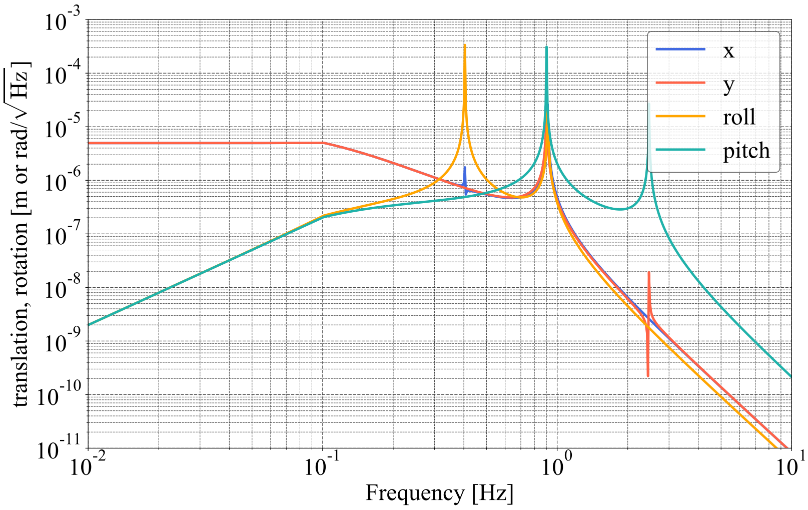

Figure A.3: Translations and rotations of the bar under the model seismic vibration.

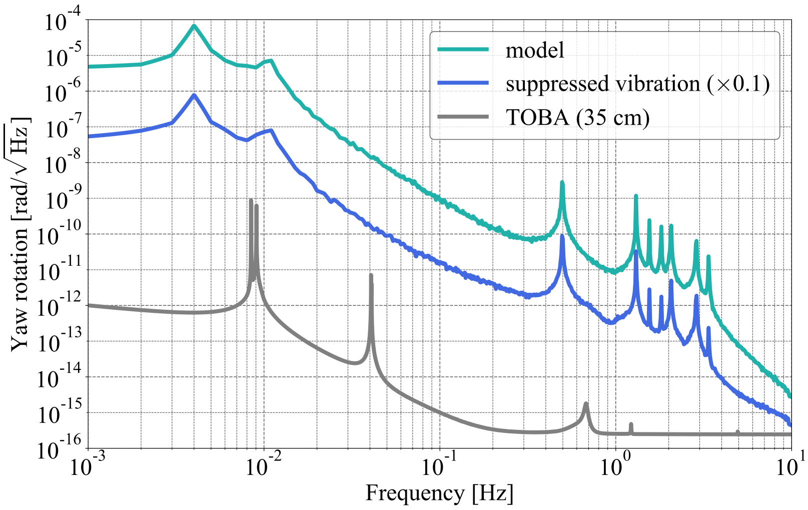

Figure A.4: Calculated nonlinear vibration noise spectrums for the model seismic vibration (green) and for the suppressed vibration by 10 times around 1 Hz (blue). The grey line shows the target sensitivity of Phase-III TOBA.

A promising way to reduce the noise is suppression of vibration at the suspension stage. When the vibration is suppressed by around 1 Hz, which is close to the resonant frequencies, the nonlinear noise is reduced at every frequency as shown with the blue line in Fig. A.4. Thus the total noise level is determined by the contribution from the resonant peaks convolved with nearby frequencies. Suppression of vibration by 10 times results in nonlinear noise reduction by 10^2 times. This is because the amount of introduced θ_Y is the product of two DoFs. Therefore vibration isolation by three orders of magnitude is required to achieve the target sensitivity of Phase-III TOBA. The requirement on the active vibration isolation system in Phase-III TOBA (see Sec. 5.2.5) is determined mainly for this reason. Dependence on the other parameters are discussed in the next section.

A.3 Approximation to analytical expression

To discuss the parameter dependence of the nonlinear vibration noise, an analytical expression of the nonlinear vibration spectrum is derived by applying some approximations to Eq. (A.6). As Eq. (A.15) indicates, f_x and f_y has almost same value. Hence the convolution between $f = f_x$ of x, θ_R and $f = f_y$ of y, θ_P has dominant contribution in the total nonlinear noise. Especially $(\omega^2\tilde{x}) * \tilde{\theta}_P$ term has the largest contributions since $\tilde{\theta}_P$ is highest as shown in Fig. A.3.

Around f_x and f_y, $\tilde{x}$ and $\tilde{\theta}_P$ are approximated to

$$\tilde{x}(f) \simeq \frac{{f_x}^2}{{f_x}^2 + i\frac{f_x}{Q_x}f - f^2}\left(\frac{1\text{Hz}}{f}\right)^2 \tilde{x}_g(1\text{Hz}), \tag{A.16}$$

$$\tilde{\theta}_P(f) \simeq \frac{4\pi^2 {f_y}^2 f^2}{g\left({f_y}^2 + i\frac{f_y}{Q_y}f - f^2\right)}\left(\frac{1\text{Hz}}{f}\right)^2 \tilde{y}_g(1\text{Hz}). \tag{A.17}$$

Here we assume the seismic vibration $\tilde{x}_g$ and $\tilde{y}_g$ have the same amplitude spectral density $\sqrt{G_{\text{seis}}(f)}$ with independent random phase. The Fourier spectrum $\tilde{x}_g$, $\tilde{y}_g$ are related to the spectral density $\sqrt{G_{\text{seis}}(f)}$ as

$$\tilde{x}_g(f) = \sqrt{\frac{T}{8\pi^2}}\sqrt{G_{\text{seis}}(f)}e^{i\theta_x(f)}, \quad \tilde{y}_g(f) = \sqrt{\frac{T}{8\pi^2}}\sqrt{G_{\text{seis}}(f)}e^{i\theta_y(f)}, \tag{A.18}$$

where $\theta_x(f)$ and $\theta_y(f)$ are the random phases, and T is the length of the timeseries. The convolution $(\omega^2\tilde{x})*\tilde{\theta}_P$ can be approximated by the contribution from the integral around $f_0 \equiv (f_x + f_y)/2$ as

$$\begin{aligned}
&\left(\omega^2\tilde{x}\right) * \tilde{\theta}_P(f) \\
&\quad = \frac{(2\pi)^4(1\,\text{Hz})^4}{g}\frac{T}{8\pi^2}G_{\text{seis}}(1\,\text{Hz}) \times \\
&\qquad \int_{f_0-\Delta f}^{f_0+\Delta f} \frac{{f_x}^2}{{f_x}^2 + i\frac{f_x}{Q_x}(f-\alpha) - (f-\alpha)^2}\frac{{f_y}^2}{{f_y}^2 + i\frac{f_y}{Q_y}\alpha - \alpha^2}e^{i(\theta_x(f-\alpha)+\theta_y(\alpha))}d\alpha,
\end{aligned} \tag{A.19}$$

where Δf is the frequency range of integral. The integral range can be extended to $[0, \infty]$ since the integral function has small value outside $[f_0 - \Delta f, f_0 + \Delta f]$. Moreover, due to the randomness of the phase $\theta_x(f-\alpha) + \theta_y(\alpha)$, the integral has a shape of Fourier transform of $A_f(\alpha)e^{i\theta(\alpha)}$, where

$$\begin{aligned} A_f(\alpha) &\equiv \frac{{f_x}^2}{{f_x}^2 + i\frac{f_x}{Q_x}(f-\alpha) - (f-\alpha)^2} \frac{{f_y}^2}{{f_y}^2 + i\frac{f_y}{Q_y}\alpha - \alpha^2}, && \text{(A.20)} \\ \theta(\alpha) &= \theta_x(f-\alpha) + \theta_y(\alpha) - \alpha t. && \text{(A.21)} \end{aligned}$$

$\theta(\alpha)$ is also a random phase. Then $(\omega^2\tilde{x}) * \tilde{\theta}_P$ has a mean power of

$$\left\langle \left| \left(\omega^2 \tilde{x}\right) * \tilde{\theta}_{\mathrm{P}}(f) \right|^2 \right\rangle = \left(\frac{(2\pi \times 1\,\mathrm{Hz})^4}{g} \frac{T}{8\pi^2} G_{\mathrm{seis}}(1\,\mathrm{Hz}) \right)^2 \left\langle \left| \mathcal{F}.\mathcal{T}.\left[A_f(\alpha) e^{i\theta(\alpha)} \right] \right|^2 \right\rangle.$$

Here the $\langle \cdot \rangle$ in the right hand term is the power of the timeseries $\left| \mathcal{F}.\mathcal{T}.\left[A_f(\alpha) e^{i\theta(\alpha)} \right] \right|$. Hence it is identical to an integral of the corresponding power spectrum as

$$\begin{aligned} &\left\langle \left| \mathcal{F}.\mathcal{T}.\left[A_f(\alpha) e^{i\theta(\alpha)} \right] \right|^2 \right\rangle \\ &\quad = \int_0^\infty \frac{8\pi^2}{T} \left| A_f(\alpha) e^{i\theta(\alpha)} \right|^2 d\alpha \\ &\quad = \frac{8\pi^2}{T} \int_0^\infty \frac{{f_x}^4 {f_y}^4}{\left| {f_x}^2 + i\frac{f_x}{Q_x}(f-\alpha) - (f-\alpha)^2 \right|^2 \left| {f_y}^2 + i\frac{f_y}{Q_y}\alpha - \alpha^2 \right|^2} d\alpha \\ &\quad \approx \frac{8\pi^2}{T} \frac{\pi Q {f_0}^5}{(f - |f_x - f_y|)^2} \left(\frac{1}{(f-2f_0)^2} + \frac{1}{(f+2f_0)^2} \right). \qquad \text{(A.22)} \end{aligned}$$

Here $Q \equiv Q_x = Q_y \gg 1$ and $|f_x - f_y| \ll f_0$ are assumed for simplicity. Therefore the amplitude spectral density of $(\omega^2\tilde{x}) * \tilde{\theta}_P$ is obtained from Eq. (A.22) and (A.22) as

$$\begin{aligned} \sqrt{G_{(\omega^2\tilde{x})*\tilde{\theta}_{\mathrm{P}}}(f)} &= \sqrt{\frac{8\pi^2}{T} \left\langle \left| (\omega^2\tilde{x}) * \tilde{\theta}_{\mathrm{P}}(f) \right|^2 \right\rangle} \\ &= \frac{(2\pi \times 1\,\mathrm{Hz})^4}{g} G_{\mathrm{seis}}(1\,\mathrm{Hz}) \sqrt{\frac{\pi Q {f_0}^5}{(f - |f_x - f_y|)^2} \left(\frac{1}{(f-2f_0)^2} + \frac{1}{(f+2f_0)^2} \right)}. \end{aligned} \qquad \text{(A.23)}$$

By multiplying $mh/|\kappa_Y - I_Y\omega^2|$, this gives an approximated formula of non-linear vibration noise (Eq. (A.6)).

Fig. A.5 compares the noise level calculated from Eq. (A.6) and the one approximated by Eq. (A.23). The approximated formula agrees well to the calculation below 0.2 Hz. Above 0.2 Hz, the convolutions between different combinations of the resonant peaks has larger contributions.

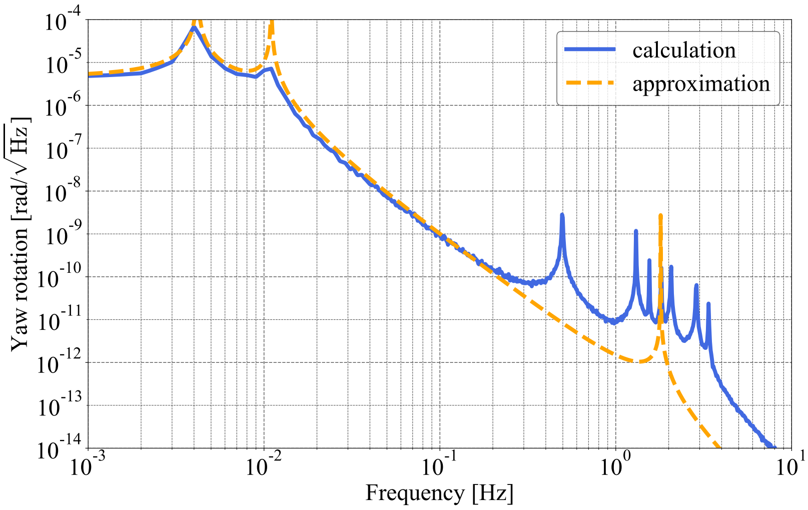

Figure A.5: Comparison between calculation and approximation Eq. (A.23).

Dependence on pendulum parameters

Eq. (A.23) shows clear dependences on G_{seis}, Q and f_0. The dependence on the seismic vibration G_{seis} is already discussed in the previous section. For the pendulum parameters, smaller Q and f_0 give lower noise levels. The damping of pendulum's translations or Pitch/Roll rotations directly affects the noise level in the torsion pendulums, while they are not the target DoFs. Note that to implement the strong damping to the pendulum, a careful mechanical design is essential to avoid the damping of Yaw rotation, which introduce the thermal noise in the main observation DoF. Using longer suspension wire to decrease the resonant frequency is also effective to suppress the nonlinear noise. However, we cannot expect sufficient noise suppression in this way since the length of the wire cannot be changed so much considering the realistic implementation. Thus, though the nonlinear noise can be suppressed by modifying the pendulum parameters, reducing the vibration of the suspension stage is more effective and essential.

B Wavefront Sensing with Coherent Angular Signal Amplification

In this appendix, the principle of the new angular sensor for TOBA is explained. The proposed method is to amplify the angular signal with an optical cavity. An optical cavity can amplify the incident electrical field when it meets the resonant condition. Then tilt of the cavity mirror converts the mode of resonating laser to the higher order mode. Though the converted higher order mode does not resonate in an ordinal cavity, some modification of the cavity enables the resonance of higher order modes, so that the angular signal is amplified. Such an idea is explained here. Detailed calculations of noise spectrum which is plotted in Chapter 5 are also shown here.

B.1 Principle

B.1.1 Gaussian beam

Spacial modes of a laser beam can generally be expanded with Hermite-Gaussian (HG) modes. Derivation of the HG modes is described in standard textbooks about lasers (see e.g. [92]). The electric field $E(\boldsymbol{x}, t)$ of a laser beam propagating along z-axis is expressed as

$$
\begin{aligned}
E(\boldsymbol{x},t) &= \sum_{l,m} E_{lm} U_{lm}(\boldsymbol{x},t), && \text{(B.1)}\\
U_{lm}(\boldsymbol{x}) &= \sqrt{\frac{1}{\pi 2^{l+m-1} l! m!}} \frac{1}{w(z)} H_l\left(\frac{\sqrt{2}x}{w(z)}\right) H_m\left(\frac{\sqrt{2}y}{w(z)}\right) \times \\
&\quad \exp\left(i(\omega_0 t - kz) - ik\frac{x^2+y^2}{2R(z)} + i(l+m+1)\zeta(z) - \frac{x^2+y^2}{w^2(z)}\right), && \text{(B.2)}
\end{aligned}
$$

where

$$
\begin{aligned}
z_R &= \frac{\pi w_0^2}{\lambda} \quad \text{(Rayleigh range)}, && \text{(B.3)}\\
w(z) &= w_0\sqrt{1+\left(\frac{z}{z_R}\right)^2} \quad \text{(beam radius)}, && \text{(B.4)}\\
R(z) &= z\left(1+\left(\frac{z_R}{z}\right)^2\right) \quad \text{(radius of curvature)}, && \text{(B.5)}\\
\zeta(z) &= \arctan\left(\frac{z}{z_R}\right) \quad \text{(Gouy phase)}. && \text{(B.6)}
\end{aligned}
$$

w_0 is the beam radius at the beam waist, where the radius is minimum. λ is the wavelength and $k = 2\pi/\lambda$ is the wave number. $H_l(x)$ is the Hermite polynomials, which are

$$H_1(x) = 1, \quad H_2(x) = 2x, \quad H_2(x) = 4x^2 - 2, \text{ ...} \qquad \text{(B.7)}$$

U_{lm} is called HG_{lm} mode. As Eq. (B.2) shows, the phase of the higher order mode differs from the fundamental mode U_{00} by $(l+m)\zeta$.

According to the recursion formula of the Hermite polynomials, U_{lm} converts

$$
\begin{aligned}
xU_{00} &= \frac{w(z)}{2} e^{-i\zeta(z)} U_{10}, && \text{(B.8)}\\
xU_{10} &= \frac{w(z)}{2} e^{i\zeta(z)} U_{00} + \frac{w(z)}{\sqrt{2}} e^{-i\zeta(z)} U_{20}, && \text{(B.9)}
\end{aligned}
$$

and so on.

B.1.2 Conversion of spacial modes by reflection

When the wavefront of the laser beam and the surface profile of the mirror is not identical, reflected beam has different expansion coefficients E_{lm} from the original beam. Here only HG_{00} mode and HG_{10} mode are taken into account for simplicity. As the simplest case, reflection at the beam waist on a tilted flat mirror as depicted in Fig. B.1 is considered. The origin of coordinate

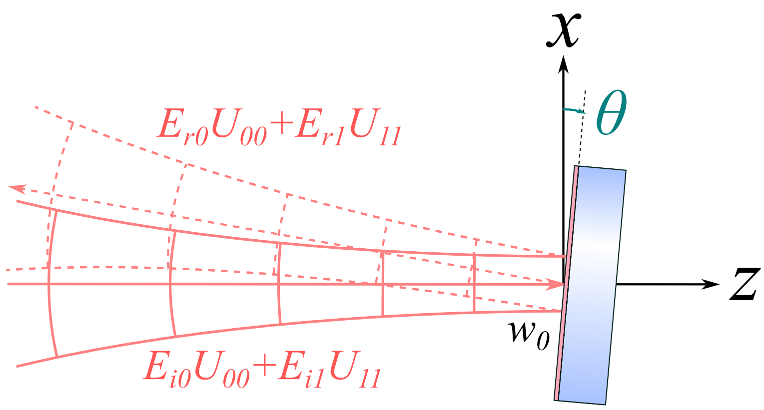

Figure B.1: Reflection of laser beam by a tilted mirror.

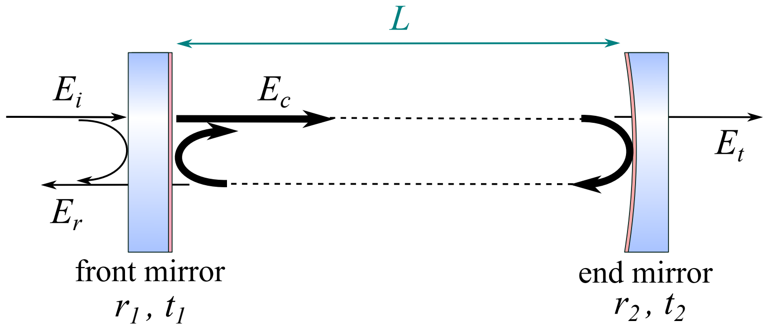

Figure B.2: An optical cavity

is set at the mirror surface, hence $w(0) = w_0$. When the mirror is tilted by $\theta \ll 1$ around the y-axis, the reflection induces phase delay of $2kx\theta$. Then the reflected beam is

$$E_r(x, y, 0, t) = E_i(x, y, 0, t) \exp(2ikx\theta) \simeq E_i(x, y, 0, t)(1 + 2ikx\theta) . \tag{B.10}$$

From Eq. (B.8) and (B.9), the expansion coefficients of E_i and E_r are converted as

$$\begin{pmatrix} E_{r0} \\ E_{r1} \end{pmatrix} \simeq \begin{pmatrix} 1 & ikw_0\theta \\ ikw_0\theta & 1 \end{pmatrix} \begin{pmatrix} E_{i0} \\ E_{i1} \end{pmatrix} . \tag{B.11}$$

HG_{10} mode is generated from HG_{00} mode in proportional to the tilt angle θ and the beam radius w_0.

B.1.3 Coherent angular signal amplification with an optical cavity

Overview of an optical cavity

An overview of an optical cavity is introduced. An optical cavity, or Fabry-Perot cavity consists of a pair of facing mirrors as Fig. B.2. Here incident

HG_{00} mode beam which has an amplitude of E_i is considered. The wavefront of the laser beam is assumed to be identical to the mirror surface. Letting r_1, t_1, r_2, t_2 as the amplitude reflectivity and transmissivity of the front mirror and the end mirror. L is the cavity length as shown in Fig. B.2. In the following discussions, loss or absorption of the cavity is ignored for simplicity, hence $t^2 + r^2 = 1$ is assumed. The reflection field E_r, the intra-cavity field E_c, and transmission field E_t can be written as

$$\begin{aligned} E_r &= -r_1 E_i + t_1 r_2 e^{i\phi_c} E_c, && \text{(B.12)} \\ E_c &= t_1 E_i + r_1 r_2 e^{i\phi_c} E_c, && \text{(B.13)} \\ E_t &= t_2 e^{i\phi_c/2} E_c, && \text{(B.14)} \\ \phi_c &= -\frac{4\pi L}{\lambda} + \zeta_c, && \text{(B.15)} \end{aligned}$$

where ζ_c is the round-trip Gouy phase of the cavity. Then they can be calculated to

$$\begin{aligned} E_r &= \left(-r_1 + \frac{t_1^2 r_2 e^{i\phi_c}}{1 - r_1 r_2 e^{i\phi_c}} \right) E_i, && \text{(B.16)} \\ E_c &= \frac{t_1}{1 - r_1 r_2 e^{i\phi_c}} E_i, && \text{(B.17)} \\ E_t &= \frac{t_1 t_2 e^{i\phi_c/2}}{1 - r_1 r_2 e^{i\phi_c}} E_i. && \text{(B.18)} \\ & && \text{(B.19)} \end{aligned}$$

When the mirrors have high reflectivity, $r_1 \simeq 1$ and $r_2 \simeq 1$, E_c is amplified under the condition of $\phi_c = 2\pi n$ (n : integer). This amplification is called "resonance" of the cavity, which is characterized by the finesse of the cavity defined as

$$\mathcal{F} \equiv \frac{\pi\sqrt{r_1 r_2}}{1 - r_1 r_2}. \qquad \text{(B.20)}$$

Using $\mathcal{F}$, the intra-cavity field can be approximated to

$$E_c \simeq \frac{t_1}{1 - (1 - \pi/\mathcal{F}) e^{i\phi_c}} E_i. \qquad \text{(B.21)}$$

$\mathcal{F}$ determines the maximum amplification factor and the sharpness of the resonance condition.

HG_{10} mode in a cavity

When one of the mirrors is tilted by θ, reflection at the mirror converts the modes as shown in Eq. (B.11). Here the behavior of HG_{10} mode generated inside the cavity by a tilted mirror as Fig. B.3 is investigated. The problem can be solved by replacing the field E_i, E_c, E_r and E_t with the corresponding vectors of the mode coefficients as used in Eq. (B.11). Taking into account the

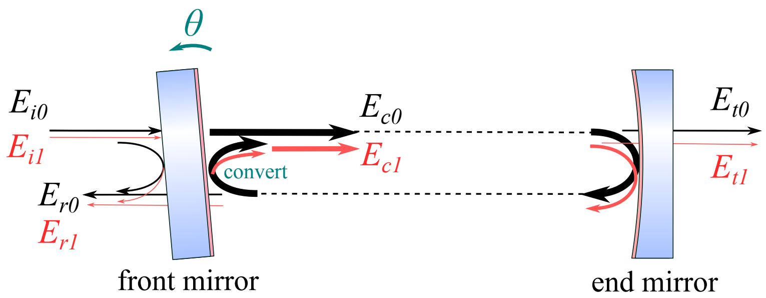

Figure B.3: An optical cavity with a tilted mirror.

Gouy phase difference between HG_{00} and HG_{10}, and the conversion between the modes (Eq. (B.11)), the equation for the intra-cavity mode coefficients is given by

$$\begin{pmatrix} E_{c0} \\ E_{c1} \end{pmatrix} = t_1 \begin{pmatrix} E_{i0} \\ E_{i1} \end{pmatrix} + r_1 r_2 \begin{pmatrix} 1 & ikw_0\theta \\ ikw_0\theta & 1 \end{pmatrix} \begin{pmatrix} e^{i\phi_c} & 0 \\ 0 & e^{i(\phi_c+\zeta_c)} \end{pmatrix} \begin{pmatrix} E_{c0} \\ E_{c1} \end{pmatrix}. \tag{B.22}$$

When the incident field contains only HG_{00} mode, i.e. $E_{i1} = 0$, the solution for E_{c0} is

$$E_{c0} = \frac{t_1(1 - r_1 r_2 e^{i(\phi_c+\zeta_c)})}{(1 - r_1 r_2 e^{i\phi_c})(1 - r_1 r_2 e^{i(\phi_c+\zeta_c)}) + (r_1 r_2 k w_0)^2 e^{i(2\phi_c+\zeta_c)}\theta^2} E_{i0} \tag{B.23}$$

$$\simeq \frac{t_1}{1 - r_1 r_2 e^{i\phi_c}} E_{i0}, \tag{B.24}$$

which corresponds to Eq. (B.17), and for E_{c1} is

$$E_{c1} = \frac{-it_1 r_1 r_2 k w_0 e^{i\phi_c}\theta}{(1 - r_1 r_2 e^{i\phi_c})(1 - r_1 r_2 e^{i(\phi_c+\zeta_c)}) + (r_1 r_2 k w_0)^2 e^{i(2\phi_c+\zeta_c)}\theta^2} E_{i0} \tag{B.25}$$

$$\simeq \frac{-it_1 r_1 r_2 k w_0 e^{i\phi_c}\theta}{(1 - r_1 r_2 e^{i\phi_c})(1 - r_1 r_2 e^{i(\phi_c+\zeta_c)})} E_{i0}. \tag{B.26}$$

As indicated in Eq. (B.11), HG_{10} mode is generated inside the cavity in proportional to θ and w_0. E_{c1} contains double amplification factor $(1-r_1 r_2 e^{i\phi_c})^{-1}$ and $(1 - r_1 r_2 e^{i(\phi_c+\zeta_c)})^{-1}$. The first amplification $(1 - r_1 r_2 e^{i\phi_c})^{-1}$ is because of the amplification in E_{c0}, which is converted into E_{c1}. The second amplification $(1 - r_1 r_2 e^{i(\phi_c+\zeta_c)})^{-1}$ is the effect of the cavity on the HG_{10} mode. When the phase satisfies $\phi_c + \zeta_c = 2\pi n$ (n : integer), the HG_{10} modes generated by reflection in each round-trip are coherently stacked and amplified. This is the basic principle of the coherent amplification of angular signal.

In a normal linear cavity, however, the two resonance conditions $\phi_c = 2\pi n$ and $\phi_c + \zeta_c = 2\pi m$ (n, m : integer) are difficult to satisfy at the same time. This is because of the Gouy phase difference ζ_c between HG_{00} and HG_{10} mode. As defined by Eq. (B.6), the Gouy phase takes a value from $-\pi/2$ to $\pi/2$.

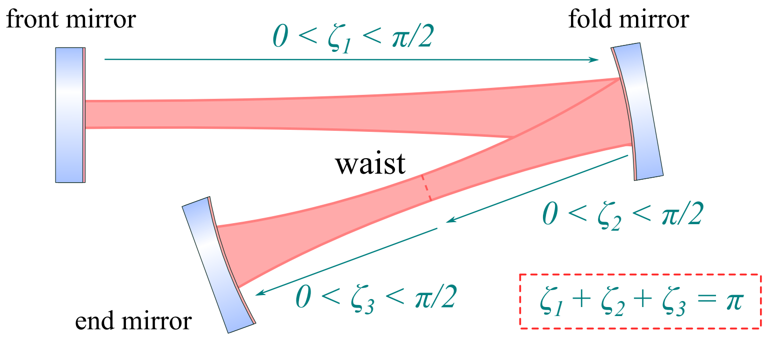

Figure B.4: A folded cavity configuration for angular signal amplification.

Hence the Gouy phase difference between two points along the laser beam can take a value between 0 and π, therefore the round-trip Gouy phase delay inside the cavity is $0 < \zeta_c < 2\pi$. This indicates that when $\phi_c = 2\pi n$, then $\phi_c + \zeta_c \neq 2\pi m$. Though it is possible to set ζ_c very close to 0 or 2π, it needs a kind of extreme configuration such as two flat mirrors at very close distance or two spherical mirrors at very long distance. Thus some modifications of the cavity configuration are required to coherently amplify the angular signal E_{c1}.

B.1.4 Configurations for coherent angular signal amplification

Here two possible configurations which can amplify the HG_{10} mode inside the cavity are proposed.

Folded cavity configuration

The simpler way is to fold the beam with a curved mirror as Fig. B.4 to make another beam waist inside the cavity. The Gouy phase delays from the waists to the mirrors, ζ_1, ζ_2 and ζ_3, can take a value between 0 and $\pi/2$, hence it is possible to set the sum of them to π by choosing a proper geometry of the cavity. In this case the round-trip Gouy phase is $\zeta_c = 2(\zeta_1 + \zeta_2 + \zeta_3) = 2\pi$, then the angular signal (Eq. (B.25)) is amplified.

Coupled cavity configuration

Another possible way is to replace the second mirror of the cavity with a cavity as shown in Fig. B.5. The additional cavity, or the auxiliary cavity, has different reflection phase for HG_{00} and HG_{10} modes. This is because the reflected field Eq. (B.16) depends on the round-trip phase inside the cavity, which differs for HG_{00} and HG_{10} by ζ_c. The reflection phase difference ϕ_a is added to the second factor of the denominator in Eq. (B.25). By adjusting ϕ_a to compensate the Gouy phase delay, the resonance conditions for HG_{00} and

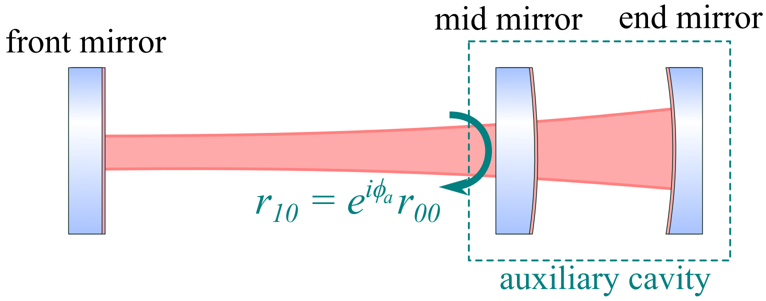

Figure B.5: A coupled cavity configuration for angular signal amplification. The reflectivity for HG_{10} mode r_{10} differs from that of HG_{00} mode r_{00}.

HG_{10} modes can be satisfied at the same time as $\phi_c = 2\pi n$ and $\phi_c + \zeta_c + \phi_a = 2\pi m$ (n, m : integer). ϕ_a can be changed by detuning the auxiliary cavity.

B.1.5 Measurement of HG_{10} mode

It can be derived that

$$U_{00}(x, y, z) + aU_{10}(x, y, z) = U_{00}(x + aw(z), y, z) \tag{B.27}$$

which means that the real part of HG_{10} mode displaces the center of HG_{00} mode. Therefore a beam position sensor such as a QPD (quadrant photo diode) can measure the HG_{10} mode amplitude through the beat with the HG_{00} mode. In the similar way, the imaginary part of HG_{10} mode tilts the wavefront of the HG_{00} mode. Tilt of the wavefront, or the difference of phase delays at $+x$ and $-x$, can be measured by modulating the input laser phase and demodulating the QPD signals.

B.2 Fundamental noise sources

In order to evaluate the performance of the sensor, quantum noise and thermal noise are calculated here. These are known as the fundamental noise in the laser interferometric gravitational wave detectors which use HG_{00} mode for length sensing. Here the noises are calculated for HG_{10} mode field in out cavity for angular sensing.

B.2.1 Quantum noise

Quantum noise originates from the fluctuation of vacuum field. Quantum noise in angular sensing is investigated in [93]. Here the calculation is applied for our system. Since the target is the angular fluctuation, quantum vacuum fluctuation of HG_{10} mode is taken into account. In the following discussions, the motion of the mirrors are assumed to be slow, hence the reflection of the mirror does not change the frequency of the field. The cavity consists of a flat front mirror and a curved end mirror as shown in Fig. B.3. Tilt of the front mirror is targeted to measure.

Consider an incident beam E_i which is dominated by HG_{00} mode. The electrical field operator can be written as

$$\hat{E}_i = \hat{E}_i^{(-)} + (\hat{E}_i^{(-)})^\dagger, \tag{B.28}$$

$$\hat{E}_i^{(-)} = \sqrt{\frac{\hbar\omega_0}{4\epsilon_0 c}}\left(D_i u_{00} + \frac{\hat{a}_1^{10} - i\hat{a}_2^{10}}{\sqrt{2}} u_{10} e^{i\zeta(z)}\right) e^{i\omega_0(t-z/c)+i\zeta(z)}, \tag{B.29}$$

where

$$\hat{a}_{1(2)}^{10} = \int_{-\infty}^{\infty} \frac{d\Omega}{2\pi} \hat{a}_{1(2)}^{10}(\Omega) e^{-\Omega(t-z/c)}, \tag{B.30}$$

$$\hat{a}_1^{10}(\Omega) \equiv \frac{\hat{a}^{10}(\omega_0+\Omega) + (\hat{a}^{10}(\omega_0-\Omega))^\dagger}{\sqrt{2}}, \tag{B.31}$$

$$\hat{a}_2^{10}(\Omega) \equiv \frac{\hat{a}^{10}(\omega_0+\Omega) - (\hat{a}^{10}(\omega_0-\Omega))^\dagger}{\sqrt{2}i}. \tag{B.32}$$

Here $\hat{a}^{10}(\omega)$ is the annihilation operator of HG_{10} mode at frequency ω. $\hat{a}_1^{10}(\Omega)$ and $\hat{a}_2^{10}(\Omega)$ are defined about the sideband frequency Ω, which is centered to the laser frequency ω_0. The incident power P_i is associated to the field amplitude D_i by $P_i = \hbar\omega_0 D_i^2$.

The reflection and amplification of the cavity can be calculated in the same way as Eq. (B.25). When a cavity satisfies both resonance conditions for HG_{00} and HG_{10}, the intra-cavity field is

$$\hat{E}_c^{(-)} = \sqrt{\frac{\hbar\omega_0}{4\epsilon_0 c}}\left(D_c u_{00} + \frac{\hat{\alpha}_1^{10} - i\hat{\alpha}_2^{10}}{\sqrt{2}} u_{10} e^{i\zeta(z)}\right) e^{i\omega_0(t-z/c)+i\zeta(z)}, \tag{B.33}$$

$$D_c = \frac{t_1\mathcal{F}}{\pi} D_i, \tag{B.34}$$

$$\hat{\alpha}_1^{10} - i\hat{\alpha}_2^{10} = \frac{t_1\mathcal{F}}{\pi}(\hat{a}_1^{10} - i\hat{a}_2^{10}) + i\frac{\mathcal{F}}{\pi}\frac{2\sqrt{2}\pi}{\lambda} w_0 D_c \theta. \tag{B.35}$$

Here $1 - r_1 r_2 \simeq \pi/\mathcal{F}$ is used. The tilt angle θ is the sum of the target angle to measure θ_s and angular fluctuation induced by the vacuum fluctuation. In the frequency space,

$$\theta(\Omega) = \theta_s(\Omega) + N_{\mathrm{rad}}(\Omega)\chi(\Omega), \tag{B.36}$$

where $\chi(\Omega)$ is the mechanical response about the rotational mode, which is given by Eq. (3.18) for a torsion pendulum. The radiation pressure torque N_{rad} from the vacuum fluctuation is

$$\begin{aligned} N_{\mathrm{rad}} &= 8\epsilon_0 \int dxdy \left(x|\hat{E}_c^{(-)}|^2\right) \\ &= \frac{2\sqrt{2}\pi\hbar}{\lambda}\frac{t_1\mathcal{F}}{\pi} D_c w_0 \hat{a}_1^{10}. \end{aligned} \tag{B.37}$$

For simplicity, the reflectivity of the end mirror r_2 is set to 1 below. In this case $t_1 = \sqrt{2\pi/\mathcal{F}}$, therefore the reflection HG$_{10}$ mode $\hat{b}^{10}_{1(2)}$ in frequency domain is given by

$$\begin{aligned}\hat{b}^{10}_1 - i\hat{b}^{10}_2 \;=\; & i\frac{4\sqrt{2}}{\lambda}D_i\mathcal{F}w_0\left(\theta_s(\Omega) + \frac{4\sqrt{2}\hbar}{\lambda}D_i\mathcal{F}w_0\chi(\Omega)\hat{a}^{10}_1(\Omega)\right.\\ & \left. -\frac{\lambda}{4\sqrt{2}}\frac{1}{D_i\mathcal{F}w_0}(\hat{a}^{10}_2(\Omega) + i\hat{a}^{10}_1(\Omega))\right). \end{aligned} \tag{B.38}$$

The second and the third terms become noise in measuring θ_s. Here the following functions are defined :

$$\theta_{\rm SQL}(\Omega) = \sqrt{2\hbar|\chi(\Omega)|}, \tag{B.39}$$

$$\mathcal{K}(\Omega) = \frac{16P_i}{\pi c\lambda}\mathcal{F}^2w_0^2\chi(\Omega). \tag{B.40}$$

Then the noise terms are expressed as

$$\theta_n(\Omega) = \frac{\theta_{\rm SQL}(\Omega)}{\sqrt{2}}\left(\sqrt{\mathcal{K}(\Omega)}\hat{a}^{10}_1(\Omega) + \frac{1}{\sqrt{\mathcal{K}(\Omega)}}(\hat{a}^{10}_2(\Omega) + i\hat{a}^{10}_1(\Omega))\right). \tag{B.41}$$

The noise depends on which quadrature of HG$_{10}$ mode to measure. When the imaginary component $\hat{b}^{10}_2$ is measured, the noise spectrum is given by

$$\sqrt{S_{\rm quantum}(f)} = \frac{\theta_{\rm SQL}}{\sqrt{2}}\sqrt{\frac{1}{|\mathcal{K}(f)|} + |\mathcal{K}(f)|}, \tag{B.42}$$

using Eq. (B.39) and (B.40). Here the vacuum is assumed to be the coherent state, therefor $\hat{a}^{10}_1$ and $\hat{a}^{10}_2$ are independent stochastic fluctuation. Then power spectral density for $\hat{a}^{10}_1$ and $\hat{a}^{10}_2$ are 1. The first and the second terms inside the square-root are the shot noise and the radiation pressure noise, respectively. In this case, $\theta_{\rm SQL}$ gives the lower limit of the quantum noise, because the shot noise and radiation pressure noise are in trade-off relation. This is why $\theta_{\rm SQL}$ is called as a standard quantum limit. Note that $\theta_{\rm SQL}$ is not the absolute limit of measurement. It can be overcome by choosing the readout quadrature or modifying the vacuum field to a squeezed state [62].

B.2.2 Mirror thermal noise

The thermal fluctuation of a mirror substrate can produce a local angular fluctuation of the surface. The effect of thermal fluctuation on the translational sensing of interferometer using Gaussian laser beam (HG$_{00}$ mode) was calculated by Y. Levin [60]. Here the effect on the angular readout (HG$_{10}$ mode) is calculated in the same manner.

The angular change of the mirror surface is measured via the HG_{10} mode in the reflected HG_{00} beam. The relation between the coefficient of the HG_{10} mode term and the angle of the surface is derived in Eq. (B.11). In general, when the surface of the mirror has a displacement $z(x, y, t)$ along the normal vector, the corresponding angle $\theta(t)$ is given by

$$\theta(t) = \frac{2}{w_0} \int d\boldsymbol{r}\, u_{10}^*(x, y) u_{00}(x, y) z(x, y, t), \tag{B.43}$$

where $u_{lm}(x, y)$ is defined as the real part of U_{lm} (Eq. (B.2)) on the mirror surface. The interaction term in the Hamiltonian of the mirror is

$$H_{\mathrm{int}} = -N(t)\theta(t) = -\int d\boldsymbol{r}\, P(x, y, t) z(x, y, t) \tag{B.44}$$

where $N(t)$ is the generalized torque corresponding to the measurement target θ, and $P(x, y)$ is the applied pressure on the surface at (x, y), which is expressed as

$$P(x, y, t) = \frac{2}{w_0} N(t) u_{10}^*(x, y) u_{00}(x, y). \tag{B.45}$$

According to the fluctuation-dissipation theorem, thermal fluctuation of θ is determined by the dissipation of the system. Specifically it is described with the real part of the admittance $\tilde{Y}(f) \equiv i\omega\tilde{\theta}(f)/\tilde{N}(f)$ as

$$S_\theta(f) = \frac{k_B T}{\pi^2 f^2} |\mathrm{Re}[\tilde{Y}(f)]|, \tag{B.46}$$

where S_θ is the power spectral density of the fluctuation of θ.

When an oscillating torque $N(t) = N_0 \sin(2\pi f t)$ is applied, dissipated energy W_{diss} is given by

$$W_{\mathrm{diss}} = \overline{N(t)\dot{\theta}(t)} = \frac{N_0^2}{2} |\mathrm{Re}[\tilde{Y}(f)]|. \tag{B.47}$$

On the other hand, the dissipated energy is expressed with the maximum elastic deformation energy U_{max} as

$$W_{\mathrm{diss}} = 2\pi f U_{max} \phi_s, \tag{B.48}$$

where ϕ_s is a loss angle of the mirror substrate, which is defined as the imaginary part of the Young's modulus normalized by the real part. From Eq. (B.47) and (B.48), the thermal noise spectrum can be rewritten as

$$S_\theta(f) = \frac{4 k_B T}{\pi f} \phi_s \frac{U_{\mathrm{max}}}{N_0^2}. \tag{B.49}$$

Below the lowest resonant frequency of the internal modes of the mirror, which is typically a few kHz, U_{max} is given by the static deformation when a static pressure $P_0(x, y) = \frac{2}{w_0} N_0 u_{10}^*(x, y) u_{00}(x, y)$ is applied on the surface.

Assuming the mirror is sufficiently larger than the beam size, then the Green's function of the mirror is given by

$$G(\boldsymbol{r},\boldsymbol{r}') = \frac{1-\nu_s^2}{\pi E_s}\frac{1}{|\boldsymbol{r}-\boldsymbol{r}'|}, \tag{B.50}$$

where ν_s and E_s are the Poisson's ratio and the Young's modulus of the mirror substrate. Therefore $U_{\max}$ is

$$\begin{aligned} U_{\max} &= \frac{1}{2}\int d\boldsymbol{r}\, P_0(x,y)z(x,y) \\ &= \frac{1}{2}\int d\boldsymbol{r}\, P_0(x,y)\int d\boldsymbol{r}'\frac{1-\nu_s^2}{\pi E_s}\frac{P_0(x',y')}{|\boldsymbol{r}-\boldsymbol{r}'|} \\ &= \frac{32(1-\nu_s^2)}{\pi^3 E_s}\frac{1}{w_0^3}\int d\boldsymbol{R}d\boldsymbol{R}'\frac{XX'}{|\boldsymbol{R}-\boldsymbol{R}'|}e^{-2(R^2+R'^2)}. \end{aligned} \tag{B.51}$$

Here $\boldsymbol{R} = (X,Y) \equiv \boldsymbol{r}/w_0$. The integral part is numerically calculated to be

$$\int d\boldsymbol{R}d\boldsymbol{R}'\frac{XX'}{|\boldsymbol{R}-\boldsymbol{R}'|}e^{-2(R^2+R'^2)} \simeq \frac{\pi^{5/2}}{64}. \tag{B.52}$$

Substituting Eq. (B.51) and (B.52) into (B.49), the amplitude spectral density of the angular thermal fluctuation is given by

$$\sqrt{S_\theta(f)} = \sqrt{\frac{2k_BT}{\pi^{3/2}f}\frac{1-\nu_s^2}{E_s}\frac{\phi_s}{w_0^3}}. \tag{B.53}$$

Comparing to the translational thermal fluctuation

$$\sqrt{S_x(f)} = \sqrt{\frac{4k_BT}{\omega}\frac{1-\nu_s^2}{\sqrt{\pi}E_s}\frac{\phi_s}{w_0}}. \tag{B.54}$$

which is derived in [60] or [61], Eq. (B.53) is equivalent to the differential translational fluctuation at two points separated by a distance of $2w_0$, each of which is measured by a beam with radius of $w_0/2$.

$$\sqrt{S_\theta(f)} = \sqrt{\frac{2}{(2w_0)^2}S_x(f;w_0/2)}. \tag{B.55}$$

The energy dissipation in the coating layer on the surface of the mirror is taken into account based on the equivalence Eq. (B.55). Thermal noise of coating layer for HG_{00} mode can be described as an additional loss angle in Eq. (B.54) [61]. Hence the angular thermal noise of HG_{10} mode is given by Eq. (B.55) with $\sqrt{S_x(f)}$ for modified loss angle. Then the total thermal noise of the mirror about HG_{10} mode is

$$\sqrt{S_{\mathrm{th,mir}}(f)} = \sqrt{\frac{2k_BT}{\pi^{3/2}f}\frac{1-\nu_s^2}{E_s}\frac{\phi_{\mathrm{mir}}}{w_0^3}}, \tag{B.56}$$

$$\phi_{\mathrm{mir}} \equiv \phi_s + \frac{2d_c}{\sqrt{\pi}w_0}\left(\frac{E_c}{E_s}\frac{(1+\nu_s)(1-2\nu_s)^2}{(1-\nu_s)(1-\nu_c^2)} + \frac{E_s}{E_c}\frac{(1+\nu_c)(1-2\nu_c)}{(1-\nu_s^2)(1-\nu_c)}\right)\phi_c, \tag{B.57}$$

where subscript s and c denote the substrate and the coating, respectively. d_c is the thickness of the coating layer.

B.3 Technical noise sources

Here some merits of the proposed angular sensor are explained.

B.3.1 Beam jitter noise

The displacement or the tilt of the laser beam are called beam jitter. They can be expressed as the incident HG_{10} mode E_{i1} in Eq. (B.22).

When both resonant conditions for HG_{00} and HG_{10} modes are satisfied, the HG_{10} mode amplitude in the reflection field of the cavity is given by solving Eq. (B.12) in the same way as Eq. (B.22).

$$E_{r1} = \frac{t_1^2 r_1 r_2}{(1 - r_1 r_2)^2} ikw_0\theta E_{i0} + \frac{-r_1 + r_2}{1 - r_1 r_2} E_{i1}. \tag{B.58}$$

The first term is the tilt signal of the mirror generated inside the cavity, and the second term is the incident jitter. As an order estimation, $t_1^2 \sim \pi/\mathcal{F}$, $r_i \simeq 1 - t_1^2/2$ and $r_1 - r_2 \sim \pi/\mathcal{F}$ give

$$E_{r1} \sim \frac{\mathcal{F}}{\pi} ikw_0\theta E_{i0} + E_{i1}, \tag{B.59}$$

which indicates the beam jitter term is not amplified while the tilt signal is amplified by $\mathcal{F}$. This is because the tilt signal is generated from the intra-cavity HG_{00} mode which is amplified by the cavity. Therefore coherent angular signal amplification method can increase the signal-to-noise ratio against the beam jitter noise.

Additionally, by setting $r_1 = r_2$ (critical-coupled cavity) for HG_{10} mode, the beam jitter term vanishes at the reflection port, which enables the beam jitter free angular sensor. Note that such an option is possible only when the reflectivity can be set independently for HG_{00} mode and HG_{10} mode. This is because when $r_1 = r_2$ is satisfied for HG_{00} mode, all of HG_{00} beam transmits through the cavity, hence HG_{10} mode signal cannot be measured via the beat with HG_{00} mode at the reflection port. The coupled-cavity configuration solves this problem since the reflectivity of the auxiliary cavity (Fig. B.5) can be chosen independently for HG_{00} and HG_{10} modes.

B.3.2 Frequency noise

Frequency fluctuation basically does not appear in the angular signal, since the fluctuation is spatially uniform in the cross section of the beam. This is an advantage over a Michelson interferometric angular readout which use two

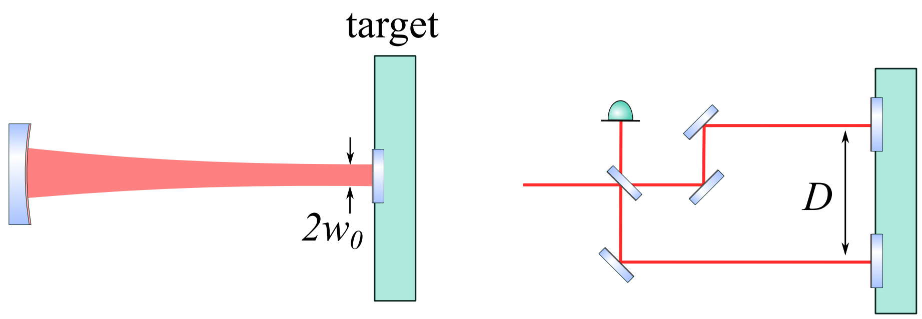

Figure B.6: Comparison of two angular sensing; an optical cavity (left) and a Michelson interferometer (right).

separated laser beams. In a Michelson interferometer, the asymmetry of the beam path length introduces the frequency fluctuation as the angular signal noise.

B.3.3 Translational coupling noise

Although translation of the mirror along the reflection surface ideally does not generate angular signal, a curvature of the surface introduces the coupling from it [21]. Hence by using a flat mirror for one of the cavity mirrors, the coupling from translations can be suppressed. Ultimately the amount of coupling is determined by the profile of the mirror surface in the scale of the beam size. It is possible in principle to find a locally flat point on the surface where the translational coupling vanishes.

B.4 Comparison to a Michelson interferometer

Here the proposed new angular sensor is compared to a Michelson interferometer, which is another sensitive interferometric angular sensor. Michelson interferometers have been used for angular sensing in the previous prototypes of TOBA so far. Two angular sensing methods are depicted in Fig. B.6. The new method amplifies the angular signal generated by a mirror, hence one of the cavity mirrors is attached on the measurement target. For an angular sensing with a Michelson interferometer, two mirrors are attached on the target separated by D, then the angular fluctuation is calculated from the differential translation between the reflection points.

As mentioned in Sec. B.2.2, the angular sensing using HG_{10} mode in the cavity is equivalent to the translational sensing at two points separated by the beam diameter $2w_0$. Though the beam diameter is usually much shorter than the separation in the Michelson interferometer D, the amplification of

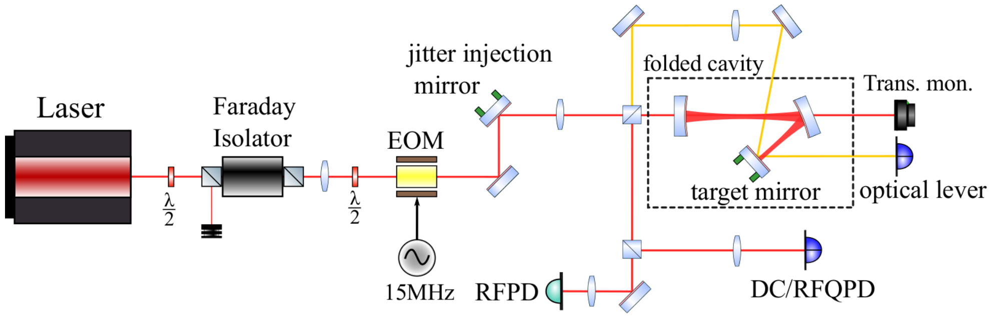

Figure B.7: An experimental setup for a demonstration of coherent angular signal amplification using a folded cavity.

the cavity can compensate the difference. In other words, when $2w_0\mathcal{F} \sim D$, both of the sensing methods can acquire the same amount of angular signal.

In terms of noise, each sensing method has merits and demerits as mentioned in the previous sections. The quantum noises are in the similar levels for the two sensing methods since their signal levels are similar. On the other hand, thermal noise is smaller in the Michelson interferometer according to the larger separation of the beams : $D \gg 2w_0$. The optical cavity method has merits in some technical noise. The frequency fluctuation does not become a noise in the optical cavity, while the Michelson interferometer is suffered from it via the asymmetry of the beam. Additionally, the use of the single beam for the cavity method can provide an easier reduction of translational coupling, because placing two mirrors in parallel at separated points for the Michelson interferometer is technically hard. Though it is possible to polish the whole surface of the target to make it parallel at two reflection points, technical difficulty rises as the size of the target increases.

In summary, when the mirror thermal noise is sufficiently small, coherent angular signal amplification with an optical cavity can provide some technical merits compared to a Michelson interferometer.

B.5 Experimental demonstration

Here an experimental resluts on the angular signal amplification with an optical cavity is reported. The folded cavity configuration is used for the experiment. The setup is shown in Fig. B.7. The length change of the cavity was measured by PDH method using the EOM (electro-optic modulator) and the RFPD (Radio frequency photo detector). Then the cavity was locked at the resonant point of HG_{00} mode. One of the cavity mirrors (a target mirror) was shaken with PZT actuators on the mirror, to measure the angular signal by a QPD at the reflection port. The QPD reads the DC signal and modulated RF (15 MHz) signal, which correspond to the real part and the imaginary part of HG_{10}

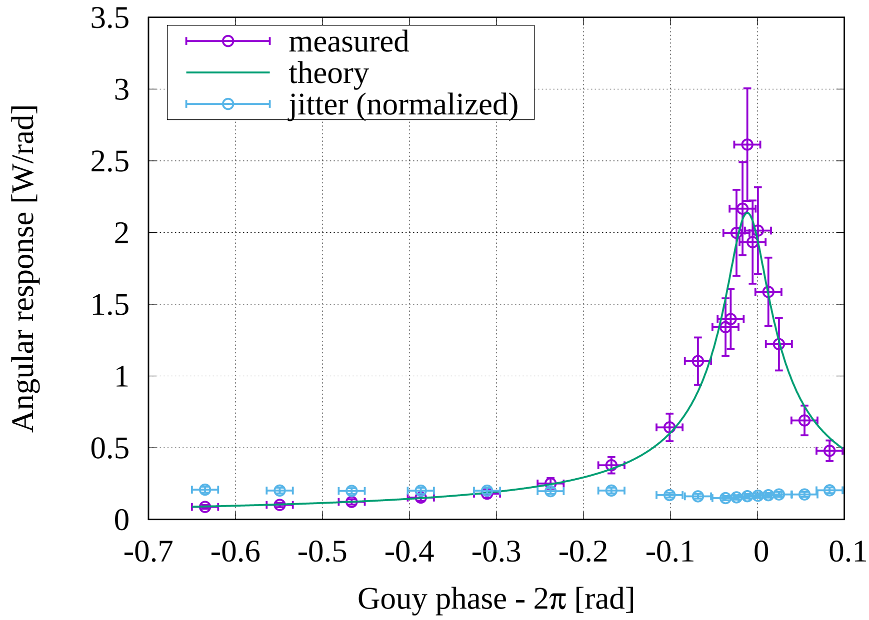

Figure B.8: Measured angular responses vs the Gouy phase of the cavity. The purple points are the response to the cavity mirror, and the green line is the theoretical line for it. The blue points are the response to the beam jitter, whose amplitude is scaled by the beam radius at the jitter injection mirror.

mode generated from the cavity, respectively. During the measurement, the tilt angle of the mirror is monitored with the optical lever (oplev) at the same time for calibration.

The Gouy phase of the cavity was adjusted by changing the positions of the mirrors. The correspondence between the positions of the mirrors and the Gouy phase was calibrated by scanning the length of the cavity. The separations of resonant points of HG_{00} mode and higher order modes is the Gouy phase. The cavity scan was performed at off-resonant points of HG_{10} mode, where the modes are separated enough to determine the Gouy phase. Around the resonant point of HG_{10} mode, the Gouy phase of the cavity was interpolated from the measurement at nearby points. The finesse of the cavity was measured at the same time, which was $\mathcal{F} = 122 \pm 5$.

Fig. B.8 shows the measured angular response of the folded cavity in unit of the differential power of the laser between the segments of the QPD. The theoretical line inferred from the measured finesse, the beam profile and the output power is also plotted in the figure. As expected from the theory, the angular response is amplified when the Gouy phase becomes 2π. The amplification factor is also agrees with the theoretical curve within the measurement error. The responses to the beam jitter injected by shaking the mirror before the cavity (the "jitter injection mirror" in Fig. B.7) are also plotted with blue circles in Fig. B.8. In contrast to the cavity mirror, the response is not amplified as expected.

In summary, this experiment has confirmed the basic principle of the coherent angular signal amplification with a folded cavity.

C Circuit Diagram

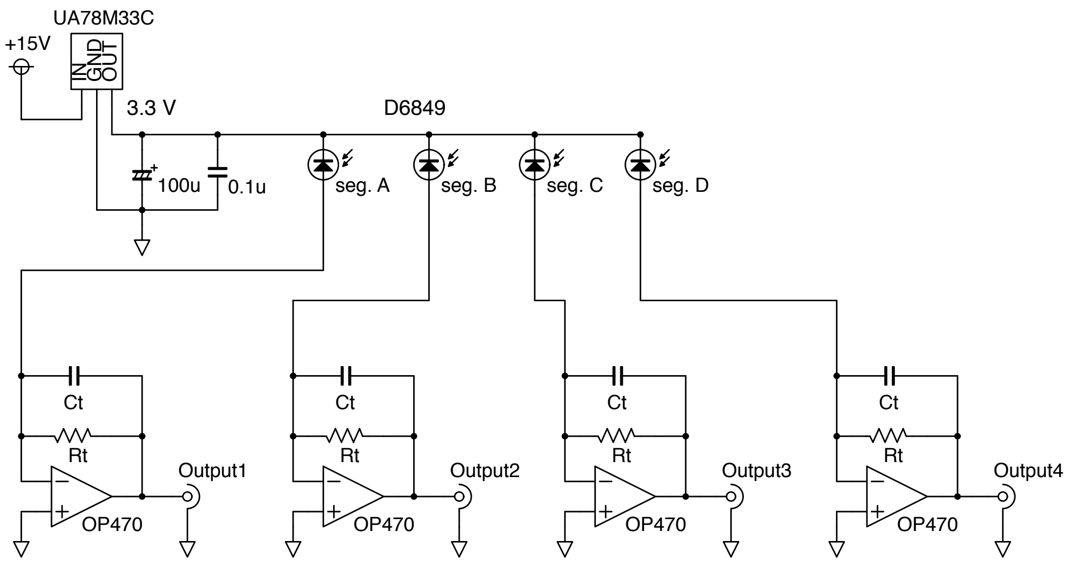

Figure C.1: A trans impedance circuit for the QPDs of the beam jitter monitors, the optical levers and the wave front sensors. For the trans impedances, $R_t = 150\text{k}\Omega, 330\text{k}\Omega$ and $C_t = 100\text{pF}$ are used.

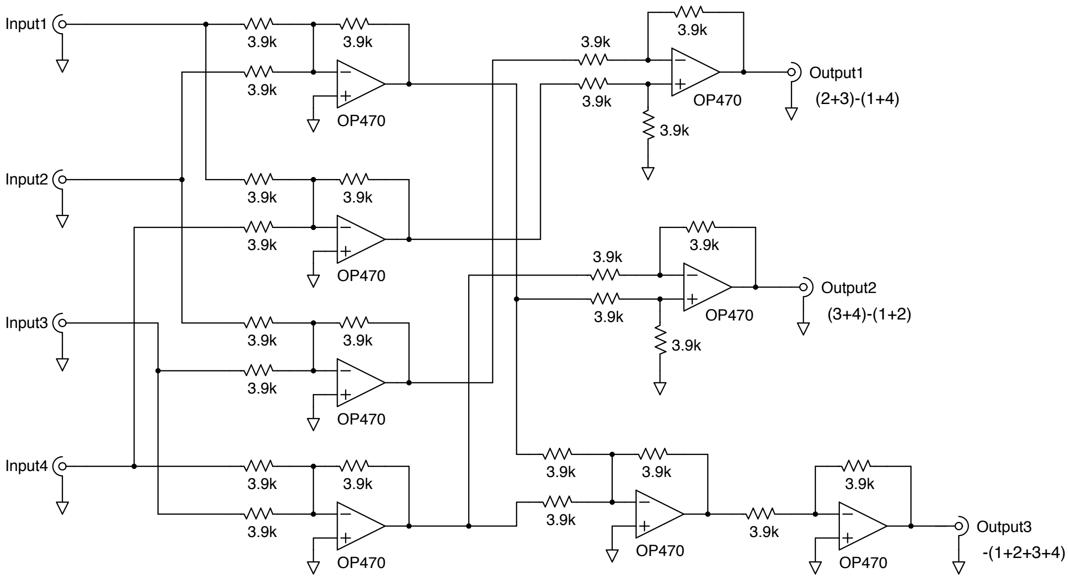

Figure C.2: A summation and differential circuit for the QPDs. From four signal of a QPD (Input 1-4), the horizontal differential signal (Output1), the vertical differential signal (Output2), and the total power signal (Output3) are calculated.

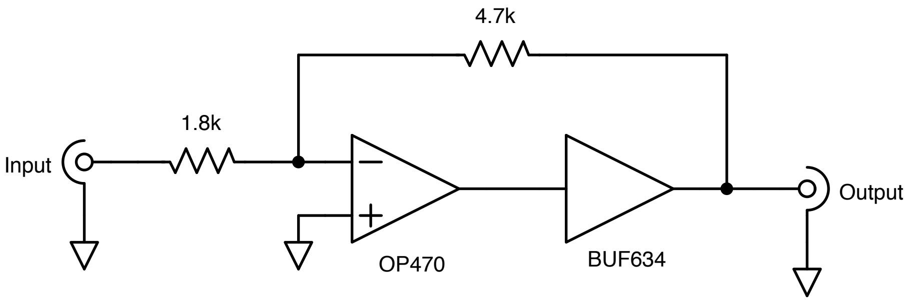

Figure C.3: A coil driver for coil-coil actuator. A current buffer BUF634 supplies current for coils.

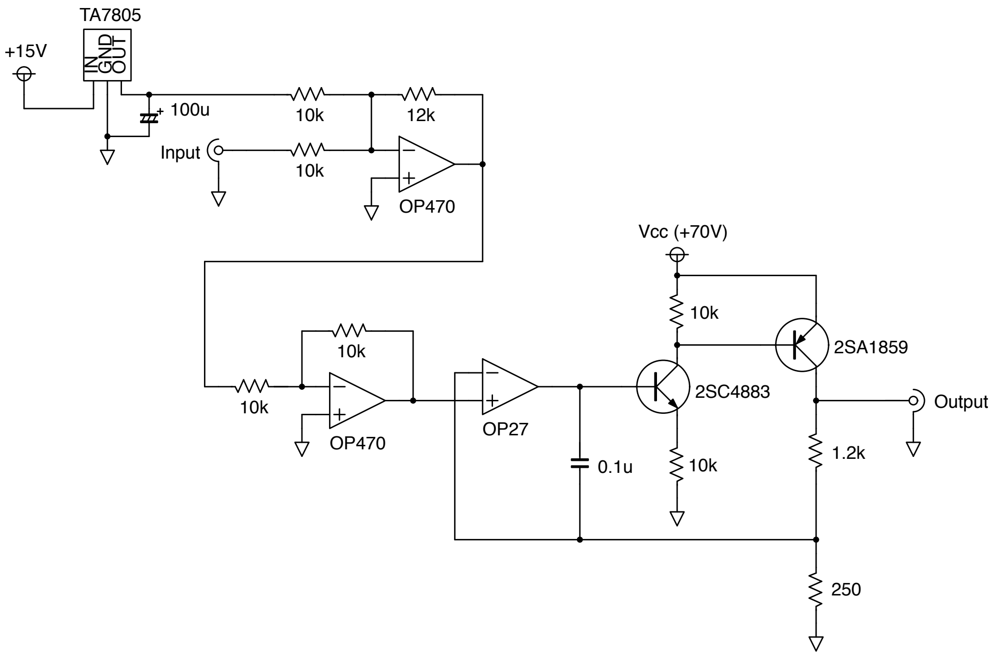

Figure C.4: A high voltage amplifier for PZT actuators. The output voltage range is determined by V_{cc}, which is set to 70 V in this thesis.

Acknowledgement

I am full of gratitude to many people who have been supported this work.

First, I greatly appreciate my supervisor Masaki Ando for his huge supports to me. I have been working in his laboratory for five years since I entered the graduate school of University of Tokyo. He told me many things about gravitational wave detectors including laser interferometer, mechanical suspension, control schemes and so on. These form the basis of my knowledge that was essential to my experiment. I could not have completed my work without the supports from him.

I am grateful to Yuta Michumura, who is an assistant professor of our laboratory. He always gave me insightful comments on my experiments, which enhanced the value of the research much. I was always impressed by his deep and wide knowledge on physics and experiments.

I deeply appreciate Takafumi Ushiba, Kunihiko Hasegawa and Takaharu Shishido for their helps about the cryogenic technique. Takafumi Ushiba gave me a lot of advices as a specialist of cryogenic technique and a laser interferometer. He told me what kind of components should be used in the cryogenic experiments, and how to treat them. I could not design the cryogenic system of TOBA without his supports. Kunihiko Hasegawa and Takaharu Shishido helped me to oxidize the suspension parts at KEK. Thanks to their helps, the high emissivity of the components, which is one of the key requirements in the cryogenic system of TOBA, was achieved. I have to apologize them about the issues of aluminum.

I was also helped a lot by Satoru Takano, Ooi Ching Pin and Yuki Miyazaki, who are the members of TOBA experiments. Satoru Takano made the design of current active vibration systems. I often worked with him about the construction of the system. Ooi Ching Pin is developing the suspension wire, which is the essential component in reducing the thermal noise. Yuki Miyazaki is working on the sensitive angular sensor which will be an essential part in TOBA. Many discussions with them deepened my understanding about each system. I could not constructed the TOBA setup without helps from them.

I am grateful to Kévin Juhel and Matteo Barsuglia, who accepted me to stay their laboratory in France for two months. During the stay, I studied a lot about gravity-based earthquakes early warning and did calculation works with them. What I learned there is a basis of the theoretical works in this thesis. This stay was one of the most exciting time for me.

I am thankful to Nobuki Kame and Masaya Kimura in Earthquake Research

Institute. I discussed with them on my localization simulation work, and they gave me fruitful comments on it. The strategy of the simulation was made based on their comments.

I also appreciate the members of Ando laboratory; Kentaro Komori, Yutaro Enomoto, Koji Nagano, Naoki Aritomi, Hiroki Takeda, Takuya Kawasaki, Naoki Kita and Hiroki Chiyoda. Many discussions with them were surely improved my laboratory life. I spent an exciting time in the laboratory thanks to them.

Togo Shimozawa and Shigemi Otsuka, who are the technical staffs in University of Tokyo, made most of the suspension components. Without their help, I could not construct the fundamental parts of the experimental setup.

I am also thankful to examiners of my thesis, Hiroyuki Sekiya, Hiroshi Fukuyama, Junji Yumoto, Katsuaki Asano and Yuichi Imanishi. Their insightful and objective comments on the thesis surely helped me to clarify the logic of this work and future prospects.

Finally, I would like to express special thanks to my parents for their continuous support since I was born. I also cannot thank my girlfriend enough for always being with me.

The work about TOBA was supported by JSPS KAKENHI Grants Number JP16H03972, JP24244031 and JP18684005. This work was also supported by MEXT Quantum Leap Flagship Program (MEXT Q-LEAP) Grant Number JPMXS0118070351. Some of the figures in this thesis uses the components of optics illustration created by Alexander Franzen. The measurement of magnetic properties of copper at cryogenic temperatures was performed using facilities of the Cryogenic Research Center, the University of Tokyo. We would like to thank Editage (www.editage.com) for English language editing for the abstract, Chapter 1, and Chapter 8.

Bibliography

[1] J. Harms, J.-P. Ampuero, M. Barsuglia, E. Chassande-Mottin, J.-P. Montagner, S. N. Somala, and B. F. Whiting. Transient gravity perturbations induced by earthquake rupture. *Geophysical Journal International*, 201(3):1416–1425, 2015.

[2] K. Juhel, J. P. Ampuero, M. Barsuglia, P. Bernard, E. Chassande-Mottin, D. Fiorucci, J. Harms, J.-P. Montagner, M. Vallée, and B. F. Whiting. Earthquake Early Warning Using Future Generation Gravity Strainmeters. *Journal of Geophysical Research: Solid Earth*, 123(12):10,889–10,902, 2018.

[3] Jean-Paul Montagner, Kévin Juhel, Matteo Barsuglia, Jean Paul Ampuero, Eric Chassande-Mottin, Jan Harms, Bernard Whiting, Pascal Bernard, Eric Clévédé, and Philippe Lognonné. Prompt gravity signal induced by the 2011 Tohoku-Oki earthquake. *Nature Communications*, 7:13349 EP –, 11 2016.

[4] Martin Vallée, Jean Paul Ampuero, Kévin Juhel, Pascal Bernard, Jean-Paul Montagner, and Matteo Barsuglia. Observations and modeling of the elastogravity signals preceding direct seismic waves. *Science*, 358(6367):1164–1168, 2017.

[5] Masaya Kimura, Nobuki Kame, Shingo Watada, Makiko Ohtani, Akito Araya, Yuichi Imanishi, Masaki Ando, and Takashi Kunugi. Earthquake-induced prompt gravity signals identified in dense array data in Japan. *Earth, Planets and Space*, 71(1):27, 2019.

[6] Martin Vallée, Jean Paul Ampuero, Kévin Juhel, Pascal Bernard, Jean-Paul Montagner, and Matteo Barsuglia. Comment on "earthquake-induced prompt gravity signals identified in dense array data in japan"by kimura et al. *Earth, Planets and Space*, 71(1):51, 2019.

[7] Masaya Kimura, Nobuki Kame, Shingo Watada, Makiko Ohtani, Akito Araya, Yuichi Imanishi, Masaki Ando, and Takashi Kunugi. Reply to comment by vallée et al. on "earthquake-induced prompt gravity signals identified in dense array data in japan". *Earth, Planets and Space*, 71(1):120, 2019.

[8] Martin Vallée and Kévin Juhel. Multiple observations of the prompt elastogravity signals heralding direct seismic waves. *Journal of Geophysical Research: Solid Earth*, 124(3):2970–2989, 2019.

[9] B. P. Abbott *et al.*,. Observation of Gravitational Waves from a Binary Black Hole Merger. *Phys. Rev. Lett.*, 116:061102, Feb 2016.

[10] B. P. Abbott *et al.*,. GW170817: Observation of Gravitational Waves from a Binary Neutron Star Inspiral. *Phys. Rev. Lett.*, 119:161101, Oct 2017.

[11] B. P. Abbott *et al.*,. Gwtc-1: A gravitational-wave transient catalog of compact binary mergers observed by ligo and virgo during the first and second observing runs. *Phys. Rev. X*, 9:031040, Sep 2019.

[12] B. P. Abbott *et al.*,. Binary black hole population properties inferred from the first and second observing runs of advanced LIGO and advanced virgo. *The Astrophysical Journal*, 882(2):L24, sep 2019.

[13] B. P. Abbott *et al.*,. Gravitational waves and gamma-rays from a binary neutron star merger: GW170817 and GRB 170817a. *The Astrophysical Journal*, 848(2):L13, oct 2017.

[14] B. P. Abbott *et al.*,. Tests of general relativity with gw150914. *Phys. Rev. Lett.*, 116:221101, May 2016.

[15] Toshikazu Ebisuzaki, Junichiro Makino, Takeshi Go Tsuru, Yoko Funato, Simon Portegies Zwart, Piet Hut, Steve McMillan, Satoki Matsushita, Hironori Matsumoto, and Ryohei Kawabe. Missing link found? the "runaway" path to supermassive black holes. *The Astrophysical Journal*, 562(1):L19–L22, nov 2001.

[16] Masaki Ando, Koji Ishidoshiro, Kazuhiro Yamamoto, Kent Yagi, Wataru Kokuyama, Kimio Tsubono, and Akiteru Takamori. Torsion-Bar Antenna for Low-Frequency Gravitational-Wave Observations. *Phys. Rev. Lett.*, 105:161101, Oct 2010.

[17] Koji Ishidoshiro, Masaki Ando, Akiteru Takamori, Hirotaka Takahashi, Kenshi Okada, Nobuyuki Matsumoto, Wataru Kokuyama, Nobuyuki Kanda, Yoichi Aso, and Kimio Tsubono. Upper Limit on Gravitational Wave Backgrounds at 0.2 Hz with a Torsion-Bar Antenna. *Phys. Rev. Lett.*, 106:161101, Apr 2011.

[18] Ayaka Shoda, Yuya Kuwahara, Masaki Ando, Kazunari Eda, Kodai Tejima, Yoichi Aso, and Yousuke Itoh. Ground-based low-frequency gravitational-wave detector with multiple outputs. *Phys. Rev. D*, 95:082004, Apr 2017.

[19] Wataru Kokuyama. *Spaceborne Rotating Torsion-Bar Antenna for Low-Frequency Gravitational-Wave Observations*. PhD thesis, The University of Tokyo, 2012.

[20] Tomofumi Shimoda, Satoru Takano, Ching Pin Ooi, Naoki Aritomi, Yuta Michimura, Masaki Ando, and Ayaka Shoda. Torsion-bar antenna: A ground-based mid-frequency and low-frequency gravitational wave detector. *International Journal of Modern Physics D*, 28:1940003, 2019.

[21] Tomofumi Shimoda, Naoki Aritomi, Ayaka Shoda, Yuta Michimura, and Masaki Ando. Seismic cross-coupling noise in torsion pendulums. *Phys. Rev. D*, 97:104003, May 2018.

[22] Tomofumi Shimoda and Masaki Ando. Nonlinear vibration transfer in torsion pendulums. *Classical and Quantum Gravity*, 36(12):125001, may 2019.

[23] Jan Harms. Terrestrial gravity fluctuations. *Living Reviews in Relativity*, 18(1):3, Dec 2015.

[24] J. Harms. Transient gravity perturbations from a double-couple in a homogeneous half-space. *Geophysical Journal International*, 205(2):1153–1164, 2016.

[25] Riley Newman, Michael Bantel, Eric Berg, and William Cross. A measurement of *G* with a cryogenic torsion pendulum. *Philosophical Transactions of the Royal Society A: Mathematical, Physical and Engineering Sciences*, 372(2026):20140025, 2014.

[26] K. Somiya (KAGRA Collaboration). Detector configuration of KAGRA - the Japanese cryogenic gravitational-wave detector. *Classical and Quantum Gravity*, 29(12):124007, 2012.

[27] Yuichi Imanishi, Tadahiro Sato, Toshihiro Higashi, Wenke Sun, and Shuhei Okubo. A network of superconducting gravimeters detects submicrogal coseismic gravity changes. *Science*, 306(5695):476–478, 2004.

[28] B. D. Tapley, S. Bettadpur, M. Watkins, and C. Reigber. The gravity recovery and climate experiment: Mission overview and early results. *Geophysical Research Letters*, 31(9), 2004.

[29] Shin-Chan Han, C. K. Shum, Michael Bevis, Chen Ji, and Chung-Yen Kuo. Crustal dilatation observed by grace after the 2004 sumatra-andaman earthquake. *Science*, 313(5787):658–662, 2006.

[30] Kosuke Heki and Koji Matsuo. Coseismic gravity changes of the 2010 earthquake in central chile from satellite gravimetry. *Geophysical Research Letters*, 37(24), 2010.

[31] Koji Matsuo and Kosuke Heki. Coseismic gravity changes of the 2011 tohoku-oki earthquake from satellite gravimetry. *Geophysical Research Letters*, 38(7), 2011.

[32] Keiiti Aki and Paul G. Richards. *Quantitative Seismology, 2nd Edition.* University Science Books, 2009.

[33] Martin Vallée and Vincent Douet. A new database of source time functions (stfs) extracted from the scardec method. *Physics of the Earth and Planetary Interiors*, 257:149 – 157, 2016.

[34] Heidi Houston. Influence of depth, focal mechanism, and tectonic setting on the shape and duration of earthquake source time functions. *Journal of Geophysical Research: Solid Earth*, 106(B6):11137–11150, 2001.

[35] Fabrice Cotton and Olivier Coutant. Dynamic stress variations due to shear faults in a plane-layered medium. *Geophysical Journal International*, 128(3):676–688, 03 1997.

[36] K Juhel, J-P Montagner, M Vallée, J P Ampuero, M Barsuglia, P Bernard, E Clévédé, J Harms, and B F Whiting. Normal mode simulation of prompt elastogravity signals induced by an earthquake rupture. *Geophysical Journal International*, 216(2):935–947, 2019.

[37] J Aasi *et al.,* (LIGO Scientific Collaboration). Advanced LIGO. *Classical and Quantum Gravity*, 32(7):074001, 2015.

[38] F. Acernese *et al.,* (Virgo Collaboration). Advanced Virgo: a second-generation interferometric gravitational wave detector. *Classical and Quantum Gravity*, 32(2):024001, 2015.

[39] B. P. Abbott *et al.,*. Multi-messenger observations of a binary neutron star merger. *The Astrophysical Journal*, 848(2):L12, oct 2017.

[40] K. Danzmann and the LISA study team. LISA: laser interferometer space antenna for gravitational wave measurements. *Classical and Quantum Gravity*, 13(11A):A247, 1996.

[41] Seiji Kawamura *et al.,*. The Japanese space gravitational wave antenna: DECIGO. *Classical and Quantum Gravity*, 28(9):094011, 2011.

[42] Jan Harms, Bram J. J. Slagmolen, Rana X. Adhikari, M. Coleman Miller, Matthew Evans, Yanbei Chen, Holger Müller, and Masaki Ando. Low-frequency terrestrial gravitational-wave detectors. *Phys. Rev. D*, 88:122003, Dec 2013.

[43] Maggiore Michele. *Gravitational Waves.* Oxford University Press, 2008.

[44] J.H. Taylor and J.M. Weisberg. Further experimental tests of relativistic gravity using the binary pulsar psr 1913 + 16. *Astrophysical Journal; (USA)*, 345, 10 1989.

[45] Dheeraj R. Pasham, Tod E. Strohmayer, and Richard F. Mushotzky. A 400-solar-mass black hole in the galaxy m82. *Nature*, 513:74 EP –, 08 2014.

[46] Bülent Kızıltan, Holger Baumgardt, and Abraham Loeb. An intermediate-mass black hole in the centre of the globular cluster 47 tucanae. *Nature*, 542:203 EP –, 02 2017.

[47] Shunya Takekawa, Tomoharu Oka, Yuhei Iwata, Shiho Tsujimoto, and Mariko Nomura. Indication of another intermediate-mass black hole in the galactic center. *The Astrophysical Journal*, 871(1):L1, jan 2019.

[48] Tristan L. Smith, Marc Kamionkowski, and Asantha Cooray. Direct detection of the inflationary gravitational-wave background. *Phys. Rev. D*, 73:023504, Jan 2006.

[49] D J McManus, P W F Forsyth, M J Yap, R L Ward, D A Shaddock, D E McClelland, and B J J Slagmolen. Mechanical characterisation of the TorPeDO: a low frequency gravitational force sensor. *Classical and Quantum Gravity*, 34(13):135002, 2017.

[50] H. A. Chan and H. J. Paik. Superconducting gravity gradiometer for sensitive gravity measurements. i. theory. *Phys. Rev. D*, 35:3551–3571, Jun 1987.

[51] Ho Jung Paik, Cornelius E Griggs, M Vol Moody, Krishna Venkateswara, Hyung Mok Lee, Alex B Nielsen, Ettore Majorana, and Jan Harms. Low-frequency terrestrial tensor gravitational-wave detector. *Classical and Quantum Gravity*, 33(7):075003, mar 2016.

[52] M. Vol Moody, Ho Jung Paik, and Edgar R. Canavan. Three-axis superconducting gravity gradiometer for sensitive gravity experiments. *Review of Scientific Instruments*, 73(11):3957–3974, 2002.

[53] Paik, Ho Jung. Sogro (superconducting omni-directional gravitational radiation observatory). *EPJ Web Conf.*, 168:01005, 2018.

[54] David W. Keith, Christopher R. Ekstrom, Quentin A. Turchette, and David E. Pritchard. An interferometer for atoms. *Phys. Rev. Lett.*, 66:2693–2696, May 1991.

[55] M. Kasevich and S. Chu. Measurement of the gravitational acceleration of an atom with a light-pulse atom interferometer. *Applied Physics B*, 54(5):321–332, May 1992.

[56] Savas Dimopoulos, Peter W. Graham, Jason M. Hogan, Mark A. Kasevich, and Surjeet Rajendran. Atomic gravitational wave interferometric sensor. *Phys. Rev. D*, 78:122002, Dec 2008.

[57] B. Canuel, A. Bertoldi, L. Amand, E. Pozzo di Borgo, T. Chantrait, C. Danquigny, M. Dovale Álvarez, B. Fang, A. Freise, R. Geiger, J. Gillot, S. Henry, J. Hinderer, D. Holleville, J. Junca, G. Lefèvre, M. Merzougui, N. Mielec, T. Monfret, S. Pelisson, M. Prevedelli, S. Reynaud, I. Riou, Y. Rogister, S. Rosat, E. Cormier, A. Landragin, W. Chaibi, S. Gaffet, and P. Bouyer. Exploring gravity with the MIGA large scale atom interferometer. *Scientific Reports*, 8(1):14064, 2018.

[58] M. Armano *et al.*,. Sub-femto-g free fall for space-based gravitational wave observatories: Lisa pathfinder results. *Phys. Rev. Lett.*, 116:231101, Jun 2016.

[59] Peter R. Saulson. Thermal noise in mechanical experiments. *Phys. Rev. D*, 42:2437–2445, Oct 1990.

[60] Yu. Levin. Internal thermal noise in the ligo test masses: A direct approach. *Phys. Rev. D*, 57:659–663, Jan 1998.

[61] Gregory M Harry, Andri M Gretarsson, Peter R Saulson, Scott E Kittelberger, Steven D Penn, William J Startin, Sheila Rowan, Martin M Fejer, D R M Crooks, Gianpietro Cagnoli, Jim Hough, and Norio Nakagawa. Thermal noise in interferometric gravitational wave detectors due to dielectric optical coatings. *Classical and Quantum Gravity*, 19(5):897–917, feb 2002.

[62] H. J. Kimble, Yuri Levin, Andrey B. Matsko, Kip S. Thorne, and Sergey P. Vyatchanin. Conversion of conventional gravitational-wave interferometers into quantum nondemolition interferometers by modifying their input and/or output optics. *Phys. Rev. D*, 65:022002, Dec 2001.

[63] Donatella Fiorucci, Jan Harms, Matteo Barsuglia, Irene Fiori, and Federico Paoletti. Impact of infrasound atmospheric noise on gravity detectors used for astrophysical and geophysical applications. *Phys. Rev. D*, 97:062003, Mar 2018.

[64] Peter R. Saulson. Terrestrial gravitational noise on a gravitational wave antenna. *Phys. Rev. D*, 30:732–736, Aug 1984.

[65] Scott A. Hughes and Kip S. Thorne. Seismic gravity-gradient noise in interferometric gravitational-wave detectors. *Phys. Rev. D*, 58:122002, Nov 1998.

[66] Teviet Creighton. Tumbleweeds and airborne gravitational noise sources for LIGO. *Classical and Quantum Gravity*, 25(12):125011, jun 2008.

[67] Jennifer C. Driggers, Jan Harms, and Rana X. Adhikari. Subtraction of Newtonian noise using optimized sensor arrays. *Phys. Rev. D*, 86:102001, Nov 2012.

[68] Jan Harms and Krishna Venkateswara. Newtonian-noise cancellation in large-scale interferometric GW detectors using seismic tiltmeters. *Classical and Quantum Gravity*, 33(23):234001, 2016.

[69] Jan Harms and Stefan Hild. Passive newtonian noise suppression for gravitational-wave observatories based on shaping of the local topography. *Classical and Quantum Gravity*, 31(18):185011, aug 2014.

[70] H. Ohta, A. Koike, K. Hoshino, H. Kotaka, E. Sudoh, K. Kato, H. Takahara, Y. Uchikawa, K. Shinada, M. Takahata, Y. Yamada, and T. Matsui. Neuromagnetic squid measurements in a helmet-type superconducting magnetic shield of bscco. *IEEE Transactions on Applied Superconductivity*, 3(1):1953–1956, March 1993.

[71] Miroslav Micic, Kelly Holley-Bockelmann, Steinn Sigurdsson, and Tom Abel. Supermassive black hole growth and merger rates from cosmological N-body simulations. *Monthly Notices of the Royal Astronomical Society*, 380(4):1533–1540, 09 2007.

[72] M. Armano *et al.*,. Beyond the required lisa free-fall performance: New lisa pathfinder results down to 20 μHz. *Phys. Rev. Lett.*, 120:061101, Feb 2018.

[73] Ayaka Shoda, Masaki Ando, Koji Ishidoshiro, Kenshi Okada, Wataru Kokuyama, Yoichi Aso, and Kimio Tsubono. Search for a stochastic gravitational-wave background using a pair of torsion-bar antennas. *Phys. Rev. D*, 89:027101, Jan 2014.

[74] Ayaka Shoda. *Development of a High-Angular-Resolution Antenna for Low-Frequency Gravitational-Wave Observation*. PhD thesis, The University of Tokyo, 2015.

[75] Kazunari Eda, Ayaka Shoda, Yousuke Itoh, and Masaki Ando. Improving parameter estimation accuracy with torsion-bar antennas. *Phys. Rev. D*, 90:064039, Sep 2014.

[76] Yuya Kuwahara, Ayaka Shoda, Kazunari Eda, and Masaki Ando. Search for a stochastic gravitational wave background at 1–5 hz with a torsion-bar antenna. *Phys. Rev. D*, 94:042003, Aug 2016.

[77] Seiya Uyeda and Hiroo Kanamori. Back-arc opening and the mode of subduction. *Journal of Geophysical Research: Solid Earth*, 84(B3):1049–1061, 1979.

[78] D. J. McManus, P. W. F. Forsyth, N. A. Holland, R. L. Ward, D. A. Shaddock, D. E. McClelland, and B. J. J. Slagmolen. Early Earthquake Detection with a Dual Torsion-Beam Gravimeter. *arXiv*, 1809.04787, 2018.

[79] D. F. McGuigan, C. C. Lam, R. Q. Gram, A. W. Hoffman, D. H. Douglass, and H. W. Gutche. Measurements of the mechanical q of single-crystal silicon at low temperatures. *Journal of Low Temperature Physics*, 30(5):621–629, Mar 1978.

[80] R Nawrodt, C Schwarz, S Kroker, I W Martin, R Bassiri, F Brückner, L Cunningham, G D Hammond, D Heinert, J Hough, T Käsebier, E-B Kley, R Neubert, S Reid, S Rowan, P Seidel, and A Tünnermann. Investigation of mechanical losses of thin silicon flexures at low temperatures. *Classical and Quantum Gravity*, 30(11):115008, may 2013.

[81] C. J. Glassbrenner and Glen A. Slack. Thermal conductivity of silicon and germanium from 3°k to the melting point. *Phys. Rev.*, 134:A1058–A1069, May 1964.

[82] W. Duffy. Acoustic quality factor of copper, brass and beryllium copper from 50 mk to 300 k. *Cryogenics*, 32(12):1121 – 1124, 1992.

[83] N.J. Simon, E.S. Drexler, and R.P. Reed. Properties of copper and copper alloys at cryogenic temperatures. 2 1992.

[84] Guy K. White. *Experimental Techniques In Low-Temperature Physics (Fourth Edition)*. Oxford University Press, 2002.

[85] Yusuke Sakakibara. *A Study of Cryogenic Techniques for Gravitational Wave Detection*. PhD thesis, The University of Tokyo, 2015.

[86] Takayuki Tomaru, Hiroaki Hoshikawa, Hiroshi Tabuchi, and Takakazu Shintomi. Conduction cooling using ultra-pure fine metal wire i -pure aluminum-. *TEION KOGAKU（J. Cryo. Super. Soc. Jpn.)*, 46:415, 2011.

[87] Eric D. Black. An introduction to pound-drever-hall laser frequency stabilization. *American Journal of Physics*, 69(1):79–87, 2001.

[88] Janyce Franc, Nazario Morgado, Raffaele Flaminio, Ronny Nawrodt, Iain Martin, Liam Cunningham, Alan Cumming, Sheila Rowan, and James Hough. Mirror thermal noise in laser interferometer gravitational wave detectors operating at room and cryogenic temperature, 2009.

[89] Eiichi Hirose, Dan Bajuk, GariLynn Billingsley, Takaaki Kajita, Bob Kestner, Norikatsu Mio, Masatake Ohashi, Bill Reichman, Hiroaki Yamamoto, and Liyuan Zhang. Sapphire mirror for the kagra gravitational wave detector. *Phys. Rev. D*, 89:062003, Mar 2014.

[90] J.R. Davis. *Copper and Copper Alloys.* ASM International, 2001.

[91] Gautam Sinha and S. S. Prabhu. Analytical model for estimation of eddy current and power loss in conducting plate and its application. *Phys. Rev. ST Accel. Beams*, 14:062401, Jun 2011.

[92] Anthony E. Siegman. *LASERS.* University Science Books, 1990.

[93] Yutaro Enomoto, Koji Nagano, and Seiji Kawamura. Standard quantum limit of angular motion of a suspended mirror and homodyne detection of a ponderomotively squeezed vacuum field. *Phys. Rev. A*, 94:012115, Jul 2016.